UNIVERSITÉ DE STRASBOURG

ÉCOLE DOCTORALE 182
Institut Charles Sadron

THÈSE

présentée par :

Swen HELSTROFFER

soutenue le : **9 décembre 2024**

pour obtenir le grade de : **Docteur de l'université de Strasbourg**
Discipline/ Spécialité : Physique

Lubrication mechanisms of lipid layers: role of water and electrostatic interactions

THÈSE dirigée par :

M. CHARITAT Thierry	Professeur, ICS, Université de Strasbourg

RAPPORTEURS :

M^{me} BARENTIN Catherine	Professeure, ILM, Université Claude Bernard (Lyon 1)
M. PINCET Frédéric	Directeur de Recherche, École Normale Supérieure de Paris, CNRS

AUTRES MEMBRES DU JURY :

M^{me} DRENCKHAN Wiebke	Directrice de Recherche, ICS, CNRS
M^{me} LOISON Claire	Chargée de Recherche, ILM, CNRS
M. SCHNECK Emanuel	Professeur, Technische Universität Darmstadt

Table of contents

Front matter

List of abbreviations and symbols

List of abbreviations

AFM	Atomic force microscopy
DPPC	1,2-dipalmitoyl-sn-glycero-3-phosphatidyl-choline
DPPS	1,2-dipalmitoyl-sn-glycero-3-phosphatidyl-L-serine
DSPC	1,2-distearoyl-sn-glycero-3-phosphatidyl-choline
FRAP	Fluorescence Recovery After Photobleaching
FRAPP	Fluorescence Recovery After Patterned Photobleaching
HA	Hyaluronic acid
LB	Langmuir–Blodgett deposition technique
MD	Molecular dynamics
NR	Neutron reflectometry
OA	Osteoarthritis
XR	X-rays reflectometry
PC	Phosphatidyl-choline
PL	Phospholipid
PS	Phosphatidyl-serine
RH	Relative humidity
SC	Strong coupling
SF	Synovial fluid
SLD	Scattering Length Density
TOF	Time of flight mode
TR	Transfer ratio
WC	Weak coupling

List of used symbols

e	Elementary charge
ϵ_0	Vacuum permittivity
ϵ_r	Relative permittivity
k_B	Boltzmann constant
F_n	Normal force
F_t	Tangential or friction force
γ	Interfacial surface pressure
H	Hamacker constant
l_B	Bjerrum length
η	Viscosity
μ	Friction coefficient
μ_GC	Gouy-Chapman length
μ_v	chemical potential of vapour
μ	chemical potential of liquid
Ω	Pressure activation volume
P_h	Hydration pressure
P_O	Osmotic pressure
p_sat	the water saturation pressure
Π	Monolayer surface pressure
Φ	Stress activation volume
$\mathbf{k}_\mathrm{i}$	Incident beam wave vector
$\mathbf{k}_\mathrm{f}$	Reflected beam wave vector
$\mathbf{q}$	Transfer wave vector
R_F	Fresnel reflectivity
Q	energy barrier
σ_S	surface charge density
SLD_n	Neutron scattering length density
SLD_X	X-ray scattering length density
T_m	Main transition temperature
τ	Shear stress
$V_\mathrm{m,w}$	molecular volume of water
Ξ	Coupling parameter

Acknowledgments

Je tiens tout d'abord à remercier les rapporteurs de ma thèse, Catherine Barentin et Frédéric Pincet, pour avoir accepté d'évaluer mon manuscrit. Merci également aux membres de mon jury, Wiebke Drenckhan, Claire Loison et Emanuel Schneck, pour leur participation et leurs précieux retours.

Je voudrais ensuite remercier mes deux directeurs de thèse, qui n'auraient pas pu mieux faire dans leur travail de guidance : Thierry Charitat, pour son soutien sans faille, sa gentillesse et ces fameuses sorties à vélo qui m'ont permis de déconnecter et de me ressourcer, et Pierre Muller, pour son attention aux détails, sa disponibilité et sa bienveillance tout au long de cette aventure.

Je souhaite également remercier chaleureusement Claire Loison, Laurent Joly et Ludovic Gardré, l'équipe lyonnaise du projet ANR Banana, pour les discussions scientifiques fructueuses, les voyages à Lyon et la découverte de la gastronomie lyonnaise. C'était vraiment chouette de travailler avec vous.

Merci à tous les membres de l'équipe pour les bons moments passés ensemble, les parties de babyfoot et cette ambiance conviviale qui ont rendu le quotidien si agréable. Un grand merci à Antonio Stocco pour ses conseils avisés et sa bonne humeur communicative. Une mention spéciale pour Florent Fessler, mon meilleur ami et partenaire de longue date : sans toi, ces trois dernières années n'auraient pas eu la même saveur.

Je tiens aussi à remercier tous les stagiaires avec qui j'ai eu la chance de travailler. Votre enthousiasme et votre sérieux ont été un vrai plus dans ce projet.

Merci à Damien Favier, Marc Basler pour leur aide précieuse lors du développement du système triboFRAPP.

Enfin, je remercie ma famille - mes parents et mes sœurs - ainsi que Maëlle, ma compagne, pour son soutien constant, sa patience et tout l'amour qu'elle m'a apporté.

Preamble

This thesis is part of an ANR project called Banana Slip, which brings together collaborators from the Institut Lumière Matière in Lyon: Claire Loison, Laurent Joly, and Ludovic Gardré, as well as our team from the Institut Charles Sadron in Strasbourg: Pierre Muller, Thierry Charitat, Fabrice Thalmann and myself. This project combines the expertise of our collaborators in molecular dynamics (MD) simulation of phospholipids with our experimental expertise on supported phospholipid layers, reflectivity and tribology.

This document will begin with an introduction in Chapter I, presenting the lubrication of biological interfaces and our current physical understanding of the topic. In Chapter II, we outline the experimental and theoretical methods and materials used in this thesis. This will be followed by Chapter III, focusing on the structural analysis of charged and zwitterionic supported layers. Chapter IV details the friction experiments conducted on zwitterionic and charged phospholipid layers, while the final results are presented in Chapter V, which showcases the findings from the TriboFRAPP setup dedicated to the localization of sliding planes.

Chapter I

Introduction

Friction is an essential force that shapes nearly every moment of our lives, whether we are aware of it or not. From the moment we wake up to when we go to bed, we continuously experience friction in various forms.

In some instances, maximizing friction is necessary, such as when we hold our coffee cup in the morning or when we ride our bike or drive our car. In these cases, increased friction is beneficial. However, in many situations, we want to minimize friction. To achieve this, the friction between two surfaces is often reduced with the help of what we call a "third body", more commonly referred to as a lubricant.

The examples are numerous. Since the Industrial Revolution, humanity has developed many situations where two surfaces in contact must be lubricated. In our modern world, the impact of friction and wear on energy consumption is significant: approximately 23% of the world's total energy consumption is attributable to friction, and of that, 20% is specifically due to frictional losses [1]. Reducing friction and preventing wear by developing new surfaces and lubricants could greatly increase energy efficiency and help reduce CO_2 emissions.

I do not usually like to distinguish between nature and humans, but it is interesting to draw a parallel regarding lubrication. Since the advent of the first machines, we have primarily relied on oil-based lubricants. In contrast, nature, through the course of evolution, has developed water-based lubricants that largely outperform our oil-based solutions. Our joints are perfect examples; they provide long-lasting and very efficient lubrication.

This thesis will focus on lubrication in biological systems, with a particular emphasis on phospholipid layers, which are among the main biological lubricants. The strategy we adopt to study lubrication is distinct from typical biological and biomechanical studies, which often examine in vivo or complex systems closely resembling biological joints. Here, we approach this from a physicist's perspective, aiming to extract essential components of the efficiency of biolubrication to gain insights that are crucial not only for maintaining joint health but also for advancing synthetic lubricants inspired by nature's efficiency.

The purpose of this section is to establish the foundational context for this research project, we will present the theoretical basis of friction necessary for this thesis and the state-of-the-art in synovial joint lubrication.

I.1 Introduction on friction

Since the first pre-historic spark produced by the friction of flint and hard stone, our comprehension of friction has significantly evolved. The study of friction, defined as the force opposing the relative motion of two solid surfaces in contact (we depict the situation in Figure I.1), originates in the early scientific work of Guillaume Amonton in 1699 and Charles-Augustin de Coulomb in 1785 [2].

Their work created the basis of modern friction research. Amonton's early

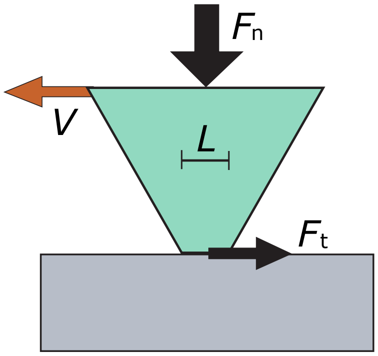

Figure I.1: Schematic representation of a dry contact between two bodies in relative motion: the normal force $\mathbf{F}_n$, the friction force $\mathbf{F}_t$ and the relative velocity V are represented on the graph as well as the size of the contact L. Adapted from [3].

findings established that the tangential frictional force F_t was directly proportional to the normal force F_t, Coulomb expanded on this, developing the concept of friction coefficient, μ such that:

$$\mu = \frac{F_t}{F_n}. \tag{I.1}$$

One can note that the relationship is independent of the apparent contact area between surfaces and the sliding velocity. This general relation surprisingly holds for many non-deformable solids and dry contacts as long as the contact is not adhesive [4].

Later, the field of tribology (derived from the Greek word "tribos," meaning "to rub") was formally defined by Peter Jost in 1966 [5]; it encompasses the principles of friction, wear, and lubrication. Specifically, in the case of surfaces lubricated by a "third body", the assumption of velocity independence no longer holds (See Figure I.2 for a schematic representation). Even a soft film of nanometric thickness can lead to deviation from Coulomb's law [6, 7].

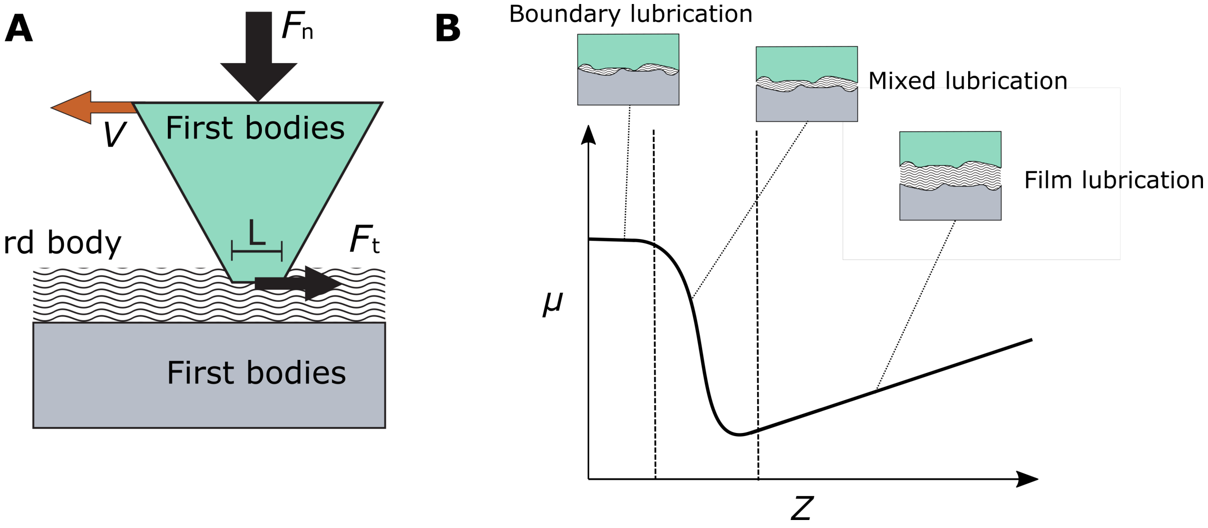

Figure I.2: (A) Schematic of a lubricated contact by a third body sandwiched by the two first bodies. (B) Stribeck curve illustrating the typical variation of the friction coefficient μ as a function of the hydrodynamic parameter Z.

Friction is considered to be an energy dissipation process. Solid dry friction is typically associated with wear and a high friction coefficient. Therefore, a lubricant is usually introduced to minimize surface degradation and energy dissipation.

Lubricants, characterized by their viscosity, form a thin layer that reduces friction and wear. The dynamic viscosity, η, of a lubricant influences the system's lubrication regime, as described by the Stribeck curve (see Figure I.2), which maps out different regimes based on the hydrodynamic parameter:

$$Z = \frac{\eta V L}{F_\mathrm{n}}, \tag{I.2}$$

where V is the relative velocity, L is the contact length, and F_n is the normal force.

The Stribeck curve identifies three primary lubrication regimes:

- **Boundary (or dry) lubrication:** High friction level with solid surfaces making direct molecular contact

- **Mixed lubrication:** Friction gradually decreases as the lubricant intermittently separates the surfaces, allowing some asperities to remain in contact.
- **Hydrodynamic or fluid film lubrication:** A thin lubricant film fully separates the surfaces, achieving low friction as the surfaces glide without direct contact.

In the case of fluid film lubrication, friction arises as the viscous film is sheared. The energy dissipation occurs within the film, and the friction force can be expressed as [8]:

$$F_{\mathrm{t}} = \frac{A\eta V}{d}, \tag{I.3}$$

where d represents the thickness of the film and A the contact area.

This equation is fundamental in fluid film lubrication, where friction is linearly dependent on velocity. Additionally, friction may depend on contact pressure and temperature, through a change of the viscosity η. Boundary lubrication is more challenging to predict since energy dissipation can result from irreversible processes such as the breaking and reforming of adhesive bonds [9]. While boundary friction is more specific, a general observation is that friction in this regime shows a limited dependence on velocity.

It becomes evident that we must define and understand the lubrication regime in which biological joints operate before going further in the friction model description.

I.2 Biolubrication in joints

When living and moving, mammals, including humans, generate numerous sliding and shearing interactions between organs and tissues, as seen in synovial joints and in the lubrication of the cornea. The most remarkable friction properties are found in major joints, such as the knee and hip, where the load is among the highest in the human body (up to 20 MPa). These systems can achieve an exceptionally low friction coefficient, down to $\mu = 0.001$ [10, 11, 12]. This value of μ under such high pressures has yet to be matched either in nature or synthetically. The current challenge in biotribology is, therefore, to decipher the mechanisms behind this highly efficient lubrication.

Osteoarthritis (OA) is a pathological condition affecting joints, with recent studies indicating that approximately one in seven Americans are affected by this disorder [13]. OA is characterized by severe pain and a significant reduction in mobility. The origin of OA is multifactorial, with hereditary factors and obesity being well-documented contributors [13]. While the condition arises from a complex interplay of factors, it has been demonstrated that OA is associated with increased friction, with friction coefficients in affected joints reaching $\mu \approx 0.01$; an order of magnitude higher than that of healthy joints [10]. This increased friction suggests a potential disruption of the lubricating mechanisms within the joint.

Understanding the pathways and components involved in joint lubrication is therefore crucial for elucidating the mechanisms underlying OA and for developing potential therapeutic strategies. Investigating the lubrication properties of healthy joints could provide insights into the dysfunctions present in pathologic joints.

I.2.A Structure and composition of cartilage

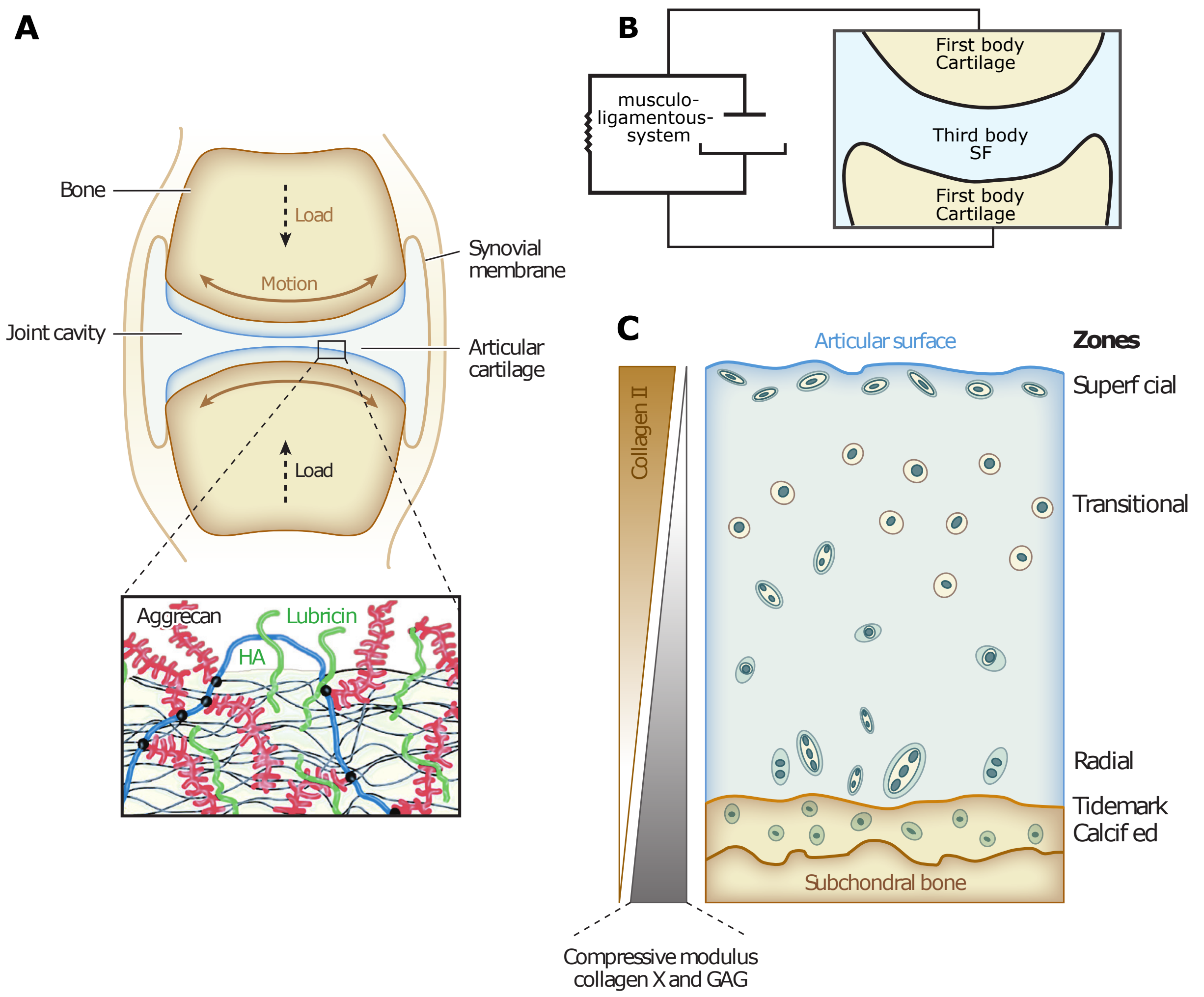

Figure I.3: (A) Illustration of a major joint: two bones separated by the joint cavity. Articular cartilage is present at the bone surface, shown with molecular details. (B) Tribological triplet as a simplified view of the system. (C) Cartilage tissue is divided into four main zones above the subchondral bone. The superficial zone forms the lubricated, articulating surface. Chondrocytes constitute less than 10% of the cartilage volume. The composition of matrix components, including collagen types and glycosaminoglycans (GAGs), as well as the tissue modulus, varies with depth. Adapted from [11, 14].

The composition of the biological joints is rather complex. In this thesis, we will detail only compounds relevant to lubrication. A good review of recent progress on biolubrication and joint composition can be found here [9] and with a more biological point of view here [15]. By oversimplifying the situation, we can reduce the system to a tribologic triplet composed of the cartilage, the synovial fluid (SF), and the musculo–ligamentous–joint system [3, 10, 16]; a schematic of the situation is represented in Figure I.3.B. It works as follows: the movement is controlled by the motor endplate of the musculo–ligamentous–joint system, the cartilage provides an efficient load transmission with maximum dumping, and friction reduction is given by the SF. We will shortly enumerate the composition of cartilage.

Articular cartilage (see Figure I.3 for an overview), which coats the ends of bones in synovial joints with a thickness of 1-4 mm [17], is specialized to transmit joint loads while maintaining a low friction coefficient. This cartilage is a highly structured connective tissue composed of a sparse distribution of chondrocytes (specialized cells in cartilage that produce and maintain the extracellular matrix, they represent about 2-5% of the volume [18]) within a dense extracellular matrix.

Articular cartilage is organized into zones: superficial, middle, and deep, each with varying collagen orientations and proteoglycan concentrations (see Figure I.3.C). The superficial zone, in particular, contains a high concentration of type II collagen aligned parallel to the surface [19, 20], optimizing it for shear and tensile stress resistance. The middle zone forms a transitional layer, and the deep zone, adjacent to the subchondral bone, supports load-bearing functions.

Water, comprising around 70% of articular cartilage’s wet weight [21], is its most abundant component, functioning as a medium for nutrient transport to the chondrocytes, which lack direct blood supply. Other primary constituents include collagen [19] (55-75% of the dry weight, mostly type II), proteoglycans (also called lubricin, about 15-30%) [22], and lipids, primarily phospholipids

(∼10%) [23].

Collagen is a structural protein whose network imparts tensile stiffness and structural integrity, while lubricin is another biopolymer that binds to hyaluronic acid (HA) to form a hydrogel-like matrix, crucial for resistance to compressive forces [24]. We show in Figures I.3 and I.4 an illustrative description of articular cartilage.

HA and phospholipids are also primary components of both the cartilage surface and SF. The viscosity of SF relies heavily on HA, a linear polysaccharide. Phospholipids, typically known as cell membrane components, also form several stacked bilayers on the cartilage surface, separated by thin water films [25], and exist as multilamellar vesicles within the SF [26] (further details on phospholipids are given in Chapter 2). The next section will discuss their essential role in joint lubrication.

I.2.B Model of lubrication

So what makes biological joints such a good lubricating system? Much work has been done to explain the mechanism by understanding the role of SF and cartilage surface lubricants. However, the exact lubrication mechanism remains unknown. Given the huge complexity of the joint, it is very likely that the answer is not unique, meaning that biological joints possess various dissipation pathways, from boundary lubrication to fluid lubrication [9, 10].

I.2.B.i Fluid film lubrication

Historically, models for joint lubrication were first inspired by human-engineered machine lubrication. The initial models developed were fluid film lubrication models that provide lubrication with a film of a few tens of nanometers [27, 28], preventing contact between cartilage surfaces. Consequently, lubrication was mainly dependent on the viscosity of SF, particularly on HA. However, it became evident that this type of dissipation mechanism alone could not explain the excellent lubrication properties of joints, especially under high physiological pressures on the order of tens of MPa. In this study, we focus specifically on the scenario when loads are high, and cartilage surfaces are in molecular contact.

As in boundary lubrication, dissipation occurs in the sheared molecular-thick film. This phenomenon justifies the possibility of studying both in vivo and ex vivo conditions, as well as reproducing the friction of biological systems using model systems with simpler surfaces like glass or mica. This has led to a vast literature on the friction of boundary lubricants in vivo and ex vivo, with varying degrees of biological resemblance. The principal cartilage lubricants are HA, phospholipids, and lubricin. A large variety of studies exist on the lubrication provided by each of these lubricants individually and in combination. The latest review by J. Klein's group [9] provides a detailed overview of these studies. In Figure I.4.B, we present selected findings from Seror et al. [29] where they measured using a surface force apparatus the frictional properties of HA and phospholipid vesicles between mica surfaces, achieving physiological friction coefficient μ. This study is one of many in the field, and here, we summarize their conclusions.

Their vision, shared by the community, is that phospholipids, HA, and lubricin work cooperatively. We show a schematic of their interpretation of boundary lubrication in Figure I.4.B. In this model, lubricin is attached to the cartilage surface within the collagen network, HA interacts with lubricin and becomes immobilized, and HA then forms complexes with layers of phospholipids in contact with SF. Although this model suggests cooperation between these components, their effects on friction are not equal. Notably, phospho-

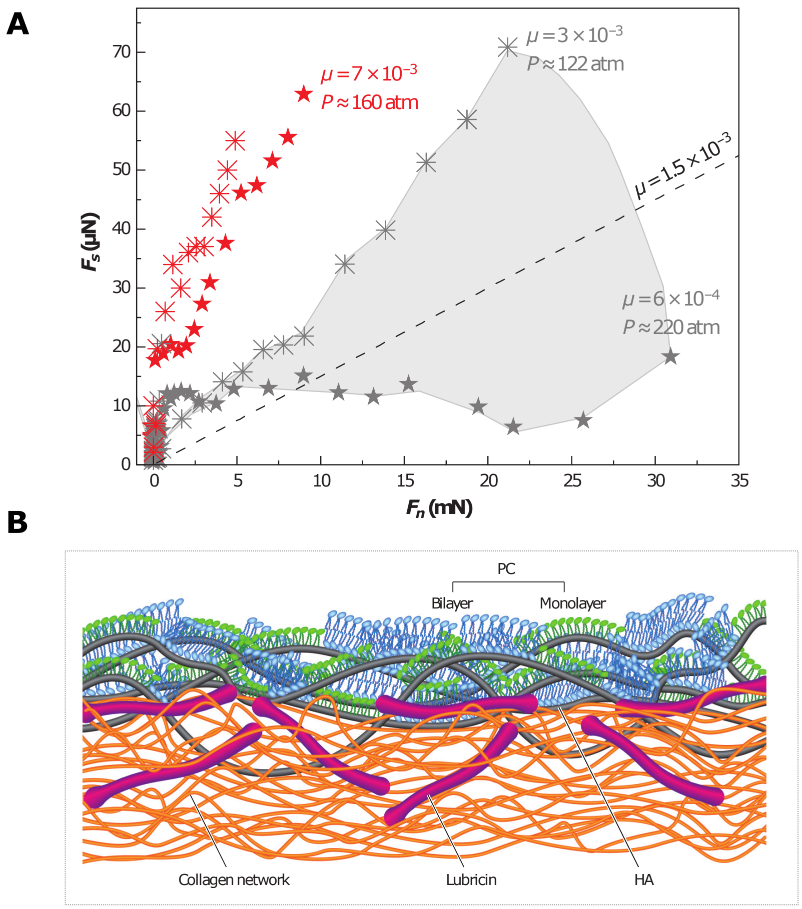

Figure I.4: Lubrication by HA and phospholipids (A) Friction up to physiologically high pressures between sliding surfaces bearing boundary layers of surface-attached HA to which neutral phospholipid small unilamellar vesicles had been added. Friction forces F_s as a function of load F_n, measured with the surface force balance method. The shaded area includes all the F_s versus F_n profiles under water. The gray symbols represent the limiting profiles across water (highest and lowest μ values at the high pressure indicated; the broken line indicates the mean value over all measurements). The red symbols represent F_s versus F_n profiles across a 0.15 M salt solution. (B) Structure of the cartilage boundary lubricant layer, proposed by Seror et al.. [29]

lipid layers alone are the only ones among the three to provide an ultra-low friction coefficient ($\mu = 0.001$) [25, 30, 31, 32].

This specific role of phospholipids as lubricants appears to extend even to studies on SF lubrication. In SF, particularly in multilamellar vesicular phases, the presence and composition of phospholipids control lubrication, as shown in [10].

I.2.B.ii Hydration lubrication

From a complex description involving many components in cartilage lubrication, we have isolated a potentialy key element behind the efficiency of biological joints: phospholipids. In boundary lubrication, the frictional properties depend on the molecular structure of the lubricant. So what exactly in the structure of phospholipid layers makes them efficient lubricants? Another way to put this question is: where is the energy dissipated when phospholipid layers are sheared?

A first conjecture, proposed by Hills at the beginning of the century [25], suggested that sliding would occur between the phospholipid tails via van der Waals (vdW) interactions. According to this model, at the surface of cartilage, the phospholipid layers would facilitate lubrication through tail–to–tail dissipation, a mechanism closely resembling classical boundary lubrication with oil. We present an illustration of Hills model in Figure I.5. Early studies on biological boundary lubricants [33] were influenced by the formalism developed for petroleum-based lubricants, where lubrication primarily depends on tail–to–tail interactions.

In 2002, not long after Hills hypothesis, a new paradigm emerged in the field after successive studies by J. Klein's group. They first investigated the lubrication of hydrated ions using a surface force balance [34] and found that hydration water could lead to highly effective lubrication. Later, they observed that hydrated surfactant layers were more efficient lubricants than dry monolayers [35]. Their conclusion was that they were witnessing a shift in the sliding plane, from tail–to–tail interactions to the water layer between the surfactant and the mica substrate, leading to enhanced tribological properties. The dissi-

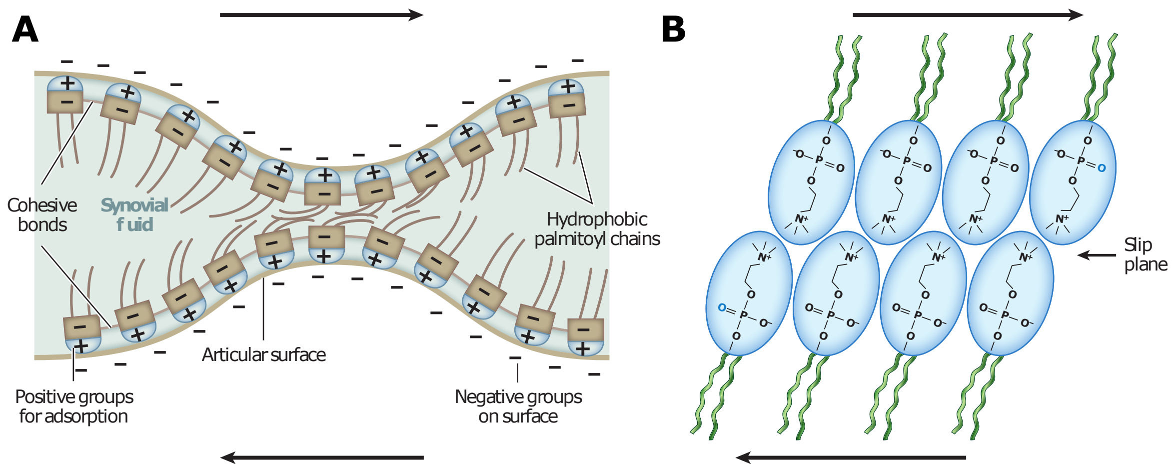

Figure I.5: (A) Representation of Hill's model, adapted from [11]. A lipid monolayer is adsorbed onto the cartilage surface through interactions between polar heads and the negatively charged cartilage surface, with dissipation occurring between the lipid tails. (B) Hydration lubrication mechanism, adapted from [11]. The assembly and complexation of phospholipid layers on the surface expose the phospholipid heads, with dissipation occurring in the hydration layer.

pation mechanism was thus associated not with tail interactions but with the shear of the hydration layer, a dissipation mechanism that became known as "hydration lubrication".

This discovery initiated a large number of publications based on the principle of hydration lubrication, including studies on polymer brushes [36], vesicles [37, 38], and bilayers [39]. A common structural feature among these systems is that they all contain a phosphocholine (PC) group, the head group of the most common type of phospholipid in biology (see Chapter II.1 for more on lipid types and structure). A unique characteristic of this zwitterionic group is its strong affinity for water due to dipole-dipole interactions, with PC heads, typically binding 10-15 water molecules [40].

J. Klein's group proposed a theory to explain hydration lubrication (illustrated in Figure I.5.B). According to this model, the strong interaction of water with the hydration shell of phospholipid heads helps resist high loads by preventing the water layer from being squeezed out, while still allowing some fluidity within the layer. The hydration water viscosity was approximately 250 times that of bulk water [41].

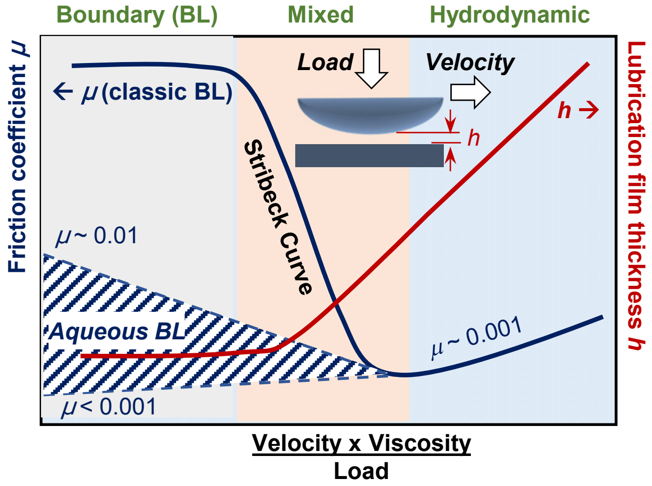

Figure I.6: The ’modified’ Stribeck curve with boundary hydration lubrication, adapted from [33]. In the classical Stribeck curve (shown in blue), the friction coefficient μ increases nonlinearly as the lubricant film thickness h approaches molecular thickness in the mixed and boundary lubrication (BL) regimes. In the case of aqueous BL (dashed area), the friction coefficient μ remains low, comparable to that in the hydrodynamic regime ($\mu \approx 0.001$).

From this point, the hydration lubrication model became a widely accepted concept in the community and is now regarded as a fundamental framework. This type of lubrication has been observed in systems beyond phospholipids and is currently used as inspiration for developing new, efficient lubricants [33]. This mechanism also highlights the contrast introduced earlier: nature relies on water–based lubrication, in contrast to human–engineered, oil–based lubrication systems. It is often said that hydration lubrication can violate the Stribeck curve by providing high lubrication for boundary lubricant films, with friction levels similar to fluid film lubrication under low–load conditions [33, 7]. This observation is illustrated in Figure I.6.

Consequently, hydration lubrication is regarded as one of the primary mechanism in biolubrication. However, despite this mechanism being well established, no direct experimental observation of a slipping plane in the water layers within stacks of phospholipid layers has been made. Most prior work has focused on single supported bilayers and monolayers of DPPC in the gel phase (refer to Chapter II.1 for details on phospholipid phases), where no–slip conditions were observed between the tip and the bilayer [42]. Experimentally measuring the velocity field within nanometric–thick films remains challenging. Molecular dynamics (MD) simulations, however, address this limitation. In a recent MD study by collaborators of our team [43], it was shown that when stacks of gel–phase DPPC bilayers are sheared, sliding indeed occurs within the water layers, supporting the hydration lubrication model (see Figure I.7).

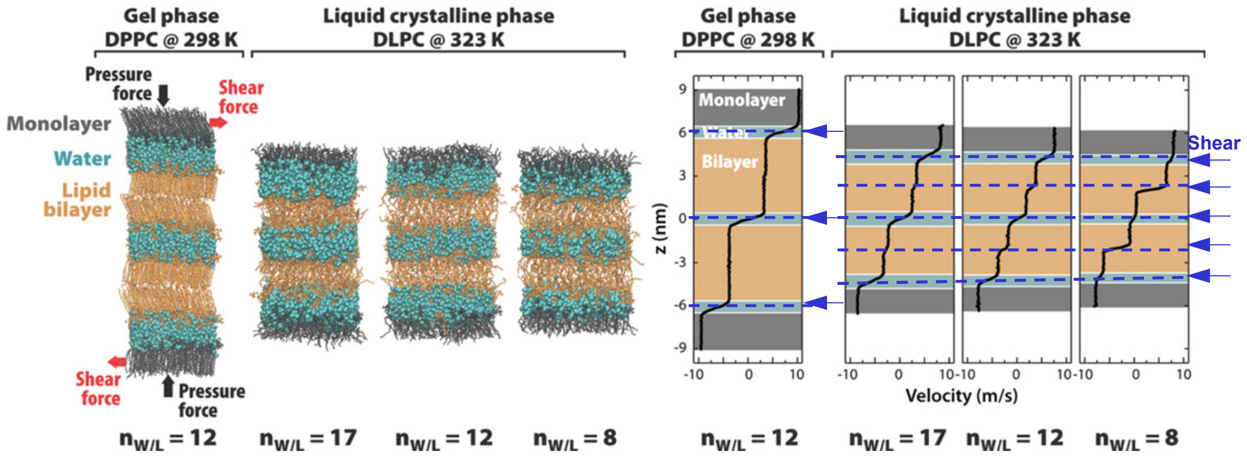

Figure I.7: (left) Bilayer stacks in an MD simulation under varying hydration levels (denoted by $n_{\mathrm{W/L}}$, the number of water molecules per lipid). From left to right: DPPC gel phase at 293 K with $n_{\mathrm{W/L}} = 12$; DLPC fluid lamellar phase at 323 K with hydration levels of $n_{\mathrm{W/L}} = 17$, 12, and 8, respectively. Constant normal pressure is applied, and two shear forces are exerted on the outer monolayers. (Right) Illustration of the associated shear planes. Adapted from [43].

However, in the fluid phase and under low hydration conditions, dissipation can also occur between lipid tails, suggesting a mixed–lubrication scenario.

Recently, J. Klein's group published a study examining friction in partially dehydrated phospholipid layers treated with Dimethyl sulfoxide (DMSO). Surprisingly, they observed no significant change in friction, indicating that other dissipation pathways, or alternative lubrication mechanisms beyond hydration, may contribute to phospholipid layer lubrication. This finding introduced ambiguity into the hydration lubrication model.

This ambiguity inspired our project, in which we sought to study the effect of hydration on friction experimentally and to identify the location of slidding planes in a manner analogous to the MD work of our project collaborator [43]. I recently discovered that H. Briscoe, in his review on hydration lubrication [33], also proposed addressing this ambiguity in mixed lubrication scenarios by performing 'readily' experiments consisting of relative humidity (RH)–controlled friction experiments on supported phospholipid layers. This is the strategy we adopted in this work, with the subtle nuance that "readily" might not be the ideal term to describe the challenges we faced in this study.

I.3 Goal of the project

The reason H. Briscoe and our group propose studying RH-controlled friction experiments on supported phospholipid layers is as follows: by doing so, we are working with a substrate at the air/solid interface, allowing the water layers between the phospholipid layers to be in equilibrium with the vapor phase. We illustrate this in Figure I.8, which depicts what we call a trilayer, consisting of three layers of phospholipids deposited on a solid substrate using the Langmuir-Blodgett method (see Chapter II.1 for more information on the samples).

Due to this geometry, a strong osmotic pressure P_O arises [44]. Indeed, if

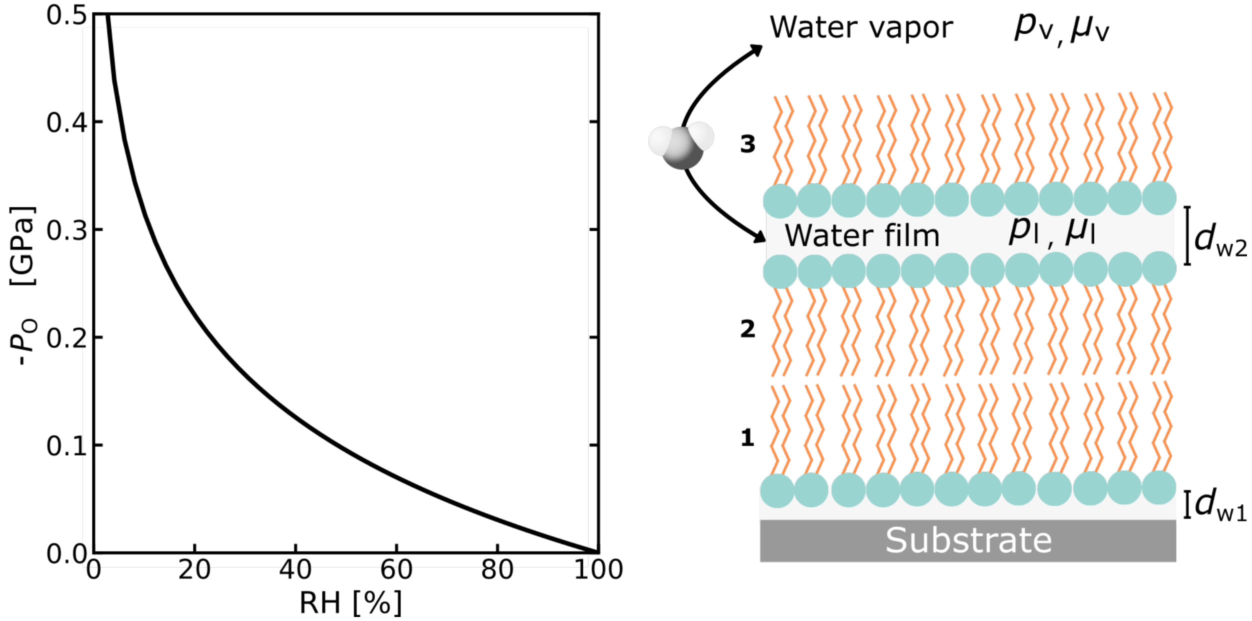

Figure I.8: (Left) Osmotic pressure as a function of relative humidity (RH). (Right) Schematic of a phospholipid trilayer deposited on a solid substrate. The first and second water layers, d_{w1} and d_{w2}, are shown. The water film between the second and third layers, with pressure p_l and chemical potential μ_l, is in equilibrium with the vapor phase, characterized by pressure p_v and chemical potential μ_v.

we apply the Gibbs-Duhem relation at constant temperature for the vapor and liquid phases of the water layers, assuming the liquid is incompressible and the vapor behaves as an ideal gas, we obtain:

$$\mu_l - \mu_{sat} = V_{m,w}(p_l - p_{sat}) \qquad \text{and} \qquad \mu_v - \mu_{sat} = k_B T \ln\left(\frac{p_v}{p_{sat}}\right), \tag{I.4}$$

where p_l and p_v are the pressures of the liquid and vapor, respectively, p_{sat} is the water saturation pressure, and $V_{m,w} = 30\,\text{Å}^3$ is the molecular volume of water.

The balance of chemical potentials leads to:

$$p_\mathrm{l} - p_\mathrm{sat} = \frac{k_\mathrm{B}T}{V_\mathrm{m,w}} \ln\left(\frac{p_\mathrm{v}}{p_\mathrm{sat}}\right). \tag{I.5}$$

Combining these equations yields the expression for the osmotic pressure:

$$P_\mathrm{O} = p_\mathrm{v} - p_\mathrm{sat} - \frac{k_\mathrm{B}T}{V_\mathrm{m,w}} \ln\left(\frac{p_\mathrm{v}}{p_\mathrm{sat}}\right). \tag{I.6}$$

Since $p_\mathrm{v} - p_\mathrm{sat}$ is negligible compared to $k_\mathrm{B}T/V_\mathrm{m,w} \ln(p_\mathrm{v}/p_\mathrm{sat})$, we can approximate the relationship between the osmotic pressure and relative humidity as:

$$P_\mathrm{O} \approx \frac{k_\mathrm{B}T}{V_\mathrm{m,w}} \ln\left(\frac{\mathrm{RH}}{100}\right), \tag{I.7}$$

where RH = $100 p_\mathrm{v}/p_\mathrm{sat}$. The osmotic pressure P_O is plotted in Figure I.8, indicating very high pressure at low RH, on the order of almost a GPa. This pressure is negative, as it represents an attractive pressure, and it contributes to the disjoining pressure of the water layers. Thus, this situation is twofold interesting. First, by controlling the RH, we can adjust the osmotic pressure in the layer. By measuring the variation of the second water layer d_w2, we can deduce other physical interactions between the second and third layers (see Figure I.8). Notably, the significant osmotic pressure allows us to study the strong repulsive hydration forces and electrostatic interactions [45]. Li Fu, a former PhD student of the team, conducted preliminary experiments using neutron reflectivity on DSPC trilayers [46]. These initial experiments showed that there is an effect on the phospholipid trilayer structure. In this study, we will use neutron and X-ray reflectivity to comprehensively characterize the structure of DPPC trilayers at varying humidity levels from low to high RH.

The second advantage of this geometry is that, after characterizing the

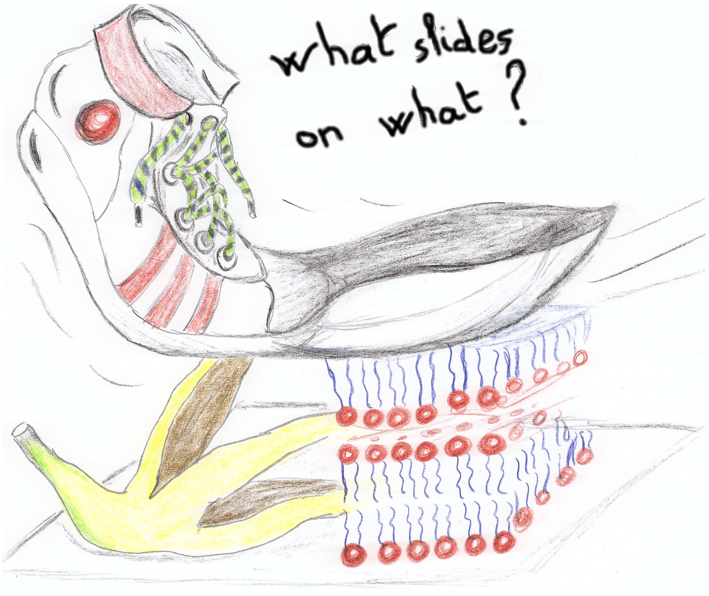

Figure I.9: Diagram representing the main idea of the ANR project. It draws an analogy between the friction of a shoe on a banana peel and the friction of lipid layers. The question is whether the shoe slips on the banana peel or if the banana slips on the ground. For our system, the goal is to determine whether the sliding occurs within the water layer or between the chains of the phospholipids. Drawing created by Thierry Charitat and used with his permission.

evolution of d_{w2} with respect to RH variation, we can establish an experimental model that allows us to finely control hydration simply by changing RH. Therefore, by conducting friction experiments at a fixed RH, we may be able to relate friction to hydration. One distinctive aspect of this project is the development of a unique experiment: the TriboFRAPP setup. This setup combines velocimetry and tribometry experiments. The objective is to measure the velocity field of sheared phospholipids, hoping to fully characterize the location of the sliding plane and the mechanisms of energy dissipation. Figure I.9 illustrates the project's concept, drawing an analogy to the friction of a banana peel.

In this project, we aim to address the following questions:

1. What are the correlations between the structure and tribology of lipid

trilayer?

2. What are the velocity profiles within the lipid stack, and where does the dissipation occur:
    (i) between the leaflets of a bilayer?
    (ii) at the lipid-water interface?
    (iii) within the confined water films?
3. What is the role of the hydrodynamics within the confined water layers?
4. Are there different friction regimes correlated with the localization of energy dissipation?

Furthermore, we sought to study the impact of negatively charged phospholipids on lubrication, a factor that is largely unexplored. This effect may be relevant, as synovial fluid contains negatively charged phospholipids, representing approximately 10–15% of the total phospholipids present in articulations [10]. The pH, which affects the charge, also modulates the friction coefficient between cartilage surfaces [47]. More broadly, charge effects clearly play a role in superlubricity, as demonstrated recently using charged surfactants [48] and between charged surfaces in the presence of monovalent [49] or multivalent salts [50].

Therefore, we aim to investigate how charged lipids may enhance or disrupt lubrication under different charge densities. This led us in Chapter III to explore the physical interactions in mixtures of charged and neutral phospholipid layers. In this chapter we explored an highly counter-intuitive electrostatic phenomenon: namely, the attractive interaction between similarly charged membranes.

Chapter II

Materials and methods

II.1 Sample preparation

II.1.A Lipids

Membrane compartmentalization is essential for life. Among the numerous components of biological membranes, lipids are the primary constituents of cellular membranes [51]. They form their structural backbone, making them a central focus in membrane biophysics research [52]. A wide variety of lipids exists across different kingdoms of life. Within a single organism, lipid compositions can vary between organelles, plasma membranes, and even within various regions of the same membrane, often exhibiting asymmetric distributions. Despite this complexity, specific general observations can be made. This brief section discusses the essential properties of lipids relevant to my thesis. For further information on membrane biology, readers are directed to [51], and for a detailed exploration of membrane biophysics, to [52].

Defining lipids can be challenging due to their extensive diversity, but one common characteristic they share is amphiphilicity. Each lipid molecule com-

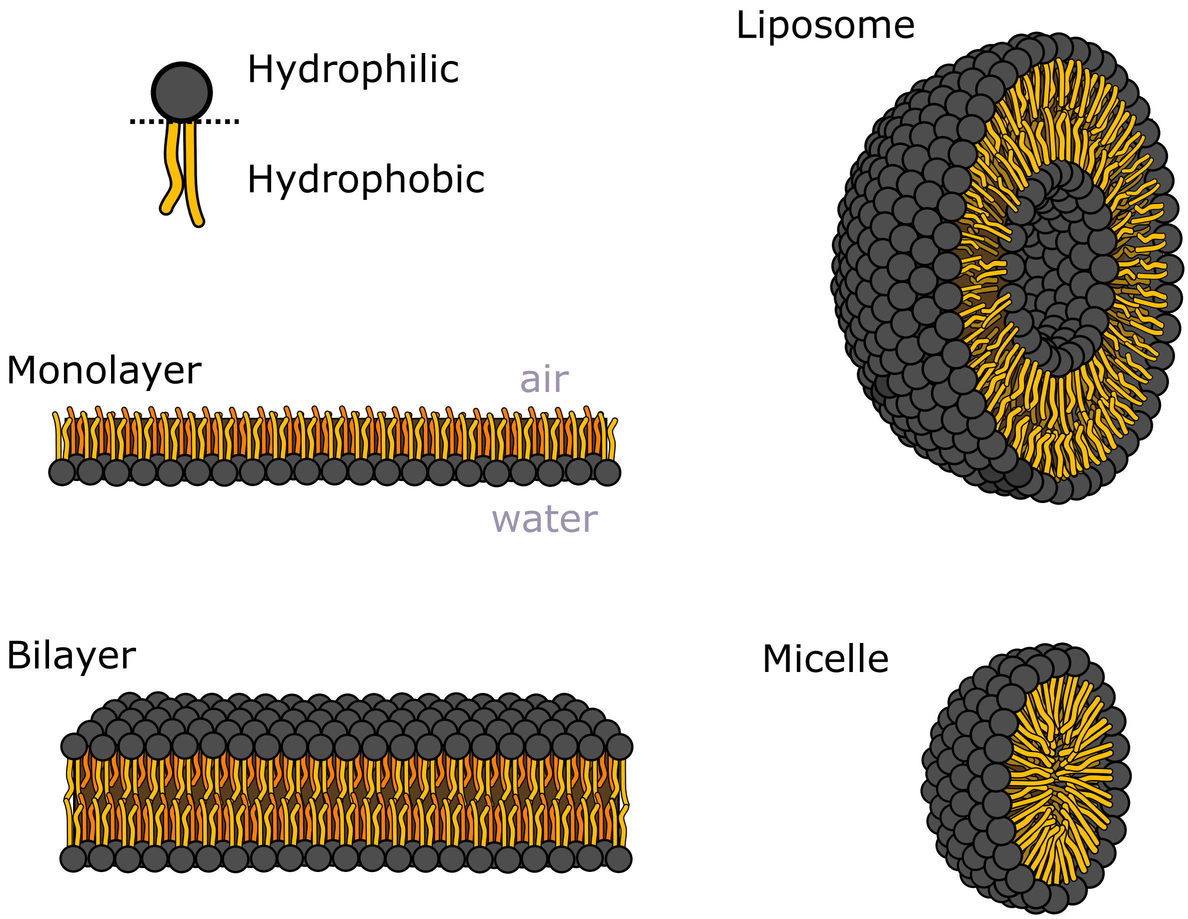

Figure II.1: Schematic views of an amphiphilic molecule and the different self-assembled structures of amphiphilic molecules: monolayer at air/water interface; bilayer in aqueous solution; liposomes and micelles in bulk solution.

prises a hydrophobic (apolar) and a hydrophilic (polar) component. The hydrophobic parts, typically made up of hydrocarbon chains, do not mix well with water. This behavior stems from the stable hydrogen-bonding network formed by water, which excludes nonpolar substances like oils. The hydrophobic tails are paired with hydrophilic head groups. These head groups are polar, either charged or neutral, allowing them to form hydrogen bonds with water molecules, making them inherently hydrophilic (see Figure II.1). This amphiphilic property is crucial for lipid self-assembly in aqueous environments.

Lipids aggregate to minimize the exposure of hydrocarbon chain with water, leading to various structural arrangements based on the specific geometries of the lipid heads and tails [45].

The simplest structure that forms at the air-water interface is a lipid monolayer. In more complex configurations, such as lipid bilayers, two monolayers align tail-to-tail, resembling a thin layer of oil in water. In biological systems, multiple lipid bilayers can organize into multilamellar structures, as seen on the cartilage surfaces in joints [9]. Due to their amphiphilic nature, lipids cannot tolerate open ends; they naturally fold in on themselves to create closed, spherical structures known as unilamellar and multilamellar vesicles, or liposomes.

In summary, the aggregation of lipids in water is fundamentally driven by the properties of water itself. The existence and stability of lipid-based structures are intricately linked to water, which is why it is often referred to as the "biological solvent" [52].

This study focused on a specific group of lipids: phospholipids (PL). These make up about 50-60% of the lipid composition in plasma membranes [52] and are similarly abundant in healthy human knee joints [10]. As a result, they are of significant interest in studies related to lubrication and membrane physics.

The first element to consider when determining phospholipid types is the head group. The most common type comprising approximately 68% of lipids in joint membranes is phosphatidylcholine (PC) [10]. This zwitterionic head contains a choline and phosphate group, resulting in a neutral molecule. Another essential type of phospholipid is the negatively charged phosphatidylserine (PS), which constitutes about 10% of the total composition of the plasma membrane and articular joints. PS has a serine group instead of choline, giving it a net negative charge of -e at physiological pH.

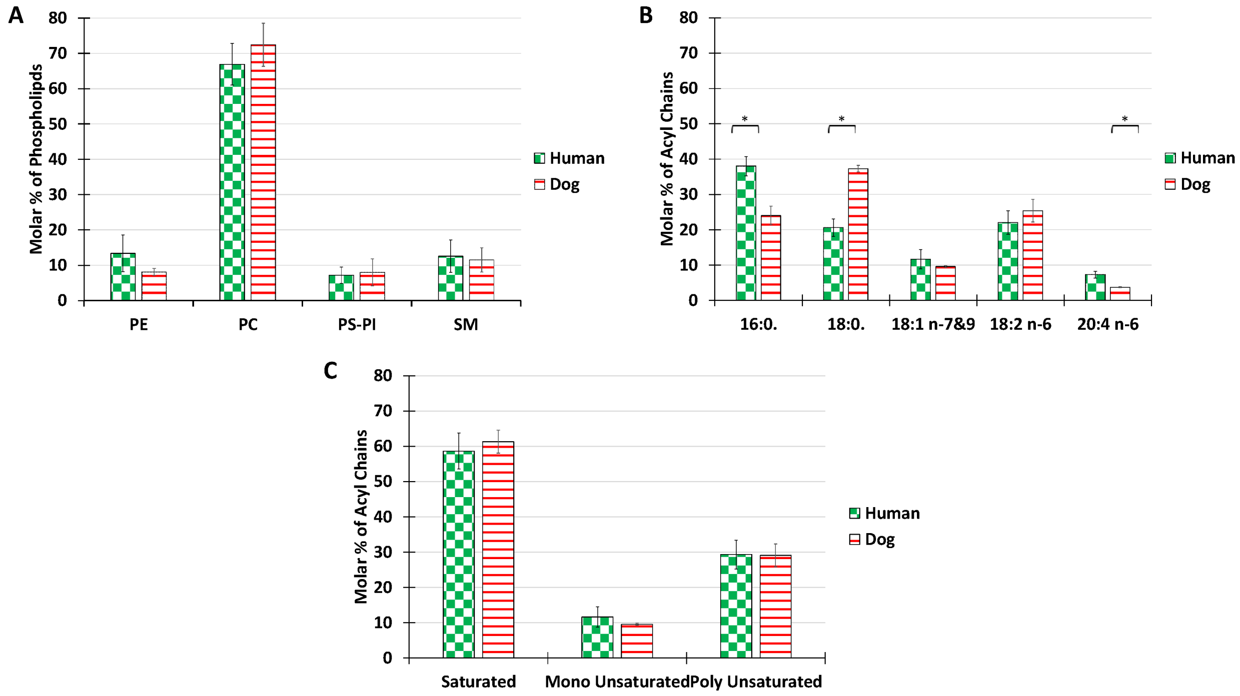

Figure II.2: (A) Lipid composition of synovial fluid from the knee joints of dogs and healthy human volunteers. (B) Distribution of acyl chains in the total phospholipid extract, shown as molar percentages of saturated, monounsaturated, and polyunsaturated acyl chains. (C) Molar percentage of saturated, monounsaturated, and polyunsaturated acyl chains. Adapted from Trunfio-Sfarghiu et al [10].

The second component to consider is the type of fatty acid tails. Phospholipids contain two fatty acid chains. While the cellular lipids contain a wide variety of chain types [53], in joints, they typically have 16 to 22 carbons per chain with unsaturated, mono, and polyunsaturated phospholipid. In Figure II.2, the work of Trunfio-Sfarghiu et al.,[10], displays the distribution of lipids in healthy dog and human joints.

Phospholipid nomenclature generally uses four letters: the first two letters denote the fatty acid chain type, while the last two indicate the head group. This study used phospholipids with either 16-carbon palmitoyl chains (16:0-16:0, DP) or 18-carbon stearoyl chains (18:0-18:0, DS) without unsaturation, specifically DPPS, DPPC, and DSPC. A summary of the phospholipids used, including their chemical structures and main transition temperatures T_{m} (from gel to fluid phase), is provided in Table II.1. Phospholipids were all purchased from Avanti Polar Lipids, and the main transition temperatures were obtained from their documentation [54].

The chain length and degree of unsaturation substantially impact the thermodynamic properties of phospholipids, especially their main transition temperature, T_{m}. The phospholipids selected for this study have T_{m} values above room temperature and represent those commonly found in biological joints (see Figure II.2).

Table II.1: Phospholipids used in this study and their properties

Name	Abbreviation	T_{m}	Charge
1,2-dipalmitoyl-sn-glycero-3-phosphocholine	DPPC	41°C	0
1,2-distearoyl-sn-glycero-3-phosphocholine	DSPC	55 °C	0
1,2-dipalmitoyl-sn-glycero-3-phospho-L-serine	DPPS	54°C	-e

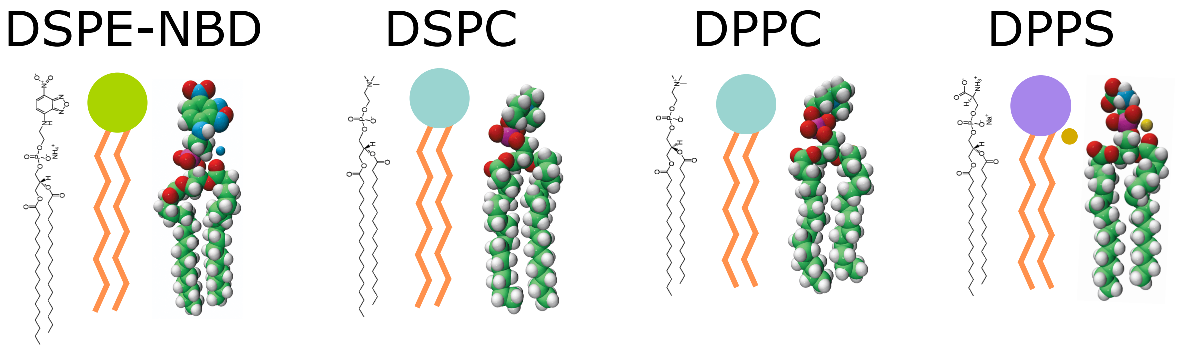

Figure II.3: Different types of lipids used in this work with their chemical structure and schematic representations. From left to right: DSPE with fluorescent labeling by NBD; zwitterionic DSPC and DPPC; charged DPPS with counter ion.

In fluorescence experiments, we used DSPE containing a fluorescent NBD (7-nitro-2-1,3-benzoxadiazol-4-yl) group attached to its head (see Figure II.3).

Its absorption spectrum peaks at approximately 460 nm, suitable for our FRAPP experiments.

II.1.B Supported phospholipid layers: Langmuir-Blodgett deposition

II.1.B.i Generalities

The current advancements in membrane physics owe much to study of supported phospholipid layers. These typically consist of phospholipid bilayers deposited onto a solid substrate and have been widely used to investigate membrane fluidity, phase separation, diffusion, and interactions between phospholipid membranes and proteins or other objects [55]. The planar geometry of such systems makes them ideal for comparisons with theoretical models, as will be explored in the next chapter.

Various experimental techniques exist for transferring lipid layers onto solid substrates, though each method has unique properties and limitations. For a recent review comparing methods for creating solid-supported bilayers, see [56]. This work focuses on creating highly controlled phospholipid layers. The aim is to develop a model system incorporating charged and zwitterionic phospholipids at the air/solid interface while minimizing defects (see Figure II.4). In this case, the Langmuir-Blodgett deposition method is particularly well suited.

II.1.B.ii Langmuir-Blodgett deposition

Old techniques don't necessarily mean outdated methods. The Langmuir-Blodgett (LB) deposition technique, developed by Irving Langmuir in 1917 [57], involves transferring a monolayer of lipid molecules from the air-water interface to a solid substrate. Later, Katherine Blodgett extended this approach to multilayer deposition [58]. While LB deposition can produce multiple layers, depending on lipid type, this flexibility is unavailable with vesicle fusion deposition, another standard technique often used with LB. A more recent method, spin coating, offers speed but not the same level of control or quality as LB, which gives fewer defects for the transferred layers. This study describes the deposition of DSPC and DPPC trilayers onto glass or silica substrates using LB. Neutral phospholipids are generally limited to three layers, as discussed in the next section. For more than three layers, the Langmuir-Schaeffer deposition technique is used [59]. However, three layers suffice as we control the second water layer (see Chapter I.3). For anionic DPPS phospholipids and certain DPPS/DPPC mixtures, it was possible to deposit more layers. We display the graphical representation of the trilayer and pentalayer in Figure II.4.

II.1.B.iii Substrate cleaning

The first critical step is substrate cleaning. Both glass and silica substrates followed a similar protocol. The glass substrates used were commercial soda lime microscope slides (76 x 26 mm) [60]. In contrast, the silica substrates were atomically smooth polished [61] with varying sizes depending on the experiment. Glass substrates were used for tribology and FRAPP experiments, and silica substrates were used for reflectivity. While mica is a popular substrate due to its ultra-low roughness (angstrom level) [56], its birefringence makes it unsuitable for optical setups. Soda-lime glass has a roughness of approximately 0.8-1 nm [56, 62], which can be reduced with base bath treatments, although results may vary depending on the glass type and carry some risk of increased roughness.

To ensure a highly hydrophilic substrate free from organic residues, the standard cleaning method involves ultrasonic baths of solvents from less polar

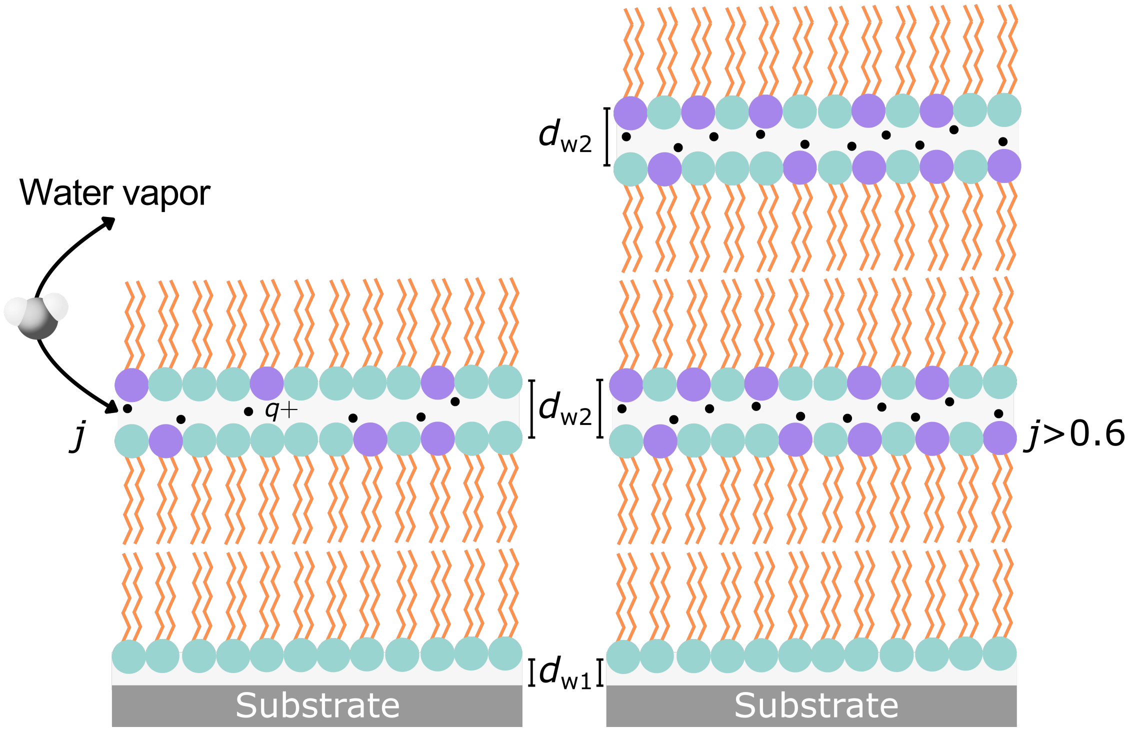

Figure II.4: Schematic representation of the lipid layers at the solid/air interface studied in this thesis. On the left a trilayer and on the right a pentalayer. The first layer, closest to the substrate, is always a layer of neutral molecules (DPPC or DSPC). The other layers are made up of a fraction j of charged lipids (DPPS) and $1-j$ of neutral lipids (DPPC). The different thicknesses of water are shown, as well as the exchange of water with air at a controlled relative humidity RH. Water molecules are not shown. Black dots represent counterions.

to more polar: chloroform, acetone, ethanol, and Milli-Q water. The substrate is then dried with nitrogen gas and exposed to UV/ozone or plasma treatment before a final rinse with Milli-Q water. Immediately afterward, the microscope slide is immersed in the Langmuir-Blodgett trough.

II.1.B.iv Langmuir isotherm

The trough, typically made of low-energy materials like Teflon, holds ultrapure Milli-Q water as the subphase. For our experiments, we used a Nima KSV large trough [63] (see Figure II.5). The substrate is first dipped into the subphase. Phospholipid molecules, acting as surfactants, modify the interface energy by localizing at the air/water interface. Since the phospholipids used here are insoluble in water, they do not form micelles or vesicles. When added, they remain at the surface, allowing precise control over the phospholipid amount at the interface.

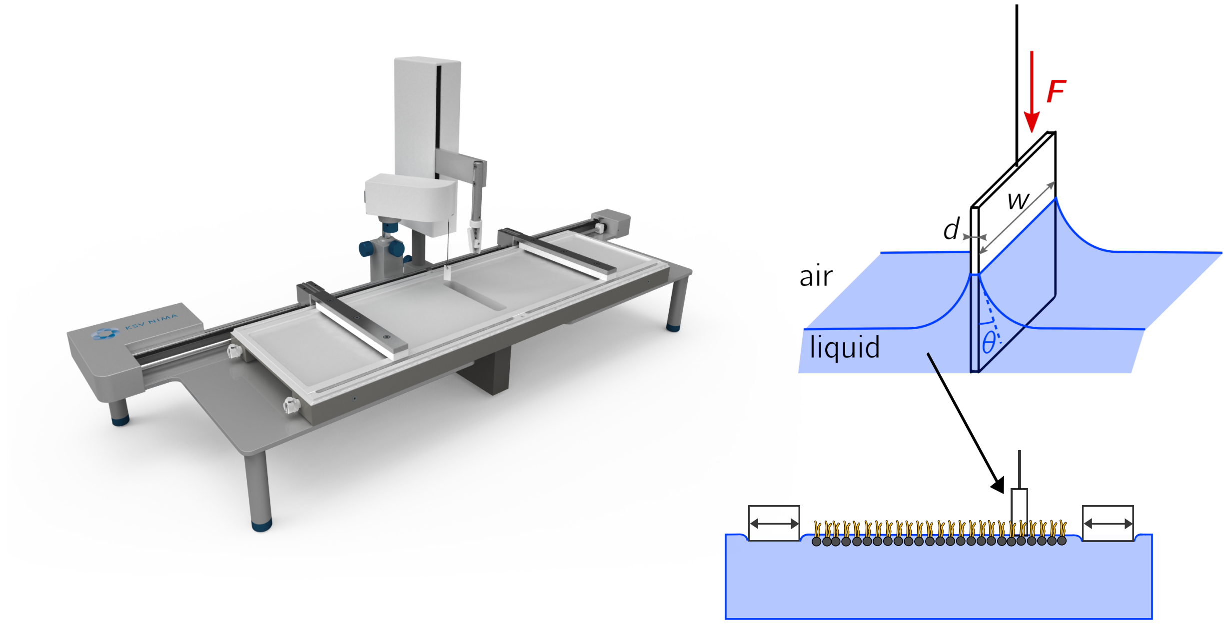

Figure II.5: (Left) Langmuir-Blodgett trough (Nima-KSV). (Top right) Wilhelmy plate used to measure surface tension. (Bottom right) Schematic view of the monolayer at the water/air interface and compression barriers.

The phospholipid solution was prepared at 1 mg/ml in chloroform for DSPC and DPPC. DPPS, which is less soluble in chloroform, required a solvent mixture of chloroform:methanol:water at a ratio of 70:29:1 to fully solubilize it at 1 mg/ml (for DPPS and DPPC/DPPS mixtures). Proper solubilization is essential for accurate phospholipid transfer to the air/water interface. Sometimes, mild heating and sonication of the DPPS solution were necessary for homogenization. The solution was then added drop-by-drop to the water surface using a Hamilton syringe. Slow, controlled deposition ensures a monolayer formation almost perfect, as the solvent evaporates in a few tens of minutes, leaving phospholipids at the water's surface.

After transferring a known quantity of phospholipids to the interface, we measure the surface tension changes induced by phospholipids, especially during monolayer compression. The Wilhelmy plate method, which uses filter paper as a tensiometer, is illustrated in Figure II.5. This paper is designed to be highly hydrophilic, ensuring that the contact angle, θ, between the liquid phase and the paper reaches zero. When the paper contacts the interface, a wetting force arises $F = \gamma\, l \cos(\theta)$ where $l = 2w + 2d$ is the perimeter of the paper, where w and d are the paper's width and thickness, respectively. The paper is attached to a microbalance, allowing for the measurement of F. The Archimedean force, tension, and weight remain stable with a constant water level. With $\theta = 0$, we obtain directly the surface tension γ as:

$$\gamma = \frac{F}{l}. \tag{II.1}$$

This measurement is not absolute; the microbalance was initialized to zero before depositing phospholipids at the interface. In this way, we measure what is known as the surface pressure, Π, defined as:

$$\Pi = \gamma_o - \gamma \tag{II.2}$$

where γ_o represents the subphase surface tension without the monolayer, and γ is the surface tension with the phospholipid monolayer present. It corresponds also to the pressure acting on the barriers (see Figure II.5). This measurement is essential for determining the state of the monolayer. Using two Teflon barriers, we can compress the monolayer and control the area per lipid, a, available for each phospholipid molecule. Predicting the surface pressure variation, Π, as a decreases, can be challenging. The phase state of these

2D monolayers is highly influenced by the phospholipid's tail length and headgroup type [64].

Isotherms depend on various interactions, including van der Waals attractions between tails, electrostatic interactions, and hydration forces that vary with headgroup types. Experiments were performed at a constant temperature of 25°C, maintained by a thermostated bath. By gradually compressing the layers (compression speed of 10 mm/min), we recorded isotherms for DPPC, DPPS, and DSPC, shown in Figure II.6.

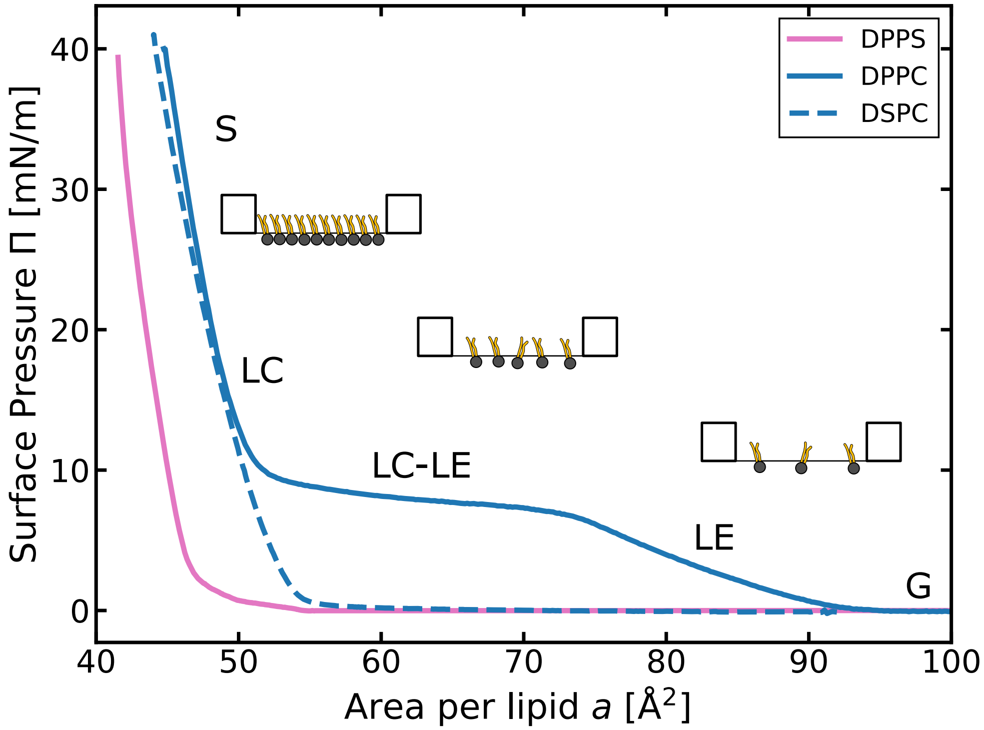

Figure II.6: Isotherms (25°) obtained on the Langmuir trough for DPPS (—), DPPC (—), and DSPC (- - -) monolayers studied in this work. The gas (G), liquid expanded (LE), liquid condensed (LC), and solid (S) phases are represented schematically.

The lipid layers undergo phase transitions through several distinct phases: liquid-expanded (LE)–gas (G) coexistence, LE, liquid-condensed (LC), solid/gel (S), and ultimately, the collapse of the layers. For DPPC specifically, a plateau is observed, corresponding to the coexistence of the LE and LC phases. Each time, we stopped in the gel phase before the collapse of the layer.

II.1.B.v Langmuir-Blodgett deposition

For the transfer of the lipid layer onto the substrate, the surface pressure was maintained at $\Pi = 40\,\mathrm{mN/m}$, corresponding to the gel phase. The gel phase is usually where $|d\Pi/d\alpha|$ is the highest, providing the best transfer. When the substrate is pulled out of the subphase (at the slow speed of 4 mm/min), the monolayer deposits on the substrate; as the monolayer transfers, the barriers compress the monolayer, targeting the gel phase value to compensate for the material lost.

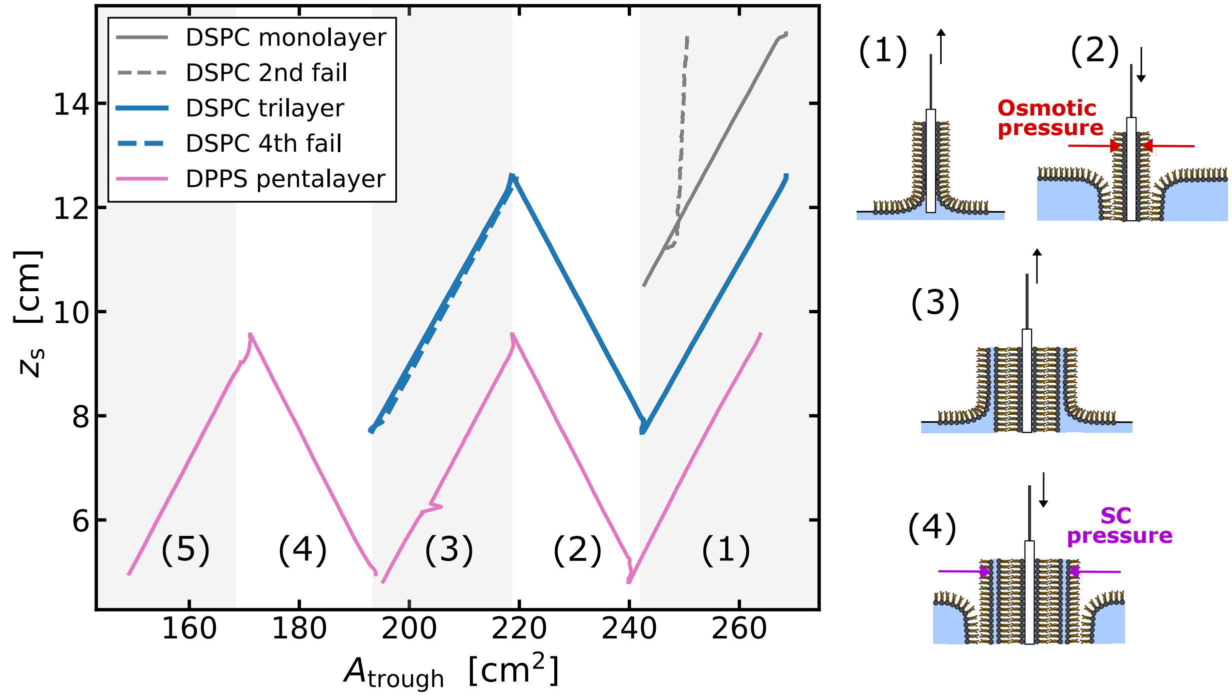

Figure II.7: Transfer rate curves representing the position of the substrate z_S as a function of the area of the barrier. Black (—, top) for a monolayer of DSPC with a failure during deposition of the second layer. In blue (—, middle) for DSPC with the deposition of a trilayer and a failure during the deposition of the 4th layer. In pink (– – –, bottom), deposition of a pentalayer of DPPS.

As the substrate is pulled out of the water, a monolayer approximately 2-3 nm thick is deposited on the macroscopic substrate. The substrate is then dipped again into the subphase, resulting in the formation of a bilayer. After the deposition of the third layer, we obtain a trilayer exposed to air, as shown in Figure II.7. For DSPC and DPPC, this represents the limit of the number of layers that can be stacked by classical LB deposition. If an attempt is made to deposit a fourth layer, the third layel is re-transferred to the air/water interface (see Figure II.7, blue dashed line).

In contrast, for DPPS and DPPS/DPPC mixtures with a mass fraction of DPPS greater than $j = 0.6$ (where $j = m_{\mathrm{DPPS}}/(m_{\mathrm{DPPS}} + m_{\mathrm{DPPC}})$), it is possible to stack an indefinite number of layers [59]; in our experiments, we limit the stacking to five layers, referred to as pentalayers.

To quantify the quality of the deposition, a good approach is to compute the transfer ratio TR defined as:

$$\mathrm{TR} = \frac{\Delta A_{\mathrm{trough}}}{\Delta A_{\mathrm{substrate}}}. \tag{II.3}$$

If $\mathrm{TR} = 1$, it indicates that all the area compressed $\Delta A_{\mathrm{trough}}$ is transferred to the substrate characterized by a deposition surface $\Delta A_{\mathrm{substrate}}$, which implies that the density of the monolayer is conserved. Typically, the transfer ratios are slightly less than one. Figure II.7 compares the transfer rate curves for DPPS pentalayer and DSPC trilayer depositions.

The value of TR is representative of the deposition quality, as observed experimentally in friction experiments, reflectivity measurements, and using Atomic Force Microscopy (AFM) (see Appendix A and [46, 56]). The substrates are in contact with air, so they are sensitive to contamination and are used as quickly as possible to minimize contamination.

II.1.B.vi Influence of ambiant humidity

One significant finding in my thesis regarding deposition quality is the influence of RH, which has not been previously mentioned in the literature. I hope this discovery will assist future students working in the field, as it was a game-changer for my research.

During the first year of my PhD, we observed a correlation between the time of year and deposition quality; at certain times, it was impossible to deposit second or third layers of phospholipids. Notably, winter proved to be more conducive to layer deposition. As we conducted RH-controlled experiments, we found that in winter, RH levels in the room dropped to 30-40% due to heaters.

Initially, we assumed that local RH around the interface would not vary significantly and that conditions in the three-phase contact zone would remain stable, leading us to believe that changes in RH would have no effect. However, it became evident in my thesis that low RH improved deposition quality. Although we do not have a quantitative analysis of this effect, we can compare the deposition of DSPC trilayers without RH control under poor conditions to those where we managed the RH. In the latter case, we injected dry air (RH=3%) into the laminar flow hood containing the Langmuir trough, allowing us to achieve a local equilibrium of 30% RH.

We did not measure local RH around the substrate, but since we began controlling the RH (with an environmental RH of 30%), we have not experienced any failed depositions. Regarding interpretation, as discussed in Chapter III, low RH corresponds to strong osmotic pressure. This osmotic pressure stabilizes the layer and prevents re-transfer to the water interface. Dipping the substrate vertically into the water may induce shear on the already deposited layer. The osmotic pressure would help to "glue" the confined layers together. This concept of binding layers also applies to anionic DPPS phospholipid layers, where we can stack more layers.

The electrostatic attraction mediated by ionic correlation enhances deposition. This analogy taken from Ivan Palaia's thesis [65], which studied electrostatic strong coupling in clay, is particularly insightful. He uses the metaphor of ionic correlation attraction resembling a zip. An illustration of my interpretation in the case of LB deposition is shown in Figure II.7.

II.2 Neutron and X-rays reflectometry

Reflectometry with neutrons (NR) and X-rays (XR) enables the investigation of thin film structures at interfaces with sub-nanometer resolution ($\approx 0.1\,\mathrm{nm}$), facilitated by the short wavelengths of these probes [66]. In this work, only elastic scattering specular reflectivity measurements are performed. The incident beam, characterized by an angle θ_i, reflects in the plane of incidence at the same angle, allowing analysis of the vertical structure of the film.

The momentum transfer vector, $\mathbf{q}$, describes the change in the wavevector upon surface interaction and is defined as $\mathbf{q} = \mathbf{k}_\mathrm{f} - \mathbf{k}_\mathrm{i}$ (see Figure II.8). For specular reflectometry, only the component perpendicular to the surface $\mathbf{q} = q_z \mathbf{e}_z$ is relevant, enabling detailed measurements of layer thickness, roughness, and density at the interface. Although not performed here, off-specular reflectivity can also be used to obtain information on lateral features of the sample, such as surface homogeneity and interfacial roughness. The theoretical foundation and much of the information in this chapter are derived from the book by Jean Daillant and Alain Gibaud [66] and Florence Blachon's Thesis [3].

Figure II.8 provides a schematic of specular reflectivity, illustrating the q_z

vector perpendicular to the surface.

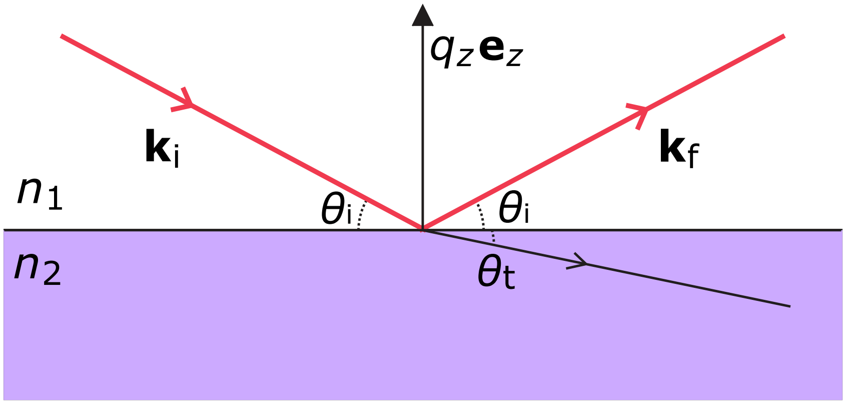

Figure II.8: Geometry of a specular reflectivity experiment on a plane interface between two media of index n_1 and n_2. The incident beam (light, neutrons, X-rays) of wave vector $\mathbf{k}_i$ makes an angle of incidence θ_i with the interface. The reflected beam with wave vector $\mathbf{k}_f$ is symmetrical with respect to the normal to the interface (specular direction) and the transmitted beam makes an angle θ_t. The transfer wave vector $\mathbf{q}$ is perpendicular to the interface.

II.2.A Comparison of X-ray and Neutron Reflectometry

X-rays reflectometry and neutron reflectometry each bring unique interaction mechanisms, which lead to distinct advantages and limitations in their applications. X-rays interact with the electron cloud of atoms, where the scattering intensity is mainly proportional to the atomic number Z. This allows for detailed structural analysis, although it also introduces a risk of ionization damage to samples.

Neutrons interact directly with atomic nuclei and are non-destructive, which is particularly useful for studying soft matter and biological interfaces. Neutrons penetrate deeply into materials with minimal scattering or absorption, but this characteristic makes them more difficult to detect. Consequently, detection statistics are lower, and the accessible wave vector transfer range is limited to around $q_z = 3\,\mathrm{nm}^{-1}$, about half that of X-rays, which slightly limits resolution.

However, with neutrons, we have the advantage of isotopic contrast. This is very helpful in soft matter, particularly in cases with solvents. Heavy water (D_2O) interacts differently from ordinary water (H_2O), allowing us to adjust contrast and refine the analysis further, as we will detail in the next sections.

II.2.B Scattering Length Density

XR and NR use Scattering Length Density (SLD) to characterize interactions at material surfaces. The nuclear $\mathrm{SLD_n}$ for NR is defined as

$$\mathrm{SLD_n} = \frac{\sum_{\mathrm{j}=1}^{\mathrm{N}} \mathrm{b_j}}{\mathrm{V_m}} \tag{II.4}$$

where b_j is the coherent scattering length of the j-th nucleus within a volume V_m. For X-rays reflectometry, an analogous measure is the electron density (ED), computed by substituting atomic number Z_j for b_j. ED is linked to the electron scattering length density $\mathrm{SLD_x}$ by

$$\mathrm{SLD_x} = \mathrm{r_e} \times \mathrm{ED} \tag{II.5}$$

where $r_e = 2.81 \times 10^{-15}\,\mathrm{m}$.

NR and X-rays reflectometry provide complementary insights because X-rays scattering increases proportionally with atomic number, whereas neutron scattering varies significantly by element and isotope and can even appear random (see [67] for a list of neutron scattering lengths). This variability is especially useful in contrast variation techniques. For instance, the scattering lengths b of H_2O and D_2O differ substantially (with values of $b_{H_2O} = -0.374 \times 10^{-15}\,\mathrm{m}$ and $b_{D_2O} = 0.667 \times 10^{-15}\,\mathrm{m}$).

II.2.C Optical Index

Reflectometry measures spatial variations in scattering profiles for thin films by examining the refractive index n of each medium. For both X-rays and neutrons, the refractive index is described as:

$$n \approx 1 - \frac{\Delta\rho\lambda^2}{2\pi} \tag{II.6}$$

where $\Delta\rho = \mathrm{SLD}_1 - \mathrm{SLD}_0$ is the contrast between the scattering length densities of adjacent media and λ is the wavelength of the incident radiation. In both cases, the refractive index can be complex:

$$n \approx 1 - \delta - i\beta \tag{II.7}$$

where the real part, $\delta = \Delta\rho\lambda^2/2\pi$, describes phase changes and the imaginary component β represents absorption. This absorption factor is typically small, especially in organic materials, and can often be neglected.

II.2.D Critical Angle for Total Reflection

For neutron and X-ray reflectometry, the incident wave undergoes total reflection if the angle of incidence θ_i is less than a critical angle θ_cr. Snell's law describes the relationship at an interface:

$$\cos(\theta_\mathrm{i}) = n\cos(\theta_\mathrm{tr}), \tag{II.8}$$

where θ_tr is the angle of the transmitted wave. Total reflection occurs when $\theta_\mathrm{tr} = 0$, leading to the condition for the critical angle θ_cr:

$$\theta_\mathrm{cr} = \sqrt{\frac{\Delta\rho\lambda^2}{\pi}}. \tag{II.9}$$

In terms of the wave vector q_z, the critical wave vector q_cr associated with θ_cr is given by:

$$q_\mathrm{cr} = 4\sqrt{\pi\Delta\rho}. \tag{II.10}$$

Experimentally, measuring θ_cr or q_cr allows us to calculate $\Delta\rho$, giving insight into layer compositions and interface structure in multilayered samples.

II.2.E Fresnel Reflectivity and Multilayer Systems

II.2.E.i Fresnel Reflectivity

At an ideal interface separating two media with refractive indices n_1 and n_2 (like Figure II.8), the reflection coefficient r is:

$$r = \frac{n_1\sin\theta_\mathrm{i} - n_2\sin\theta_\mathrm{t}}{n_1\sin\theta_\mathrm{i} + n_2\sin\theta_\mathrm{t}}, \tag{II.11}$$

yielding the Fresnel reflectivity:

$$R_\mathrm{F} = |r|^2 = \left|\frac{n_1\sin\theta_\mathrm{i} - n_2\sin\theta_\mathrm{t}}{n_1\sin\theta_\mathrm{i} + n_2\sin\theta_\mathrm{t}}\right|^2. \tag{II.12}$$

This reflectivity varies with incidence angle θ_i and neutron wavelength. For angles above the critical angle θ_C, the transmitted wave vector approximates as:

$$k_\mathrm{t} = k\sqrt{\sin\theta_\mathrm{i} - \sin\theta_\mathrm{C}}. \tag{II.13}$$

When $\theta_\mathrm{i} \gg \theta_\mathrm{C}$, the reflectivity simplifies to:

$$R_\mathrm{F}(q_z) \approx \frac{16\pi^2\rho^2}{q_z^4}, \tag{II.14}$$

characteristic of specular reflection from a smooth, flat interface.

II.2.E.ii Reflection from a rough Stratified Interface

The Abeles matrix formalism provides an efficient way to calculate specular reflectivity for a stratified interface as a function of the perpendicular momentum transfer q_z. It models multilayers with distinct thickness, SLD, and interface roughness for each layer represented in Figure II.9.

The perpendicular momentum transfer, q_z, is defined as:

$$q_z = \frac{4\pi}{\lambda}\sin\theta = 2k_z, \tag{II.15}$$

where θ is the angle of incidence and λ is the wavelength. The SLD profile $SLD(z)$ varies along z, and is approximated using discrete layers with properties d_m and SLD_m.

In layer m, the wave vector $\mathbf{k}_m$ accounts for refraction as:

$$k_m = \sqrt{k_z^2 - 4\pi(\Delta\rho_m)}, \tag{II.16}$$

where $\Delta\rho_m = SLD_m - SLD_0$ is the SLD difference between the layer and the

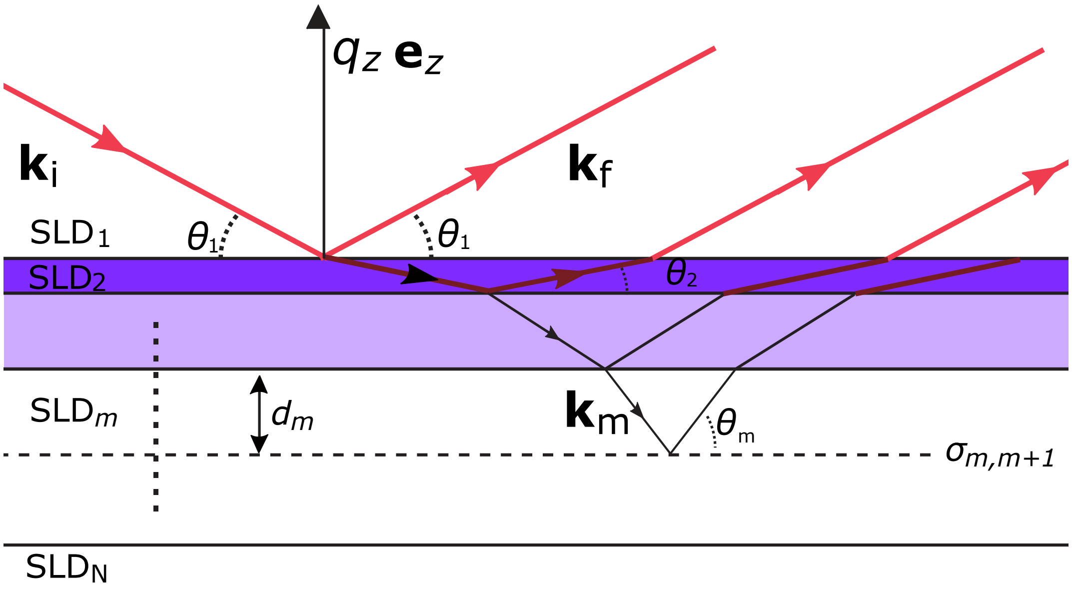

Figure II.9: Geometry of a specular reflectivity experiment on a multilayer interface. Each layer m is characterized by a scattering length density SLD_m and a thickness d_m. An interface between 2 layers m and $m+1$ by a roughness $\sigma_{m,m+1}$.

incident medium.

The Fresnel reflection coefficient between two adjacent layers m and $m+1$ is:

$$r_{m,m+1} = \frac{k_m - k_{m+1}}{k_m + k_{m+1}} \exp(-2k_m k_{m+1}\sigma^2_{m,m+1}), \tag{II.17}$$

where $\sigma_{m,m+1}$ represents the RMS roughness at the interface between layers m and $m+1$. This exponential factor accounts for diffuse scattering due to roughness, which diminishes reflectivity.

To account for the thickness d_m, we define the phase factor β_m:

$$\beta_0 = 0, \tag{II.18}$$

$$\beta_m = ik_m d_m, \tag{II.19}$$

where i is the imaginary unit. Each m layer is characterised by a matrix c_m which allows to calculate the amplitude of the beams reflected and transmitted at each layer:

$$c_m = \begin{pmatrix} \exp(\beta_m) & r_{m,m+1}\exp(\beta_m) \\ r_{m,m+1}\exp(-\beta_m) & \exp(-\beta_m) \end{pmatrix}. \tag{II.20}$$

The total reflectivity of the multilayer structure is determined by calculating the ordered product of the characteristic matrices of each layer:

$$M = \prod_m c_m. \tag{II.21}$$

The reflectivity R is derived from matrix M:

$$R = \left|\frac{M_{10}}{M_{00}}\right|^2, \tag{II.22}$$

where M_{10} and M_{00} are elements of M, encapsulating cumulative effects across all interfaces.

The Abeles matrix formalism allows refining complex multilayer models by fitting calculated reflectivity to experimental data, adjusting parameters d_m, ρ_m, and $\sigma_{m,m+1}$.

II.2.F Comparison of simple interfaces

To illustrate the reflectivity formalism described above, we present in Figure II.10 various reflectivity models alongside their corresponding SLD profiles. We modeled a smooth air/silica interface using X-rays (grey solid line). At low q_z values, we observe a plateau corresponding to total reflectivity. As q_z increases, R decays due to partial transmission into the second medium.

Also shown is the $1/q_z^4$ approximation (green dotted line), which accurately predicts Fresnel reflectivity for $q_z > q_{\text{cr}}$. In pink, we depict the same interface with a roughness of $\sigma = 0.3$ nm, resulting in a faster reflectivity decay. Finally, we calculate the reflectivity for an air/water/silica interface with a water film of thickness $d = 3$ nm and roughness $\sigma = 0.3$ nm, where we clearly see the characteristic Kiessig fringes due to interference.

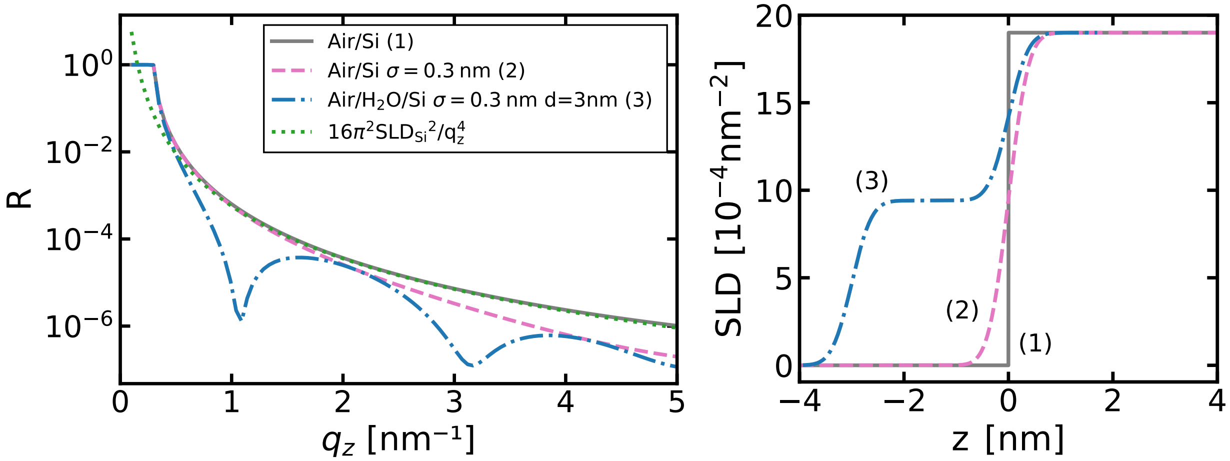

Figure II.10: (Left) Examples of specular reflectivity (x-rays) curves calculated with for a (1, —) perfectly flat Si/air interface, (2, – – –) a Si/air interface with a roughness of 0.3 nm, (3, – – –) a 3 nm thick water layer with a roughness of 0.3 nm, (4, · · ·) large q approximation. (Right) Corresponding SLD_X profiles.

II.3 Experimental devices

II.3.A Neutron reflectometer D17 (Institut Laue-Langevin)

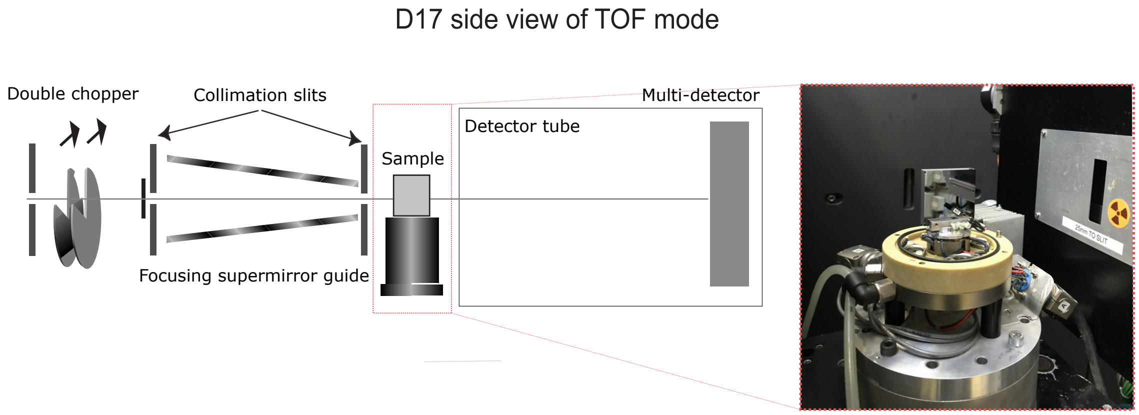

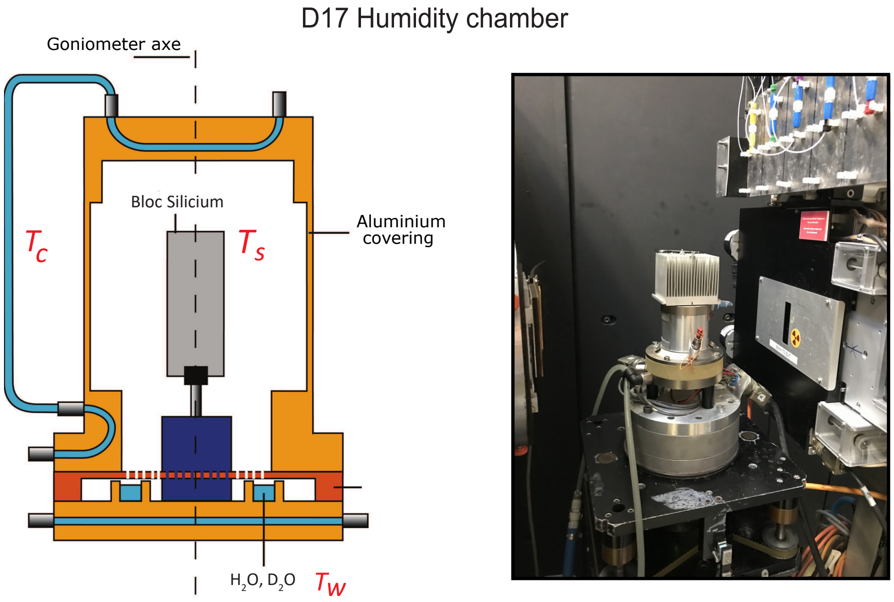

Figure II.11: (Top) Geometry of the D17 reflectometer. The double chopper is used to control the wavelength distribution of incident neutrons. The sample is placed vertically on the goniometer. The 2d detector measures the intensity collected on each pixel and the time of flight, leading to the wavelength of the neutrons detected. (Bottom) Schematic view and photograph of the humidity chamber with the sample in place. The temperature of the sample T_S, the chamber T_C, and the solvent cuvettes T_W are tuned. Scheme adapted from [68].

The neutron reflectivity experiments were carried out at the Institut Laue-Langevin de Grenoble (ILL) on line D17, in collaboration with Giovanna Fragneto. D17 is a neutron reflectometer working in a horizontal geometry (the sample surface is vertical and the detector moves in the horizontal plane, see Figure II.11). The pixels of the two-dimensional detector were calibrated at the start of the experiment. For more details on D17 the reader can refer to [69].

Reflectivity measurements on D17 were carried out in time of flight mode (TOF), using a wavelength range from 0.2 to 3 nm and two different angles of incidence of 0.8° and 3.2°, which enabled us to cover a wave vector range q_z from 0.005 to 3 nm^{-1}.

The samples, made up of $1 \times 5 \times 5$ cm^3 silicon blocks on which the lipid layers are deposited, are placed vertically in a humidity chamber which is itself mounted on a goniometer. During neutron reflectivity experiments, an area of several square centimeters was illuminated by the incident beam while at the same time ensuring to avoid over-illumination.

The humidity chamber developed at ILL is used to control the temperature and relative humidity (RH) of the sample (see Figure II.11, bottom). The humidity is set by controlling the temperature difference between the sample, the chamber enclosure and the temperature of the solvent reservoirs (H_2O, D_20 or a mixture of these). The relative humidity can thus vary between 5 and 90%, while controlling the temperature of the sample and the isotopic contrast of the solvent present between the layers.

The reflectivity curves are obtained after subtraction of the background and normalization with the measurement of a direct beam.

II.3.B Reflectivity experiments at SIRIUS beamline (SOLEIL)

X-rays reflectivity experiments were performed at synchrotron SOLEIL on SIRIUS beamline, in close collaboration with Arnaud Hemmerle [70].

SIRIUS (Soft Interfaces and Resonant Investigation on Undulator Source) is a beamline allowing structural studies in an energy range from 1.4 to 13 keV. It is particularly well suited for the study of condensed matter, and in particular soft interfaces as air/water interface, Langmuir monolayers, Langmuir-Blodgett, biomimetic systems,... SIRIUS is optimized for diffraction (GIXD), scattering (GISAXS) and fluorescence (XRF) in grazing incidence conditions and it is also possible to perform specular and off-specular reflectivity experiments.

The specular reflectivity measurements were performed on lipid layers deposited on silicon substrates. The X-ray beam energy was 8 keV, which corresponds to a wavelength of 0.155 nm. The incident beam is 500 μm wide and 70 μm high, giving a footprint on the sample that is 500 μm wide and 18 mm long, thus avoiding over-illumination.. The footprint of the beam on the sample was moved by 1 mm every 30 min, which prevents sample degradation.

The reflectivity curves are obtained after subtraction of the background and normalization by the measured of a direct beam intensity.

II.4 Modeling the reflectivity of phospholipid layers

To fit our experimental reflectivity data, we model our supported phospholipid layers using a stratified model, dividing the system into layers with specific thickness, SLD values and interbilayer roughness. Below, we detail the model structure and the SLD values used for XR and NR analysis.

Supported lipid layers are planar structures well-suited for stratified models. Here, we describe a trilayer model for XR and NR, though this approach also applies to pentalayers. Each leaflet is divided into a head group and a tail group. For high-resolution XR data, we added an additional layer for the central methyl group between the two leaflets. The water layers are modeled separately, and an oxide layer is included on the silica substrate. Solvent fractions are incorporated into the phospholipid headgroup layer. In the analysis, we fixed the SLD to one we computed (shown in Table 1 for XR and Table 2 for NR), and the thickness and roughness and the solvent fraction (for heads) of each layer are free parameters.

Table II.2: Neutron scattering length density of used phospholipids

Name	Structure	b_n	V_m [nm^3]	SLDn [10^{-4} nm^{-2}]
PC head	$C_{10}H_{18}O_8PN$	60.054	0.319	1.88
PS head	$C_8H_{11}O_{10}PNa$	81.55	0.31	2.63
DS tail	$C_{34}H_{70}$	-35.836	0.917	-0.39
DP tail	$C_{30}H_{62}$	-32.5	0.825	-0.39

Table II.3: X-ray scattering length density of used phospholipids

Name	Structure	Z_el	V_m [nm^3]	SLDx [10^{-4} nm^{-2}]
PC head	$C_{10}H_{18}O_8PN$	164	0.319	14.45
PS head	$C_8H_{11}O_{10}PNa$	172	0.31	15.5
DS tail	$C_{34}H_{70}$	274	0.917	8.4
DP tail	$C_{30}H_{62}$	274	0.825	8.4
CH_3	CH_3	9	0.038	6.65

Table II.4: Scattering length density of solvents and substrate

Material	SLDn [10^{-4} nm^{-2}]	SLDx [10^{-4} nm^{-2}]
H_2O	-0.56	9.41
D_2O	6.36	-
Si	2.07	18
SiO_2	3.41	19

We report in Figure II.12 a model of SLD_x and SLD_n profiles for a trilayer composed of a DPPC layer as the first layer and two DPPS layers as the second and third layers. Both profiles are calculated using H_2O as the solvent. We display the profiles with solid lines representing a roughness of $\sigma = 0.3$ nm and dotted lines representing profiles without roughness, which clearly delimitates the slabs.

NR and XR experiments were performed in humidity chambers, allowing for fine control of RH. The goal of the XR and NR experiments here is to measure the evolution of hydration of phospholipid heads at various RH values (or osmotic pressures). NR experiments were conducted in contact with H_2O and D_2O vapor, allowing for co-refinement of the reflectivity profiles (see Appendix B). This method usually enhances the resolution of fitted parameters; however, it assumes that the exchange between vapor phase and phospholipid heads is complete, which, in our case, is uncertain. To address this uncertainty, we decided to fix the fraction of solvent in phospholipid heads to the value obtained from XR experiments. Since XR experiments are performed solely with H_2O and XR provides high resolution, this approach is justified. Lastly, since it is difficult to distinguish between free water and water bound to phospholipid heads, we imposed a constraint on the thickness of the phospholipid heads,

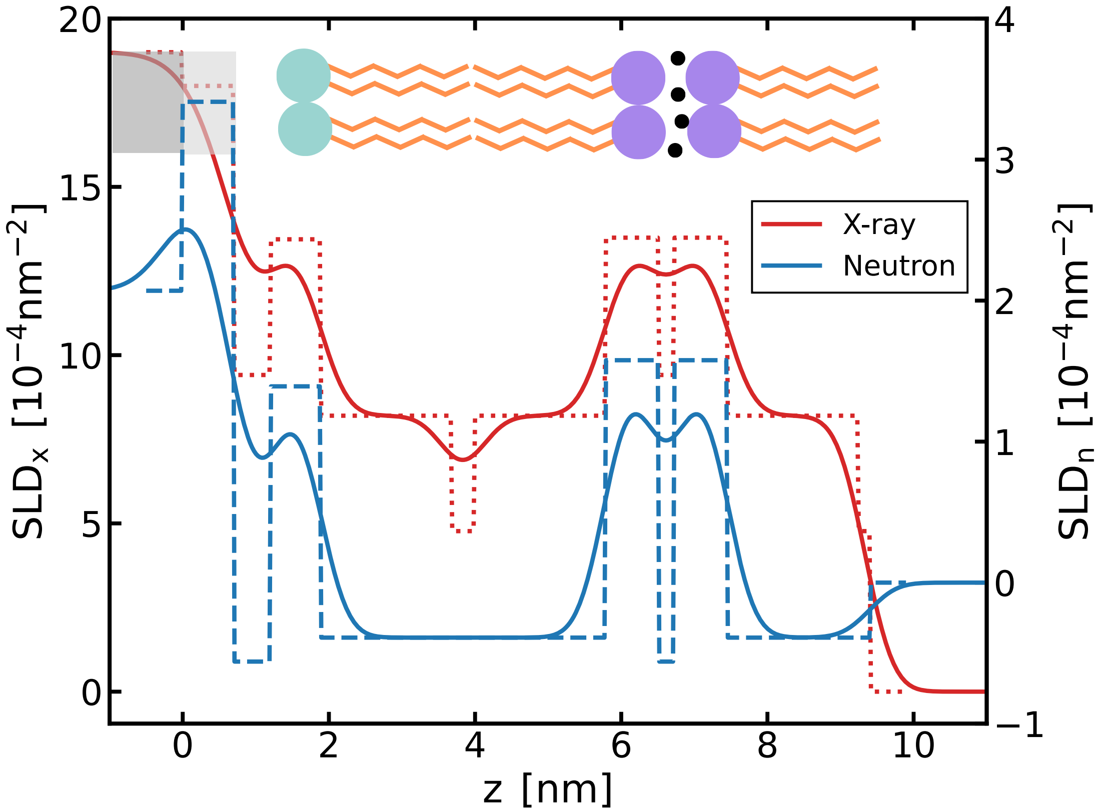

Figure II.12: SLD profiles in the case of a trilayer for X-rays (SLD_X, in red, left axis) and for neutrons (SLD_n, in blue, right axis). The dotted line shows the profiles without roughness to highlight the slab model. A schematic representation of the trilayer with lipids and counterions (black dots) is also shown.

denoted as d_{head}. If the thickness of the tail of the corresponding leaflet is d_{tail}, we express d_{head} as:

$$d_{\text{head}} = \frac{V_{\text{m, head}} \cdot d_{\text{tail}}}{V_{\text{m,tail}}}$$

where $V_{\text{m,head}}$ and $V_{\text{m,tail}}$ are the theoretical volumes of the head and tail, respectively.

We define the second water layer thickness d_{w2} as

$$d_{\text{w2}} = d_{\text{S}} + 2 f_{\text{sol}} d_{\text{head}} \tag{II.23}$$

where d_S is the thickness of the second water slab and f_{sol} is the water fraction in the head slab. f_{sol} was first fitted on XR experiments and found to be equal to 0.38 for PS and PC heads.

II.5 Micro Visio Scratch setup

To study the rheology of phospholipid layers, we used two setups. The first is the MVS or "Micro-Visio-Scratch", developed by the MIM team from Institut Charles Sadron [71, 72]. This setup was used in Chapter V for DSPC experiments related to pressure, velocity, and temperature. The remaining friction experiments were conducted using the triboFRAPP setup, described in the next section.

The MVS is a tribometer with an in situ view of the contact, allowing measurement of contact surface for transparent substrates. It consists of a motorized table with a humidity/temperature chamber. The normal force range F_n attainable was 0.1–2 N. The spherical indenter used was BK7 glass with a radius of 51 mm. The main advantages of this setup are the direct visualization of the contact and the ability to program a range of various velocities and pressures at specific distances. A schematic of the setup is shown in Figure II.13.

II.6 TriboFRAPP setup

One of the most significant and rewarding parts of my thesis work has been improving the triboFRAPP setup. This setup is a collaborative project from two teams of the Institut Charles Sadron, combining the MIM team’s expertise in tribology and contact mechanics, particularly the contributions of Christian

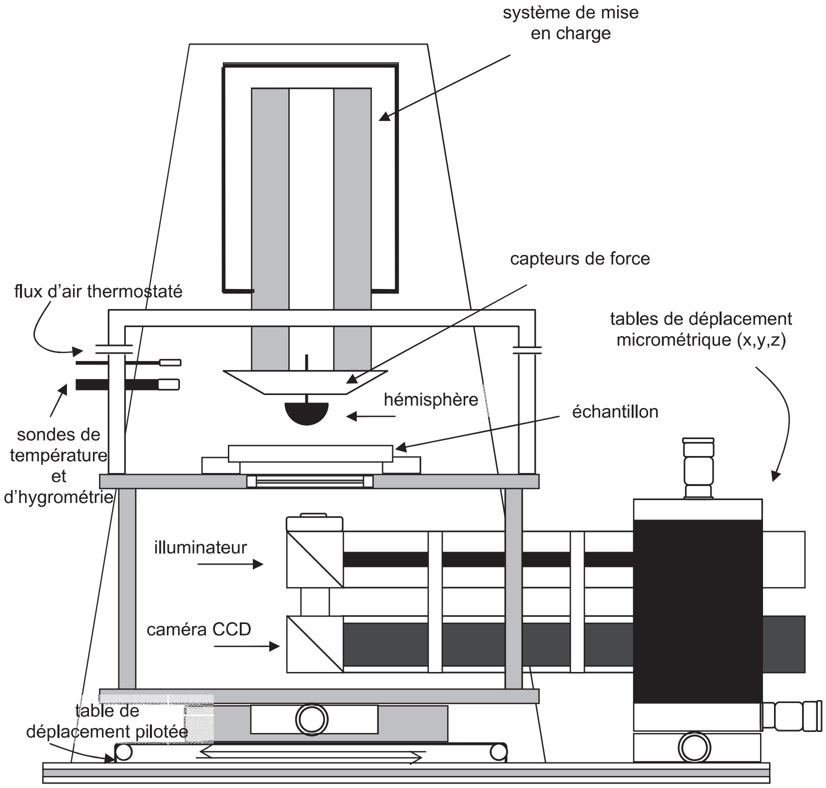

Figure II.13: Scheme of MVS setup [73]. A load system enables contact between a spherical indenter and the sample. Sensors measure friction and normal forces in a temperature- and humidity-controlled environment. A CCD camera allows recording of the contact between the indenter and the sample from below, provided the sample is transparent.

Gauthier and Anne Rubin, with the engineering insights of Damien Favier, who has substantial experience in the development of friction experiments. The setup also draws from the expertise of FRAPP (Fluorescence Recovery After Patterned Photobleaching) velocimetry from Thierry Charitat and Pierre Muller (Mcube team).

The triboFRAPP began taking shape in 2015 during Li Fu's Ph.D. project. Fu's work focused on developing setup, which ended in a publication in 2016 [74]. I will begin by describing the concept of the original setup developed by Fu, followed by an overview of the improvements we implemented during my thesis.

II.6.A Previous setup: piezoelectric modulation

This unique setup combines two experimental techniques: a nano-tribometer, which provides in situ measurements of shear forces, and a fluorescence photobleaching-based velocimetry device (FRAPP), which captures velocity field information and diffusion. The primary challenge lies in achieving precise velocity measurements within a nanometer-scale film, which is confined and subjected to shear forces over a micrometer-sized contact area.

The nano-tribometer captures the confined shear forces by controlling the sliding motion and measuring both the normal load force F_n and the tangential force F_t. These forces enable the calculation of the mean contact pressure $P = F_\mathrm{n}/A$ and the mean shear stress $\tau = F_\mathrm{t}/A$, with A representing the contact area. This setup also includes a visualisation system (using a CCD camera) to monitor the real-time contact area between the tip of an AFM and the surface. The system uses two force sensors with a high precision in the μN range.

In typical FRAP experiments (with only one P: Fluorescence Recovery After Photobleaching), photobleaching is achieved using a circular beam, which enables the investigation of the transport dynamics of fluorescent molecules by measuring the recovery of fluorescence signal. In FRAPP experiments, the bleaching and the detection processes utilize a fringe pattern. This modification enhances the resolution of diffusion measurements and permits velocimetry [75, 76].

The FRAPP setup (illustrated in Figure II.14) is adapted from the work of Davoust et al. [75]. It is essential to outline the specifications of the optical setup. There are three key requirements: (1) the ability to produce a fringe pattern with configurable fringe spacing i, (2) numerical control over the position of the fringes, and (3) numerical control of the laser intensity, which can operate in two modes: full intensity and low intensity (bleaching and reading phase).

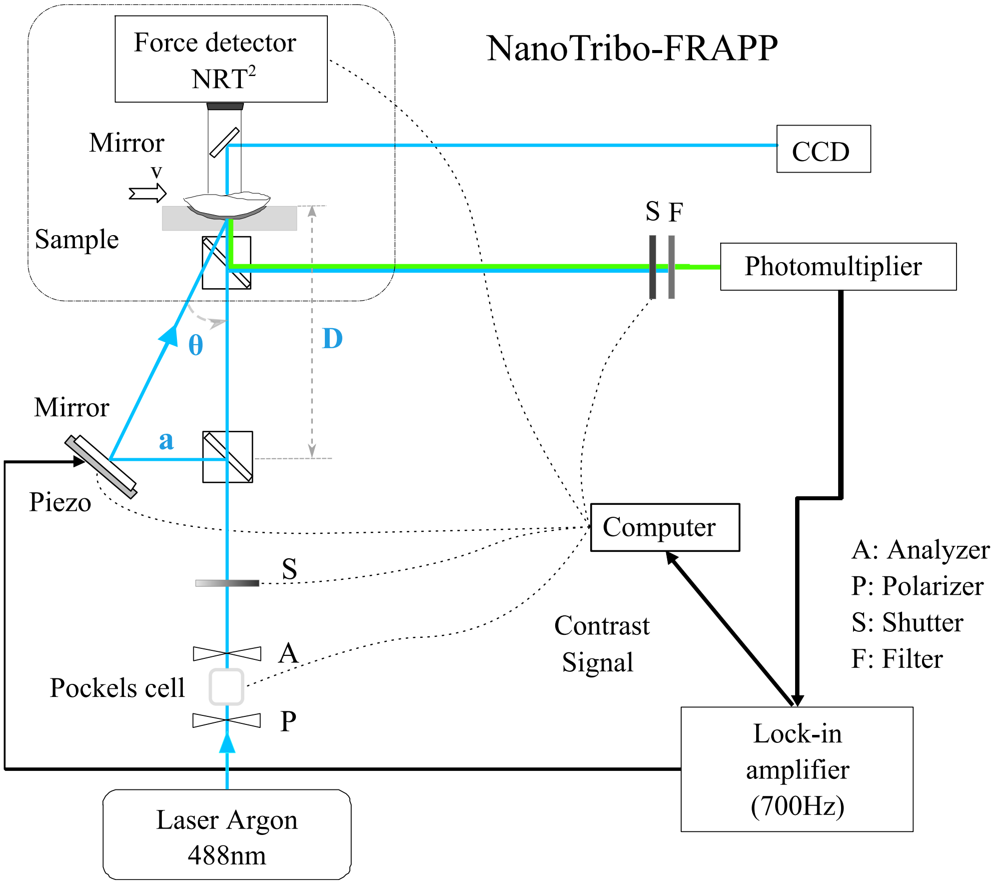

Figure II.14: FRAPP experimental setup in the initial configuration. The setup is divided into two parts: a NanoTribo section providing an in-situ view of the contact and friction measurement, and the FRAPP interferometry setup, which produces a fringe pattern on the sample and records fluorescence recovery after photobleaching. The distances a and D can be adjusted to control the fringe spacing i.

The setup consists of an interferometer based on beam separation and recombination. A laser beam with a wavelength of 488 nm is split into two beams using a semi-reflective plate: one is sent directly to the substrate, while the other is reflected off a mirror before generating a fringe interference pattern. This configuration allows for the adjustment of fringe spacing by controlling the position of the mirror, which changes θ, the angle between the two interfering beams. The fringe spacing is defined by $i = \lambda/2\sin(\theta/2)$. To spatially control the position of fringes, the mirror is mounted on a piezoelectric device alimented with a sinusoidal frequency $\nu = 705$ Hz. The amplitude u is such that the phase difference between the two beams reaches π. During the reading phase, the fringes oscillate, and a photomultiplier measures the fluorescence contrast. The signal is processed with a lock-in amplifier, allowing synchronous detection by selecting the piezoelectric pulsation $\omega = \nu/(2\pi)$. This type of detection dramatically increases the signal-over-noise ratio allowing precise fluorescence measurement for nanoscopic films. Finally, The intensity modulation is done with a Pockels cell positioned in the beam between a polariser and an analyzer. By turning on or off the Pockels cell intensity, we can go from low to high intensity of the laser (Azurlight System-fiber laser 2W).

II.6.B FRAPP theory

Here we detailed the FRAPP signal theory, originally described by Davoust et al. [75].

The interference setup creates an intensity pattern described by:

$$I = I_0(1 + \cos(q_0 x)) \tag{II.24}$$

where I_0 is the maximum intensity, and $q_0 = 2\pi/i$ represents the wave vector of the fringe pattern. Photobleaching generates a concentration of fluorescent markers modeled as:

$$c(x, t = 0) = c_0 e^{-K \cdot I} \tag{II.25}$$

with $K = \alpha I_\mathrm{b} \Delta t$, where α represents bleaching kinetics, I_b is the bleaching laser intensity, and Δt is the exposure time.

If the photobleached fringes move with velocity V_s, this adds a phase $q_0 V_\mathrm{s} t$

to the cosine term. The concentration profile can be Fourier-expanded as:

$$c(x,t=0)=c_0\sum_{n=-\infty}^{\infty}A_n(K,0)e^{jnq_0x} \tag{II.26}$$

where $A_n(K,0) = (-1)^n I_n(K)e^{-K}$, and I_n is the modified Bessel function of the first kind. Each harmonic decays with characteristic diffusion time $\tau_q = 1/\left(Dn^2q^2\right)$:

$$c(q,t)=c_0A_n(K,0)e^{-Dn^2q^2t}. \tag{II.27}$$

The detected fluorescence signal $F(t)$ at the photomultiplier is:

$$F(t)=c_0I_0\Big[A_0+A_1(K,0)e^{-Dq_0^2t}\cos(\phi(t)+q_0V_\mathrm{s}t)\Big] \tag{II.28}$$

where $\phi(t)$ is the phase shift of the interfered beams, which is modulated by the lock-in:

$$\phi(t)=\phi_0+u\sin(\omega t). \tag{II.29}$$

Expanding $F(t)$ in harmonics sum, we get:

$$\begin{aligned}\frac{F(t)}{F_0}&=A_0+A_1(K,0)\mathrm{J}_0(u)e^{-Dq_0^2t}\cos(\phi_0+q_0V_\mathrm{s}t)\\&+2A_1(K,0)\mathrm{J}_1(u)e^{-Dq_0^2t}\sin(\phi_0+q_0V_\mathrm{s}t)\sin(\omega t)\\&+2A_1(K,0)\mathrm{J}_2(u)e^{-Dq_0^2t}\cos(\phi_0+q_0V_\mathrm{s}t)\cos(2\omega t)\\&+\cdots\end{aligned} \tag{II.30}$$

Where J_i is the i^{th} Bessel function of the first kind. It can be observed that the two first harmonics are decreasing as $e^{-Dq_0^2t}$, allowing measurement of the diffusion time τ_q at all harmonics. They are all modulated by sinusoidal functions of frequency q_0V_s. Thus, from a velocimetry perspective, we can directly measure the velocity of a layer moving at V_s by extracting the frequency of the fluorescence signal. With the lock-in amplifier, we could select the first and second harmonics. In this work, ϕ_0, the phase shift between the bleaching and reading beams, was always zero. In this configuration, the first harmonic is null, so we focused on the second harmonic, $f_2(t)$:

$$f_2(t) = 2A_1(K,0)J_2(u)e^{-Dq_0^2 t}\cos(\phi_0 + q_0 V_s t). \tag{II.31}$$

It is clear from this computation that the measurement of the velocity V_s is sensitive to potential phase shifts of the fringe pattern, denoted as ϕ_t. The main issue with the setup described above is its instability with temperature changes. A change of 1°C could result in a phase shift of several fringe spacings over the course of hours (see Chapter V). In the next part, we will describe the new interferometer we installed on the setup to counter phase shift.

II.6.C New setup: Pockels cell modulation

To tackle this issue, we aimed to implement a symmetric interferometer with electro-modulation, ensuring that both interfering beams travel the same optical path. We anticipated this design would enhance stability against temperature fluctuations (see Chapter V for results). Our intention was to adopt the interferometer design from [77], which employs Pockels cells to modulate the phase of two beams separated by a Wollaston prism. The new interferometer setup is depicted in Figure II.15. The laser beam passes through the first Pockels cell, used for intensity modulation as in the former setup. The new Pockels cell is positioned afterward and is oriented such that its principal axes are at 45° to the electric field of the beam (fixed by an analyzer at the end of the intensity Pockels cell). The phase modulation Pockels cell is driven by a sinu-

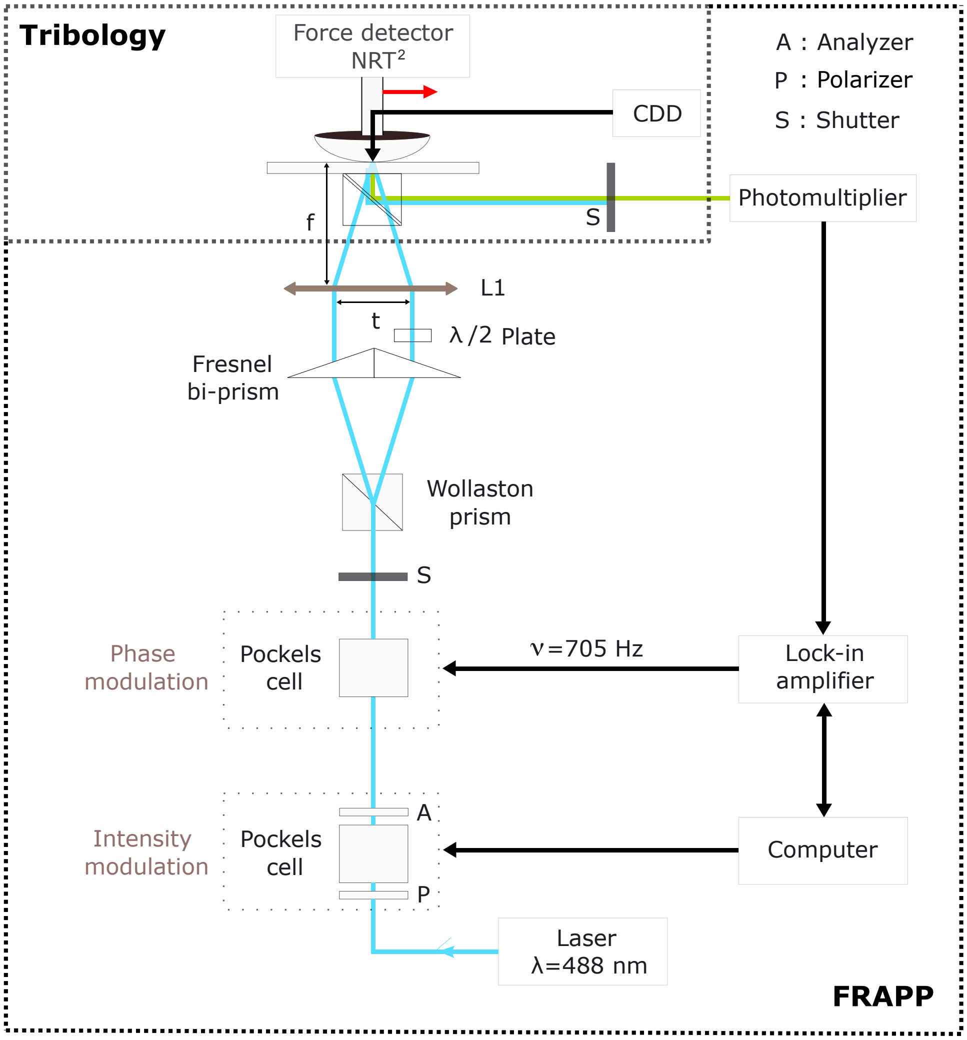

Figure II.15: Modified FRAPP setup using two Pockels cells for modulation of laser intensity and phase. The distances *t* and *f* can be adjusted.

soidal voltage of frequency ν, introducing a phase shift $\phi_p = u\sin(\omega t)$ between the two projections (p and s) of the electric field. As in the previous setup, the amplitude is $u = \pi$. The laser beam then travels through a Wollaston prism (with principal axes parallel to the Pockels cell axes), which splits the beam into two with a characteristic angle of 30°. To make the two beams parallel, a Fresnel biprism with geometry adapted to the Wollaston prism is used. The polarization of one beam is rotated by 45° using a half-waveplate. The beams interfere after passing through a lens.

We end up with a system similar to the Young's double-slit experiment. The fringe spacing is given by:

$$i = \frac{\lambda f}{t}, \tag{II.32}$$

where f is the focal length of the lens and t is the distance between the two beams when they arrive at the lens (see Figure II.15). One drawback of this setup compared to the previous one is that it is inherently more difficult to change the fringe spacing i. One option is to modify the focal length or t. To change t, we developed home-made support for the Fresnel biprism and the half-wave plate (see Figure II.16). This small support allows us to move the position of the Fresnel prism in the direction perpendicular to the beam. By adjusting the distance between the Wollaston prism, we can control t. In our setup, using lenses of 10 cm and 30 cm focal lengths, we can achieve a range of approximately 1 to 100 microns.

Aside from the development of the interferometer, we collaborated with Damien Favier to create a humidity system and a humidity chamber tailored for the triboFRAPP setup. This enhancement enabled us to conduct experiments under controlled RH and temperature conditions. An image of the new tribology section is shown in Figure II.16. Additionally, a view of the interference pattern at $i = 23\,\mu\mathrm{m}$ is provided, along with a close-up of the contact surface between a BK7 indenter and a glass substrate at $F_\mathrm{n} = 0.5\,\mathrm{N}$.

II.6.D TriboFRAPP for supported phospholipid layers

We conclude this chapter with a qualitative summary of the triboFRAPP project setup and its underlying concept. Figure II.17 visually explains the FRAPP procedure adapted to supported phospholipid layers. By photobleaching with a fringe pattern and recording the fluorescence contrast, we can measure the

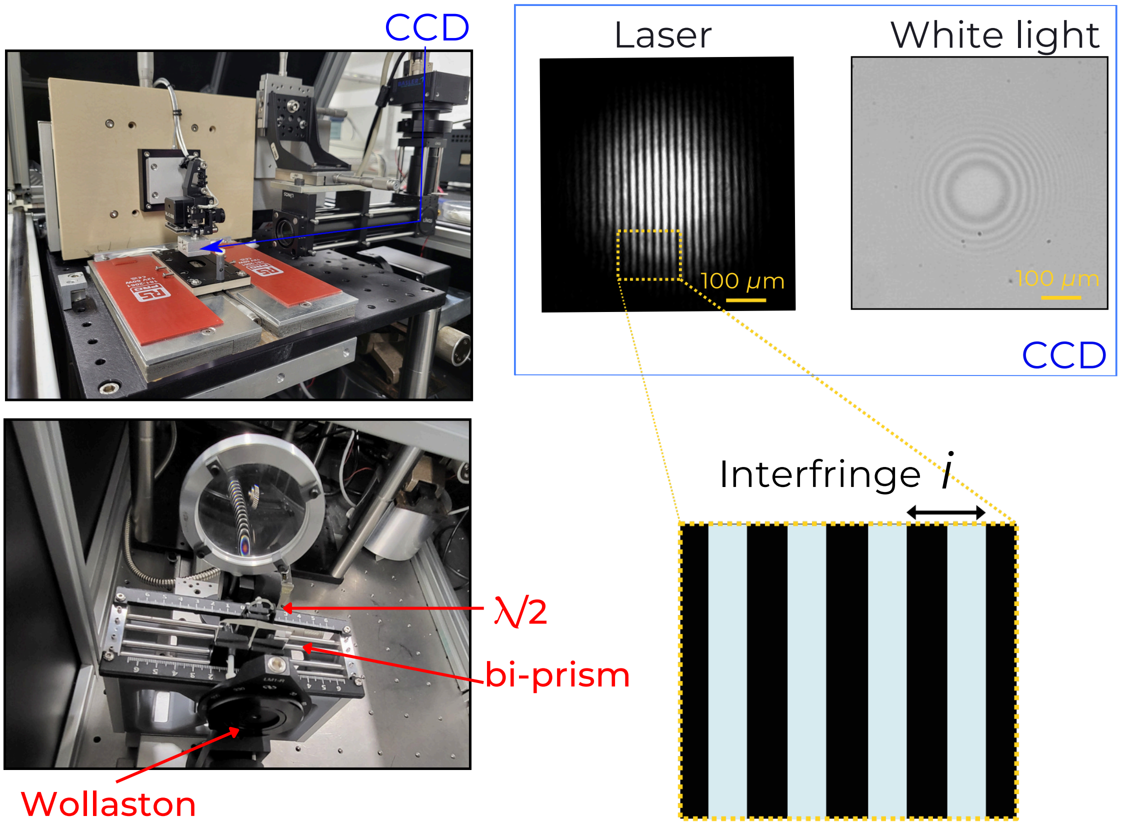

Figure II.16: (Left, Top) Photograph of the open sample environment with the tribology head and force transducers. (Left, Bottom) Photograph of the new optical interferometer with the Wollaston prism, Fresnel biprism and lens. (Right, Top) Interference pattern and image of the sphere-plane contact. (Right, Bottom) Schematic view of the fringes and definition of the interfringe *i*.

diffusion of fluorescently labeled supported phospholipid layers.

The project's novelty is its combination of velocimetry and shear layer velocity measurement. By analyzing fluorescence contrast, we can extract velocity, potentially identifying the slipping plane within fluorescently tagged layers.

Before exploring the friction and FRAPP experiments, we first characterize and study the physical interactions of zwitterionic and charged phospholipids.

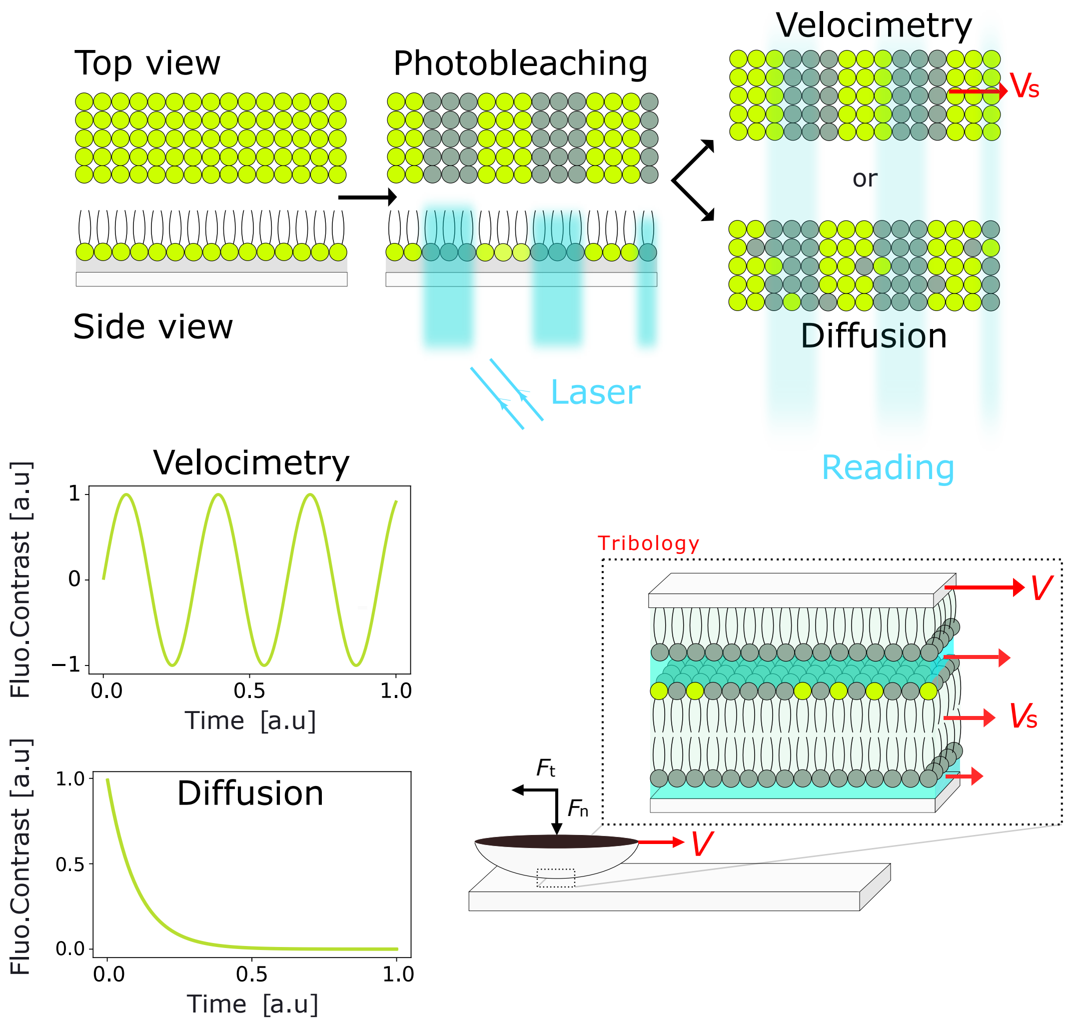

Figure II.17: Summary of Tribo-FRAPP experiments. (Top) The fringe pattern is imprinted on the lipid layer by photobleaching. A rift velocity V_S implies a modulation of the fluorescence signal shown in the lower left figure. Lipid diffusion leads to homogenisation of the fluorescence and an exponential decrease in fluorescence contrast (figure bottom left). (Bottom, right) Geometry of the sphere-plan contact in the case of a trilayer and possible location of the sliding planes.

II.7 Stress-augmented thermal activation

A missing part of the study of boundary lubrication in phospholipids is developing a theoretical framework to describe friction, especially hydration friction. A commonly used model in boundary friction is called the Stress-Augmented

Thermal Activation model [78]. This model encompasses theories capable of connecting molecular-scale behavior to macroscale friction.

Eyring in 1936 [79] and Prandtl in 1928 [80] developed the model in parallel. It is based on the concept that an applied mechanical force on molecules couples with the thermal energy the molecules possess, which can increase the rate of certain processes; in our case, sliding. Other processes described by this model can include chemical reactions and fluid flow.

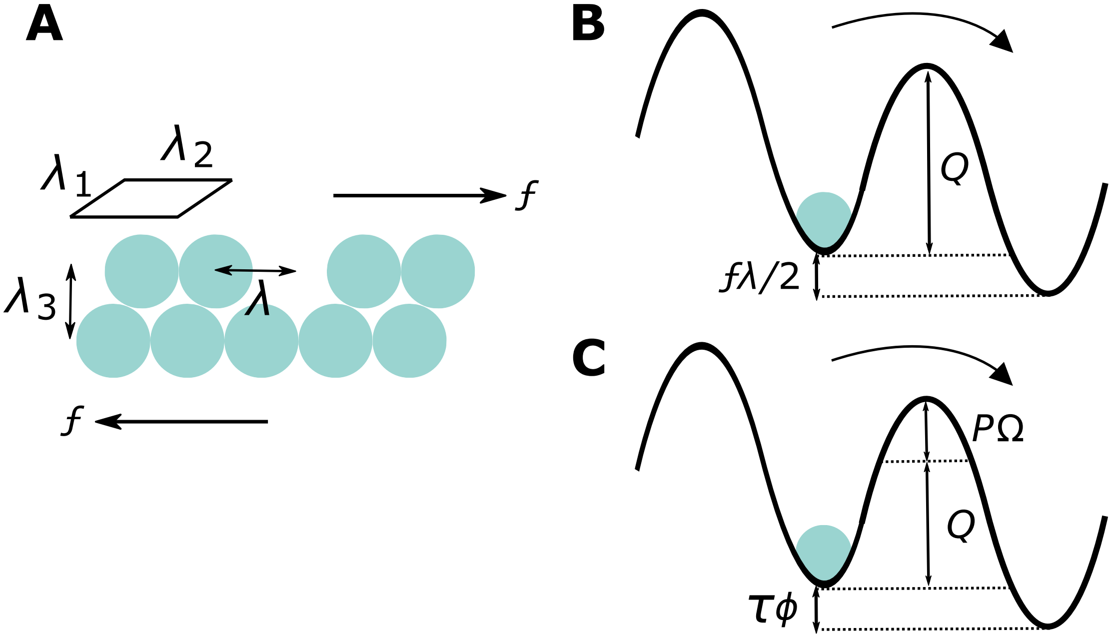

Figure II.18: (A) Schematic of the plane of molecules from the Eyring model [79]. λ is the distance between molecules, $\lambda_1\lambda_2$ represents the cross-sectional area, λ_3 is the typical thickness of the molecular plane involved in shear, and f is the molecular force acting on the molecules. (B) Potential well from [79]. (C) Potential well from Briscoe and Evans [81]. Q is the intrinsic energy barrier modified by a work term $f\lambda/2$. τ and P represent shear stress and normal pressure, respectively, while ϕ and Ω are activation volumes.

The concept is straightforward: if we consider molecules trapped in a potential well, coupled with a mechanical force f (see Figure II.18), we can calculate the rate at which molecules cross the energy barrier using the Arrhenius rate equation:

$$k_\mathrm{f} = Ae^{-(Q - f\lambda/2)/k_\mathrm{B}T}, \tag{II.33}$$

where the energy barrier Q is reduced by the work done by the mechanical force $f\lambda/2$. Here, λ represents the typical distance between molecules, and A is a constant. This modification introduces an asymmetric energy barrier (see Figure II.18). The equation above expresses the forward rate where the energy barrier is lowered; in the opposite direction, the well increases by the work term, leading to a backward rate:

$$k_\mathrm{b} = Ae^{-(Q + f\lambda/2)/k_\mathrm{B}T}. \tag{II.34}$$

Substracting these two rates yields the overall net reaction rate:

$$\begin{aligned} k_\mathrm{net} &= Ae^{-Q/k_\mathrm{B}T}\left(e^{f\lambda/2k_\mathrm{B}T} - e^{-f\lambda/2k_\mathrm{B}T}\right) && \text{(II.35)} \\ &= 2Ae^{-Q/k_\mathrm{B}T}\sinh\left(\frac{f\lambda}{2k_\mathrm{B}T}\right). && \text{(II.36)} \end{aligned}$$

This rate induces molecular movement in the work plane at a given molecular velocity:

$$v = 2\nu_f \lambda e^{-Q/k_\mathrm{B}T}\sinh\left(\frac{f\lambda}{2k_\mathrm{B}T}\right), \tag{II.37}$$

where ν_f is the vibration frequency of the sliding molecules, and λ is the distance between molecules. In their pioneering work on dry surfactant monolayers [81], Biscoe and Evans adapted this equation to investigate the influence of sliding velocity V, load pressure P, and temperature T on boundary friction within these monolayers.

They proposed that the molecular velocity is proportional to the sliding velocity V and decomposed the energy barrier term into two components: Q, the intrinsic barrier, and $P\Omega$, an energy term arising from the pressure exerted by the contact with the tip. Here, $\Omega = \lambda_1\lambda_2\lambda_3$ represents the pressure activation volume (see Figure II.18). In experiments, shear stress is typically measured rather than the molecular friction force, so they related the friction force f to the shear stress τ using $\tau = f/(\lambda_1\lambda_2)$, with $\lambda_1\lambda_2$ as the cross-sectional area (depicted in Figure II.18).

The work term then becomes $f\lambda/2 = \tau\phi = \tau\lambda\lambda_1\lambda_2/2$. It is important to note that the activation volumes Ω and ϕ are defined as cross-sectional area times activation length. By defining $V_0 = \nu_f\lambda$, an unknown velocity, we obtain:

$$V = 2V_0 e^{-(Q+P\Omega)/k_\mathrm{B}T} \sinh\left(\frac{\tau\phi}{k_\mathrm{B}T}\right), \tag{II.38}$$

From this expression, we derive a direct relationship between macroscopic quantities such as τ, V, P, and T and microscopic volumes ϕ and Ω. We can then express the shear stress τ as:

$$\tau = \frac{k_\mathrm{B}T}{\phi} \sinh^{-1}\left(\frac{V}{V_0} e^{-(Q+P\Omega)/k_\mathrm{B}T}\right), \tag{II.39}$$

This model has been successfully used to study the boundary friction of hydration water around confined ions [41, 82]. However, to our knowledge, it has not yet been applied to hydration lubrication of phospholipid layers. Typically, this expression effectively captures the behavior of boundary friction and Newtonian fluids, though predicting Q, ϕ, and Ω is challenging, as they are often treated as fitting parameters.

Chapter III

Structure of charged phospholipid layers

III.1 Introduction

Surfaces immersed in water naturally acquire charges, leading to complex interactions mediated by mobile ions. Historically, the first approach to address this many-body problem was through a mean-field description, known as the Poisson-Boltzmann or Weak Coupling (WC) theory. WC theory has one principal hallmark: it predicts only repulsion between charged bodies [83, 84]. However, when ionic correlation becomes significant, the WC theory fails, and the system enters the SC regime, where correlation can lead to the electrostatic attraction between like-charged surfaces [84, 85]. Although counter-intuitive, this attraction appears to be quite universal and is necessary to explain the cohesion of cement [86], biopolymers such as DNA [87] or microtubules [88], mica surfaces [89], vesicles [90], or layers of charged phospholipids [59]. Until recently, the SC regime was restricted only to systems with multivalent counterions, but recent studies have demonstrated that in nanoconfined water, monovalent counterions can also induce attraction [59, 86, 91]. This occurs as the out-of-plane dielectric constant approaches its optical value [92], enhancing ionic correlations. This work will explore the conditions under which SC attraction emerges in nanoconfined environments.

Zwitterionic phospholipids in the multilamellar phase have long been a valuable model for physicists to probe neutral surface interactions through nanoconfined water [93]. The flat geometry of this model and the ability to perform pressure-distance measurements make it ideal for comparison with theoretical models. It is particularly adapted for studying the hydration force, a repulsive force that appears between polar surfaces [45]. This interaction is known to prevent the collapse of neutral matter by dominating van der Waals attraction at separation below 2 nm. Initially thought to be universal and dependent only on the structuring of water near interfaces, it has recently been shown to be surface-specific [94]. It has been demonstrated that charged phospholipids exhibit enhanced water ordering around their heads [95, 96], but to our knowledge, there has been no quantitative analysis of their hydration repulsion. Therefore, our motivations in this chapter are threefold: we aim to quantify hydration repulsion for negatively charged phospholipids, determine how this force balances with SC attraction, and finally, decipher when SC attraction appears in phospholipid layer interactions.

Our strategy was to study various mixtures of negatively charged DPPS phospholipids and zwitterionic DPPC phospholipids deposited on a silica substrate. Our model system, consisting of phospholipid layers at an air/solid interface, significantly differs from the geometry of biological phospholipid membranes. However, this geometry uniquely allows for studying physical interactions between phospholipid layers. The water layers confined between the phospholipids are in equilibrium with their vapor phase. Due to the equality of the chemical potential between these phases, a high osmotic pressure arises [44]

$$P_{\mathrm{O}} = \frac{k_{\mathrm{B}}T}{V_{\mathrm{M}}} \ln\left(\frac{\mathrm{RH}}{100}\right), \tag{III.1}$$

as explained in Section I.3. This pressure contributes to the disjoining pressure of the water films. By measuring the variation in water layer thickness with changes in RH, we can deduce the underlying physical interactions in the system. We tuned the osmotic pressure by controlling RH, and the changes in layer spacing were measured using neutron and X-rays reflectivity.

By employing a model for the disjoining pressure, we fitted the second water thickness and extracted hydration constants for DPPS in the gel phase. We argue that in nanoconfined water, where the dielectric constant decreases toward its optical value, SC attraction becomes significant even at a low DPPS fraction. Our model successfully describes the system's behavior by balancing DPPS and DPPC hydration repulsion with SC attraction, revealing the complex interplay between nanoconfined charged surfaces.

III.2 Charged phospholipid layers deposited on silica

Samples consist of an odd number of phospholipid layers deposited at the air/silicon interface. The substrates were polished to be atomically smooth, as described in [61]. We used zwitterionic phospholipid DPPC and anionic phos-

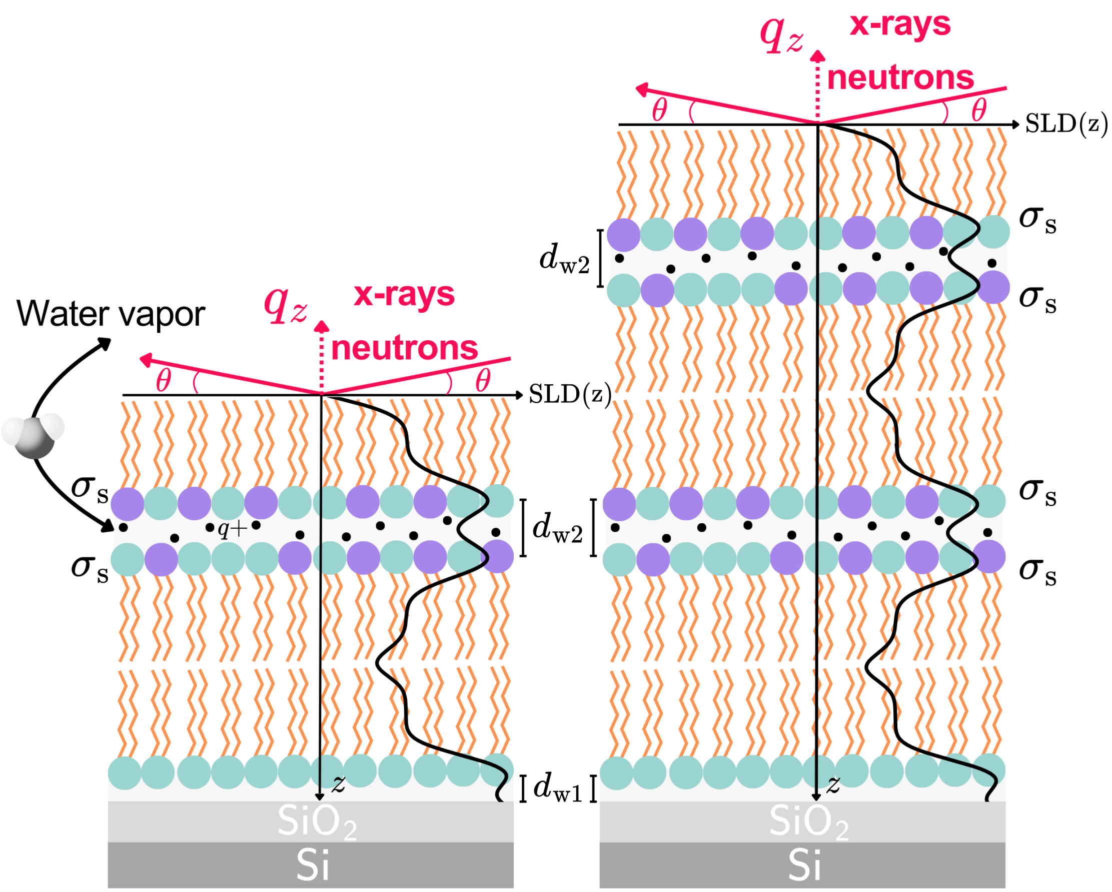

Figure III.1: Schematic of charged trilayer and pentalayer, featuring a mixture of DPPS (purple head) and DPPC (blue head) with a corresponding negative surface charge density, σ_S. DPPS heads are associated with a counterion. The specular incoming and reflected beams are represented in red, with $q_z = 4\pi/\lambda \sin\theta$ as the wave vector transfer. We obtain the scattering length density (SLD) by fitting the specular reflectivity. d_{w1} and d_{w2} are shown, definition of d_{w2} is detailed in section II.2

pholipid DPPS. The first layer transferred to the substrate was always composed solely of DPPC since neutral phospholipids adhere more strongly to the substrate [59], improving the overall deposition quality. We studied six different DPPC/DPPS mixtures with varying DPPS mass fractions $j = m_{DPPS}/(m_{DPPS} + m_{DPPC})$, where j takes on the values 0, 0.2, 0.6, 0.7, 0.8, and 1. All samples were prepared using the Langmuir-Blodgett (LB) technique (see Section II.1.B for further details). LB generally limits the deposition to three layers (trilayer) for neutral phospholipids. However, for DPPS fractions above 0.6, we could stack additional layers, indicative of the SC attraction regime. We limited ourselves to five layers (pentalayer) at j = 0.7 and j = 0.8. No signs of phase separation between the two lipids were observed during deposition for any mixtures or in the AFM experiment we performed at j = 0.6 (shown in Appendix A). Typically, phase separation in DPPC/DPPS mixtures is triggered by the presence of $C\alpha^{2+}$ counterions [97].

III.3 Results: Neutron and X-Ray reflectometry experiments

III.3.A Measuring Reflectivity

We employed neutron reflectivity (NR) and X-ray reflectivity (XR) to achieve high-resolution characterization ($\sim$ 0.1 nm) of trilayer and pentalayer phospholipid structures. NR measurements were carried out on the D17 reflectometer at the Institut Laue-Langevin (ILL) in Grenoble, France, while XR experiments were conducted on the Sirius beamline at Synchrotron SOLEIL in Paris-Saclay, France, using an 8 keV X-ray beam (wavelength $\lambda = 0.155$ nm). Further experimental details can be found in Section II.2.

The reflectivity, $R(q_z)$, is the ratio of the intensity of the specular reflected beam to that of the incident beam. It is expressed as a function of the wave vector transfer, $q_z = 4\pi/\lambda \sin\theta$, where θ is the grazing angle of incidence and reflection. Figure III.1 shows a schematic of the reflectivity setup. XRR and NR experiments were performed in humidity-controlled chambers, allowing precise control of RH. Figure III.2 presents $R(q_z)$ profiles for $j = 0$ (pure DPPC) and

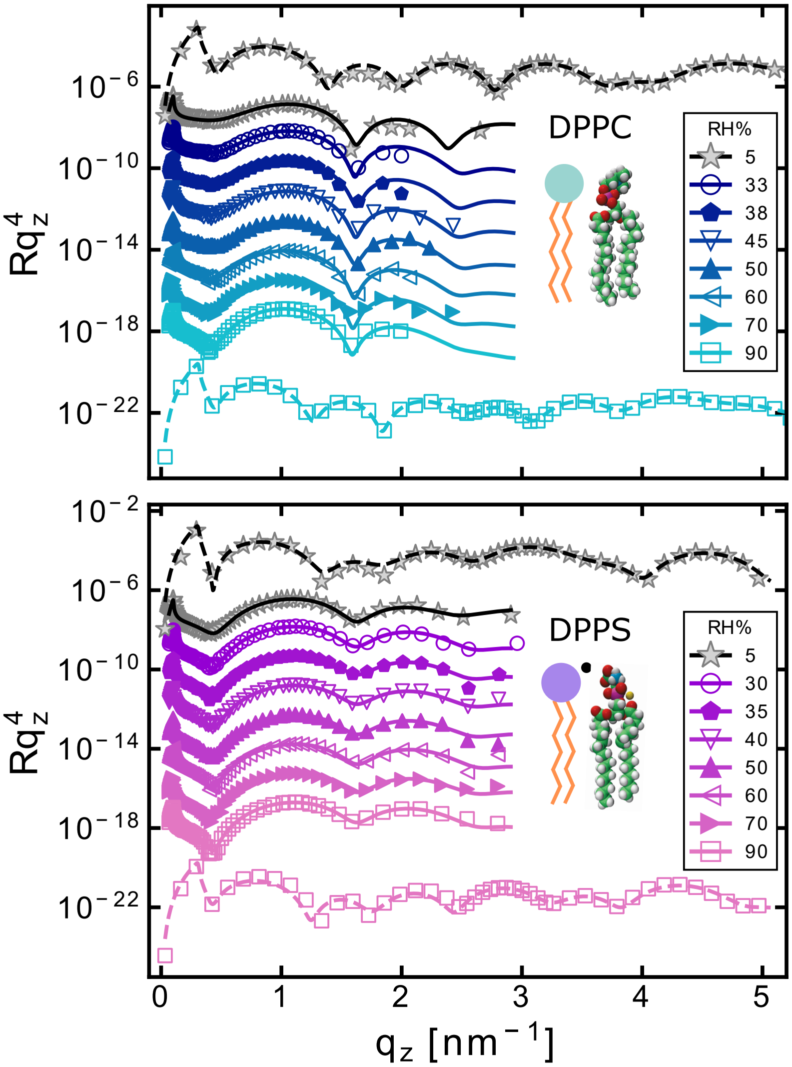

Figure III.2: NR and XR data are presented as Rq_z^4 on a semilog scale. NR data show D_2O contrast, while XR is performed with H_2O. Blue markers correspond to DPPC and purple markers to DPPS. Reflectivity is shown at RH ranging from 5% to 90%, with each humidity profile successively shifted by 1.5 decades for clarity. Solid lines represent the best fits corresponding to the SLD_n profiles, and dashed lines are associated with SLD_x, both depicted in Figure III.3.

$j = 1$ (pure DPPS) at $T = 293\,K$, with XR at RH = 5% and 90%, and NR at RH ranging from 5% to 90%. The profiles of the remaining mixtures are included in the Appendix B.

III.3.B Scattering Length Density Profiles

Reflectivity analysis is inherently model-dependent. In our case, experimental data are interpreted using a classical slab model. Our system, composed of stacked phospholipid layers, is particularly well-suited for this approach. Each part of the lamellar sample is characterized by thickness, scattering length density (SLD), and an inter-slab roughness. These parameters define the SLD profile, which is then related to the reflectivity, $R(q_z)$, through the Névot-Croce/Parratt formalism [98]. The NR and XRR data were analyzed using the refnx Python package [99]. Further details on the fitting procedure and model constraints can be found in Section II.2.

We achieved highly accurate fits across all DPPS fractions for the XRR and NR data, providing consistent results. For simplicity, only the SLD profiles corresponding to Figure III.2 are shown in Figure III.3. Additional profiles and structural parameters for all samples are provided in the Appendix B.

For NR, we used two isotopic water contrasts: H_2O with an SLD of $-0.56 \times 10^{-4}\,\mathrm{nm}^{-2}$ and D_2O with an SLD of $6.36 \times 10^{-4}\,\mathrm{nm}^{-2}$. Using multiple contrasts in NR generally helps to constrain the fit and improve the robustness of the analysis. However, two assumptions must hold: first, that H_2O/D_2O exchange does not alter the structure of the phospholipid layers, which is typically assumed to be true, and, second, that the solvent exchange is complete. The latter assumption is less certain for phospholipid layers at the air/solid interface, as hydration water molecules are strongly bound to the phospholipid heads, especially when the water film becomes very thin, such as in highly charged phospholipid layers.

In the D_2O experiments, we found clear evidence that solvent exchange

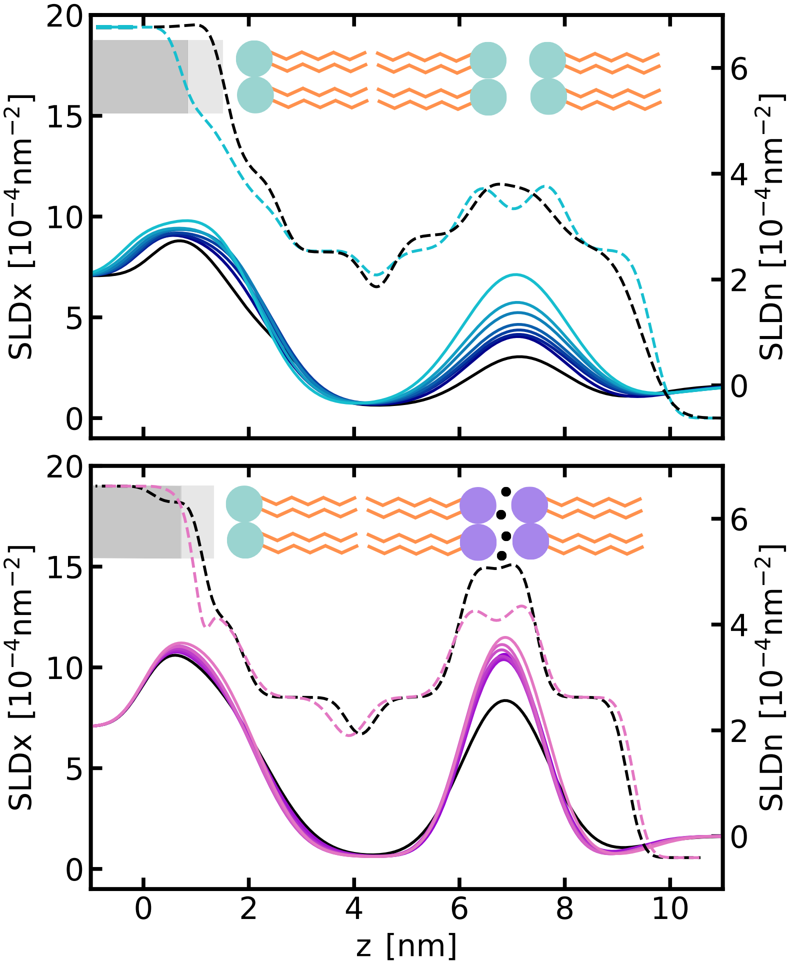

Figure III.3: SLD profiles for NR (solid lines, right axis) and XR (dashed lines, left axis). The color coding follows Figure III.2. All profiles have been centered on the midpoint of the bilayer tails.

was incomplete. The fitted SLD values for the heavy water layers (shown in the Appendix B) ranged between $5 \times 10^{-4}\,\mathrm{nm}^{-2}$ and the value for pure D_2O. In extreme cases, this corresponded to approximately 2 out of every 10 water molecules remaining as H_2O. Accurately determining the SLD and thickness of the water layers is challenging. To bypass this limitation, we used the XR data as a reference, fixing the fraction of water in the phospholipid head region to match the XR analysis. Since the XR data was conducted entirely in H_2O and provides very accurate thickness measurements, it serves as a reliable reference. All relevant structural informations, such as the area per lipid and hydration number, are provided in the Appendix B.7.

III.3.C Second water thickness d_{w2}

This study focuses on the *second* water layer, whose thickness, d_{w2}, accounts for the solvation water within the head region, as explained in Section II.2. This approach avoids the need to differentiate between solvation water and bulk water in the layer and also allows for comparison with numerical simulation results. The first water layer, d_{w1}, located between the substrate and the first DPPC layer, remains highly confined (< 1 nm). In this asymmetric case, a complex balance between van der Waals forces, electrostatic interactions, and roughness-related interaction leads to strong adhesion between the bilayer and the substrate [100].

We extracted d_{w2} in Figure III.4 (Right) from the SLD profiles, with an RH ranging from very dry conditions (RH = 3-4%) to high humidity (RH = 90%). At low humidity, d_{w2} reaches a minimum of roughly 0.6-0.7 nm, corresponding to the thickness of the phospholipid heads. Under these high osmotic pressure conditions, the phospholipid heads are in close contact, leaving only the last hydration water molecules. As RH increases, the osmotic pressure decreases, and d_{w2} increases accordingly. This trend is also apparent in the x-ray SLD_x profiles shown in Figure III.3, where there is a change from single to double head peaks, and in the neutron SLD_n profiles, where the height and width of the peak increase, indicating more D_2O in the layer.

In Figure III.4, the significant reduction in d_{w2} for DPPS compared to DPPC suggests the presence of attractive interactions, as previously observed in double DPPS bilayers [59]. Interestingly, when examining d_{w2} variations with

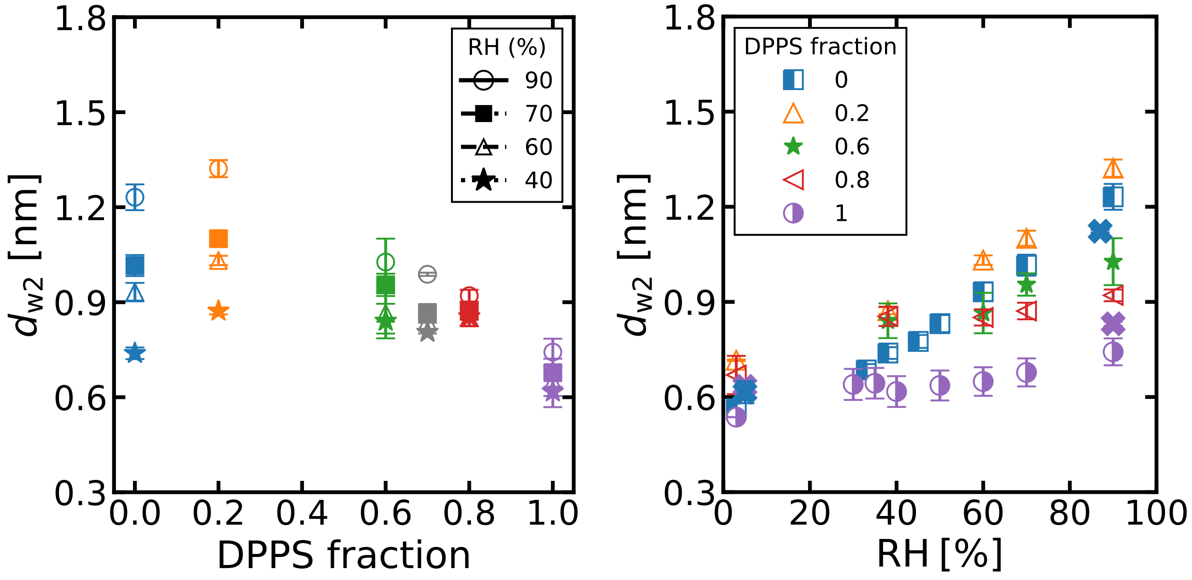

Figure III.4: Variation of water thickness d_{w2} with DPPS fraction (Left) and with RH (Right).

j, an initial increase in d_{w2} occurs at $j = 0.2$, followed by a decrease up to $j = 1$. This behavior is more clearly depicted in Figure III.4(Left), which shows d_{w2} variations with changing DPPS fraction at fixed RH.

III.4 Discussion: modeling interactions

In this second part of the chapter, we will attempt to model the behavior of d_{w2} reported in Section III.3.

III.4.A Neutral Phospholipids

The structure of DPPC phospholipid layers in the gel phase has been extensively studied and is well established. Therefore, it serves as a reliable starting point to validate our experiment. For DPPC, or $j = 0$, the behavior of d_{w2} can be described using only the osmotic pressure P_O and the hydration pressure $P_h = P_{0h,PC} \exp(-z/z_{h,PC})$ (see [45]). At equilibrium, the following relationship holds:

$$-P_{\mathrm{O}} = P_{\mathrm{h}}. \tag{III.2}$$

In the case of air/solid phospholipid layers, the vdW pressure can be neglected, as it stays several orders of magnitude smaller than P_{O} and P_{h} below 2 nm (see Figure III.7).

This results in a direct relationship between RH and d_{w2}. From the fit shown in Figure III.7, we extracted the hydration pressure constants $P_{0\mathrm{h,PC}} = (5.7 \pm 1.9) \times 10^{9}\,\mathrm{Pa}$ and $z_{\mathrm{h,PC}} = 0.205 \pm 0.02\,\mathrm{nm}$, which are consistent with literature values for DPPC in the gel phase [93, 94, 101, 102].

III.4.B Weak or Strong coupling?

We then aimed to understand the variation of d_{w2} for $j > 0$. The question is: are we in the WC or SC regime?

At first glance, we suspected that the behavior of d_{w2} might indicate a crossover between the WC and SC regimes. It is tempting to associate the bell curve shape observed with a crossover signature. To determine whether the system falls into the WC or SC regime, we calculate the coupling parameter:

$$\Xi = \frac{q^2\, l_{\mathrm{B}}}{\mu_{\mathrm{GC}}} \propto \frac{q^3 \sigma_{\mathrm{S}}}{\epsilon_{\mathrm{r}}^2}, \tag{III.3}$$

where l_{B} is the Bjerrum length, μ_{GC} is the Gouy-Chapman length, q the counterion valency and σ_{S} the surface charge density. For $\Xi < 12$, the coupling between ions is low, indicating the WC regime characterized by repulsion.

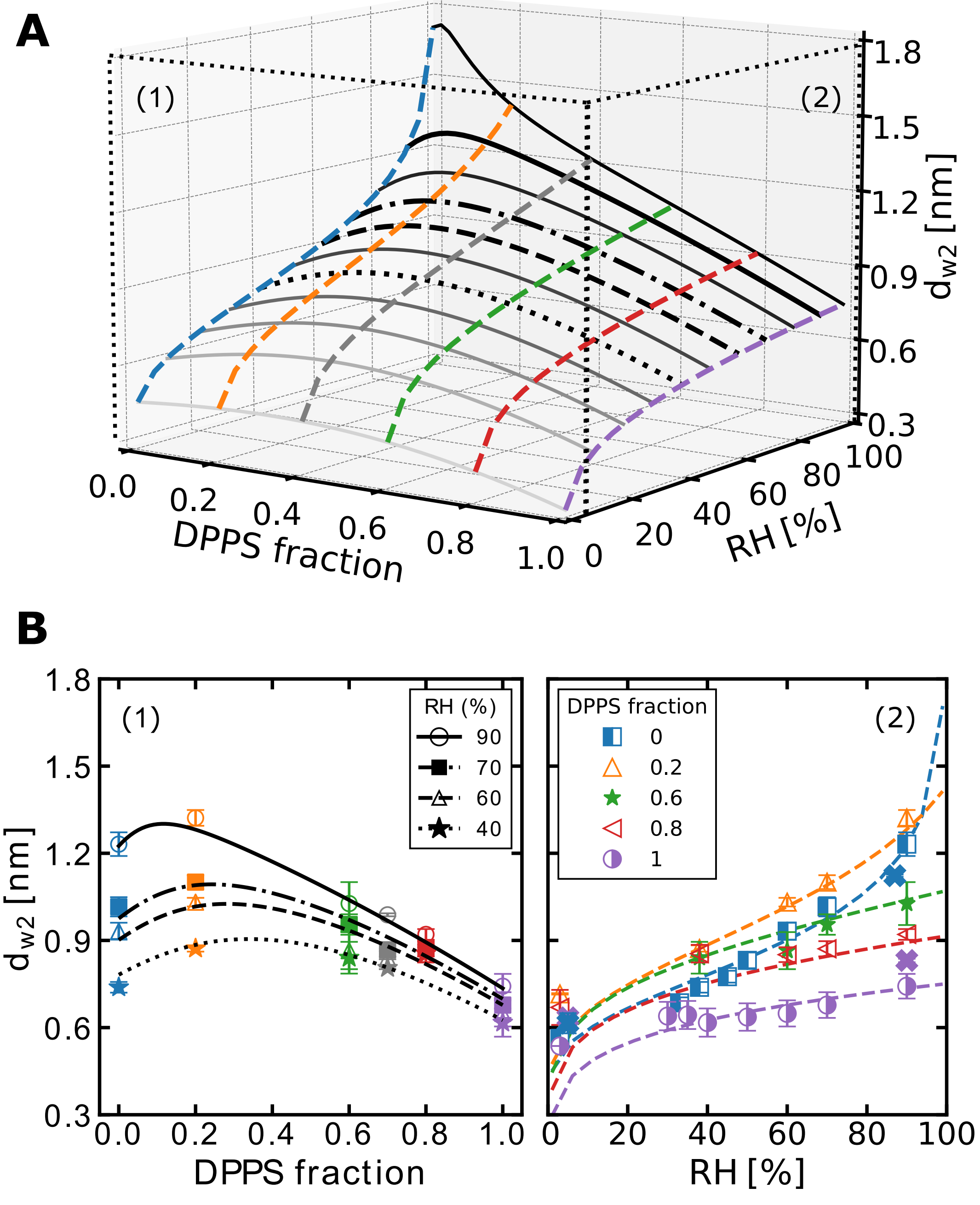

Figure III.5: Representation of the variation in d_{w2} thickness for changes in DPPS fraction and RH. (A) The 3D plot shows the model's prediction. (B, Right), we show d_{w2} extracted from SLD in two different representations. (B, Left) We limit ourselves to data points at 4 constant RH. Minimization for the fit was done globally, all fits share the same 2 parameters, namely DPPS hydration constants $P_{h0,PS}$ and $z_{h,PS}$.

Above this value, correlations become significant, leading to SC attraction [84].

The key to understanding monovalent counterion electrostatic attraction is that Ξ scales inversely with the square of the permittivity. A standard surface charge density in bulk water ($1\, e^{-}/\mathrm{nm}^2$) with $\epsilon_\mathrm{r} \simeq 80$ gives $\Xi = 4$ [59], which corresponds to the WC regime. However, water with a low rotational degree of freedom, such as hydration water, potentially leads to lower permittivity, resulting in significantly higher Ξ values.

Figure III.6A illustrates how Ξ varies with ϵ_r and σ_S, ranging from bulk to optical values across our DPPS fractions (assuming a surface charge density of $\sigma_\mathrm{PS} = 0.5/0.42\, e^{-}/\mathrm{nm}^2$ and $\sigma_\mathrm{PC} = 10^{-3}\, e^{-}/\mathrm{nm}^2$, leading to a total surface charge density, depending on the DPPS fraction j, of $\sigma_\mathrm{S} = j\sigma_\mathrm{PS} + (1 - j)\sigma_\mathrm{PC}$). If ϵ_r indeed decreases toward the optical value, as measured experimentally and numerically in recent studies [91, 92], Figure III.6 shows that all charged mixtures discussed in this paper would fall into the SC regime.

We also compared the WC pressure,

$$P_\mathrm{WC} = \frac{(k_\mathrm{B}T)^2 \pi \epsilon_0 \epsilon_\mathrm{r}}{2e^2 z^2}, \tag{III.4}$$

to SC and hydration pressures for two charged surfaces at distance z in Figure III.7. Even at the highest humidity studied, the WC pressure is at least two orders of magnitude lower, allowing us to neglect this contribution to the disjoining pressure balance.

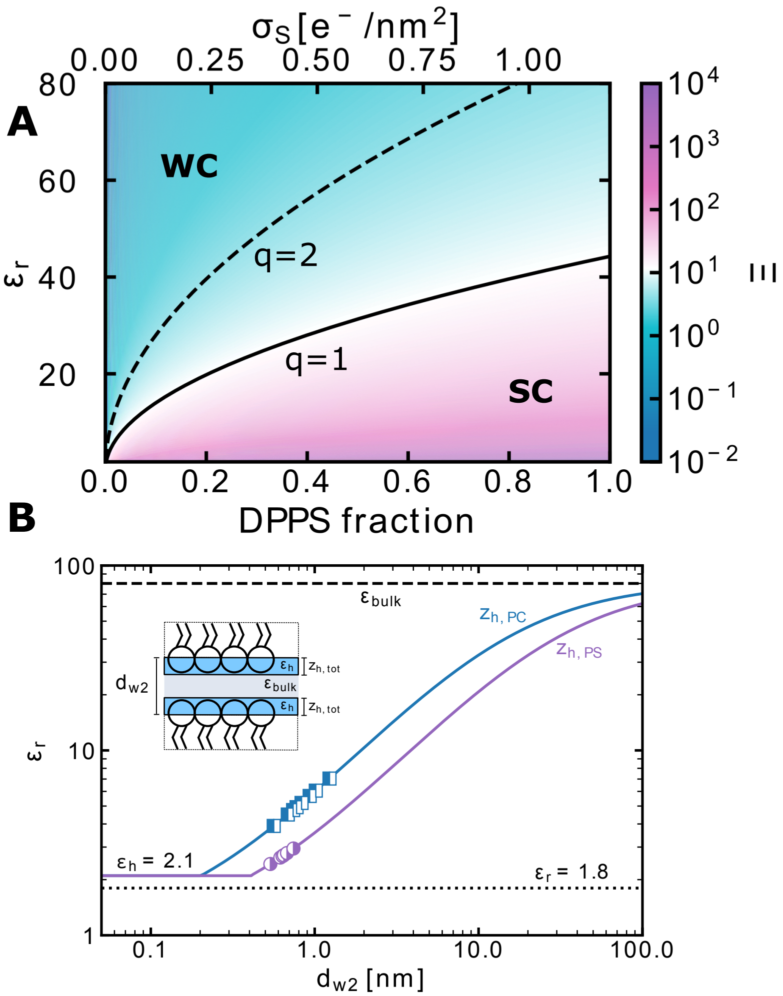

Figure III.6: (A) Variation of the coupling parameter Ξ as a function of the relative dielectric constant and the DPPS fraction. The corresponding surface charge density σ_S is shown on the top x-axis and is calculated using $\sigma_{PS} = 0.5/0.42\, e^{-}/\mathrm{nm}^2$. The solid line represents $\Xi = 12$, marking the boundary between the WC and SC regime [103] for monovalent counterions (q=1). The dashed line indicates the boundary for divalent counterions (q=2). (B) The dielectric constant model is adapted from [92] and represent capacitors in series. In this layer model, we define bound hydration water with a dielectric constant $\epsilon_h = 2.1$, close to the optical value ϵ_r, and thickness z_h, and free bulk water with a bulk dielectric constant ϵ_{bulk}. In blue, we depict an example with $z_{h,PC}$ corresponding to the DPPC hydration decay length, and in purple with $z_{h,PS}$ corresponding to the DPPS hydration decay length.

III.4.C Charged phospholipids

Two key aspects must be considered when modeling charged phospholipids. First, water interacts specifically with the lipid heads. We modeled the behavior of the system by incorporating the hydration repulsion of lipid mixtures [104], so we have:

$$P_{\mathrm{h}}(z,j) = P_{0\mathrm{h,tot}}(j)\exp\left(-\frac{z}{z_{\mathrm{h,tot}}(j)}\right), \tag{III.5}$$

with:

$$\log\left(P_{0\mathrm{h,tot}}(j)\right) = (1-j)\,\frac{z_{\mathrm{h,PC}}}{z_{\mathrm{h,tot}}}\log\left(P_{0\mathrm{h,PC}}\right) + j\frac{z_{\mathrm{h,PS}}}{z_{\mathrm{h,tot}}}\log\left(P_{0\mathrm{h,PS}}\right), \tag{III.6}$$

and:

$$z_{\mathrm{h,tot}} = (1-j)z_{\mathrm{h,PC}} + jz_{\mathrm{h,PS}}. \tag{III.7}$$

Here, $P_{0\mathrm{h,PS}}$, $z_{\mathrm{h,PS}}$, $P_{0\mathrm{h,PC}}$, and $z_{\mathrm{h,PC}}$ are the hydration constants related to DPPS and DPPC, respectively.

The second important point is to model the permittivity. We adapted the approach from Fumagalli et al. [92], where only a few water molecules near the surface are considered "frozen" with a dielectric constant of 2.1, while the water farther from the surface retains its bulk value. In our model, the thickness of the frozen water layer corresponds directly to the correlation length of hydration water, $z_{\mathrm{h,tot}}$ (see Section III.4.E for more justification). Treating the system as three capacitors in series (see inset of Figure III.6B for more details on the model), we obtain an effective permittivity dependent on j and z:

$$\epsilon_{\mathrm{r}} = \frac{z}{\frac{2z_{\mathrm{h,tot}}}{\epsilon_{\mathrm{i}}} + \frac{(z-2z_{\mathrm{h,tot}})}{\epsilon_{\mathrm{bulk}}}}. \tag{III.8}$$

As for neutral phospholipid, at equilibrium, the total pressure balance is given by:

$$-P_{\mathrm{O}} = P_{\mathrm{SC}} + P_{\mathrm{h}}. \tag{III.9}$$

Where we added the SC electrostatic attraction term

$$P_{\mathrm{SC}} = 2\pi l_{\mathrm{B}} \sigma_{\mathrm{S}}^2 k_{\mathrm{B}} T \left(\frac{2\mu_{\mathrm{GC}}}{z} - 1 \right). \tag{III.10}$$

In Figure III.5, we performed a global fit across all DPPS fractions, with two fitting parameters: $P_{0\mathrm{h,PS}}$ and $z_{\mathrm{h,PS}}$. The fits match the data well for all relative humidity values and DPPS fractions. Our fitted hydration constants for DPPS are $P_{\mathrm{h,PS}} = 4.1 \pm 1.1 \times 10^9$ Pa and $z_{\mathrm{h,PS}} = 0.41 \pm 0.08$ nm, indicating a more substantial correlation length compared to neutral DPPC. This result aligns with both experimental and numerical observations. It was not possible to fit the data using bulk permittivity values.

The balance between hydration repulsion and SC attraction dictates the variations in d_{w2}. We present the model's prediction in Figure III.5. We plotted the hydration and SC pressures in Figure III.7. These graphs show that when DPPS is added at a low fraction, the resulting increase in hydration pressure dominates over SC attraction. At a certain point, depending on the relative humidity, the SC attraction becomes dominant, leading to a decrease in d_{w2}.

As the DPPS fraction increases, although the variations in thickness are

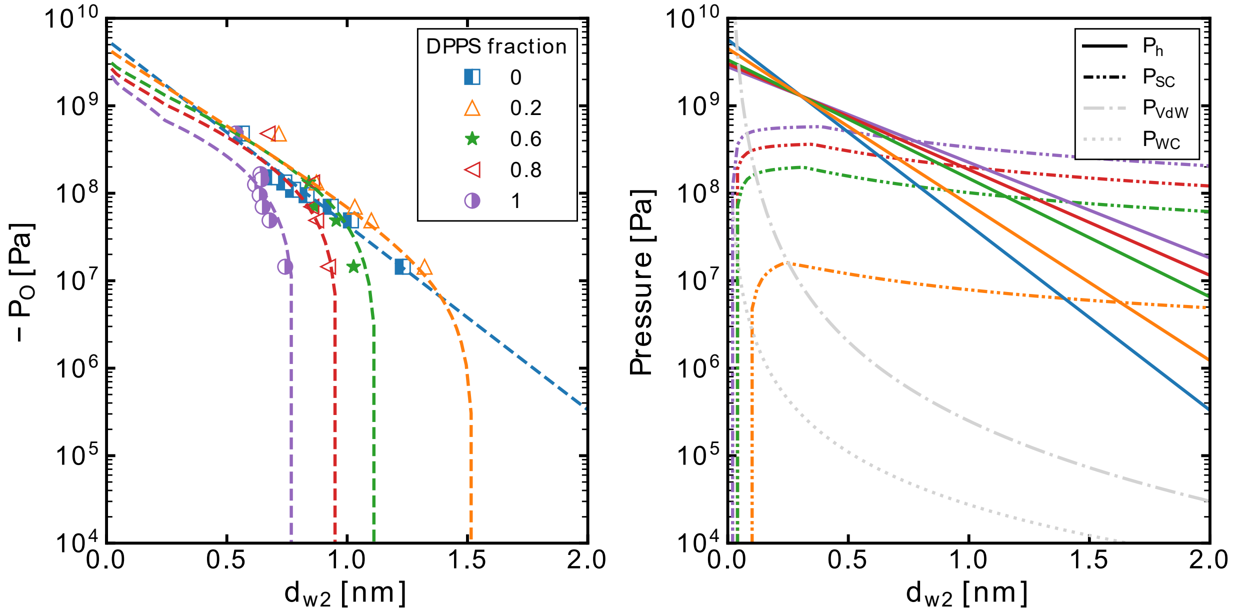

Figure III.7: (Left) Osmotic pressure versus d_{w2} for all DPPS fractions. Dashed lines represent the best fit obtained from the sum of hydration and SC pressures, $P_{SC} + P_h$. (Right) Representation of the different contributions to pressure. For negative pressure as P_{vdW} and P_{SC}, the absolute value is taken. $P_{vdW} = -H/6\pi d^3$. The Hamaker constant is $H = 4.75 \cdot 10^{-21}$ J. Both pressures are calculated assuming $\epsilon_r = 80$. When the permittivity approaches its optical value, H decreases to $1.7 \cdot 10^{-21}$ J. P_{WC} is computed using the surface charge density σ_S, corresponding to $j = 0.2$.

minor, the changes in pressure are significant. Without the rise in hydration pressure, the system would undergo a rapid collapse driven by SC attraction. The introduction highlights that hydration pressure is the final barrier against vdW attraction for neutral surfaces. Here, we show that hydration pressure plays a protective role against SC attraction.

III.4.D Limits of the model

Many questions arise from these findings. The first that comes to mind is whether it is possible to trigger vesicle adhesion with monovalent counterions, similar to what has been observed with divalent ions [90]. Figure III.6 shows that due to the low dielectric permittivity, the Ξ value would already be in the

SC regime at separations above 2 nm. To our knowledge, no experimental observations of this phenomenon exist, and the opposite is typically observed. For instance, in the multilamellar phase described here, indefinite swelling was reported [105].

The first criterion for the applicability of SC theory, as used in this chapter, is, of course, a high Ξ, but there is another essential criterion. Situations exist where the system's geometry determines the validity of the SC. To estimate this, we must compare the lateral counterion distance $a_\perp$ to the thickness of the water layer d_{w2} [84]. Specifically, SC holds if:

$$d_{\mathrm{w2}} < a_\perp. \tag{III.11}$$

This situation is represented in Figure III.8. Thus, SC holds only at small wall separations. Above $a_\perp$, represented in the blue zone in Figure III.8, SC interactions diminish, as recently demonstrated in [91]. Therefore, we propose that the main criterion for SC attraction between membranes is comparing the lateral counterion distance and membrane separation. We represented $a_\perp$ in Figure III.8 for $q = 2$. The effect of having divalent ions is to increase the lateral distance, which may be a decisive factor in triggering SC attraction between vesicles.

We then asked ourselves whether predicting the water thickness in a double bilayer system was possible, as reported in [59]. To this end, we incorporated vdW pressure terms were added to our model, and the osmotic term was removed. The results are shown in Figure III.8. The model nicely predicts the water thickness $d_{\mathrm{w2}} = 0.2 - 0.3\,\mathrm{nm}$ observed in several references [59] for $j = 0$, and for $j = 1$, it also accurately captures the experimental observations for DPPS. Without osmotic pressure, our model does not predict an increase in water thickness upon adding charged phospholipids but rather a monotonic decrease. The thickness d_{w2} remains below $a_\perp$ for all DPPS mixtures, both at air/solid and modeled water/solid interfaces, supporting the use of the SC model.

We believe the main reason behind the observation of SC attraction triggered by monovalent ions is the osmotic pressure that confines the layers, allowing the thickness to reach values below the counterion lateral distance. There is no osmotic pressure in the double-double bilayer at the water interface. However, during the sample fabrication, the substrate alternates between air and water, leading to phases where the water layers are confined by osmotic pressure. This suggests that the deposition process may be the key to triggering SC attraction by monovalent ions.

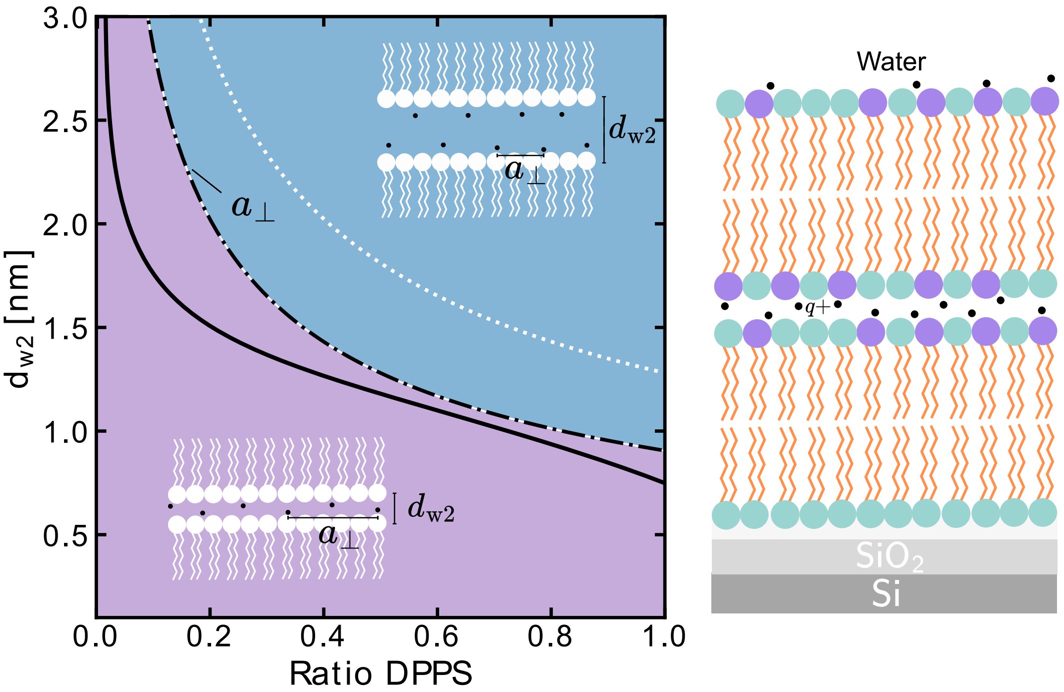

Figure III.8: Prediction of d_{w2} for DPPS/DPPC mixtures in double bilayer geometry, shown in solid black line. The counterion-counterion distance $a_\perp$ is represented for $q = 1$ in black and $q = 2$ in white dashed lines.

III.4.E Numerical simulations (Collaboration with ILM (Lyon))

This thesis is part of an ANR project called Banana_Slip, in collaboration with Claire Loison, Ludovic Gardré, and Laurent Joly, who are doing theory and numerical simulations at the Institut Lumière Matière in Lyon. They carry out numerical simulations using the Gromacs package versions 2023.4 or 2024.3 [106], the C36-CHARMM36 force field [107] for DPPS (negatively charged) and its sodium counterion (Na^+) and the OPC water model [108]. The OPC water model is known to predict the dielectric properties of water more accurately than the mTIP3P force field typically used in CHARMM [109].

Two monolayers, each made up of 100 DPPS molecules, were first built up in the gel phase and then assembled in two layers separated by a solvent of 200 sodium ions and 7000 water molecules with periodic boundary conditions in the three dimensions (see Figure III.9 for snapshots of the simulated systems). The monolayers were progressively dehydrated by progressive removal water molecules, leading to stronger confinement. Each system is characterized by its Hydration Number (HN): the number of water molecules per lipid that varies from 35 (7000/200) down to 0.

The $\mathrm{SLD_n}$ and $\mathrm{SLD_X}$ profiles in the direction normal to the bilayers were calculated by averaging the products of the number density of each atom by its corresponding neutron scattering length or electron number (for the atom i, $Z_i + q_i$ where Z_i is the electron number and q_i the partial charge of the force field) over equilibrated snapshots. The neutron scattering length for each of the atom types was taken from [111].

The numerical and experimental scattering length density profiles are shown in Figure III.10 for neutrons ($\mathrm{SLD_n}$, left) and X-rays ($\mathrm{SLD_X}$, right). The numerical

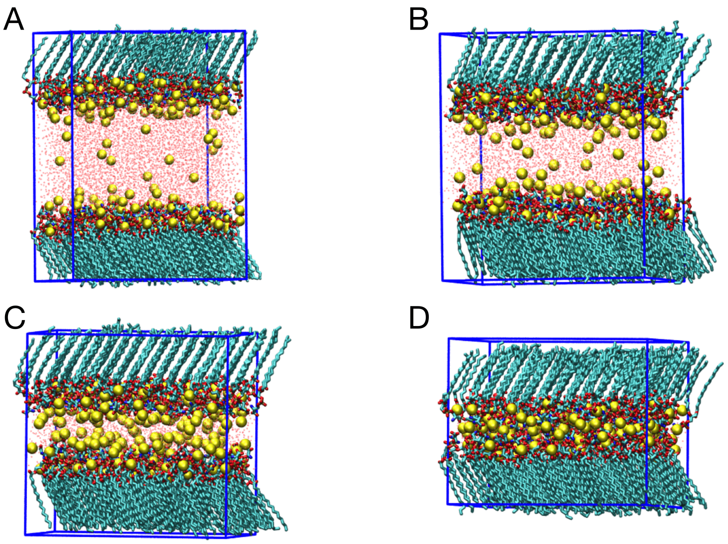

Figure III.9: Typical snapshots of the simulated systems. Periodic boundary conditions are used in the three dimensions, with simulation boxes depicted by blue frames. After cooling towards 293K, the lipids are in a L'_{β} gel phase. A, B, C, and D correspond to final systems after dehydration, equilibration for hydration numbers of 35, 25, 15, and 5, respectively. Water molecules are represented by red dots at the position of the oxygen, Sodium ions by big yellow spheres, and the bonds of DPPS lipids by cylinders. Hydrogens are not shown. Illustration adapted from Claire Loison and created using VMD [110].

profiles shown correspond to HN equivalent to the number of water molecules per lipid calculated from the experimental profiles: between 0 and 2 water molecules per lipid at low humidity (RH=5±2%, black lines and symbols) and between 4 and 6 water molecules at high humidity (RH=90±5%, pink lines and symbols). For the experimental profile, only the part consisting of the second and third monolayer is represented, shifted to center the water layer with the one of the simultations. In all cases, the agreement between the different profiles is remarkable. It is important to note that: (i) the experimental profiles correspond to an average over lateral scales much larger than the size of the simulated systems, which explains why certain details are smoothed out on the experimental profiles (hole of the methyl groups, for example); (ii) the numerical profiles are calculated averaging over the positions of the atoms in

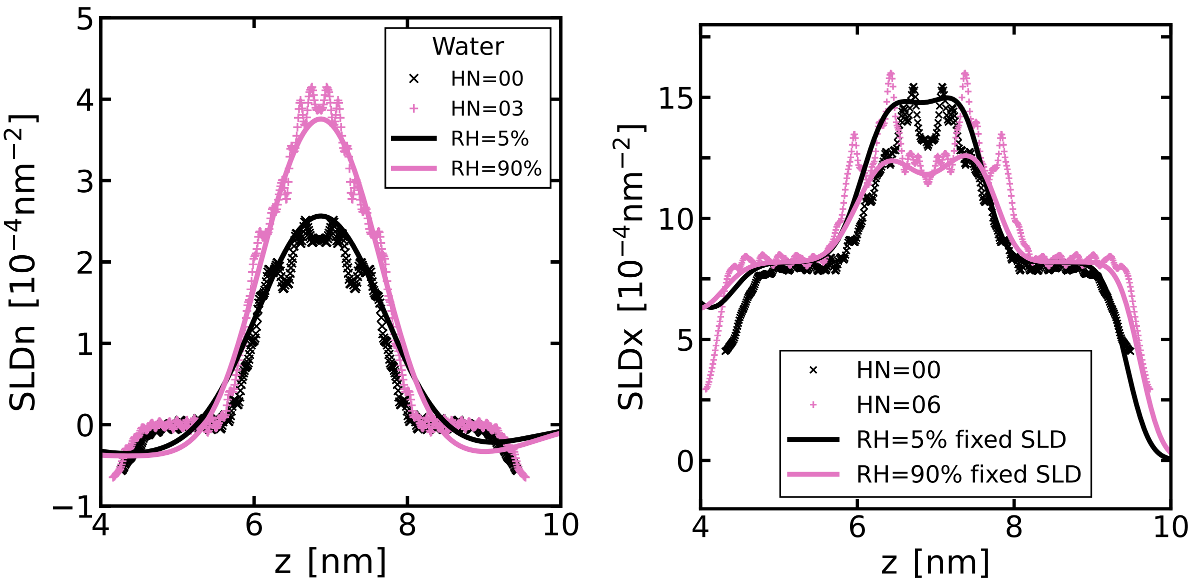

Figure III.10: (Left) Solid lines correspond to the scattering length density profiles obtained by neutron reflectivity for HR=5% (black curve) and RH=90% (pink curve). HR=5% (black curve) corresponds to HN= 3.5 ± 0.25 water molecules per lipid and HR= 90 % (pink curve) to HN= 4.75 ± 0.25 water molecules per lipid. The symbols correspond to the $\mathrm{SLD_n}$ profiles calculated from numerical simulations for hydration numbers of HN=0 (×) and HN=3 (+). (Right) Same figure as on the left but for X-rays reflectivity for HR=5% (black,HN= 1.75 ± 0.25 water molecule per lipid) and HR=90 % (pink, HN= 6.75 ± 0.25 water molecules per lipid). The symbols correspond to the $\mathrm{SLD_X}$ profiles calculated from numerical simulations for hydration numbers for HN=0 (×) and HN=6 (+).

the snapshots while the experimental profiles are fits using only a few boxes.

From the numerical simulations, using the MDanalysis package [112], it is also possible to calculate the polarization density profiles of the water molecules in the z direction (perpendicular to the layer plane) $P_z(z)$ in the direction normal to the bilayers.

We compare them with the Landau-Ginzburg (LG) model proposed by Schlaich et al. [94], which predicts the variation in the polarisation of water molecules between two layers separated by a distance d:

$$P_z(z,d) = P_0 \frac{\sinh(z/z_\mathrm{h})}{\sinh\left(d/(2z_\mathrm{h})\right)}, \tag{III.12}$$

with two parameters, P_0 the polarization at the surface and z_h a characteristic length scale per curve, i.e. per d value (itself depending on HN).

To fit the numerical results, we limit the z-range to the region with a local density of OPC molecules ($\rho_\mathrm{OPC}(z) \geq 32$ molecules/nm^3, to be compared to the bulk OPC density at 293K and 1 bar of 33.6 molecules/nm^3, value set to exclude the phospholipid head region). The thickness of this region is used as the d parameter of the LG model. Within this region, the profiles were fitted with the equation III.12 with two parameters (P_0, z_h) per curve, i.e. per d value.

The resulting fits are shown in Fig. III.11 for HN ranging from 20 to 35. For values of HN below 20, the curves are very close to a straight line and the fits are no longer sensitive to the value of z_h (relative error greater than 100%). The corresponding values of z_h as a function of d are plotted in Figure III.11 (Right), showing that z_h is almost constant and equal to 4.8 ± 0.5 nm. These results are in perfect agreement with the values of $z_\mathrm{h,PS}$ obtained from the modeling of the interaction potential as described above and strongly support the interpretation of the experiments described previously (see Figure III.5), and illustrated by the horizontal purple area.

Finally, we can try to compare the water thickness obtained experimentally (due to different HR value) with the thickness deduced from the numerical simulations for the different hydration number HN. Figure III.12 (Left) shows the thickness d of the water layer, determined from numerical simulations using the density criterion described above (○). We observe a linear behaviour cross-

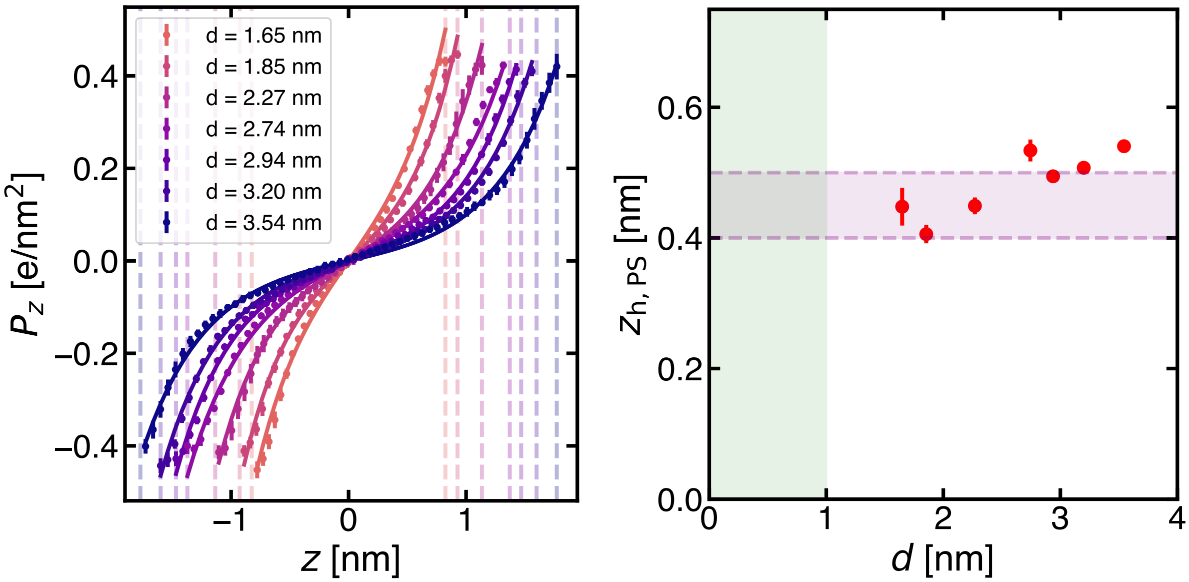

Figure III.11: (Left) Water dipolar polarization profiles, within the solvent layer of thickness d, for system of different hydration number. The dashed vertical lines indicate the surface positions at $\pm d/2$. The d values are given in the legends. Solid lines are fits according to Eq. III.12 leading to the parameter $z_{\mathrm{h,PS}}$ (functions are only drawn inside the fitting range). (Right) Variations of $z_{\mathrm{h,PS}}$ for different hydration level, i.e. different d. The error bars are obtained from the square root of the covariances of the fit. The purple rectangle corresponds to the acceptable range for describing the experimental data. The green rectangle corresponds to the confinements obtained in the experiments.

ing the x-axis for a number of water molecules $n_{\mathrm{H_2O}}$, where $n_{\mathrm{H_2O}}$ corresponds to the number of water molecules inside the head region per lipid head. A linear fit gives $n_{\mathrm{H_2O}} = 8 \pm 1$, in qualitative agreement with the literature [113].

The fit also makes it possible to determine the value d_0, negative value of the intercept of the linear fit for HN=0, which makes it possible to estimate at what depth the water penetrates the heads. This value enables to shift the thickness d determined numerically to obtain a value $d - d_0$ more directly comparable with the water thickness $d_{\mathrm{w,2}}$ measured experimentally. All the experimental (neutron and X-rays) and numerical values are shown in Figure III.12 (Right), together with the linear law corresponding to the expected value for a water layer of density $\rho_{\mathrm{H_2O}}$:

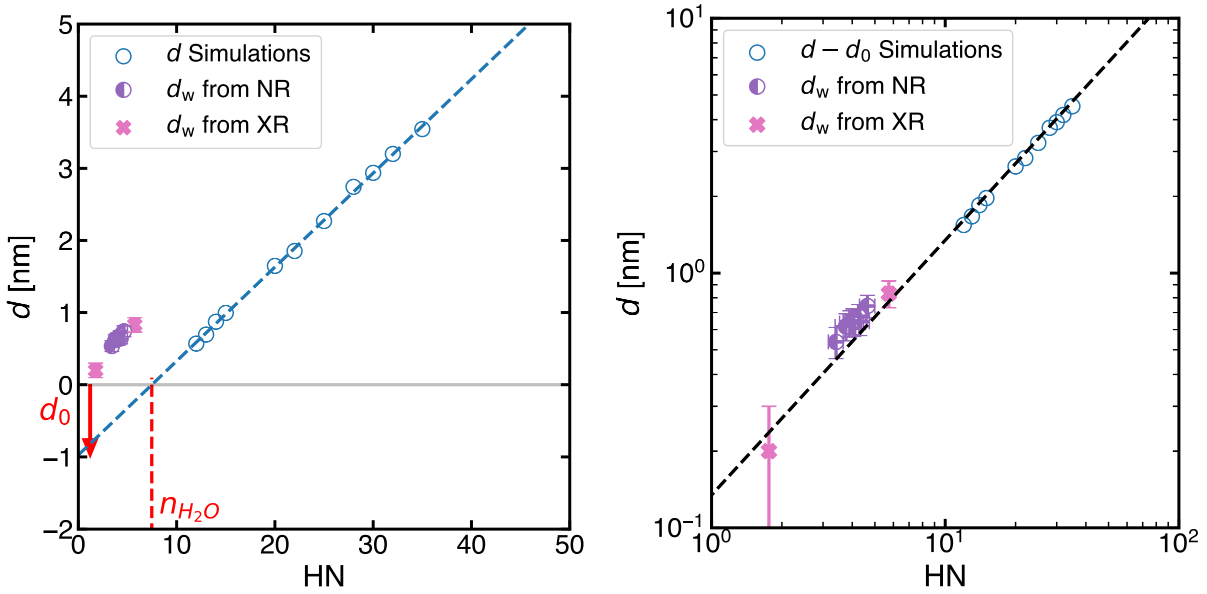

Figure III.12: (Left) (○) Raw thickness *d* of the water layer determined from numerical simulations using the density criterion described in the text as a function of the number of water molecules HN per lipid. Water thickness d_w determined experimentally by neutron reflectivity (◐) or X-rays reflectivity (✖) as a function of the number of water molecules per lipid determined from SLD profiles. The straight line corresponds to the best fit giving the depth of penetration of water into the lipid heads d_0. (Right) Same figure as left but with the numerical thickness of the water layer taking into account the penetration of water into the $d-d_0$ heads. The dashed line corresponds to the expected value for a bulk water layer.

$$\mathrm{HN} = \frac{\rho_{\mathrm{H_2O}} A d_w}{2} \Rightarrow d_w = \frac{2\mathrm{HN}}{A\rho_{\mathrm{H_2O}}} \tag{III.13}$$

where A is the surface area per lipid and $\rho_{\mathrm{H_2O}}$ the bulk water number density. Again the agreement between experiments and numerical simulations is very good.

Numerical simulations of DPPS monolayers carried out by our collaborators at ILM have produced some very interesting initial results, which are in very good quantitative agreement with our neutron and ray reflectivity experiments. They confirm that we are characterising the structure of the water layer with excellent resolution and that the thicknesses measured for the water layer in strong confinement are realistic. They also provide independent confirmation of the value of the hydration length of the PS heads, which is higher than that of the PC heads. This last point is an important validation of the analysis of interactions between charged membranes in the strong coupling regime.

III.5 About counterions

Until now in this work, we have not discussed the counterions present in our system. This subject remains under debate. We used DPPS with sodium counterions. During the deposition procedure, the DPPS monolayer was in contact with bulk Milli-Q water. Although the water is deionized, its pH rapidly decreases to 5.5-6 upon contact with air due to the dissociation of CO_2 and the resulting increase in hydrogen ion concentration. Recent studies have also shown that Milli-Q water can be contaminated with calcium ions [114]. The concentration of calcium ions in the bulk solution is likely several orders of magnitude higher than the amount of sodium ions added by the 2D monolayer deposition at the air/water interface. Consequently, sodium ions are probably rapidly exchanged for protons or calcium ions. This raises the question of which counterions are present in our supported phospholipid layers.

In XR experiments, we are sensitive to the number of electrons present in the system. Whether we have Na^+, H^+ (which are often associated with anions like hydrogenocarbonates), or calcium ions, the effective number of electrons Ne per PS head is approximately the same. NR does not provide sufficient precision with a single contrast, as the solvent does not exchange well, making proper analysis difficult.

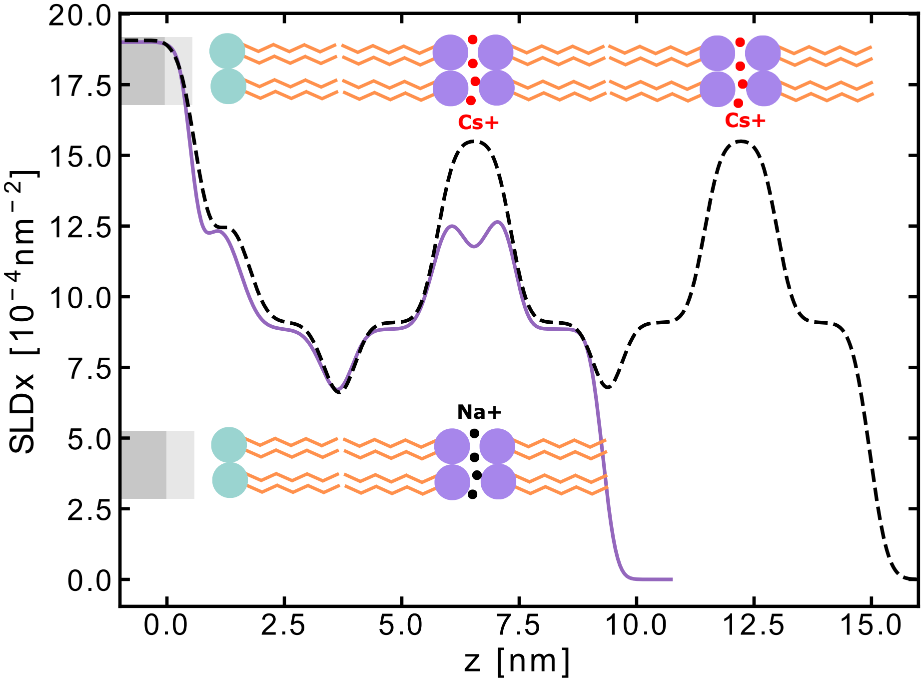

Figure III.13: Comparison of X-ray SLD between DPPS trilayer with Na^+ counterions and DPPS pentayer with Cs^+ counterions at RH = 90%.

To demonstrate that SC attraction is possible with monovalent ions, we attempted to deposit a DPPS pentalayer with Cs^+ ions. We succeeded in LB deposition with a 1 mM concentration of Cs^+ in the solution, allowing for potential ion exchange. We then measured XR and extracted the SLD_X profile shown in Figure III.13. This profile was compared to the SLD_x of a DPPS trilayer without Cs^+ ions in the buffer. To fit the reflectivity profiles, we allowed the SLD of the PS heads to be a free parameter. Typically, the SLD is fixed at $15.5 \times 10^{-4}\,\mathrm{nm}^{-2}$, calculated using a number of electrons of $N_e = 172$ per head with a theoretical volume of $V_\mathrm{m} = 310$ Å^3. This SLD takes into account Na^+ ions. If Na^+, Ca^{2+}, or protons were exchanged for Cs^+ ions, it would add 44 electrons per PS head, resulting in an SLD of $19.5 \times 10^{-4}\,\mathrm{nm}^{-2}$. During the fitting procedure, allowing the SLD of the heads to vary while maintaining the same volume and water content found in DPPS trilayers, we obtained this value precisely. This strongly indicates Cs^+ ion exchange and proves that SC attraction can occur with monovalent ions, as the water thickness remains comparable to that of DPPS without Cs^+ and the successful deposition of a pentalayer. However, this does not specify which ions are present in the general case.

III.6 Conclusion

This study provides a comprehensive analysis of the interplay between SC attraction and hydration repulsion in nanoconfined water between charged phospholipid layers. Our experimental results reveal that hydration water significantly reduces the screening of electrostatic interactions, leading to conditions where SC attraction becomes significant even with monovalent counterions. The balance between SC attraction and hydration repulsion governs the behavior of charged phospholipid layers. These findings enhance our understanding of the fundamental forces in biological and colloidal systems, particularly under nanoconfinement conditions.

Chapter IV

Hydration lubrication in neutral and charged phospholipids

IV.1 Introduction

If you were to ask a tribologist about their primary goal, they might say it is to understand the molecular origins of macroscopic friction. Although friction is well understood at the macroscopic level, linking it to molecular-scale physical interactions remains one of the major challenges in current friction research. This chapter will focus on exploring the frictional properties of stacked phospholipid layers. We will build on the knowledge developed in Chapter III, particularly on our understanding of the physical interactions within zwitterionic and charged phospholipid layers, to investigate whether friction can be linked to these interactions.

Upon further reflection, the tribologist might express a desire to control friction at the molecular or nanoscopic level. In this chapter, we aim to take steps toward realizing that goal. Specifically, we can precisely control the thickness of water layers between phospholipids, allowing us to examine how hydration modulation can influence friction. This is particularly relevant because hydration lubrication (as discussed in Chapter I) is considered the primary mechanism behind the efficient lubrication of phospholipid layers.

IV.2 Measuring macroscopic friction

We studied zwitterionic DPPC and DSPC phospholipid layers, charged DPPS layers, and mixtures of DPPC and DPPS layers using the same procedure outlined in Chapter III.

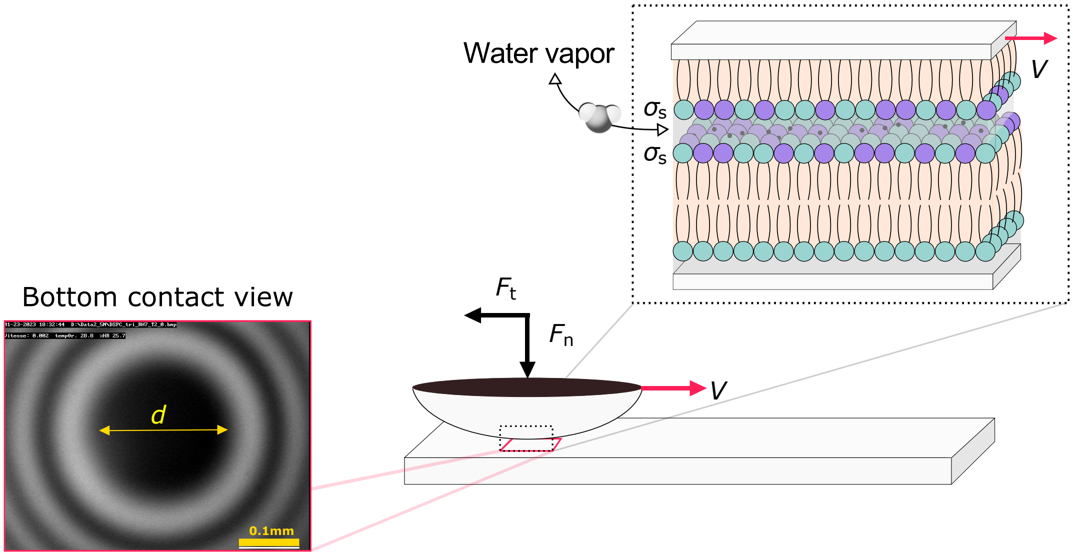

Figure IV.1: Scheme of the friction experiments on a phospholipid trilayer. A white light microscope image of the contact zone is also shown.

However, in this case, the layers were deposited on a commercial soda-lime glass substrate (see Figure IV.1). While the roughness of soda-lime glass is higher than that of a polished silica substrate, typically ranging from 1 to 20 nm [62], we do not expect this to significantly impact the friction behavior of supported phospholipid layers. This is because, in the gel phase, friction is generally less influenced by substrate roughness compared to the fluid phase [31, 14]. Any potential drawbacks of increased roughness are, in our view, outweighed by the advantages of using a transparent and non-birefringent substrate. The transparency allows for direct visualization of the contact area through white-light interference, and it is also essential for the FRAPP (Fluorescence Recovery After Patterned Photobleaching). In the tribology community, mica is commonly chosen as a substrate due to its extremely low roughness when freshly cleaved [62]. However, mica is birefringent, which makes it unsuitable for FRAPP experiments or common optical setups, as discussed in Chapter V. Accurate measurement of the contact area is critical, as friction force F_t is typically normalized by the contact area when compared to models [78].

In our experiments, we used a spherical borosilicate glass indenter with a radius of curvature of 51 mm. Upon contact between the substrate and the indenter, we observed the formation of Newton's rings, as shown in Figure IV.1. From these images, we extracted the contact area via image analysis. We report in the Appendix C the evolution of the contact area A as a function of the applied normal force F_n, which follows the Derjaguin, Muller, and Toporov (DMT) theory [115]. This theory describes the contact mechanics between two elastic, adhesive bodies.

Additionally, in the Appendix C, we provide predictions for the variation of the interlayer water thickness d_{w2} under surface contact pressure for all humidities investigated in this study. Notably, the contact area did not change as a function of relative humidity (RH) or the type of substrate used. Whether the substrate was bare, coated with a monolayer, trilayer, or pentalayer of phospholipids, the contact area remained load-dependent only.

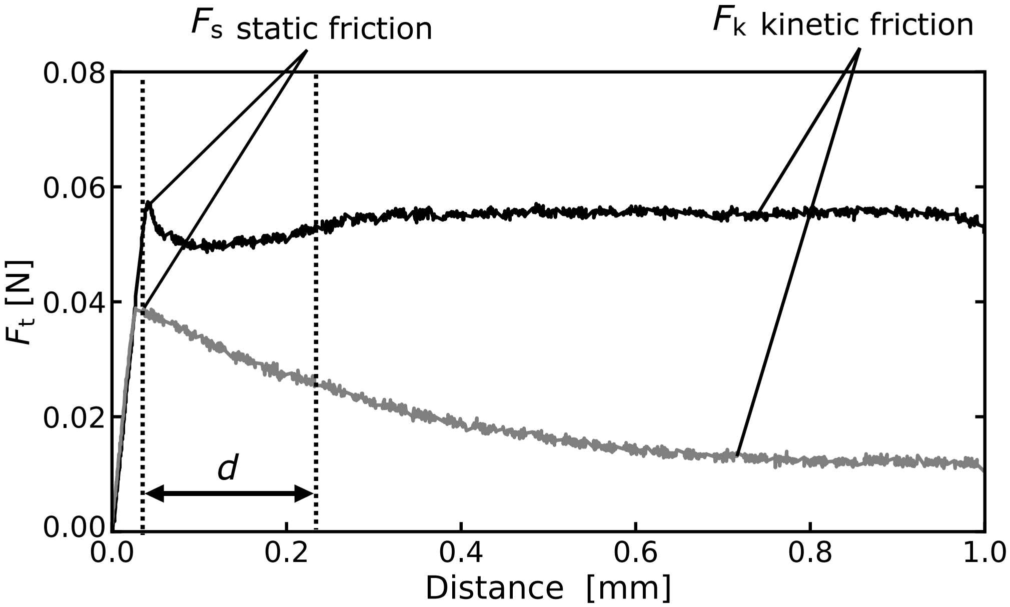

Figure IV.2: Friction profile of DSPC trilayer at RH = 30% (black) and RH = 70% (gray), measured at $T = 298\,\mathrm{K}$, $F_n = 0.5\,\mathrm{N}$, and $V = 10\,\mu\mathrm{m/s}$.

In Figure IV.2, we show the typical evolution of the friction force F_t for a DSPC trilayer in controlled humidity experiments. The system was sheared at a constant velocity of $V = 10\,\mu\mathrm{m/s}$, and three distinct regimes were observed. Initially, in the elastic deformation regime, F_t increases linearly. Once the friction reaches F_s, the static friction threshold, the system begins to move. After the indenter moves beyond the initial contact zone, the friction force reaches a plateau corresponding to the kinetic friction force F_k. In this study, and in the subsequent analyses, we consider F_t as the average value of the plateau, representing the kinetic friction. While static friction F_s is of interest, it is less relevant for studies focused on sliding friction, particularly in comparison with biolubrication, where dynamic friction is more pertinent. Even though our system differs from the complex, fluid-based, and multicomponent friction found in biolubrication, we aim to simulate conditions similar to extreme situations

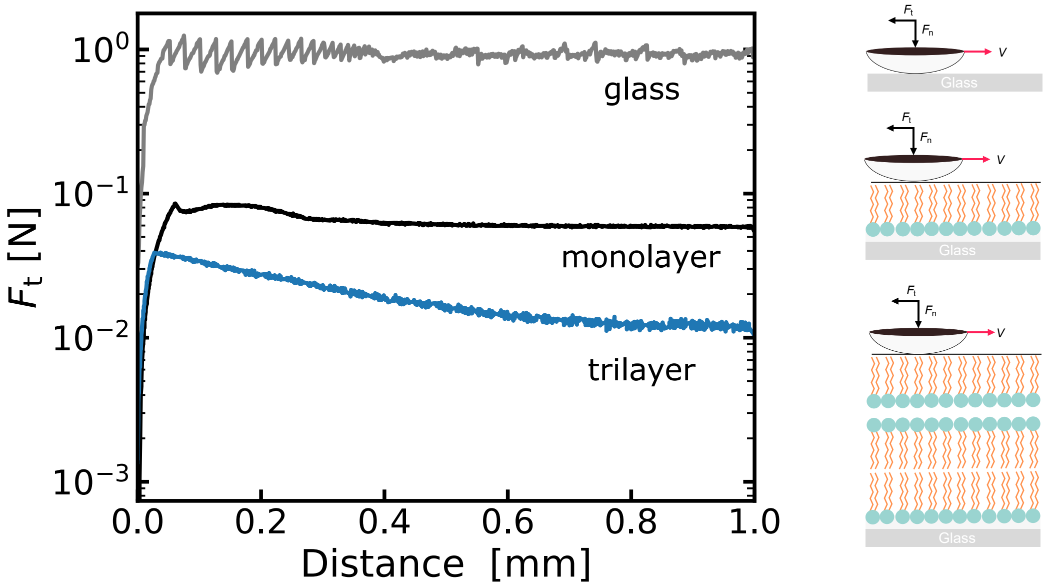

Figure IV.3: Friction force comparison between glass-glass, glass-DSPC monolayer, and glass-DSPC trilayer. Sliding speed: $V = 10\,\mu$m/s, normal force: $F_n = 0.5\,$N, and relative humidity: RH = 70%.

in joints. In these scenarios, where cartilage surfaces come into direct contact, pressures can reach approximately 20-25 MPa [116]. In our experiments, this corresponds to a normal force of $F_n = 0.5\,$N with the indenter.

IV.3 Friction on neutral phospholipid layers

IV.3.A Glass and phospholipid friction comparison

Investigations of phospholipid friction is a well-established field, and the lubrication efficiency of supported layers is not a novel discovery. However, the remarkable efficiency of these layers still warrants attention and justifies the interest in studying such biolubricants. In Figure IV.3, we compare the friction forces for a glass-glass contact, a glass-DSPC monolayer, and a glass-DSPC trilayer. The friction experiments were conducted under the same conditions. Glass-glass friction resulted in a friction force on the order of $F_t = 1\,$N, with

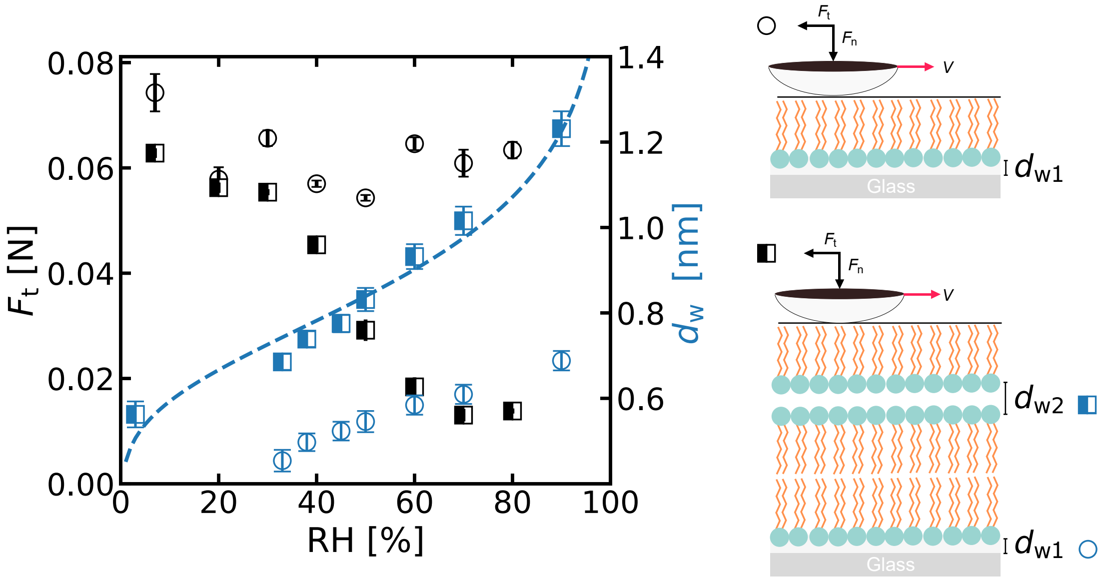

Figure IV.4: (Left axis, black symbols) Variation of the friction force at different relative humidities (RH) for both monolayer and trilayer DPPC. (Right axis, blue symbols) The variation of d_{w2} and d_{w1} is shown with blue markers. Schematics of both situations are presented together with the associated symbol. Sliding speed: $V = 10\,\mu\text{m/s}$, normal force: $F_n = 0.5\,\text{N}$.

clear evidence of stick-slip phenomena, as already documented in the literature. This type of friction is associated with wear and irreversible plastic deformation of the surfaces, consistent with previous work [117].

Strikingly, when a DSPC monolayer was added, the friction force decreased by an order of magnitude, and wear was eliminated. This result is particularly astonishing-how a nanometric film can so drastically reduce friction is remarkable. Moreover, adding two additional layers to form a DSPC trilayer led to another order of magnitude reduction in the friction force, showcasing the impressive lubrication properties of these multilayers.

IV.3.B Tuning friction with relative humidity

This section serves as a foundational point in my thesis, highlighting the significance of phospholipid layers deposited at the air/solid interface, not only for studying physical interactions but also for investigating friction. The ability to tune friction is a highly relevant topic in current interface science. For phospholipid friction, this tuning is often achieved by numerical studies either by adjusting the hydration number per lipid, H_n [43, 118], or even by using topologically manipulated membranes via electrostatic forces [119]. Molecular dynamics (MD) simulations are typically the most effective tool for linking structural properties to frictional behavior. However, thanks to our previous reflectivity experiments and analysis of physical interactions between layers, we can precisely control the number of water molecules per phospholipid, making our experimental system a suitable candidate for studying and tuning friction in a manner analogous to MD simulations.

In Figure IV.4, we report the variations of the frictional force F_t as a function of RH at constant normal force $F_\mathrm{n} = 0.5\,\mathrm{N}$ and sliding speed $V = 10\,\mu\mathrm{m/s}$. The results are shown for a DSPC trilayer and monolayer. We have performed similar experiments on DPPC trilayers (see Appendix C), which exhibit the same behavior. The plot also shows the variations of d_w2 and d_w1, which are consistent for both DPPC and DSPC (see Appendix C). At low humidity, the trilayer friction is equivalent to that of a monolayer sample, with $F_\mathrm{t} \approx 0.06 - 0.08\,\mathrm{N}$. As RH increases, the friction decreases monotonically to $F_\mathrm{t} \approx 0.01\,\mathrm{N}$, reaching values comparable to the superlubricity observed in articular joints [9]. The monolayer, however, remains constant across all RH levels, indicating that F_t is well correlated with the increase in d_w2, whereas the monolayer system remains highly confined, with minimal variations in d_w1.

This result is particularly interesting because it indicates that the nanoscopic water layer thickness d_w2 can indeed significantly influence macroscopic friction, as F_t decreases by nearly an order of magnitude. This finding underscores the crucial role of hydration water in phospholipid lubrication. However, many questions remain unanswered. Are we witnessing a shift in the sliding plane or dissipation mechanism, from friction dominated by phospholipid chains to that dominated by the water layer, as observed in numerical simulations [43]? And is it possible to model this behavior using the formalism introduced in Chapter III? These questions will be addressed in the following sections.

IV.3.C Systematic investigation of friction

A common approach in macroscopic friction studies is to investigate how the friction force varies with macroscopic quantities changes and determine if any laws govern this behavior. We begin by exploring how friction varies with changes in sliding velocity V. Due to experimental limitations, velocity experiments are often conducted at low speeds, even though biological contact speeds during activities like sprinting or intense running can reach velocities on the order of meters per second [120]. Typical sliding speeds are usually on a fraction of a mm/s. In this work, we reached velocities ranging from 1 μm/s to 100 μm/s.

Regarding normal pressure $P = F_\mathrm{n}/A$, where F_n is the normal force and A is the contact area, our experimental macroscopic friction setup, adapted to solid mechanics systems, allowed us to measure normal forces in the range of 0.1 to 2 N. Using a spherical indenter with a large radius of 51 mm (designed with low curvature to achieve the lowest possible normal pressure), we achieved normal pressures between 20 and 50 MPa, which is above the maximum pressures observed in human joints.

We began by examining how the shear stress $\tau = F_\mathrm{t}/A$, where F_t is the frictional force and A is the contact area, varies with changes in V and P, at

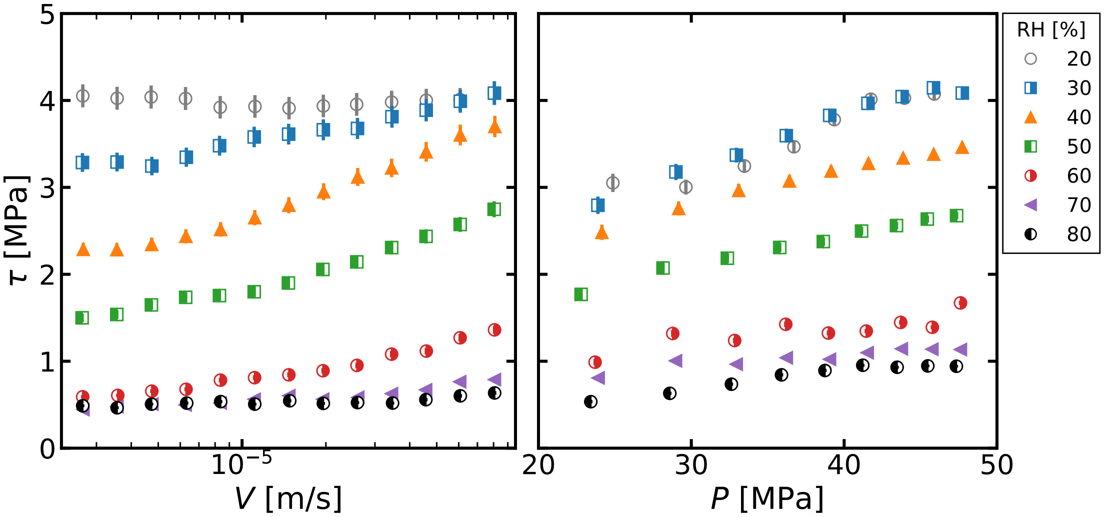

Figure IV.5: Shear stress variation as a function of sliding velocity V (left with P=0.5 N) and contact pressure P (Right with $V = 10$ μm/s) at different RH.

fixed humidity levels ranging from 20% to 80%. The results are shown in Figure IV.5. As expected, we observe the same behavior as in Figure IV.4, where RH controls the shear stress, decreasing from 3—4 MPa at low humidity to 0—1 MPa at high humidity for a given P and V. What is particularly interesting is how τ varies: τ increases linearly with P, and its dependence on V appears to be logarithmic or follows a $\sinh^{-1}$ trend. This is significant, as it corresponds to the hallmark behavior of boundary lubrication models, which will be discussed in detail in the following section.

IV.3.D Stress-augmented thermal activation of hydration barrier

IV.3.D.i General discussion

The stress-augmented activation model, also known as the Eyring/Prandtl model, is based on the coupling of thermal energy and mechanical stress to overcome an energy barrier. This model is commonly used to describe sliding friction processes or, more generally, any process that can be modeled by molecules traversing a potential barrier (see Section II.7 for more details). It was first successfully applied to describe the friction of surfactant monolayers [81], and more recently to the friction of hydration water [82]. More broadly, it is used to model solid friction, or boundary lubrication [78]. The model connects macroscopic friction quantities to molecular/microscopic parameters. Typically, the shear stress τ is expressed as:

$$\tau = \frac{k_\mathrm{B}T}{\phi}\sinh^{-1}\left(\frac{V}{V_0}\exp\left(\frac{Q+\Omega P}{k_\mathrm{B}T}\right)\right). \tag{IV.1}$$

Here, τ relates macroscopic values such as sliding speed V, temperature T, and contact pressure P, to microscopic quantities such as Q, the energy barrier, and Ω and ϕ, which represent the pressure and shear activation volumes, respectively. V_0 is the velocity intrinsic to the system. A full derivation of the model and more details are provided in Section II.7.

We were both puzzled and excited by our observation of the behavior of τ with respect to V. It appears to exhibit a $\sinh^{-1}$ dependence, which is a signature of a barrier-crossing model. To our knowledge, this is the first experimental study to observe this $\sinh^{-1}$ dependence, which had only been previously observed numerically [121]. In experimental studies, high shear rates typically result in a $\ln(V)$ dependence for τ, as $\sinh^{-1}(x) \to \ln(x)$ for $x \gg 1$. At high shear stresses, this model also captures the linear dependence of τ on P.

As discussed earlier, we initially attempted to model the $\sinh^{-1}$ behavior using the Eyring model. However, it was impossible to fit our data with reasonable physical parameters. What is possible, however, is to model the data using an extension of the Eyring model that includes flows of different sizes and dissipation mechanisms. Essentially, this leads to a sum of two $\sinh^{-1}$ terms with different activation volumes and energy barriers, as theoretically developed by Ree and Eyring [122]. While this model worked, it lacks elegance and can easily lead to overfitting.

Another approach is to consider two distinct regimes, each characterized by different dissipation mechanisms, resulting in two distinct slopes in the $\ln(V)$ dependency. In the following, we will assume that each phospholipid layer is trapped in different potential wells, as depicted in Figure IV.6. These wells are determined by local physical interactions, and different sliding planes or flow regimes would correspond to different slopes in $\ln(V)$.

The next question is whether we can apply the insights developed in Chapter 3 regarding structure to model friction using the Eyring model. We begin by attempting to model the third layer in contact with air. It is reasonable to assume that the activation energy Q depends on the hydration level of the phospholipid heads, given its role in modulating friction. A plausible hypothesis is that the energy barrier Q corresponds to the energy required to dehydrate a phospholipid. Baumgart et al. [123] have already computed this value when modeling diffusion in supported phospholipid bilayers (see Section II.7 for more details). Here, we propose extending this concept to shear processes. This energy is directly related to RH, and for DSPC or DPPC, it can be expressed as:

$$Q_1 = a P_{0\mathrm{h,PC}} z_{\mathrm{h,PC}} \exp\left(-\frac{d_{\mathrm{w2}}}{2 z_{\mathrm{h,PC}}}\right), \tag{IV.2}$$

where $P_{0\mathrm{h,PC}} = 5.7 \times 10^{9}\,\mathrm{Pa}$ and $z_{\mathrm{h,PC}} = 2.05\,\mathrm{nm}$ are constants from Chapter

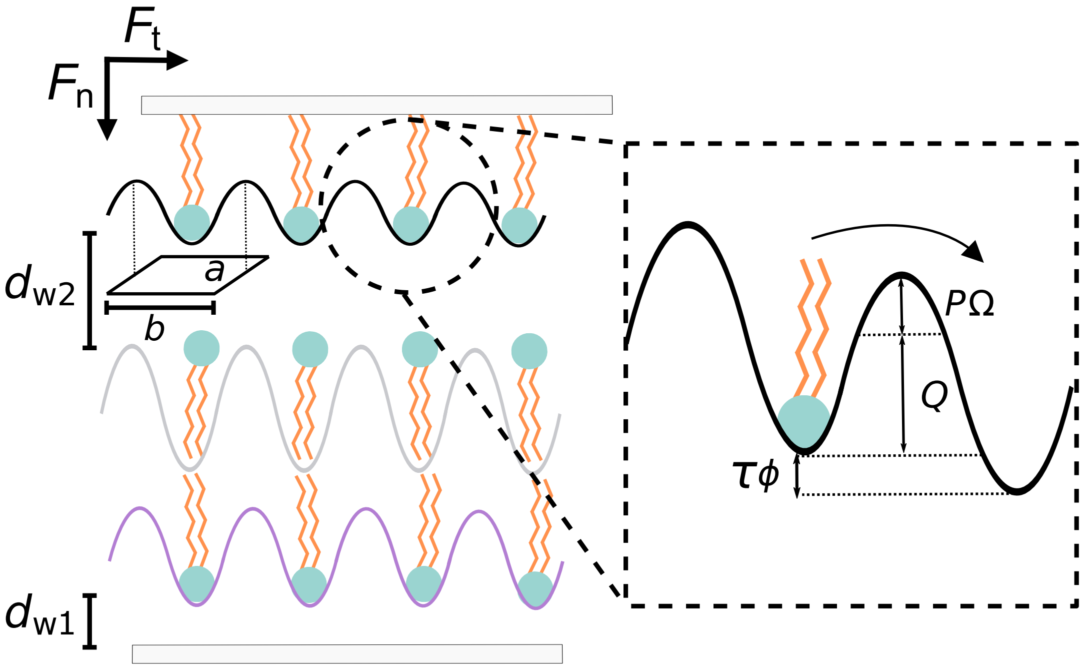

Figure IV.6: Stress-augmented thermal activation of a trilayer. Each layer is trapped in a different potential well with an energy barrier Q. The area per lipid, a, is obtained from reflectivity analysis, with $a = 47\text{Å}^2$ for DSPC."

3, and d_{w2} is modeled using hydration and van der Waals pressures:

$$d_{w2} = z_{h,PC} \ln\left(\frac{P_{0h,PC}V_m}{k_BT} \ln\left(\frac{RH}{100}\right)\right). \tag{IV.3}$$

Figure IV.8 shows the behavior of Q_1 under these conditions.

Next, we address the modeling of activation volumes. Activation volumes are the product of a cross-sectional area and an activation distance (see Figure IV.6 and Section II.7). For Ω, which represents the volume that must be crossed for shear to occur, a reasonable assumption is that the area corresponds to the area of lipid, for DSPC and DPPC we could extract a similar value in gel phase from XR and NR analysis from Chapter III, detailed in Appendix B of $a = 47\,\text{Å}^2$, while the activation distance, here in the plane of the load, is reasonably taken as the water layer thickness, d_{w2}. Therefore, $\Omega_1 = \alpha d_{\mathrm{w2}}$, assuming dissipation occurs within the water layer.

For ϕ, the shear activation volume, the situation is more complex. The literature contains some ambiguity about its definition, as the activation distance is parallel to the cross-sectional area because it is encompassed in the plane of the shear stress. The activation distance is interpreted as the spacing between phospholipids as it corresponds to half the barrier spacing b. However, modeling the area is problematic because it is associated with the number of molecules involved in the shear, which is hard to predict, which is why we treat it as a fitting parameter in our model and will be denoted ϕ_1 for the hydration lubrication. Both volumes are represented in Figure IV.8.

Finally, V_0 is an unknown velocity constant, estimated as $V_0 = b\nu_f = 0.2 \times 10^{-9} \times 10^{11}$ m/s, where ν_f is the frequency of attempted rearrangements, typically related to the vibrational frequency of molecules, which is around 10^{11} Hz for fatty acid chains [81].

The fit is shown in Figure IV.7 with solid lines and accurately predicts the behavior of τ across the entire range of RH and P. However, there are two instances where the model fails to capture the behavior: at low V and high RH.

One possible explanation could be a change in the sliding plane, shifting from the second water layer to the first water layer for example. To explore this possibility, we attempted to fit the data using an activation volume $\Omega_2 = \alpha \cdot d_{\mathrm{l}}$, where $d_{\mathrm{l}} = 8\,\mathrm{nm}$ is the thickness of the DSPC trilayer, as extracted from reflectivity data [46]. To model the energy barrier, we used measurements from Briscoe et al. [81], who studied a monolayer of fatty acid tails. They

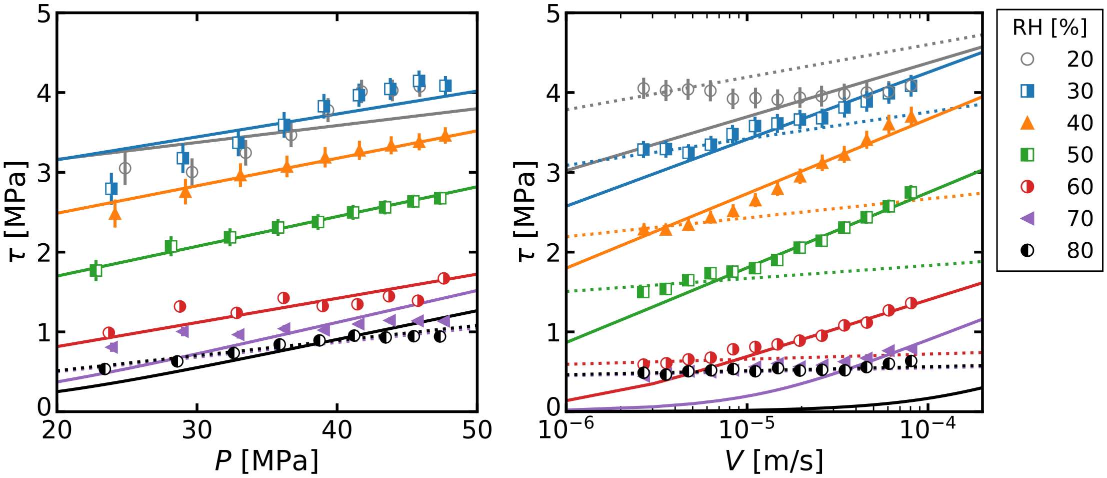

Figure IV.7: (Left) Shear stress variation as a function of sliding velocity V, with constant normal force $F_n = 0.5\,\mathrm{N}$. (Right) Shear stress variation as a function of contact pressure P with constant sliding speed $V = 10\,\mu\mathrm{m/s}$. Both figures show different relative humidity (RH) values. At RH = 20%, we display two fits: one model for hydration lubrication (solid line) and one for tail lubrication (dashed line).

found a Q value on the order of $20\,k_\mathrm{B}T$ for the same V_0. It is worth noting that at low humidity, it can be challenging to distinguish between the friction of the tails and low hydration energy, as both are of the same order (see Figure IV.8). As before, we took ϕ as a free parameter, denoted ϕ_2. The results are shown in dashed lines in Figure IV.7. Strikingly, this second model appears to close the gap, fitting the part where the hydration model failed. This suggests a potential change in the sliding plane at low speeds and low humidity/high. However, the second model could not capture the behavior observed in the pressure experiments.

The shear activation volume ϕ_1 remains constant across all humidity levels, while ϕ_2 increases with RH, indicating that more molecules are involved in the frictional process as hydration increases. Notably, ϕ_2 moves from a value similar to ϕ_1 to approximately three times its magnitude.

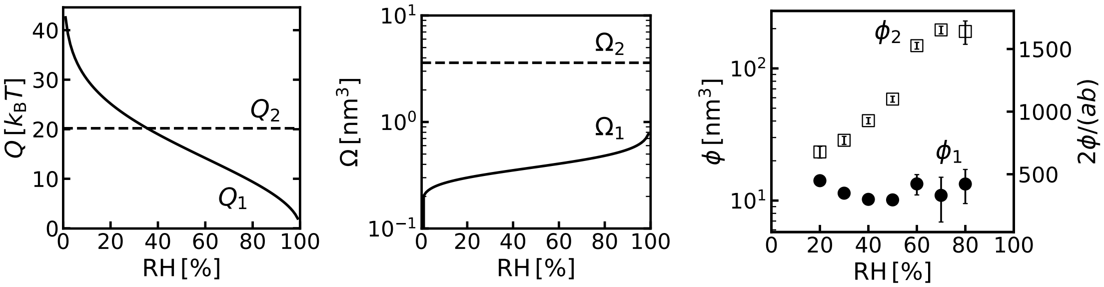

Figure IV.8: Model of the hydration energy barrier Q (Left) and the shear activation volume Ω (Right) vs relative humidity RH. Shear activation volume Φ vs relative humidity RH.

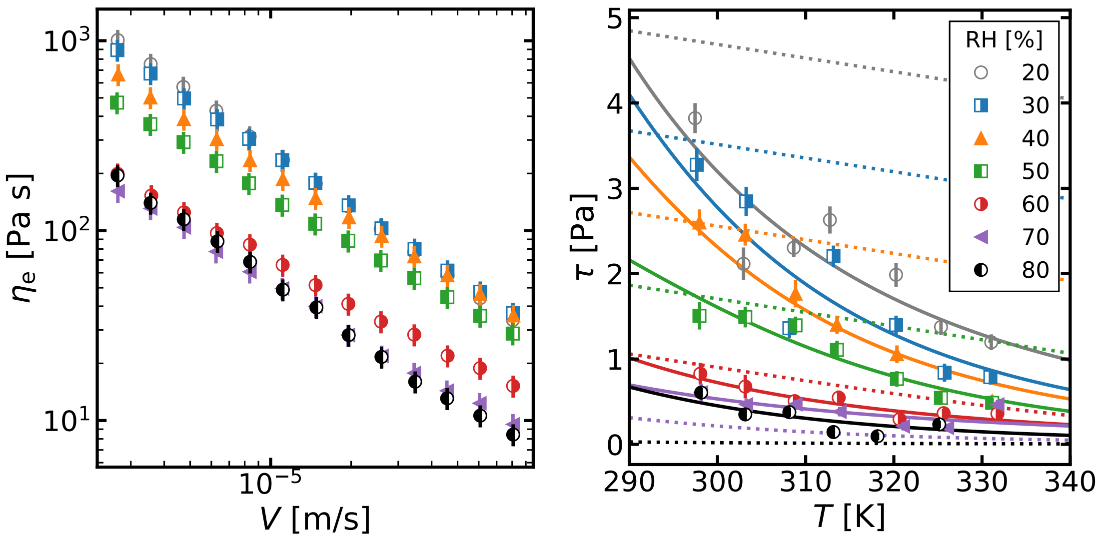

Figure IV.9: (Left) Effective viscosity as a function of sliding velocity (V). (Right) Variation of τ with temperature (T). Sliding speed: $V = 10\,\mu$m/s, normal force: $F_n = 0.5\,$N. The dashed line represents the hydration lubrication model, and the solid line corresponds to Eyring with free parameters

From our calculations (see Figure IV.8), the number of molecules involved ranges from a few tens to hundreds. A small number, on the order of tens, implies that a high stress is applied to a low number of molecules, leading to high localized friction. In contrast, when hundreds of molecules are involved, the value aligns with more typical figures reported in the literature [81, 78].

IV.3.D.ii Effective Viscosity and temperature dependence

Since we know the thickness d_{w2} of the water film, it is possible to compute an effective viscosity using the expression:

$$\eta_{\mathrm{e}} = \frac{\tau d_{\mathrm{w2}}}{V}. \tag{IV.4}$$

The results for the variation with sliding velocity are shown in Figure IV.9. As the sliding velocity increases, we observe a decrease in the effective viscosity, indicative of shear-thinning behavior, as expected from the Eyring sinh law across all humidity levels. This also provides an estimate of the hydration water's viscosity, which we found to be 4 to 6 orders of magnitude higher than that of bulk water [118]. This is a rough viscosity estimation since we cannot explicitly determine if the dissipation occurs solely in the water layer.

We studied the influence of temperature on friction properties. It was impossible to fit the temperature experiments using the previously developed model (see dashed line in Figure IV.9). However, it was still possible to fit the data by allowing all physical parameters to vary freely (see solid lines in Figure IV.9). In this way, we obtained values for the activation energy and activation volumes that seemed reasonable, but they are difficult to interpret and should be taken cautiously, as we likely overfitted the data.

IV.4 Friction on charged phospholipid layers

After successfully studying zwitterionic phospholipids, we investigated charged phospholipids, specifically DPPS. While the influence of charged phospholipids on friction properties has been observed recently [124], no quantitative analysis has been conducted. Here, we have all the necessary information to address this gap. In Figure IV.10, we show how the shear stress τ varies with the DPPS fraction j. This figure illustrates that the friction properties rapidly decrease until monolayer behavior is reached, which is exactly what was expected.

Indeed, in Chapter 3, we demonstrate that the addition of DPPS phospholipids alters the hydration constants of phospholipids by increasing correlation length z_{h}. As we are also able to predict variations in d_{w2} Consequently, we can attempt to compute Q, the energy required to dehydrate a mixture of DPPS and DPPC phospholipids. If j represents the fraction of DPPS, we then have:

$$Q = \alpha P_{\mathrm{h,tot}} z_{\mathrm{h,tot}} \exp\left(-\frac{d_{\mathrm{w2}}}{z_{\mathrm{h,tot}}}\right), \tag{IV.5}$$

To obtain a direct expression for d_{w2}, we must neglect the repulsive components in strong coupling pressure. This is a reasonable approximation because the repulsive forces become significant only when d_{w2} is less than an angstrom (see Chapter 3). By balancing strong coupling, osmotic pressure, and hydration pressure, we derive a direct relationship between d_{w2}, RH, and σ_{S}:

$$d_{\mathrm{w2}} = -z_{h_{\mathrm{tot}}} \ln\left(2\pi l_{\mathrm{b}} \sigma_{\mathrm{S}}^2 \frac{k_{\mathrm{B}}T}{P_{h_{\mathrm{tot}}}} + \frac{k_{\mathrm{B}}T}{P_{h_{\mathrm{tot}}} V_{\mathrm{m}}} \ln\left(\frac{100}{\mathrm{RH}}\right)\right). \tag{IV.6}$$

We show how Q varies with DPPS fraction change in Figure IV.10. Even though the prediction is imperfect, it predicts reasonably well, as there is no fitting in this case-we took ϕ_1 from the previous section. This demonstrates that energy dissipation occurs in the water layers via dehydration of phospholipid heads. As we increase the DPPS fraction j, we observe an increase in Q,

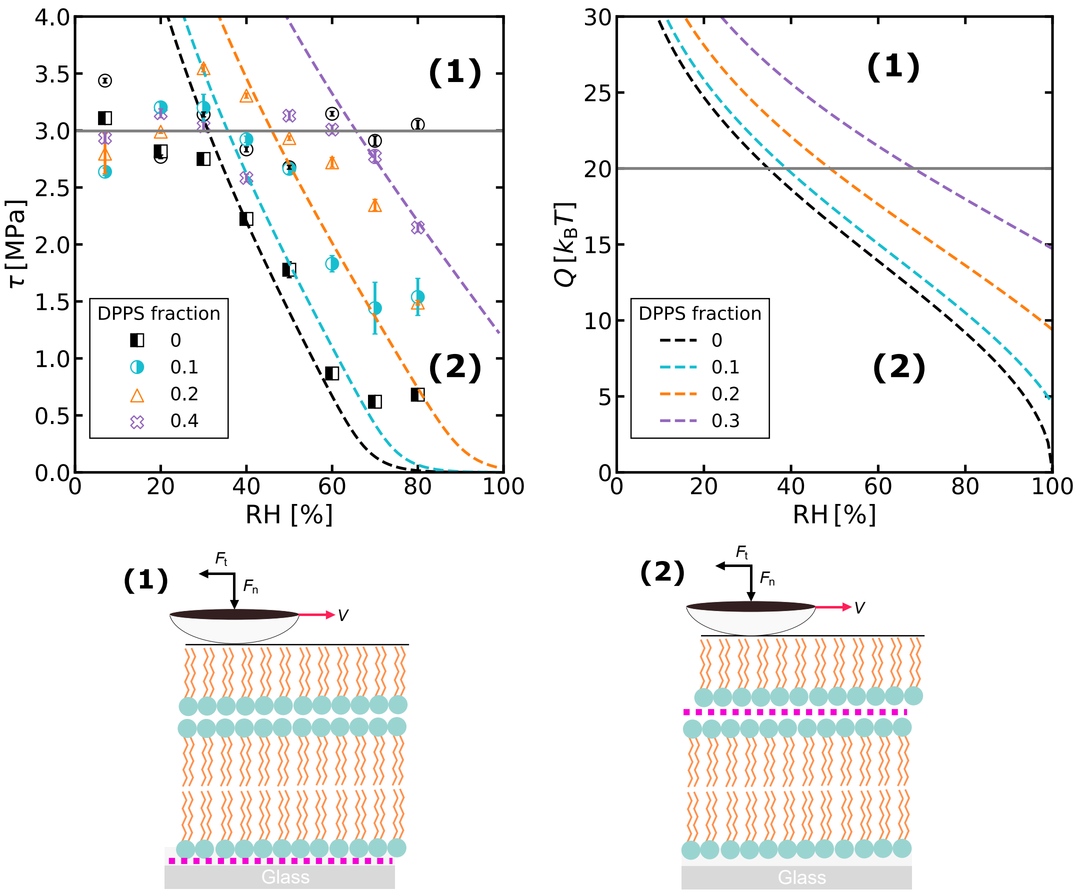

Figure IV.10: Shear stress as a function of RH for varying fractions of DPPS. Hypothetical locations of the slipping plane are indicated.

leading to a rise in the shearing stress. When the shearing stress surpasses the threshold of 20 $k_B T$, the shear remains constant at the value observed for the DPPC monolayer or low-humidity DPPC trilayer. This reinforces the idea that multiple sliding planes compete. When Q is below the threshold, lubrication occurs in the second water layer; above it, dissipation may localize in the first water layer (see Figure IV.10). This also aligns with the findings of the previous chapter, where we identified an increase in the correlation length $z_{h,PS}$ for DPPS. Altogether, this study provides a solid foundation for understanding hydration lubrication in both charged and neutral phospholipids.

IV.5 Conclusion

In this chapter, using a model system of phospholipid layers deposited at the air/solid interface, we could study the friction of phospholipids in a highly controlled manner analogous to MD simulations. We successfully tuned friction by controlling the hydration of our phospholipid layers, highlighting the critical role of water in lubrication. By applying the Eyring model, combined with the knowledge built in Chapter III, we could relate friction to the hydration pressure of zwitterionic and charged phospholipids.

Chapter V

TriboFRAPP experiments: localization of sliding planes

V.1 Introduction

This chapter focuses on developing a system to measure friction and quantify the flow of molecules involved in shear, commonly referred to as the third body [125]. In boundary lubrication systems such as phospholipids, where friction is directly linked to the molecular state, it is highly relevant to probe and determine the movement of molecules involved in the process. However, combining friction measurements with molecular motion detection is a significant challenge.

Since the pioneering work of Evans and Sackmann [126, 127] on the friction of supported phospholipids, no clear evidence of a sliding plane within the water layer has been demonstrated. The work of Klein et al. [35, 128, 129] highlighted the remarkable lubricating properties of hydration water. However, typical setups like the Surface Force Apparatus (SFA) or Quartz Crystal Microbalance (QCM) [130] allow only for friction and surface interaction measurements without directly probing molecular movement. Although systems combining friction and fluorescence imaging exist [30], they do not provide quantitative information on molecular dynamics.

More recently, microfluidic devices [131] have been used to measure interleaflet friction in supported bilayers by inducing flow-related friction. While MD simulations can easily access molecular movement, experimental validation remains limited. In a recent MD study [43], they examined the location of sliding planes in sheared DPPC multilayers in both the gel and fluid phases, showing that the position of the sliding plane changes with phase and hydration levels.

In this chapter, we aim to develop an experimental analog to MD simulations to address this gap. Inspired by the FRAPP experiments [75], which have been used to probe liquid movement near walls [130] and polymer flow [132], our team has developed a unique experimental setup. This setup combines friction measurements containing in situ visualization of the surface contact with a velocimetry FRAPP experiment [74] (see Chapter 2.2 for details on the setup). The velocimeter can probe the velocity of the nanometer-thick layer confined and sheared over a micrometer-scale contact area.

V.2 Improvement of the setup

V.2.A Interferometer

The triboFRAPP experiment is a unique setup developed in a collaboration between the Mcube team and the MIM team from the Institut Charles Sadron, before my arrival [46]. One of the first tasks of my PhD was to modify the interferometer. All the details regarding the setup and its operation are presented in Section II.6.C. The previous interferometer, which is the same as the one used by Davoust et al. [75], is of the amplitude-difference type. This kind of interferometer splits the laser beam in two using a semi-reflective plate: one beam goes directly to the substrate, while the other passes over a mirror mounted on a piezoelectric device before being directed to the substrate. This produces interference fringes that can be spatially electro-modulated (see Figure V.1 without indenter and substrate contact).

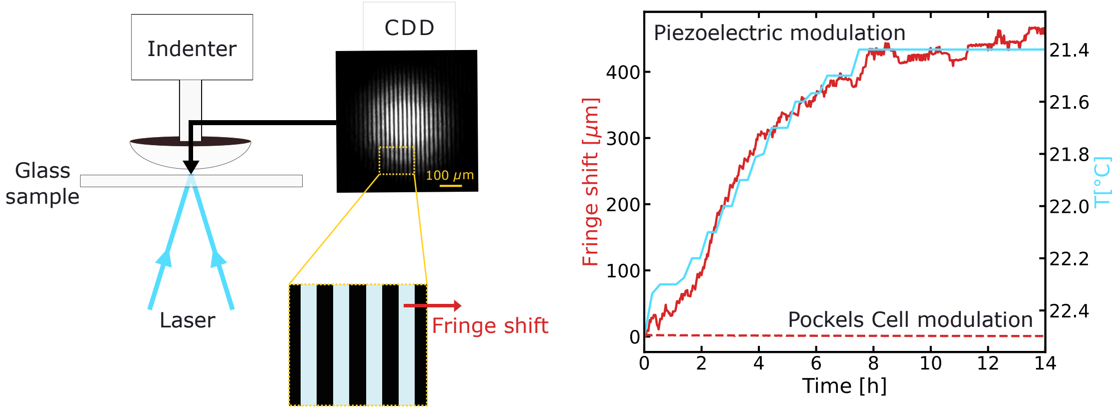

Figure V.1: (Right) Zoom-in view on the interference fringe of the setup, displaying the microscopy image of the interference pattern at $i = 23\,\mu$m. (Left) Fringe shift alongside temperature evolution.

For the modulation of the fringe position, the system worked perfectly. However, we observed a drift in the position of the fringes (of the order of 10-20 interfringes over 12 hours). This shift was correlated with temperature changes, as reported in Figure V.1. We hypothesized that this effect might arise from the difference in the path length of the two beams. Despite room temperature regulation, we detected temperature changes of around 1°C, likely caused by door opening. Additionally, localized heating from the laser during the bleaching phase, particularly on the mirror, could contribute to the shift. A change of 1°C and the resulting alteration in the refractive index can significantly affect the phase between the two beams, as the length difference in the setup was on the order of a meter, leading to fringe shifts. Although the drift is slow, it poses a problem for studying the diffusion of highly confined and hence solwly diffusing molecules like phospholipids at the air/solid interface.

To address this, we sought to implement a symmetric interferometer with electro-modulation, ensuring both interfering beams share the same optical path, which we expected would result in stability against refractive index changes. We aimed to implement the interferometer design from [77]. This setup uses Pockels cells to modulate the phase between two beams separated by a Wollaston prism, with full details of the setup provided in Section II.6.C. We performed the same fringe position measurements under identical temperature shifts, and the results are shown in Figure V.1.

The results are conclusive: the new setup exhibited almost no phase shift and was stable against temperature variations.

V.2.B Validation of the setup

FRAPP experiments can be used to probe the diffusion or velocity of a sheared layer. In this study, we focus on the velocimetry of phospholipid layers. To validate the FRAPP setup, we first tested whether the system is capable of detecting the movement of a slide. The FRAPP system relies on the photobleaching of fluorescent molecules. In this study, we used phospholipids modified with NBD fluorophores attached to the head group (DSPE-NBD). For labeled phospholipid layers, we used 4% DSPE-NBD mixed with DSPC. Although 4% is quite high, it was necessary to obtain a good fluorescence signal.

We deposited a labeled layer on the same glass substrate as used in Chapter 4. Figure V.2 explains the experimental procedure. In the triboFRAPP setup, the substrate is typically fixed, and the tribometer moves. For this validation, we reversed the configuration by fixing the substrate to the tribometer to control its position and velocity. The first phase involves photobleaching, for which we used our laser at 1 W for 8 seconds. The resulting pattern on the substrate can be seen in Figure V.2.

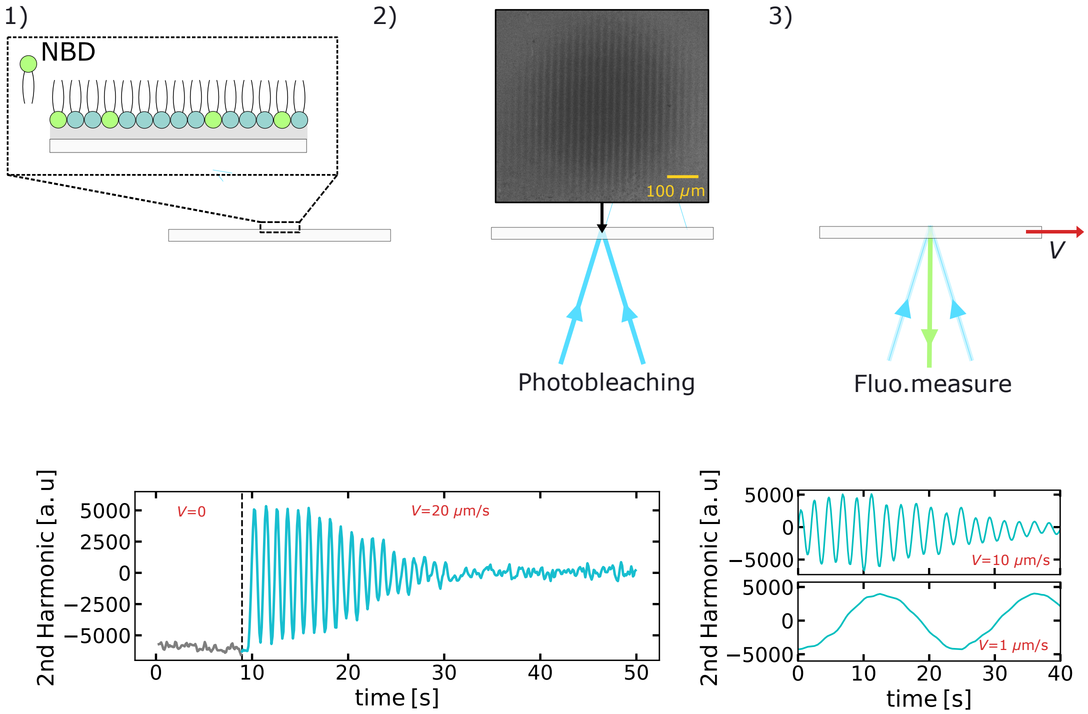

Figure V.2: (Top) Protocol for FRAPP measurement. (Bottom) Contrast intensity of FRAPP experiments at different *V* of the monolayer sample.

During the reading phase, we waited 10 seconds before moving the substrate at $V = 20\,\mu\text{m/s}$. The resulting fluorescence contrast intensity is shown in Figure V.2 For the first 10 seconds, we observed a constant value, and then, once the plate started moving, we observed a sinusoidal modulation of the intensity. When the photobleached pattern moved out of the beam zone, the signal dropped to zero. The fringe spacing used throughout the study was fixed at $i = 23 \pm 2\,\mu$m. By extracting the frequency ν of the intensity oscillation, we can calculate the velocity as $V = \nu \cdot i$. We successfully recovered the imposed velocity and repeated the experiment for $V = 10\,\mu$m/s and $V = 1\,\mu$m/s (see Figure V.2). Each velocity was accurately measured by extracting the intensity frequency.

The new setup is not only more stable with respect to temperature, but it also provides better contrast intensity. This is remarkable, as these tests were performed on a nanometric fluorescent monolayer, yet we obtained a clear sinusoidal signal with almost no noise, demonstrating the sensitivity of the setup. This improvement may stem from several optimizations detailed in Section II.6.C.

V.3 Velocimetry experiments

V.3.A DSPC monolayer

In Chapter 4, we used the Eyring model to describe the friction behavior and to predict potential sliding planes. In this section, we will evaluate whether those predictions were accurate. We begin by studying the DSPC monolayer deposited on a glass substrate. In the standard configuration, the substrate is fixed, and the spherical indenter (51 mm, BK7) is in motion. This is the same indenter used in Chapter 4.

To maintain consistency with the previous chapter, we selected a similar configuration: the normal force F_n was set to 0.5 N, and shear was applied at $V = 10\,\mu$m/s. The FRAPP experiment allows control of both RH and temperature; here, we report results at RH = 30% and T = 20°C in Figure V.3. In the figure, two regimes are shown: the indenter in motion (blue) and the indenter

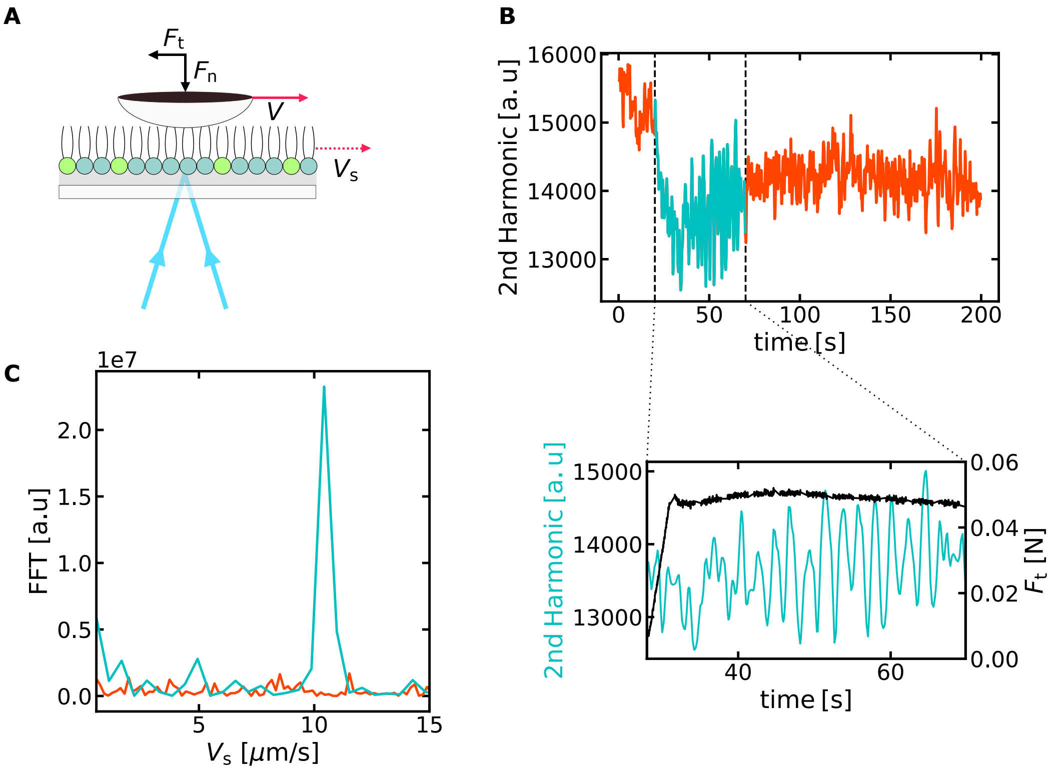

Figure V.3: (A) Scheme of the FRAPP experiments on the DSPC monolayer. (B) Contrast intensity with a zoom in blue on the part corresponding to the friction measurement. (C) FFT of the contrast intensity. Frequency is directly converted to velocity $V_s = \nu i$. Experimental conditions: RH=30%, $T = 20°$C, $F_n = 0.5$ N and V=10 μm/s.

at rest (red). A zoomed-in section of the friction measurement is displayed, where we overlay the corresponding friction force to observe both friction and layer entrainment.

We can clearly distinguish modulation in the fluorescence signal. The amplitude is lower than in the previous section, which is expected, as the contact area is only a fraction of the laser beam area (1 mm^2 compared to 0.2 mm^2). Additionally, it is unlikely that the entire layer is in motion; in the case of a gel phase layer, as we observed in the previous chapter, the behavior is well-described by boundary lubrication theory. This effect is even more pronounced for a monolayer in direct contact with the substrate, where strong adhesion generates high shear stress associated with a low number of molecules involved in the flow. Overall, these factors may reduce the fluorescence contrast.

To confirm that the observed modulation in the signal was due to movement, we performed an FFT on the blue (moving) and red (static) sections of the signal. These results are reported in Figure V.3. We then directly converted the modulation frequency into the velocity of the layer, V_{s}. This velocity was found to be equal to V, the entrainment speed, which is reasonable given the nanometric thickness of the film in the context of boundary lubrication.

The friction experiments in Chapter 4 suggest that RH does not influence the tribology of the DSPC monolayer. To verify this, we repeated the triboFRAPP experiments at various RH levels. The fluorescence signals are included in the Appendix D, while a summary of the results is shown in Figure V.4. This figure compares the friction force of the DSPC monolayer with and without NBD fluorescent markers. The friction force was consistently found to be constant. The results are reasonably consistent, even with the high percentage of fluorescent markers used in these experiments. This friction comparison helps validate our velocimetry experiments, as it is essential that they reflect the same tribological behavior.

In the same figure, we also present the FFT of the sliding part at various RH levels (7%, 30%, 50%, and 70%), providing a representative sample of all RH conditions tested. In all cases, we found that the layer was moving at the velocity of the indenter. However, the amplitude of the FFT peak decreased as RH increased. Although it might be tempting to conduct a quantitative analysis of the fluorescence signal amplitude, it is highly sensitive to experimental parameters such as alignment, bleaching conditions, initial bleaching zone,

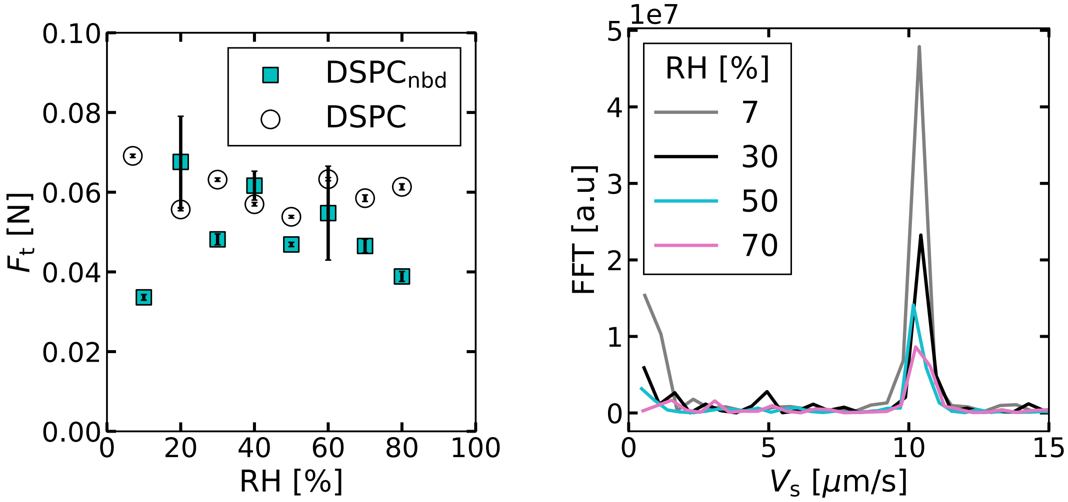

Figure V.4: Friction force comparison between DSPC monolayer and DSPC labeled with NBD. FFT of contrast intensity are detailed in the Appendix D.

artifacts, and acquisition settings.

Interestingly, we observed that the monolayer was always in motion, suggesting that dissipation occurs within the water layers. From XR and NR experiments, where d_{w1} was measured and found to remain nearly constant, it was previously unclear whether dissipation occurred in the water layers or between the indenter and the monolayer tails. Here, we demonstrate the presence of hydration lubrication even in the case of a DSPC monolayer.

V.3.B DSPC trilayer

The previous section demonstrated that the triboFRAPP system can reliably probe molecular motion within a monolayer. In this section, we extend its application to a DSPC trilayer to investigate the localization of sliding planes. In these experiments, one of the layers was labeled with NBD and triboFRAPP measurements were performed under three distinct conditions, as illustrated in Figure V.5. Since layer flip-flop occurs on timescales of hours for fluid phases [133], we expect this phenomenon to be negligible, especially in the gel phase at the air/solid interface, where phospholipid diffusion is minimal.

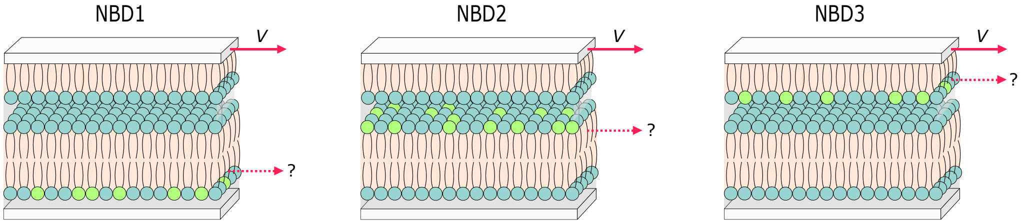

Figure V.5: Scheme of the DSPC trilayer labeled with NBD in the first, second, and third layers.

While the quantification of diffusion using the FRAPP setup could offer insights-such as examining the impact of RH on phospholipid diffusion and linking this to dehydration energy through an Arrhenius process similar to the work of Baumgart et al. [123], here diffusion measurements were not the primary focus of this work. Notably, at ambient humidity (RH = 45–60%), all layers appeared immobilized with negligible diffusion. Though increasing the temperature may have activated diffusion, we opted to concentrate on velocimetry, as phospholipid diffusion has been widely characterized in prior studies [3].

In Figure V.6, we present velocimetry results for three experimental scenarios at RH levels of 30%, 50%, and 80%, with a shear velocity $V = 10$ μm/s and a normal force $F_\mathrm{n} = 0.5$ N. The fluorescence signals correspond to the kinetic friction plateau discussed in Chapter 4, assuring that velocimetry was conducted under the same measurement conditions as F_t.

The FFT of these signals is also shown. When all three layers exhibited motion, sliding was inferred to occur within the first water layer. This was observed at both RH = 30% and RH = 70%. At RH = 50%, however, only the third layer in contact with air was observed to move, indicating a transition in the sliding plane. At low RH, sliding occurs within the first water layer; above

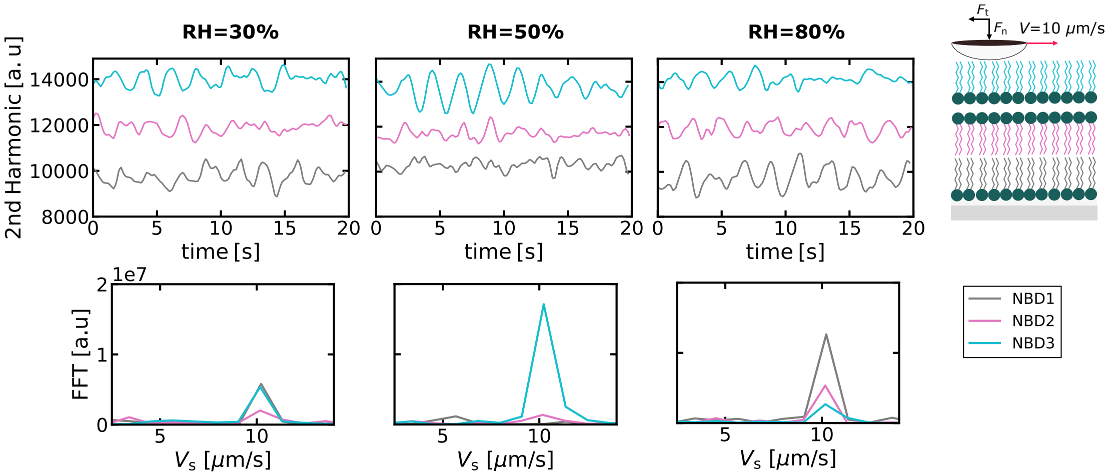

Figure V.6: FRAPP experiments on DSPC trilayers with corresponding FFT analysis.

30% RH, it shifts to the second layer, and at RH = 70%, it returns to the first water layer. These observations align with the predictions made in Chapter IV.

To clarify the relationship between shear stress and velocity, we considered slip within both water layers. At low shear velocities, friction is expected to occur primarily in the first water layer. Repeating the experiments at V = 1 μm/s (see Appendix D) showed that all layers were in motion across all RH levels, confirming that at low velocities, the slipping plane lies in the first water layer. At $V = 10$ μm/s, Figure V.7 suggests that this speed falls near the threshold for transitions in sliding planes. So, it would have been interesting to reach higher velocities. However, due to time constraints, we could not extend triboFRAPP experiments to higher velocities.

Figure V.7 summarizes the findings at V = 10 μm/s. At low humidity, the friction of the trilayer is comparable to that of the monolayer, with dissipation occurring primarily in the first layer. Above 30% RH, the friction decreases as the slipping plane shifts to the second water layer, where the energy required to dehydrate the phospholipids is reduced. Interestingly, at high humidity, the shear reverts to the first layer, which is unexpected, as one might anticipate that slipping would occur more readily in the second layer due to energetic considerations.

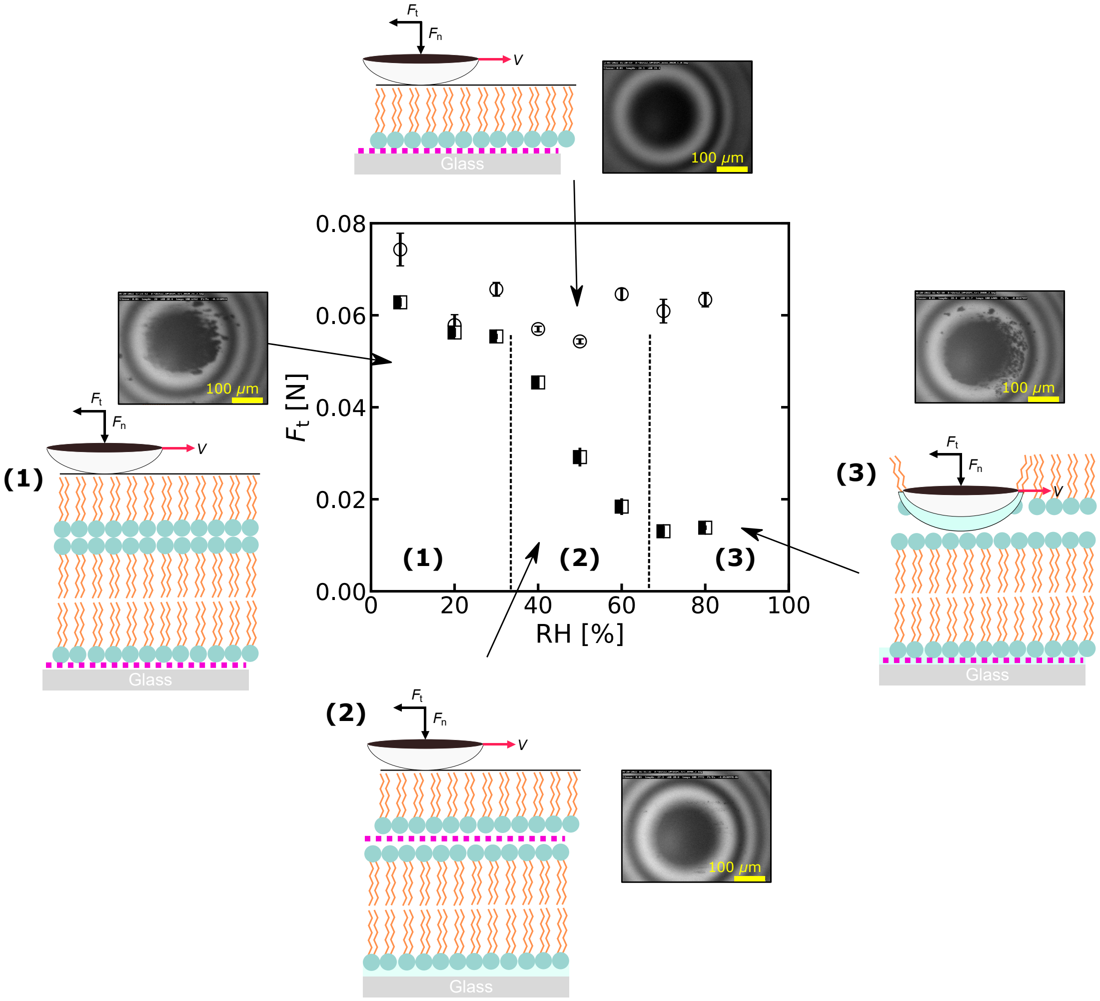

Figure V.7: Friction force for DSPC monolayer and trilayer at different RH, accompanied by an understanding of the sliding planes and microscopy images of the surface contact.

Initially, we were skeptical about this result. However, microscopic images of the surface contact at the end of shear testing reveal a noticeable accumulation of material for both low and high RH conditions (see Figure V.7). In contrast, no accumulation is observed for the monolayer or in cases where the second water layer provides lubrication. This accumulation could occur when the entire trilayer is displaced, resulting in additional material collecting on the tip.

It is relatively straightforward to understand that at low humidity, the entire trilayer could be mobilized. However, it is surprising to observe this behavior at high RH.

One possible explanation is that at high humidity, water adsorption on the glass indenter might lead to the formation of a thin water layer, potentially reaching a thickness of approximately 1 nm [46, 44]. This water layer could interfere with the phospholipid layers hydrophobic part and disrupt the first layers, as reported in previous studies [56]. Thus, the scenario could be more complex, as depicted in Figure V.7, where the structural integrity of the layers may be significantly affected.

V.4 Conclusion

In this chapter, we developed a unique experimental setup, the triboFRAPP system, to measure friction and probe molecular motion within phospholipid layers. Through a series of velocimetry experiments, we examined both monolayer and trilayer configurations of DSPC phospholipids at varying humidity levels and shear velocities. Our results indicated that the slipping planes varied with hydration; at low humidity, friction occurred primarily in the first water layer, while at intermediate levels, it shifted to the second layer and surprisingly returned to the first layer at high humidity. We attribute this last observation to a potential disruption of the layers caused by water adsorbed on the indenter.

Chapter VI

Conclusions and perspectives

In this thesis, we present a coherent analysis of phospholipid boundary lubrication friction. Our strategy for this project focused on studying a model system in which we could precisely control hydration levels and electrostatic interactions to elucidate energy dissipation pathways in multilamellar phospholipid lubrication.

The first step involved studying the structure of supported DPPC and DPPS phospholipid trilayers and pentalayers using XR and NR. This approach provided detailed insights into the hydration of our samples, which was essential for linking structural properties to frictional behavior. In the process, we were able to investigate the physical interactions between the layers. Notably, we report an experimental measurement of the emergence of strong coupling (SC) electrostatic attraction with monovalent counterions, whereas multivalent counterions are typically considered to be required to trigger SC attraction.

In hydration water layers, where the degrees of freedom of water molecules are restricted, the dielectric constant of water decreases to the optical value, thereby enhancing electrostatic interactions. We successfully modeled the experimentally observed behaviour using a disjoining pressure model. To accurately describe the system, three key components were necessary: the SC attractive pressure, a modified hydration pressure accounting for the different hydration repulsions of PS and PC head groups, and the assumption that the dielectric permittivity of water bound to phospholipid heads reaches an optical value of approximately 2.1.

By incorporating these factors, we obtained the first estimation of the hydration correlation length, $z_{\mathrm{h,PS}}$, for PS head groups. Notably, PS head groups interact more strongly with water than PC head groups. Our collaborators from ILM (Lyon) on the project performed MD simulations on two DPPS monolayers, enabling the extraction of SLD profiles that were directly comparable to our experimental measurements. These simulation results were in excellent agreement with our experiments, further confirming our high resolution measurement.

Additionally, by applying a Landau-Ginzburg model, the simulations yielded a numerical value for the correlation length of PS head groups, $z_{\mathrm{h,PS}}$, which closely matched our experimental findings. These MD simulations confirmed the validity of our continuous model, a significant result given our sub-nanometric working distances where the continuous model might otherwise be questioned. Surprisingly, this model holds effectively even down to molecular-scale separations.

Our work also reveals that at sub-nanometric distances, physical interactions become highly correlated. Specifically, water interacts strongly with phospholipid head groups, creating repulsive forces; however, this strong interaction simultaneously reduces water's permittivity, thereby amplifying electrostatic attraction. This chapter, therefore, advances our understanding of the physics within this challenging regime where interactions are tightly interconnected.

One area that remains unclear is the counterion distribution within the water layers. According to SC theory, counterions are expected to organize themselves into a two-dimensional correlated lattice structure [84]. However, this prediction has yet to be observed experimentally. Using our model system, we aim to investigate whether counterion crystallization can indeed occur within these water layers.

In December 2024, we plan to conduct an experiment at the Sirius Beamline at SOLEIL (Paris, France) utilizing their advanced X-ray reflectivity fluorescence techniques in conjunction with GIXD and GISAXS experiments. These methods will be applied to charged DPPS layers, in which the counterions have been exchanged with Cs^+ ions. Our preliminary results suggest successful transfer of Cs^+ ions into the layers, which is a promising indication for these future experiments.

The second part (Chapter IV) of this project involved conducting friction experiments on DSPC/DPPC and DPPS trilayers. Building on the insights gained in the chapter III, we established a correlation between friction and hydration levels. Our findings demonstrate that increasing hydration reduces friction forces, underlining the critical role of hydration in lubrication.

The primary innovation in this section is that, by employing the Eyring model and incorporating the physical interactions discussed in Chapter III, particularly hydration forces, we were able to predict the friction forces of the trilayer based on hydration levels and electrostatic interactions. Additionally, we propose a hypothesis regarding the location of the slipping planes: they are situated within the two water layers.

We also addressed whether charged phospholipids enhance or reduce lubrication properties. In our experiments, the friction force increased with the addition of charged phospholipids. This behaviour aligns with our findings from Chapter III; specifically, by incorporating PS phospholipids, we strengthen hydration interactions, thereby raising the energy required to dehydrate each phospholipid and, consequently, increasing friction. In this way, we outline the energy dissipation pathways that contribute to macroscopic friction, directly linking molecular interactions to observable frictional forces.

In the last part (Chapter V), we used the TriboFRAPP setup to localize the sliding planes in DSPC trilayers. We observed that sliding planes are located within the two water layers, as predicted in Chapter IV. These experiments serve as a proof of concept for our new setup, as measuring sliding planes in nanometric films is highly challenging. The success of these initial experiments is promising for future research directions.

Our observations align with the hydration lubrication model, supporting the notion that lubrication occurs within the water layers. However, we conducted these experiments within a limited range of velocities and exclusively in the gel phase at room temperature. Attempts to perform experiments at $T > T_\mathrm{m}$ of DSPC were hindered by condensation in the setup, which prevented reliable FRAPP signal measurement. This limitation is particularly unfortunate, as friction experiments at controlled temperatures showed deviations from the Eyring model based on hydration lubrication. This suggests the possibility of an alternative energy dissipation pathway, potentially within the phospholipid tails. Tail friction could depend on phospholipid tail viscosity, which varies exponentially with temperature, making this a plausible scenario.

An initially surprising observation was that, at high humidity levels, where the second water layer was highly hydrated, we observed sliding within the first layer. We hypothesize that this may be due to disruption of the layer caused by water adsorption on the tip. A potential way to confirm this hypothesis would be to perform symmetric friction experiments, where a monolayer or trilayer would also be deposited on the tip.

Another interesting experiment to bring this model closer to biological systems would be to conduct TriboFRAPP experiments on double-bilayer systems or even on systems made more complex by adding HA or lubricin.

We conclude this thesis by discussing the biological significance of our findings. Effective lubrication in phospholipid layers requires a balance between load resistance and energy dissipation pathway, giving a low friction coefficient. Our study reveals that the lubrication mechanism in our model system operates through the dehydration of phospholipids, which is closely related to the hydration correlation length, z_h. A larger correlation length enhances the repulsive hydration force, thus increasing load resistance. However, this also raises the energetic cost required to dehydrate a phospholipid, increasing friction.

Given that we found significant differences in z_h values between PS and PC head groups, it is plausible that nature has evolved to find an optimal PS-to-PC ratio to maximize load resistance without excessively increasing friction. This balance may be key in biological systems to achieve efficient lubrication under varying physiological conditions.

Chapter VII

Résumé en français

VII.1 Introduction et motivations

Les membranes lipidiques jouent un rôle fondamental dans le fonctionnement des systèmes biologiques. Elles compartimentent et protègent le matériel génétique au niveau cellulaire et assurent la lubrification des surfaces biologiques soumises à des frottements. Au cours de l'évolution, la nature a mis au point un lubrifiant d'une efficacité remarquable [9], encore inégalée par les lubrifiants industriels dérivés du pétrole.

Un aspect unique de la lubrification biologique est l'utilisation de l'eau. Cela est surprenant, car l'eau, en raison de sa faible viscosité, ne semble pas être un lubrifiant idéal. L'astuce réside dans le confinement de l'eau ; il s'agit ici d'eau nanoconfinée entre les couches de phospholipides [93], présentant des propriétés physiques très différentes de celles de l'eau en volume [92, 91].

Pour comprendre l'efficacité de ce lubrifiant biologique, il est crucial d'étudier les interactions entre les couches de phospholipides via l'eau confinée. L'eau hydrate les têtes polaires des phospholipides, limitant ainsi considérablement le degré de liberté des molécules d'eau [91]. Par conséquent, les interactions électrostatiques entre les couches de phospholipides sont amplifiées, car l'eau d'hydratation n'écrante plus ces interactions.

En présence d'eau confinée, ces interactions peuvent générer des forces de répulsion ou d'attraction [83, 84, 90], ce qui influence directement les propriétés de friction. Comprendre comment l'équilibre de ces forces contribue à la résistance à la pression ainsi qu'à la dissipation d'énergie lors du cisaillement des couches lipidiques est essentiel pour élucider les mécanismes de lubrification.

L'objectif de cette thèse est de relier les interactions physiques, notamment les forces d'hydratation et les interactions électrostatiques, aux propriétés de friction des films lipidiques. Nous cherchons à identifier les mécanismes précis et les lieux de dissipation de l'énergie lors du glissement sur des couches lipidiques. Pour cela, notre stratégie repose sur l'étude d'un système modèle composé de couches de phospholipides déposées sur un substrat solide.

Le projet de thèse s'articule autour de trois axes principaux :

1. Étude de la structure des couches lipidiques en utilisant la réflectivité des neutrons et des rayons X. L'objectif est de comprendre les forces physiques à l'œuvre dans les couches de phospholipides chargées.

2. Analyse de la friction des couches de phospholipides. Cette partie vise à corréler les résultats de l'analyse structurelle obtenus par réflectivité avec les propriétés de friction macroscopique.

3. Développement d'un dispositif expérimental (triboFRAPP) permettant de

coupler des mesures de friction avec de la vélocimétrie, afin d'identifier précisément les plans de glissement.

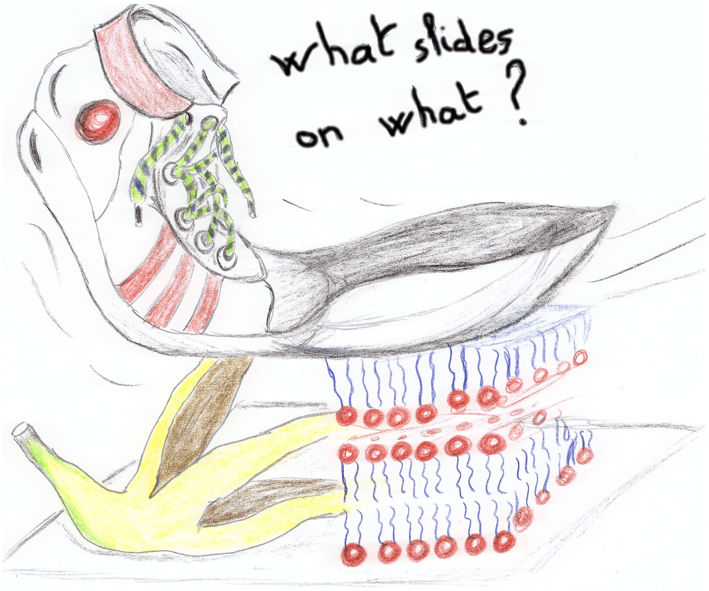

Figure VII.1: Schéma représentant l'identité du projet. Il fait l'analogie entre le frottement d'une chaussure sur une peau de banane et la friction des couches de lipides. La question est de savoir si la chaussure glisse sur la peau de banane ou si la banane glisse sur le sol. Pour notre système, il s'agit de déterminer si le glissement se produit dans la couche d'eau ou entre les chaînes des phospholipides. Dessin réalisé par Thierry Charitat et utilisé avec son accord.

Ce travail s'inscrit dans le cadre d'un projet ANR mené en collaboration avec une équipe de l'Institut Lumière Matière à Lyon et notre équipe à l'Institut Charles Sadron à Strasbourg. Nos collaborateurs se concentrent sur des simulations numériques des couches de phospholipides. Dans ce qui suit, nous présenterons le travail expérimental réalisé durant ma thèse.

VII.2 Étude de la structure des couches lipidiques chargées

Dans ce premier axe de recherche, nous avons étudié les interactions électrostatiques entre des couches de phospholipides chargés. Nous avons contrôlé la densité de charge surfacique σ_S en modulant la proportion de deux phospholipides : le DPPS, chargé négativement, et le DPPC, neutre [59].

La géométrie singulière de notre système a permis de sonder les interactions entre ces couches de phospholipides. Situé à l'interface air/solide, le système est soumis à une forte pression osmotique, résultant de l'équilibre entre les films d'eau et la vapeur d'eau [44]. Cette pression s'ajoute à la pression de disjonction, c'est-à-dire à la pression issue des interactions physiques entre les couches. Un des avantages de la pression osmotique est qu'elle peut être contrôlée en modulant l'humidité relative (RH). Nous avons mesuré la variation de l'épaisseur de la deuxième couche d'eau d_{w2} (voir Figure VII.2) pour différentes valeurs de RH ainsi que pour divers mélanges. Ces résultats ont ensuite été comparés à des modèles théoriques.

La géométrie plane de cet échantillon facilite la comparaison entre les données expérimentales et les modèles théoriques. Pour modéliser le comportement de d_{w2}, en fonction de la RH et de la densité surfacique de charge, trois contributions sont prises en compte : la pression osmotique mentionnée précédemment, la répulsion d'hydratation due aux interactions spécifiques entre les molécules d'eau et les têtes polaires des phospholipides, et l'attraction électrostatique de couplage fort, résultant des corrélations entre les contre-ions présents dans le film d'eau. Nous avons pu décrire le comportement de notre système avec seulement deux paramètres d'ajustement : la longueur

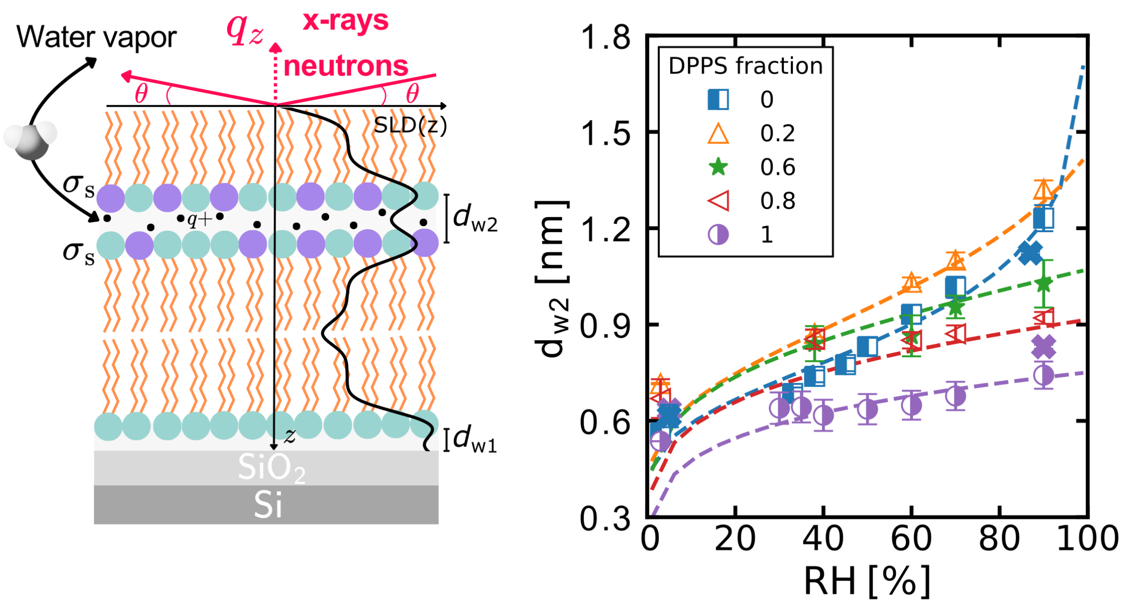

Figure VII.2: (Gauche) Schéma d'une tricouche de phospholipides chargés, illustrant un mélange de DPPS (têtes violettes) et de DPPC (têtes bleues) avec une densité de charge surfacique négative σ_S. Les têtes de DPPS sont associées à des contre-ions représentés par des points noirs. Les faisceaux incidents et réfléchis spéculaires sont représentés en rouge, avec $q_z = 4\pi/\lambda \sin\theta$ comme vecteur de transfert. La densité de longueur de diffusion (SLD) est obtenue en ajustant les profils de réflectivité spéculaire. Les deux épaisseurs des couches d'eau, d_{w1} et d_{w2}, sont également indiquées. (Droite) Variation de d_{w2} pour différentes humidités relatives et différents mélanges.

caractéristique de décroissance $z_{h,PS}$ associée aux lipides chargés (DPPS) et la pression d'hydratation $P_{0h,PS}$. Si ces deux constantes sont bien établies pour le DPPC, elles n'avaient pas encore été mesurées pour le DPPS. Nous avons déterminé que $z_{h,PS}$ est deux fois plus grand pour le DPPS que pour le DPPC, ce qui traduit une répulsion d'hydratation accrue pour les lipides à tête PS.

Un point clé du cadre théorique concerne la permittivité de l'eau. Pour expliquer l'attraction électrostatique observée expérimentalement, il est nécessaire d'invoquer une réduction de la constante diélectrique de l'eau d'hydratation due à la restriction de ses degrés de liberté. L'étude pionnière de Fumagalli et al. [92] propose un modèle de capacité en série, distinguant l'eau proche de l'interface (avec une permittivité proche de la valeur optique) de l'eau libre, qui se comporte comme en volume. Notre innovation réside dans l'établissement d'un lien entre l'épaisseur de cette couche d'eau et la longueur caractéristique de décroissance z_h des lipides.

En conclusion, pour décrire les interactions dans un mélange de phospholipides, il est essentiel de considérer à la fois la variation de densité de charge surfacique et la répulsion d'hydratation.

Ainsi, ce chapitre a un double intérêt : il permet une caractérisation complète de la structure des couches de lipides, pour comparaison avec des expériences de friction, et offre une analyse détaillée de l'équilibre entre attraction électrostatique de couplage fort et répulsion d'hydratation dans l'eau nanoconfinée entre les couches de phospholipides chargées.

Ce premier axe de recherche a également servi de point de départ à nos collaborateurs pour des simulations de couches de phospholipides chargés. En utilisant un système analogue, où ils contrôlent le taux d'hydratation des couches, ils ont obtenu une structure en accord remarquable avec nos résultats expérimentaux. Ces simulations ont permis de déterminer numériquement la valeur de $z_\mathrm{h,PS}$, en accord quantitatif avec notre mesure. Cette comparaison expérimentation/simulation renforce la fiabilité de nos conclusions.

VII.3 Étude de la friction

Dans ce chapitre, nous explorons les propriétés tribologiques des empilement de couches de phospholipides, en s'appuyant sur les connaissances développées dans le chapitre précédent sur les interactions physiques entre couches de phospholipides zwitterioniques et chargées. L'objectif principal est de relier ces interactions à la friction macroscopique, une démarche innovante dans le domaine de la tribologie. Alors que la friction est bien comprise au niveau macroscopique, établir un lien direct avec les interactions moléculaires reste un défi majeur.

Nous avons premièrement utilisé des tricouches de phospholipides neutres (DPPC, DSPC) déposées sur un substrat en verre. Nous avons mesuré la force tangentielle, c.-à-d., la force de friction entre notre échantillon et un indenteur en verre sphérique (rayon de courbure $R = 0.051$ m) en contrôlant l'humidité et ainsi l'épaisseur de la deuxième couche d'eau d_{w2}. Les expériences montrent que l'hydratation joue un rôle clé dans la lubrification des phospholipides, où la modulation de l'épaisseur d'eau permet de réduire considérablement la force de friction (voir Figure VII.3).

Bien que révélatrices de l'importance de l'eau dans la biolubrification, ces expériences restent insatisfaisantes du point de vue d'un physicien. Pour relier le taux d'hydratation des couches de lipides à leurs propriétés tribologiques, nous avons utilisé le modèle d'Eyring, que nous avons adapté à notre système. Ce modèle décrit la friction comme le passage à travers des puits de potentiel : chaque lipide est piégé dans un puits, et sous l'application d'une contrainte de cisaillement, l'énergie Q correspondant à la hauteur du puits de potentiel est réduite par le travail de la force de friction.

Ce type de modèle est généralement bien adapté pour décrire la lubrification par des films nanométriques. Habituellement, il est nécessaire d'ajuster les données expérimentales avec plusieurs paramètres. Dans notre cas, nous avons pu déduire ces paramètres directement à partir de l'analyse de réflectivité. En particulier, pour l'énergie Q, nous avons montré qu'elle pouvait être interprétée comme l'énergie associée à la déshydratation des têtes des phos-

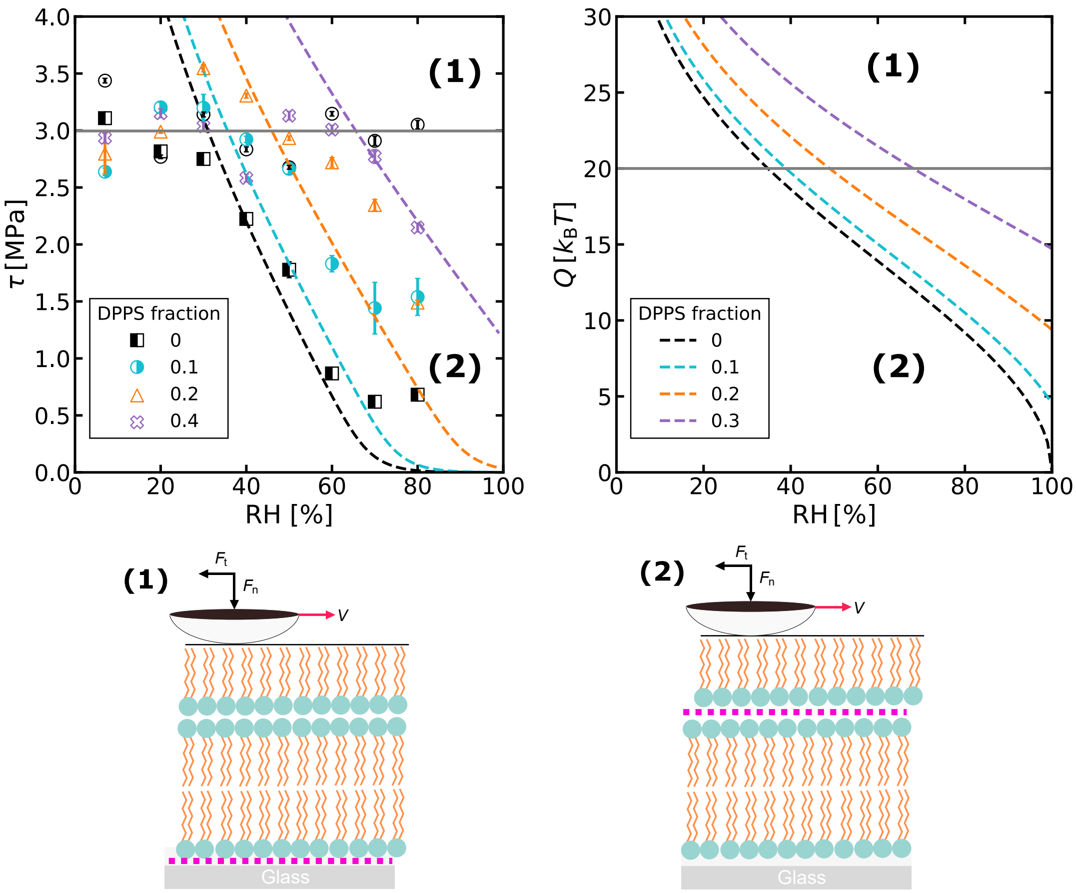

Figure VII.3: (En haut à gauche) Variation du taux de cisaillement $\tau = F_t/A$, où F_t est la force de friction et A l'aire de contact, en fonction de la fraction de DPPS et de l'humidité relative (RH). Les marqueurs en forme de cercle noir vide correspondent à une monocouche de DSPC. Les autres marqueurs correspondent à des tricouches de mélange DPPC/DPPS (seulement la deuxième et troisième couche). Les lignes pointillées correspondent à la prédiction du modèle d'Eyring sans ajustement. (En haut à droite) Valeur de la barrière d'énergie Q utilisée dans le modèle d'Eyring. (En bas) Prédiction des plans de glissement pour les tricouches.

pholipides.

Une question centrale de ma thèse était de déterminer si les phospholipides chargés (DPPS) avaient un effet positif ou négatif sur la lubrification. L'énergie nécessaire pour déshydrater la tête des phospholipides dépend directement de la longueur caractéristique de décroissance z_h. Par conséquent, le DPPS devrait augmenter Q, ce que nos expériences confirment. En effet, en augmentant la proportion de phospholipides chargés, nous observons une augmentation de la force de friction, comme représenté en Figure VII.3.

Pour des systèmes fortement chargés, la force de friction est indépendante de l'humidité relative (RH) et de la fraction de DPPS dans nos couches. Ce comportement est similaire à celui d'une monocouche de phospholipides neutres. Nous interprétons ce phénomène comme un changement de plan de glissement, passant de la deuxième à la première couche d'eau entre le substrat et les phospholipides. Lorsque l'énergie de déshydratation des phospholipides des deuxième et troisième couches devient supérieure à celle de la première couche, le glissement se produit dans la première couche.

VII.4 Localisation des plans de glissements

Cette section présente le développement et l'utilisation du dispositif triboFRAPP, conçu pour mesurer la friction et analyser les mouvements moléculaires dans les couches de phospholipides. L'objectif principal était de comprendre la localisation des plans de glissement en fonction des conditions d'humidité relative (RH) et des vitesses de cisaillement.

Le système initial a été modifié pour améliorer la stabilité face aux variations de température, grâce à un interféromètre symétrique utilisant des cellules de Pockels. Ces optimisations ont éliminé les dérives liées aux variations thermiques et ont permis de détecter avec précision les mouvements d'une couche fluorescente de phospholipides.

Le dispositif repose sur le photoblanchiment des molécules fluorescentes, ici des phospholipides marqués par le fluorophore NBD.

Les expériences de velocimétrie ont montré que dans une monocouche de DSPC :

- Le glissement s’effectue dans la première couche d’eau, même à différents niveaux d’humidité relative.
- Les forces de friction restent constantes, validant que les marquages fluorescents n’altèrent pas les propriétés tribologiques.

Les expériences sur les tricouches ont révélé que :

- À faible humidité (RH < 30 %), le glissement se produit dans la première couche d’eau, comme pour les monocouches.
- À une humidité intermédiaire (30 % < RH < 70 %), le glissement migre vers la deuxième couche d’eau, où la friction diminue en raison d’une moindre énergie nécessaire à la déshydratation.
- À forte humidité (RH > 70 %), le glissement revient à la première couche d’eau, un phénomène surprenant, possiblement lié à une adsorption d’eau sur l’indenteur perturbant la structure des couches.

Les mesures de vélocimétrie sont corroborées par des images de microscopie montrant une accumulation de matériau sur la pointe de l’indenteur. À faible humidité et à forte humidité, elles montrent une accumulation significative de matériau, suggérant une mobilisation complète de la tricouche. À une humidité intermédiaire, en revanche, peu d’accumulation est observée, ce qui pourrait indiquer une mobilisation limitée à la troisième couche uniquement.

VII.5 Conclusion

Cette thèse présente une analyse des mécanismes de lubrification des couches de phospholipides, en explorant les relations entre hydratation et interactions électrostatiques

Première partie : Nous avons étudié la structure des tricouches et pentacouches de phospholipides (DPPC/DPPS) par réflectivité des rayons X et des neutrons. Nous avons mis en évidence l'attraction électrostatique en régime de strong coupling (SC) avec des contre-ions monovalents, et avons modélisé ce phénomène à l'aide d'un modèle de pression de disjonction intégrant l'effet de la faible permittivité de l'eau d'hydratation. Nos travaux ont permis une estimation expérimentale de la longueur caractéristique de décroissance $z_{\mathrm{h,PS}}$ du DPPS, confirmée par des simulations de dynamique moléculaire.

Deuxième partie : Les expériences de friction ont montré que l'hydratation module les forces de friction et que la friction dépend de l'énergie de déshydration de phospholipides. L'ajout de phospholipides chargés (DPPS) augmente la friction en renforçant les interactions d'hydratation. Nous pouvons comprendre nos résultats en faisant l'hypothèse d'une localisation des plans de glissement dans les différentes couches d'eau.

Dernière partie : Avec un nouveau dispositif (TriboFRAPP), nous avons pu localiser les plans de glissement dans des tricouches DSPC. Ces expériences confirment que la lubrification se produit dans les couches d'eau. Cependant, à haute humidité, un glissement inattendu dans la première couche d'eau a été observé, possiblement dû à une perturbation causée par l'adsorption d'eau sur la pointe.

Enfin, nos résultats suggèrent que dans les systèmes biologiques, un équilibre entre charge (résistance à la charge) et dissipation d'énergie est nécessaire pour minimiser la friction. La différence entre les longueurs caractéristiques de décroissances des têtes PS et PC pourrait expliquer un ratio optimal PS/PC dans les systèmes biologiques pour une lubrification efficace.

Appendix A

AFM on supported trilayer

Atomic Force Microscopy image of a DPPS(60%)/DPPC(40%) trilayer at RH= 30% (ICS, Christophe Contal). No inhomogeneity can be seen, which could be the signature of a phase separation.

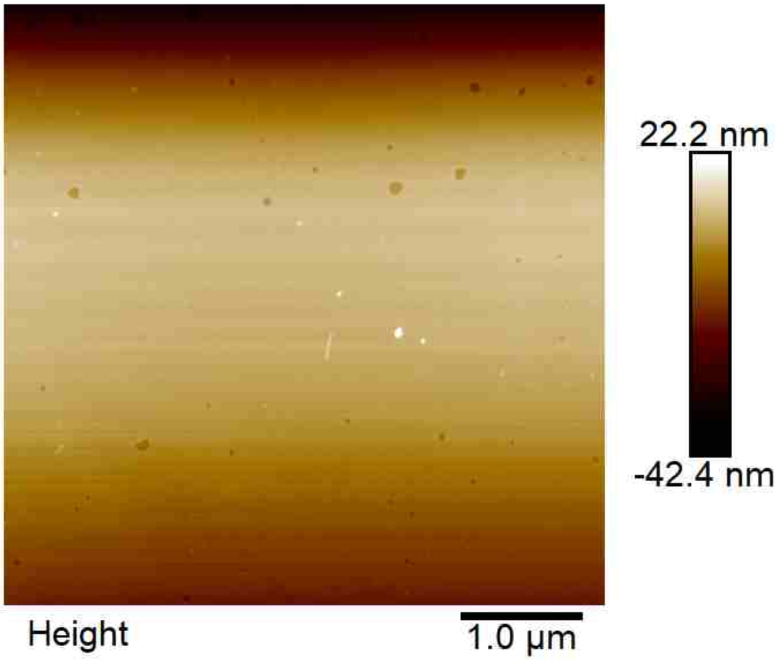

Figure A.1: AFM image of supported trilayer (DPPS(60%) and DPPC(40%)) showing no phase transition (image taken by Christophe Contal, ICS).

Appendix B

Neutron reflectivity

This appendix presents the Neutron reflectivity data measured at ILL (D17) for all samples investigated in this work:

1. a pure DPPC trilayer (Trilayer DPPC), section B.1;
2. a trilayer made of a first DPPC monolayer and two layers composed of 20% DPPS and 80% DPPC (Trilayer PS(20%)-PC(80%)), section B.3;
3. a trilayer made of a first DPPC monolayer and two layers composed of 60% DPPS and 40% DPPC (Trilayer PS(60%)-PC(40%)), section B.4;
4. a pentalayer made of a first DPPC monolayer and four layers composed of 70% DPPS and 30% DPPC (Pentalayer PS(70%)-PC(30%)), section B.5;
5. a pentalayer made of a first DPPC monolayer and four layers composed of 80% DPPS and 20% DPPC (Pentalayer PS(80%)-PC(20%)), section B.6.

For each sample, we display in the first section *Data and best fits* the reflectivity curves, using the Rq^4 representation. The color scale corresponds to the various RH imposed. Lines represent the best fit, using D_2O (solid lines) and/or H_2O (dashed lines) contrasts.

The corresponding neutron SLD profiles are displayed in the section *SLD profiles*. The origin of z axis is placed at the interface between air and the tail part of the third monolayer. The evolution of the overall thickness with RH can be seen in the progressive shift to the right of the last interface between the SiO_2 layer and bulk silicon when RH is increased. The same RH dependent color scale as for the reflectivity data is used.

Finally, the parameters of the double contrast fit for different RH values forthe different samples are given in tables regrouped in section *Fitted parameters*. Several parameters are coupled, as can be seen from the fact that exactly the same values are obtained. Some parameters are fixed (not fitted). They can be easily detected because they have no associated uncertainties.

B.1 Trilayer DPPC

B.1.A Data and best fits-Trilayer DPPC

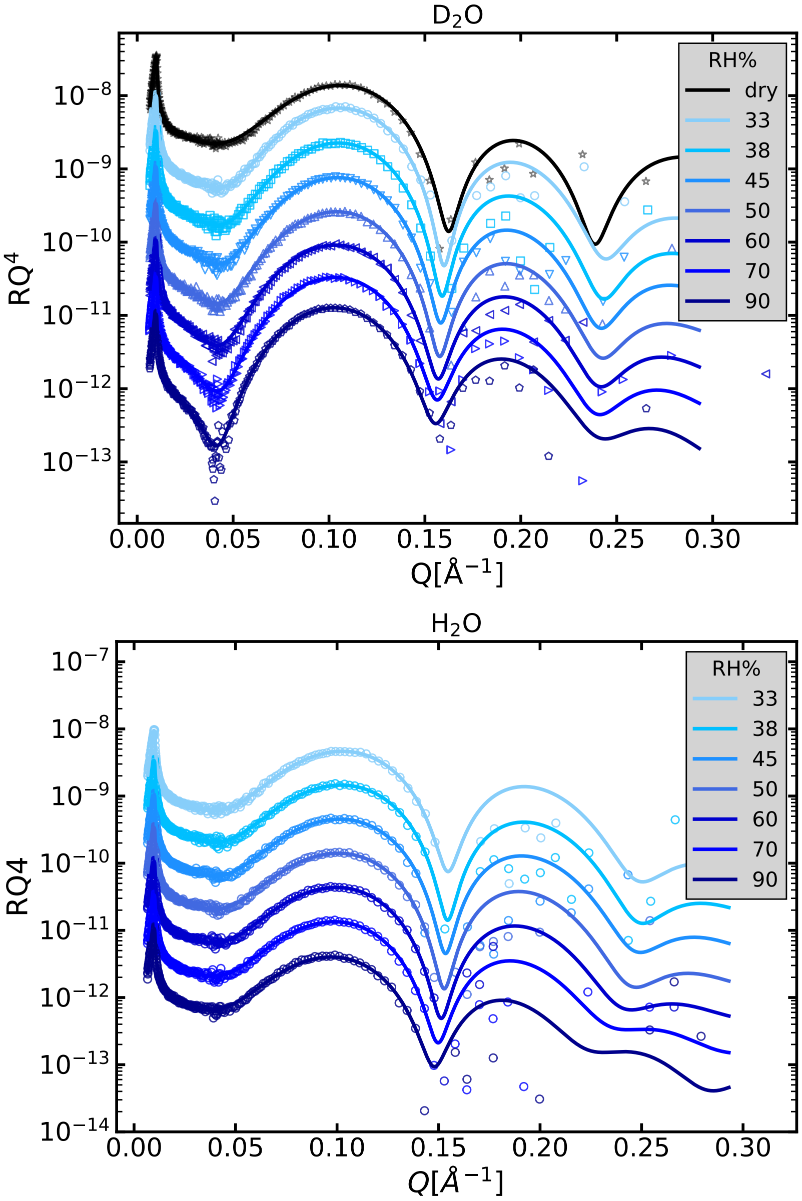

Figure B.1: NR data of pure DPPC trilayer are presented as Rq_z^4 on a semilog scale with two contrasts (top: D_2O and bottom: H_2O). Solid lines represent the best fits corresponding to the SLD_n profiles.

B.1.B SLD profiles-Trilayer DPPC

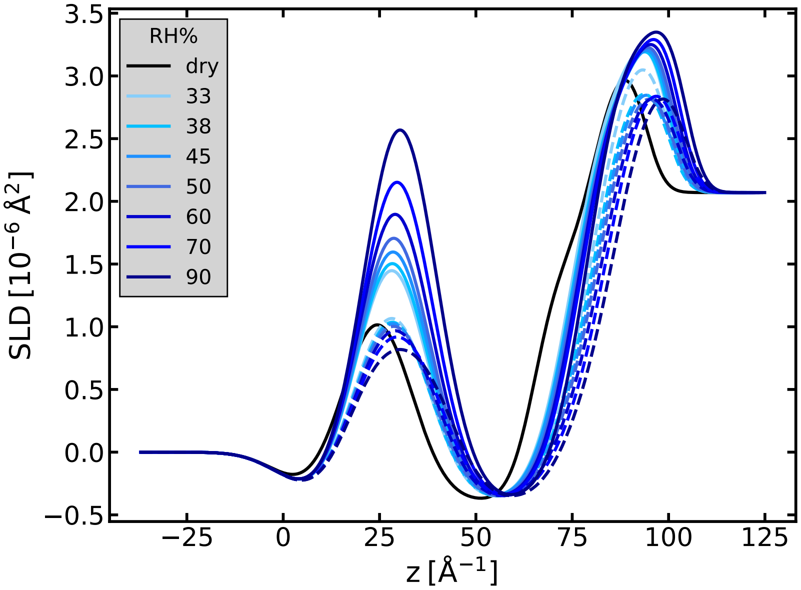

Figure B.2: SLD profiles for NR obtained by combined fitting of reflectivity data for two contrasts (see Figure B.1).

B.1.C Fitted parameters-Trilayer DPPC

B.1.C.i Trilayer DPPC (HR=5%)

RH=05 %

Slab	Thickness (Å)	SLD (x10^{-6} Å^{-2})	Roughness (Å)	vfsolv (%)
Air	0.0	0.0	0.0	0.0
tail	17.42 +/- 0.05	-0.39	7.87 +/- 0.12	0.0
head PC	6.76 +/- 0.02	1.88	7.87 +/- 0.12	0.38
H2O	0.49 +/- 0.3	-0.56	7.87 +/- 0.12	0.0
head PC	6.76 +/- 0.02	1.88	7.87 +/- 0.12	0.38
tail	17.42 +/- 0.05	-0.39	7.87 +/- 0.12	0.0
tail	17.42 +/- 0.05	-0.39	5.61 +/- 0.28	0.0
head PC	6.76 +/- 0.02	1.88	5.61 +/- 0.28	0.44 +/- 0.07
H2O	3.91 +/- 0.11	-0.56	5.61 +/- 0.28	0.0
SiO2	16.9	3.41	6.9	0.13
Si	0.0	2.07	3.9	0.0

Table B.1: Best fitted parameters: DPPC trilayer at HR=5%

B.1.C.ii Trilayer DPPC (HR=33%)

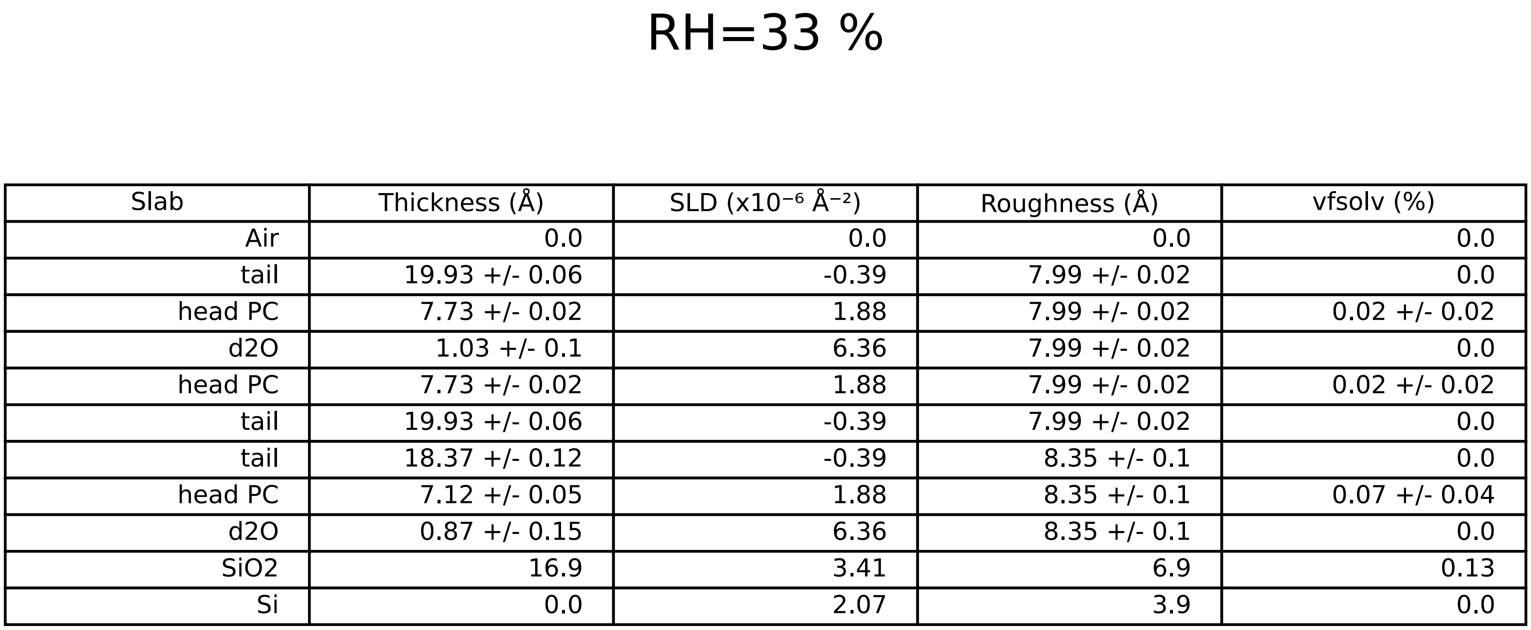

RH=33 %

Slab	Thickness (Å)	SLD (x10^{-6} Å^{-2})	Roughness (Å)	vfsolv (%)
Air	0.0	0.0	0.0	0.0
tail	19.93 +/- 0.06	-0.39	7.99 +/- 0.02	0.0
head PC	7.73 +/- 0.02	1.88	7.99 +/- 0.02	0.02 +/- 0.02
d2O	1.03 +/- 0.1	6.36	7.99 +/- 0.02	0.0
head PC	7.73 +/- 0.02	1.88	7.99 +/- 0.02	0.02 +/- 0.02
tail	19.93 +/- 0.06	-0.39	7.99 +/- 0.02	0.0
tail	18.37 +/- 0.12	-0.39	8.35 +/- 0.1	0.0
head PC	7.12 +/- 0.05	1.88	8.35 +/- 0.1	0.07 +/- 0.04
d2O	0.87 +/- 0.15	6.36	8.35 +/- 0.1	0.0
SiO2	16.9	3.41	6.9	0.13
Si	0.0	2.07	3.9	0.0

Table B.2: Best fitted parameters: DPPC trilayer at at HR=33%

B.1.C.iii Trilayer DPPC (HR=38%)

RH=38 %

Slab	Thickness (Å)	SLD ($x10^{-6}$ Å^{-2})	Roughness (Å)	vfsolv (%)
Air	0.0	0.0	0.0	0.0
tail	19.97 +/- 0.03	-0.39	7.99 +/- 0.02	0.0
head PC	7.75 +/- 0.01	1.88	7.99 +/- 0.02	0.02 +/- 0.01
d2O	1.19 +/- 0.05	6.36	7.99 +/- 0.02	0.0
head PC	7.75 +/- 0.01	1.88	7.99 +/- 0.02	0.02 +/- 0.01
tail	19.97 +/- 0.03	-0.39	7.99 +/- 0.02	0.0
tail	18.42 +/- 0.06	-0.39	8.49 +/- 0.11	0.0
head PC	7.14 +/- 0.02	1.88	8.49 +/- 0.11	0.01 +/- 0.01
d2O	0.84 +/- 0.09	6.36	8.49 +/- 0.11	0.0
SiO2	16.9	3.41	6.9	0.13
Si	0.0	2.07	3.9	0.0

Table B.3: Best fitted parameters: DPPC trilayer at HR=38%

B.1.C.iv Trilayer DPPC (HR=45%)

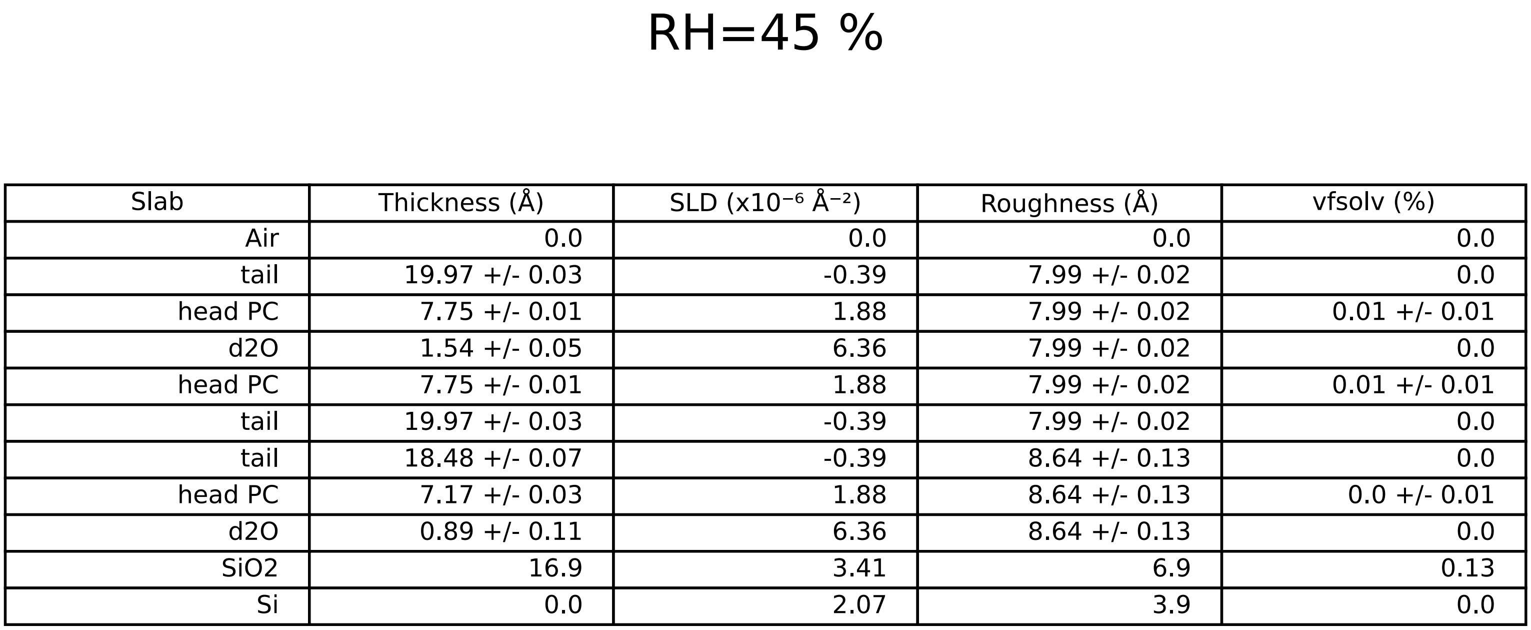

RH=45 %

Slab	Thickness (Å)	SLD (x10^{-6} Å^{-2})	Roughness (Å)	vfsolv (%)
Air	0.0	0.0	0.0	0.0
tail	19.97 +/- 0.03	-0.39	7.99 +/- 0.02	0.0
head PC	7.75 +/- 0.01	1.88	7.99 +/- 0.02	0.01 +/- 0.01
d2O	1.54 +/- 0.05	6.36	7.99 +/- 0.02	0.0
head PC	7.75 +/- 0.01	1.88	7.99 +/- 0.02	0.01 +/- 0.01
tail	19.97 +/- 0.03	-0.39	7.99 +/- 0.02	0.0
tail	18.48 +/- 0.07	-0.39	8.64 +/- 0.13	0.0
head PC	7.17 +/- 0.03	1.88	8.64 +/- 0.13	0.0 +/- 0.01
d2O	0.89 +/- 0.11	6.36	8.64 +/- 0.13	0.0
SiO2	16.9	3.41	6.9	0.13
Si	0.0	2.07	3.9	0.0

Table B.4: Best fitted parameters: DPPC trilayer at HR=45%

B.1.C.v Trilayer DPPC (HR=50%)

RH=50 %

Slab	Thickness (Å)	SLD (x10^{-6} Å^{-2})	Roughness (Å)	vfsolv (%)
Air	0.0	0.0	0.0	0.0
tail	19.97 +/- 0.03	-0.39	7.99 +/- 0.01	0.0
head PC	7.75 +/- 0.01	1.88	7.99 +/- 0.01	0.01 +/- 0.0
d2O	1.94 +/- 0.05	6.36	7.99 +/- 0.01	0.0
head PC	7.75 +/- 0.01	1.88	7.99 +/- 0.01	0.01 +/- 0.0
tail	19.97 +/- 0.03	-0.39	7.99 +/- 0.01	0.0
tail	18.44 +/- 0.06	-0.39	8.41 +/- 0.09	0.0
head PC	7.15 +/- 0.02	1.88	8.41 +/- 0.09	0.0 +/- 0.01
d2O	1.14 +/- 0.08	6.36	8.41 +/- 0.09	0.0
SiO2	16.9	3.41	6.9	0.13
Si	0.0	2.07	3.9	0.0

Table B.5: Best fitted parameters: DPPC trilayer at HR=50%

B.1.C.vi Trilayer DPPC (HR=60%)

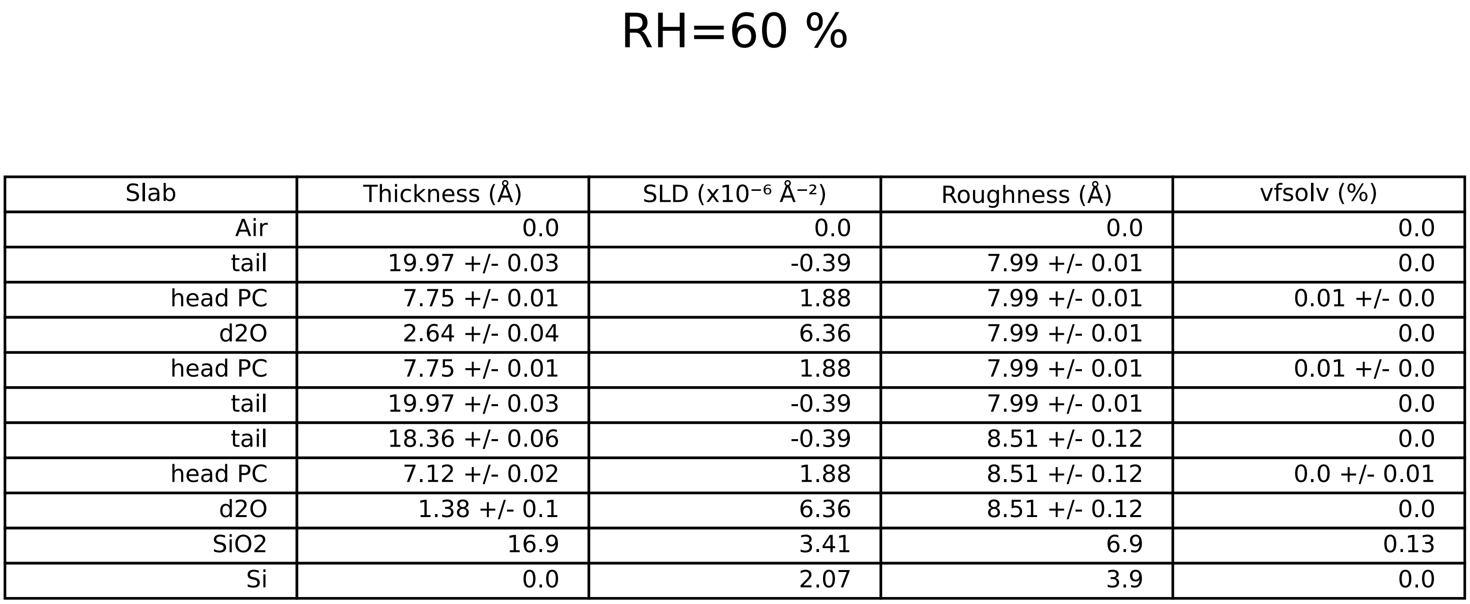

RH=60 %

Slab	Thickness (Å)	SLD (x10^{-6} Å^{-2})	Roughness (Å)	vfsolv (%)
Air	0.0	0.0	0.0	0.0
tail	19.97 +/- 0.03	-0.39	7.99 +/- 0.01	0.0
head PC	7.75 +/- 0.01	1.88	7.99 +/- 0.01	0.01 +/- 0.0
d2O	2.64 +/- 0.04	6.36	7.99 +/- 0.01	0.0
head PC	7.75 +/- 0.01	1.88	7.99 +/- 0.01	0.01 +/- 0.0
tail	19.97 +/- 0.03	-0.39	7.99 +/- 0.01	0.0
tail	18.36 +/- 0.06	-0.39	8.51 +/- 0.12	0.0
head PC	7.12 +/- 0.02	1.88	8.51 +/- 0.12	0.0 +/- 0.01
d2O	1.38 +/- 0.1	6.36	8.51 +/- 0.12	0.0
SiO2	16.9	3.41	6.9	0.13
Si	0.0	2.07	3.9	0.0

Table B.6: Best fitted parameters: DPPC trilayer at HR=60%

B.1.C.vii Trilayer DPPC (HR=70%)

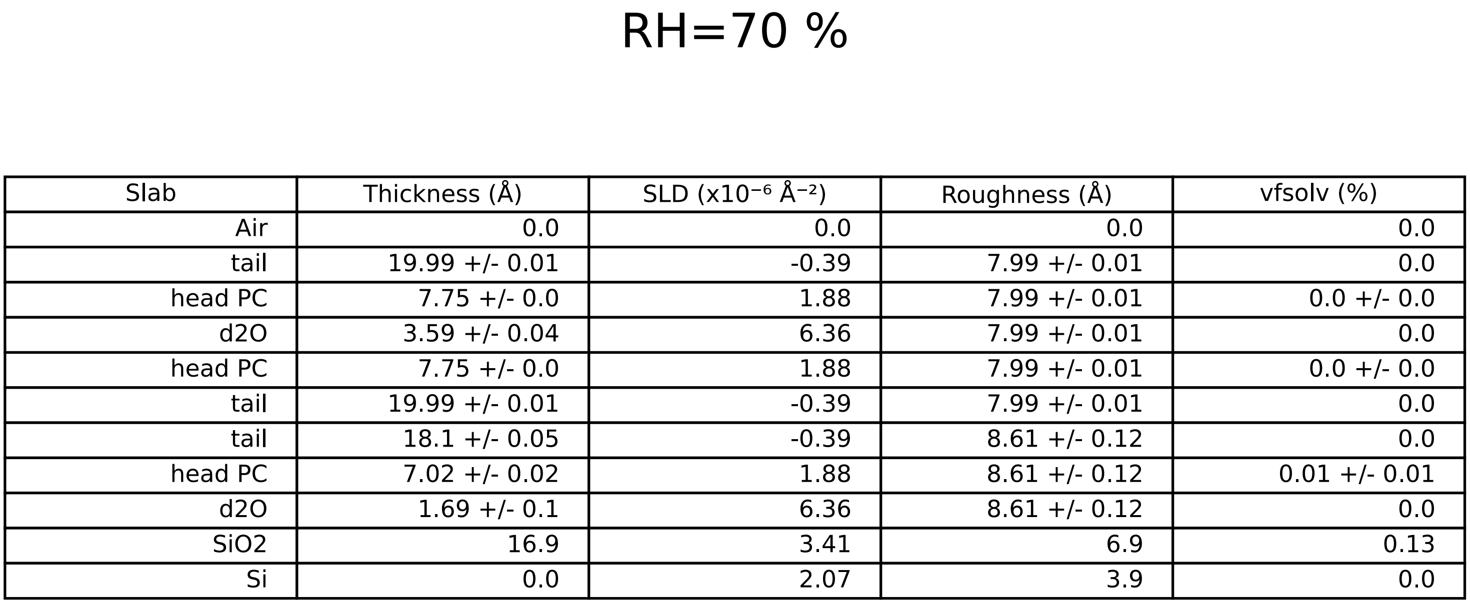

RH=70 %

Slab	Thickness (Å)	SLD (x10^{-6} Å^{-2})	Roughness (Å)	vfsolv (%)
Air	0.0	0.0	0.0	0.0
tail	19.99 +/- 0.01	-0.39	7.99 +/- 0.01	0.0
head PC	7.75 +/- 0.0	1.88	7.99 +/- 0.01	0.0 +/- 0.0
d2O	3.59 +/- 0.04	6.36	7.99 +/- 0.01	0.0
head PC	7.75 +/- 0.0	1.88	7.99 +/- 0.01	0.0 +/- 0.0
tail	19.99 +/- 0.01	-0.39	7.99 +/- 0.01	0.0
tail	18.1 +/- 0.05	-0.39	8.61 +/- 0.12	0.0
head PC	7.02 +/- 0.02	1.88	8.61 +/- 0.12	0.01 +/- 0.01
d2O	1.69 +/- 0.1	6.36	8.61 +/- 0.12	0.0
SiO2	16.9	3.41	6.9	0.13
Si	0.0	2.07	3.9	0.0

Table B.7: Best fitted parameters: DPPC trilayer at HR=70%

B.1.C.viii Trilayer DPPC (HR=90%)

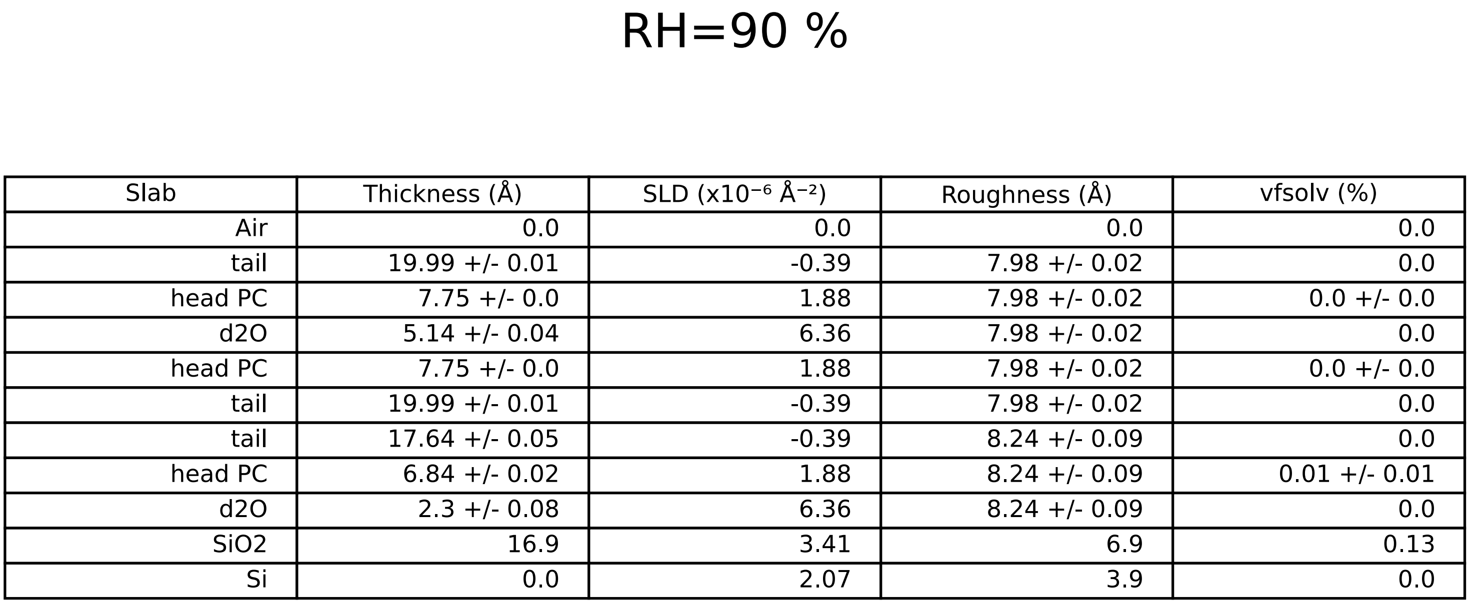

RH=90 %

Slab	Thickness (Å)	SLD (x10^{-6} Å^{-2})	Roughness (Å)	vfsolv (%)
Air	0.0	0.0	0.0	0.0
tail	19.99 +/- 0.01	-0.39	7.98 +/- 0.02	0.0
head PC	7.75 +/- 0.0	1.88	7.98 +/- 0.02	0.0 +/- 0.0
d2O	5.14 +/- 0.04	6.36	7.98 +/- 0.02	0.0
head PC	7.75 +/- 0.0	1.88	7.98 +/- 0.02	0.0 +/- 0.0
tail	19.99 +/- 0.01	-0.39	7.98 +/- 0.02	0.0
tail	17.64 +/- 0.05	-0.39	8.24 +/- 0.09	0.0
head PC	6.84 +/- 0.02	1.88	8.24 +/- 0.09	0.01 +/- 0.01
d2O	2.3 +/- 0.08	6.36	8.24 +/- 0.09	0.0
SiO2	16.9	3.41	6.9	0.13
Si	0.0	2.07	3.9	0.0

Table B.8: Best fitted parameters: DPPC trilayer at HR=90%

B.2 Trilayer DPPS(100%)

B.2.A Data and best fits-Trilayer DPPS(100%)

Data and best fits are shown in Figure III.2 of the main document.

B.2.B SLD profiles-Trilayer DPPS(100%)

SLD are shown in Figure III.3 of the main document.

B.2.C Fitted parameters-Trilayer DPPS(100%)

B.2.C.i Trilayer DPPS (HR=3%)

RH=3 %

Slab	Thickness (Å)	SLD (x10^{-6} Å^{-2})	Roughness (Å)	vfsolv (%)
Air	0.0	0.0	0.0	0.0
tail	18.79 +/- 0.06	-0.39	6.88 +/- 0.07	0.0
head PS	7.06 +/- 0.02	2.63	6.88 +/- 0.07	0.33
d2O	0.0	6.36	6.88 +/- 0.07	0.0
head PS	7.06 +/- 0.02	2.63	6.88 +/- 0.07	0.33
tail	18.79 +/- 0.06	-0.39	6.88 +/- 0.07	0.0
tail	18.69 +/- 0.1	-0.39	7.99 +/- 0.01	0.0
head PC	7.25 +/- 0.04	1.88	7.99 +/- 0.01	0.0 +/- 0.0
d2O	0.0 +/- 0.0	6.36	7.99 +/- 0.01	0.0
SiO2	16.9	3.41	6.9	0.13
Si	0.0	2.07	3.9	0.0

Table B.9: Best fitted parameters: DPPS trilayer at HR=3%

B.2.C.ii Trilayer DPPS (HR=30%)

RH=30 %

Slab	Thickness (Å)	SLD (x10^{-6} Å^{-2})	Roughness (Å)	vfsolv (%)
Air	0.0	0.0	0.0	0.0
tail	19.22 +/- 0.95	-0.39	5.21 +/- 0.13	0.0
head PS	7.22	2.63	5.21 +/- 0.13	0.33
d2O	0.91 +/- 0.49	6.36	5.21 +/- 0.13	0.0
head PS	7.22	2.63	5.21 +/- 0.13	0.33
tail	19.22 +/- 0.95	-0.39	5.21 +/- 0.13	0.0
tail	17.83 +/- 1.27	-0.39	6.93 +/- 0.42	0.0
head PC	6.91	1.88	6.93 +/- 0.42	0.0 +/- 0.38
d2O	0.03 +/- 1.97	6.36	6.93 +/- 0.42	0.0
SiO2	16.9	3.41	6.9	0.13
Si	0.0	2.07	3.9	0.0

Table B.10: Best fitted parameters: DPPS trilayer at at HR=30%

B.2.C.iii Trilayer DPPS (HR=35%)

RH=35 %

Slab	Thickness (Å)	SLD (x10⁻⁶ Å⁻²)	Roughness (Å)	vfsolv (%)
Air	0.0	0.0	0.0	0.0
tail	18.33 +/- 0.95	-0.39	5.51 +/- 0.11	0.0
head PS	6.89	2.63	5.51 +/- 0.11	0.33
d2O	1.2 +/- 0.48	6.36	5.51 +/- 0.11	0.0
head PS	6.89	2.63	5.51 +/- 0.11	0.33
tail	18.33 +/- 0.95	-0.39	5.51 +/- 0.11	0.0
tail	18.51 +/- 1.22	-0.39	7.56 +/- 0.37	0.0
head PC	7.18	1.88	7.56 +/- 0.37	0.0 +/- 0.35
d2O	0.0 +/- 1.85	6.36	7.56 +/- 0.37	0.0
SiO2	16.9	3.41	6.9	0.13
Si	0.0	2.07	3.9	0.0

Table B.11: Best fitted parameters: DPPC trilayer at HR=35%

B.2.C.iv Trilayer DPPS (HR=40%)

RH=40 %

Slab	Thickness (Å)	SLD (x10⁻⁶ Å⁻²)	Roughness (Å)	vfsolv (%)
Air	0.0	0.0	0.0	0.0
tail	19.85 +/- 0.93	-0.39	5.19 +/- 0.14	0.0
head PS	7.46	2.63	5.19 +/- 0.14	0.33
d2O	0.5 +/- 0.49	6.36	5.19 +/- 0.14	0.0
head PS	7.46	2.63	5.19 +/- 0.14	0.33
tail	19.85 +/- 0.93	-0.39	5.19 +/- 0.14	0.0
tail	17.12 +/- 1.38	-0.39	7.36 +/- 0.42	0.0
head PC	6.64	1.88	7.36 +/- 0.42	0.0 +/- 0.44
d2O	0.02 +/- 2.18	6.36	7.36 +/- 0.42	0.0
SiO2	16.9	3.41	6.9	0.13
Si	0.0	2.07	3.9	0.0

Table B.12: Best fitted parameters: DPPS trilayer at HR=40%

B.2.C.v Trilayer DPPS (HR=50%)

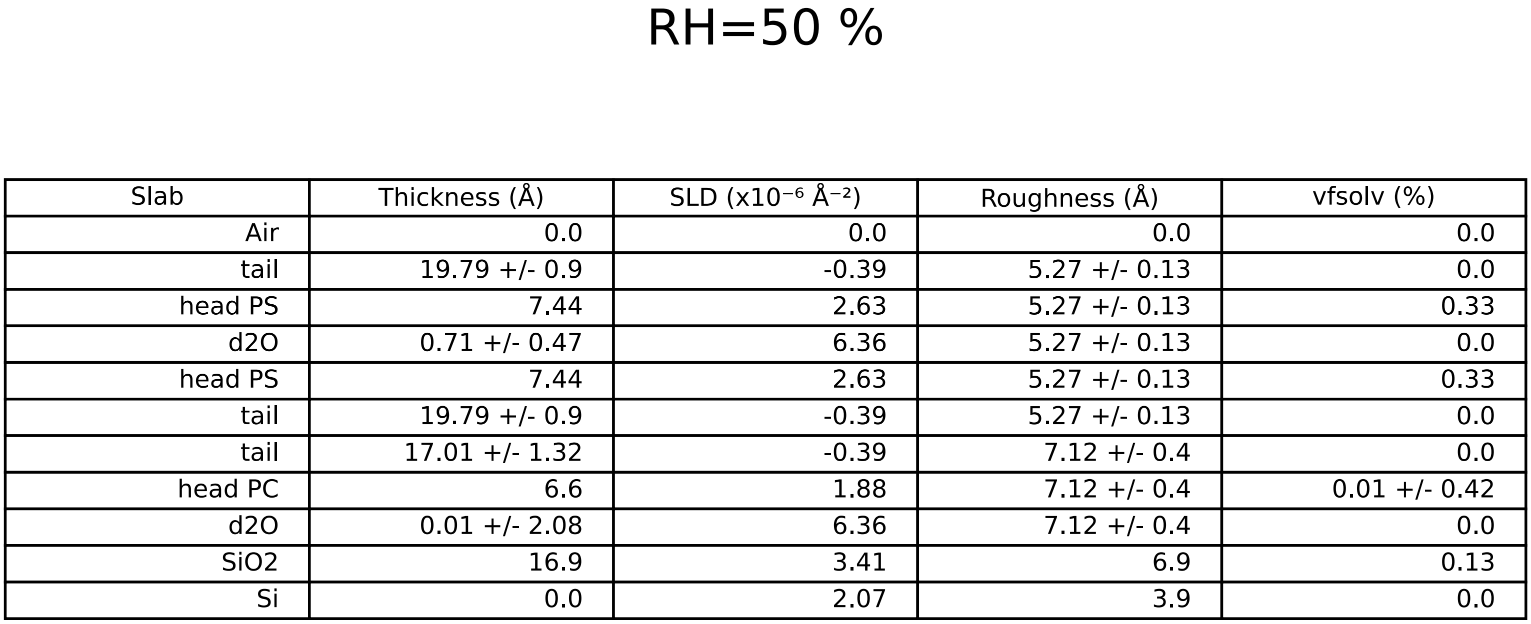

RH=50 %

Slab	Thickness (Å)	SLD (x10⁻⁶ Å⁻²)	Roughness (Å)	vfsolv (%)
Air	0.0	0.0	0.0	0.0
tail	19.79 +/- 0.9	-0.39	5.27 +/- 0.13	0.0
head PS	7.44	2.63	5.27 +/- 0.13	0.33
d2O	0.71 +/- 0.47	6.36	5.27 +/- 0.13	0.0
head PS	7.44	2.63	5.27 +/- 0.13	0.33
tail	19.79 +/- 0.9	-0.39	5.27 +/- 0.13	0.0
tail	17.01 +/- 1.32	-0.39	7.12 +/- 0.4	0.0
head PC	6.6	1.88	7.12 +/- 0.4	0.01 +/- 0.42
d2O	0.01 +/- 2.08	6.36	7.12 +/- 0.4	0.0
SiO2	16.9	3.41	6.9	0.13
Si	0.0	2.07	3.9	0.0

Table B.13: Best fitted parameters: DPPS trilayer at HR=50%

B.2.C.vi Trilayer DPPS (HR=60%)

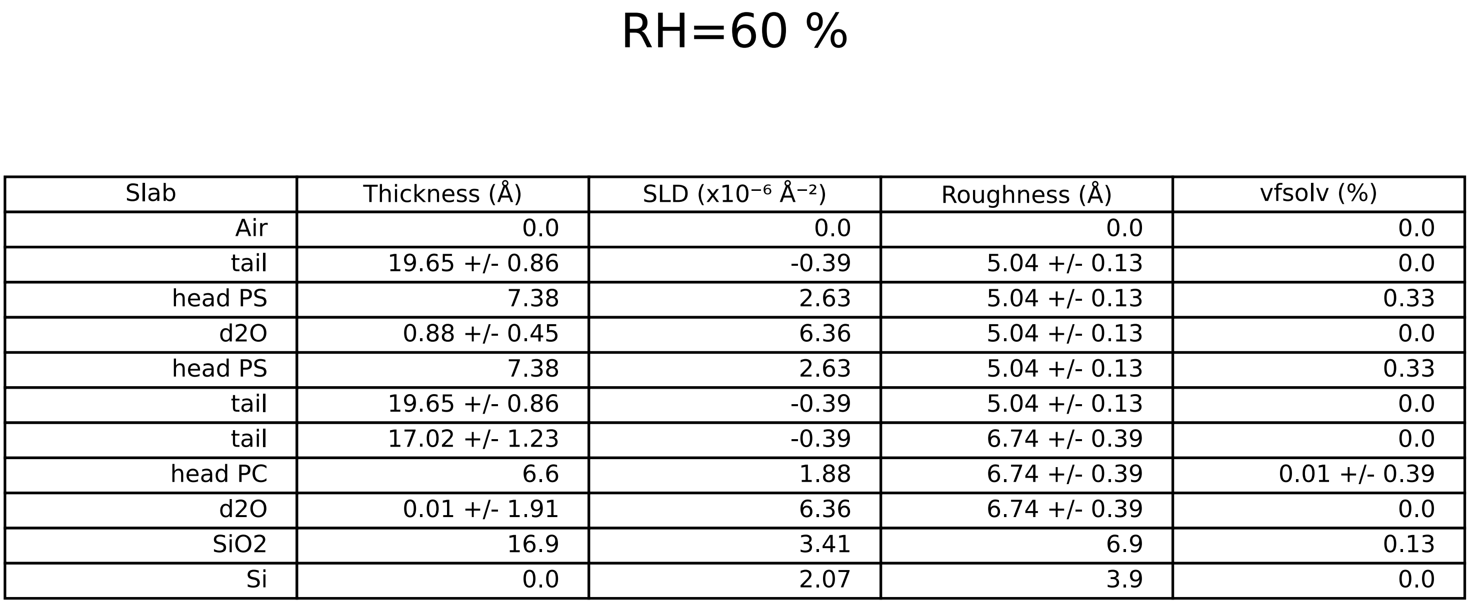

RH=60 %

Slab	Thickness (Å)	SLD ($x10^{-6}$ Å^{-2})	Roughness (Å)	vfsolv (%)
Air	0.0	0.0	0.0	0.0
tail	19.65 +/- 0.86	-0.39	5.04 +/- 0.13	0.0
head PS	7.38	2.63	5.04 +/- 0.13	0.33
d2O	0.88 +/- 0.45	6.36	5.04 +/- 0.13	0.0
head PS	7.38	2.63	5.04 +/- 0.13	0.33
tail	19.65 +/- 0.86	-0.39	5.04 +/- 0.13	0.0
tail	17.02 +/- 1.23	-0.39	6.74 +/- 0.39	0.0
head PC	6.6	1.88	6.74 +/- 0.39	0.01 +/- 0.39
d2O	0.01 +/- 1.91	6.36	6.74 +/- 0.39	0.0
SiO2	16.9	3.41	6.9	0.13
Si	0.0	2.07	3.9	0.0

Table B.14: Best fitted parameters: DPPS trilayer at HR=60%

B.2.C.vii Trilayer DPPS (HR=70%)

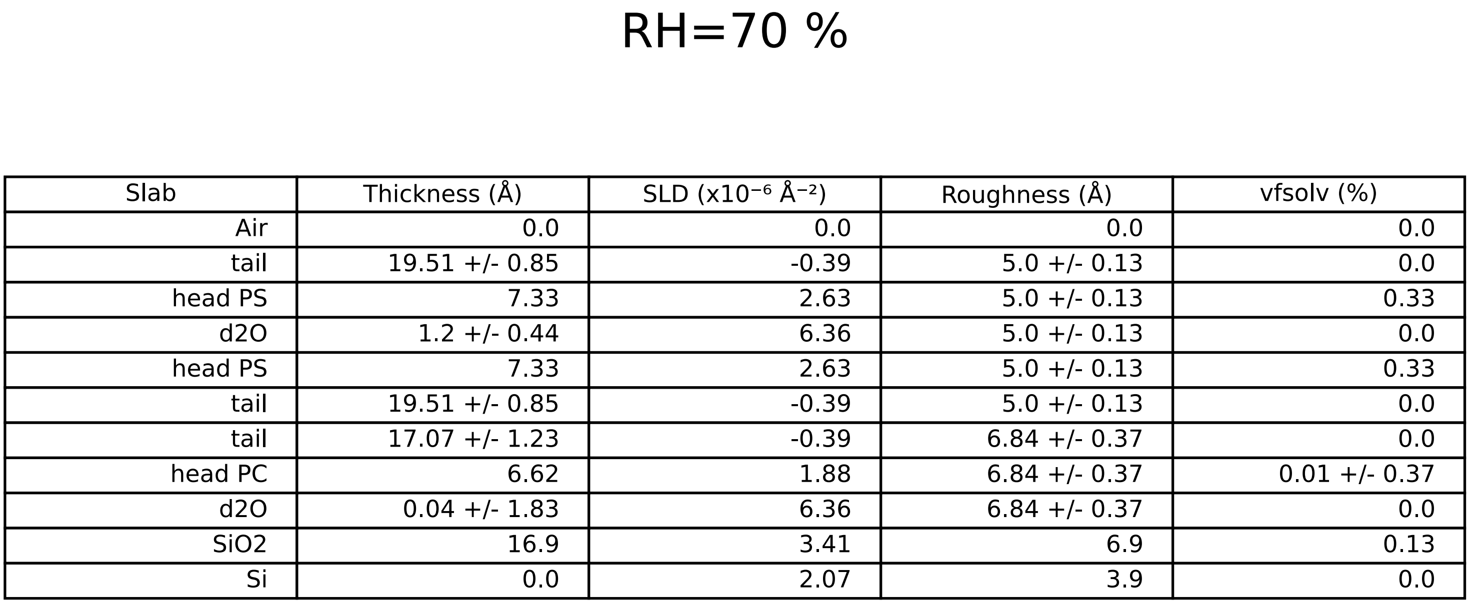

RH=70 %

Slab	Thickness (Å)	SLD (x10⁻⁶ Å⁻²)	Roughness (Å)	vfsolv (%)
Air	0.0	0.0	0.0	0.0
tail	19.51 +/- 0.85	-0.39	5.0 +/- 0.13	0.0
head PS	7.33	2.63	5.0 +/- 0.13	0.33
d2O	1.2 +/- 0.44	6.36	5.0 +/- 0.13	0.0
head PS	7.33	2.63	5.0 +/- 0.13	0.33
tail	19.51 +/- 0.85	-0.39	5.0 +/- 0.13	0.0
tail	17.07 +/- 1.23	-0.39	6.84 +/- 0.37	0.0
head PC	6.62	1.88	6.84 +/- 0.37	0.01 +/- 0.37
d2O	0.04 +/- 1.83	6.36	6.84 +/- 0.37	0.0
SiO2	16.9	3.41	6.9	0.13
Si	0.0	2.07	3.9	0.0

Table B.15: Best fitted parameters: DPPS trilayer at HR=70%

B.2.C.viii Trilayer DPPS (HR=90%)

RH=90 %

Slab	Thickness (Å)	SLD (x10^{-6} Å^{-2})	Roughness (Å)	vfsolv (%)
Air	0.0	0.0	0.0	0.0
tail	19.77 +/- 0.8	-0.39	5.13 +/- 0.13	0.0
head PS	7.43	2.63	5.13 +/- 0.13	0.33
d2O	1.78 +/- 0.42	6.36	5.13 +/- 0.13	0.0
head PS	7.43	2.63	5.13 +/- 0.13	0.33
tail	19.77 +/- 0.8	-0.39	5.13 +/- 0.13	0.0
tail	17.03 +/- 1.0	-0.39	6.55 +/- 0.22	0.0
head PC	6.61	1.88	6.55 +/- 0.22	0.1 +/- 0.29
d2O	0.07 +/- 1.46	6.36	6.55 +/- 0.22	0.0
SiO2	16.9	3.41	6.9	0.13
Si	0.0	2.07	3.9	0.0

Table B.16: Best fitted parameters: DPPS trilayer at HR=90%

B.3 Trilayer DPPS(20%)-DPPC(80%)

B.3.A Data and best fits-Trilayer PS(20%)-PC(80%)

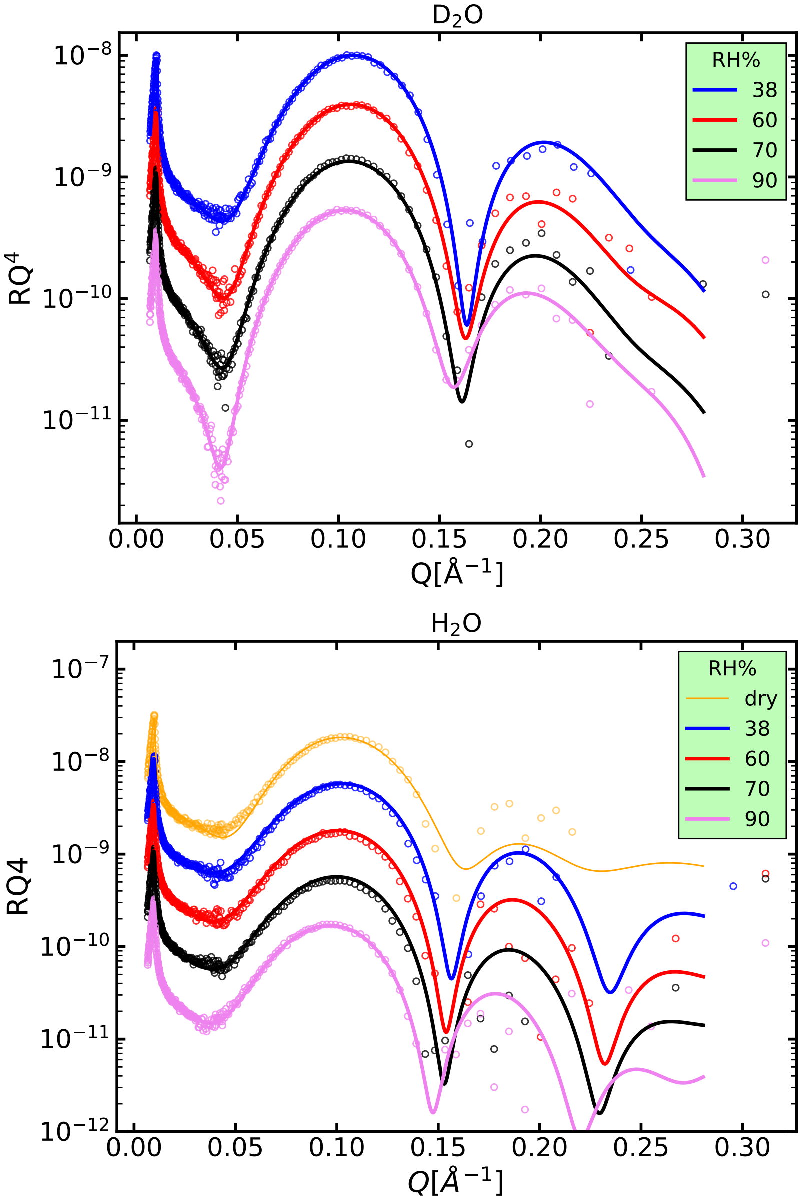

Figure B.3: NR data for PS(20%)-PC(80%) trilayer are presented as Rq_z^4 on a semilog scale with two contrast (D_2O and H_2O). Solid lines represent the best fits corresponding to the SLD_n profiles.

B.3.B SLD profiles-Trilayer PS(20%)-PC(80%)

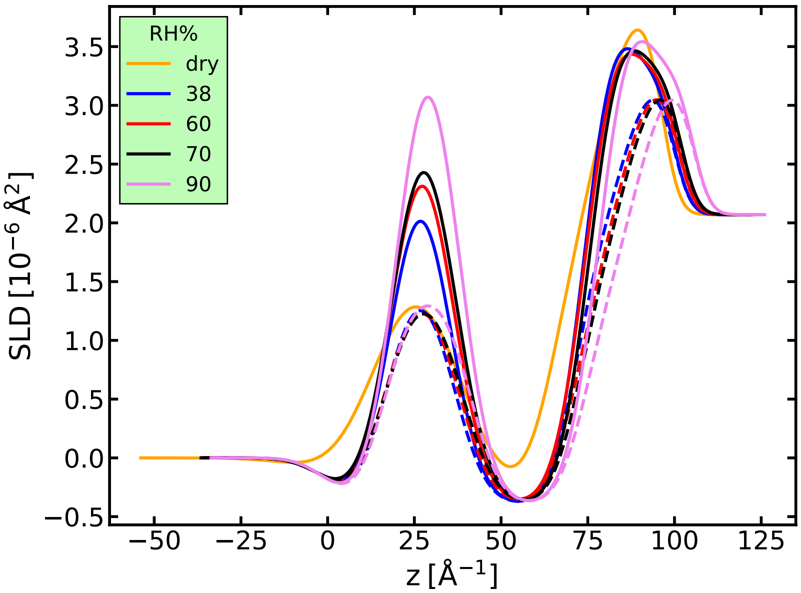

Figure B.4: SLD profiles for NR of trilayer with 20% DPPS obtained by combined fitting of reflectivity data for 2 contrasts (see Figure B.3).

B.3.C Fitted parameters-Trilayer PS(20%)-PC(80%)

B.3.C.i Trilayer PS(20%)-PC(80%) (HR=3%)

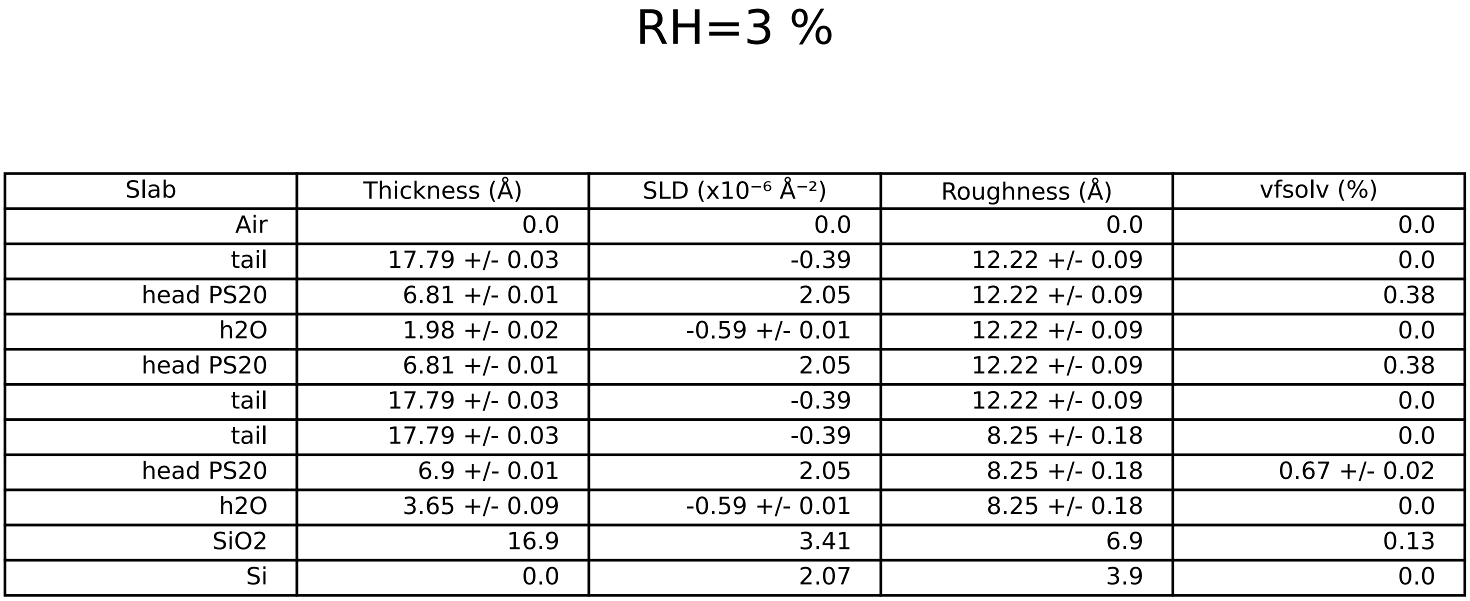

RH=3 %

Slab	Thickness (Å)	SLD (x10^{-6} Å^{-2})	Roughness (Å)	vfsolv (%)
Air	0.0	0.0	0.0	0.0
tail	17.79 +/- 0.03	-0.39	12.22 +/- 0.09	0.0
head PS20	6.81 +/- 0.01	2.05	12.22 +/- 0.09	0.38
h2O	1.98 +/- 0.02	-0.59 +/- 0.01	12.22 +/- 0.09	0.0
head PS20	6.81 +/- 0.01	2.05	12.22 +/- 0.09	0.38
tail	17.79 +/- 0.03	-0.39	12.22 +/- 0.09	0.0
tail	17.79 +/- 0.03	-0.39	8.25 +/- 0.18	0.0
head PS20	6.9 +/- 0.01	2.05	8.25 +/- 0.18	0.67 +/- 0.02
h2O	3.65 +/- 0.09	-0.59 +/- 0.01	8.25 +/- 0.18	0.0
SiO2	16.9	3.41	6.9	0.13
Si	0.0	2.07	3.9	0.0

Table B.17: Best fitted parameters: Trilayer PS(20%)-PC(80%) at HR=3%

B.3.C.ii Trilayer PS(20%)-PC(80%) (HR=38%)

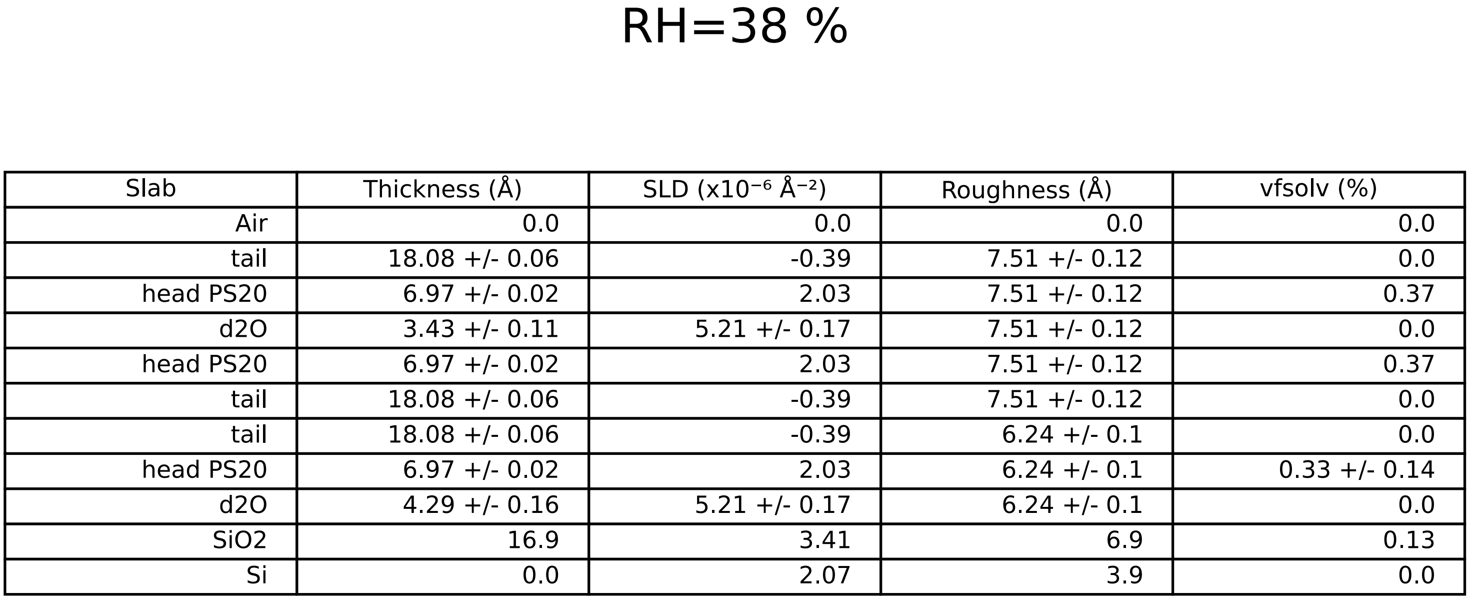

RH=38 %

Slab	Thickness (Å)	SLD ($\times 10^{-6}$ Å^{-2})	Roughness (Å)	vfsolv (%)
Air	0.0	0.0	0.0	0.0
tail	18.08 +/- 0.06	-0.39	7.51 +/- 0.12	0.0
head PS20	6.97 +/- 0.02	2.03	7.51 +/- 0.12	0.37
d2O	3.43 +/- 0.11	5.21 +/- 0.17	7.51 +/- 0.12	0.0
head PS20	6.97 +/- 0.02	2.03	7.51 +/- 0.12	0.37
tail	18.08 +/- 0.06	-0.39	7.51 +/- 0.12	0.0
tail	18.08 +/- 0.06	-0.39	6.24 +/- 0.1	0.0
head PS20	6.97 +/- 0.02	2.03	6.24 +/- 0.1	0.33 +/- 0.14
d2O	4.29 +/- 0.16	5.21 +/- 0.17	6.24 +/- 0.1	0.0
SiO2	16.9	3.41	6.9	0.13
Si	0.0	2.07	3.9	0.0

Table B.18: Best fitted parameters: Trilayer PS(20%)-PC(80%) at HR=38%

B.3.C.iii Trilayer PS(20%)-PC(80%) (HR=60%)

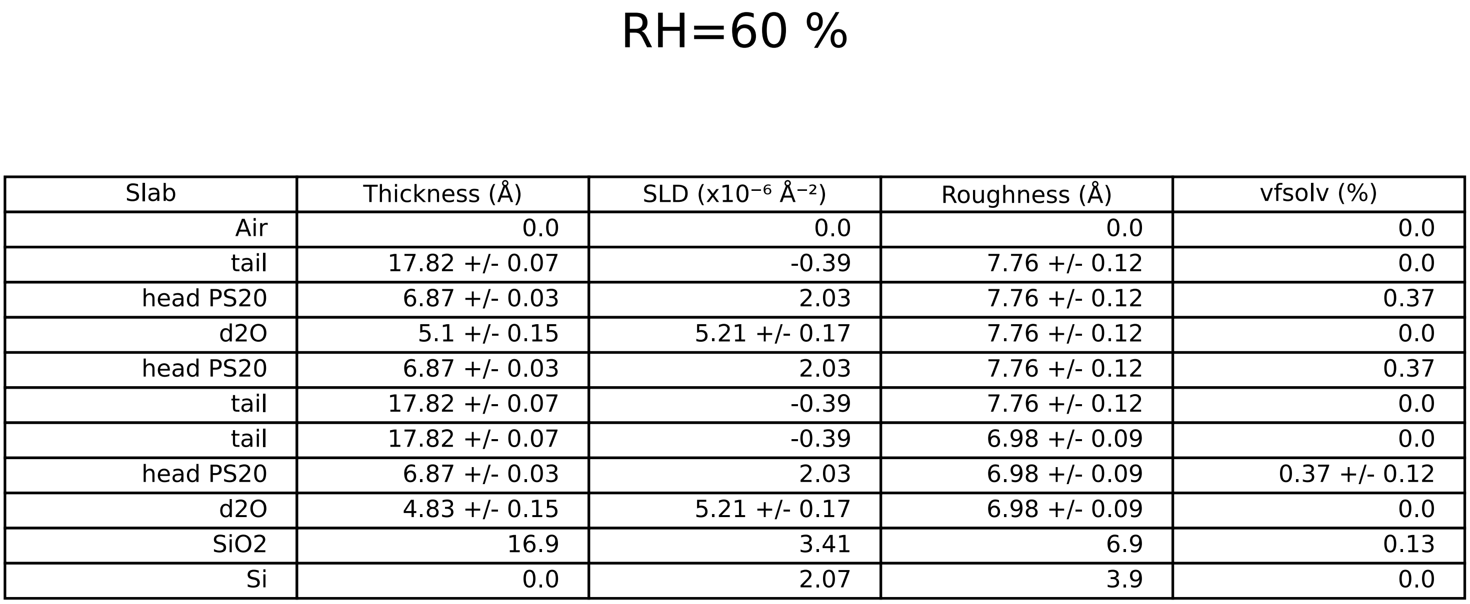

RH=60 %

Slab	Thickness (Å)	SLD (x10⁻⁶ Å⁻²)	Roughness (Å)	vfsolv (%)
Air	0.0	0.0	0.0	0.0
tail	17.82 +/- 0.07	-0.39	7.76 +/- 0.12	0.0
head PS20	6.87 +/- 0.03	2.03	7.76 +/- 0.12	0.37
d2O	5.1 +/- 0.15	5.21 +/- 0.17	7.76 +/- 0.12	0.0
head PS20	6.87 +/- 0.03	2.03	7.76 +/- 0.12	0.37
tail	17.82 +/- 0.07	-0.39	7.76 +/- 0.12	0.0
tail	17.82 +/- 0.07	-0.39	6.98 +/- 0.09	0.0
head PS20	6.87 +/- 0.03	2.03	6.98 +/- 0.09	0.37 +/- 0.12
d2O	4.83 +/- 0.15	5.21 +/- 0.17	6.98 +/- 0.09	0.0
SiO2	16.9	3.41	6.9	0.13
Si	0.0	2.07	3.9	0.0

Table B.19: Best fitted parameters: Trilayer PS(20%)-PC(80%) at HR=60%

B.3.C.iv Trilayer PS(20%)-PC(80%) (HR=70%)

RH=70 %

Slab	Thickness (Å)	SLD (x10^{-6} Å^{-2})	Roughness (Å)	vfsolv (%)
Air	0.0	0.0	0.0	0.0
tail	17.93 +/- 0.1	-0.39	7.87 +/- 0.13	0.0
head PS20	6.91 +/- 0.04	2.03	7.87 +/- 0.13	0.37
d2O	5.75 +/- 0.24	5.21 +/- 0.17	7.87 +/- 0.13	0.0
head PS20	6.91 +/- 0.04	2.03	7.87 +/- 0.13	0.37
tail	17.93 +/- 0.1	-0.39	7.87 +/- 0.13	0.0
tail	17.93 +/- 0.1	-0.39	6.72 +/- 0.12	0.0
head PS20	6.91 +/- 0.04	2.03	6.72 +/- 0.12	0.36 +/- 0.12
d2O	4.76 +/- 0.2	5.21 +/- 0.17	6.72 +/- 0.12	0.0
SiO2	16.9	3.41	6.9	0.13
Si	0.0	2.07	3.9	0.0

Table B.20: Best fitted parameters: Trilayer PS(20%)-PC(80%) at HR=70%

B.3.C.v Trilayer PS(20%)-PC(80%) (HR=90%)

RH=90 %

Slab	Thickness (Å)	SLD (x10⁻⁶ Å⁻²)	Roughness (Å)	vfsolv (%)
Air	0.0	0.0	0.0	0.0
tail	17.99 +/- 0.11	-0.39	7.15 +/- 0.08	0.0
head PS20	6.93 +/- 0.04	2.03	7.15 +/- 0.08	0.37
d2O	7.95 +/- 0.27	5.21 +/- 0.17	7.15 +/- 0.08	0.0
head PS20	6.93 +/- 0.04	2.03	7.15 +/- 0.08	0.37
tail	17.99 +/- 0.11	-0.39	7.15 +/- 0.08	0.0
tail	17.99 +/- 0.11	-0.39	6.94 +/- 0.12	0.0
head PS20	6.93 +/- 0.04	2.03	6.94 +/- 0.12	0.33 +/- 0.13
d2O	5.78 +/- 0.22	5.21 +/- 0.17	6.94 +/- 0.12	0.0
SiO2	16.9	3.41	6.9	0.13
Si	0.0	2.07	3.9	0.0

Table B.21: Best fitted parameters: Trilayer PS(20%)-PC(80%) at HR=90%

B.4 Trilayer DPPS(60%)-DPPC(40%)

B.4.A Data and best fits-Trilayer PS(60%)-PC(40%))

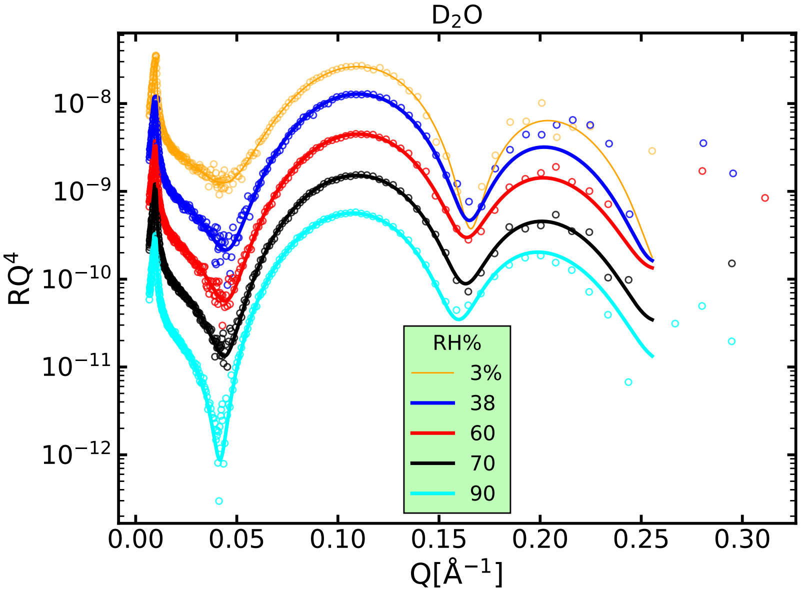

Figure B.5: NR data are presented as Rq_z^4 on a semilog scale with one contrast (D$_2$O). Solid lines represent the best fits corresponding to the SLD$_n$ profiles.

B.4.B SLD profiles-Trilayer PS(60%)-PC(40%)

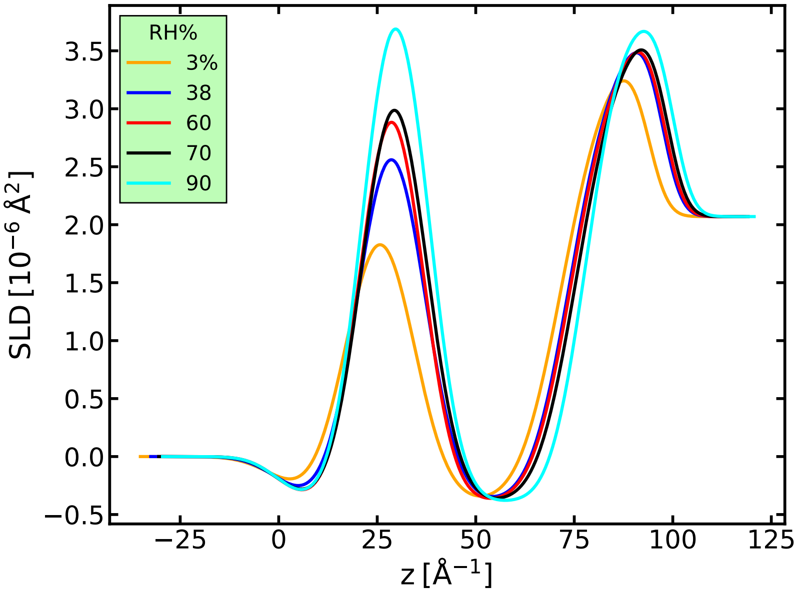

Figure B.6: SLD profiles for NR obtained by fitting D_2O curves (see Figure B.5).

B.4.C Fitted parameters-Trilayer PS(60%)-PC(40%)

B.4.C.i Trilayer PS(60%)-PC(40%) (HR=3%)

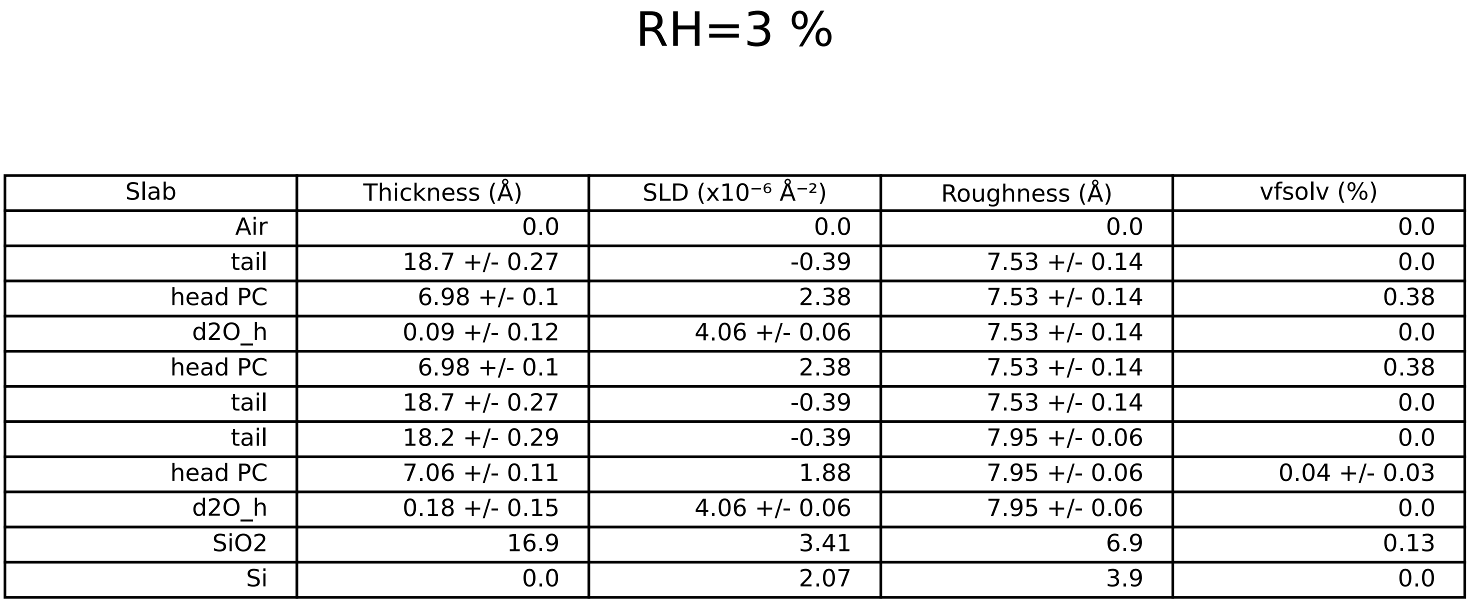

RH=3 %

Slab	Thickness (Å)	SLD ($x10^{-6}$ Å^{-2})	Roughness (Å)	vfsolv (%)
Air	0.0	0.0	0.0	0.0
tail	18.7 +/- 0.27	-0.39	7.53 +/- 0.14	0.0
head PC	6.98 +/- 0.1	2.38	7.53 +/- 0.14	0.38
d2O_h	0.09 +/- 0.12	4.06 +/- 0.06	7.53 +/- 0.14	0.0
head PC	6.98 +/- 0.1	2.38	7.53 +/- 0.14	0.38
tail	18.7 +/- 0.27	-0.39	7.53 +/- 0.14	0.0
tail	18.2 +/- 0.29	-0.39	7.95 +/- 0.06	0.0
head PC	7.06 +/- 0.11	1.88	7.95 +/- 0.06	0.04 +/- 0.03
d2O_h	0.18 +/- 0.15	4.06 +/- 0.06	7.95 +/- 0.06	0.0
SiO2	16.9	3.41	6.9	0.13
Si	0.0	2.07	3.9	0.0

Table B.22: Best fitted parameters: Trilayer PS(60%)-PC(40%) at HR=3%

B.4.C.ii Trilayer PS(60%)-PC(40%) (HR=38%)

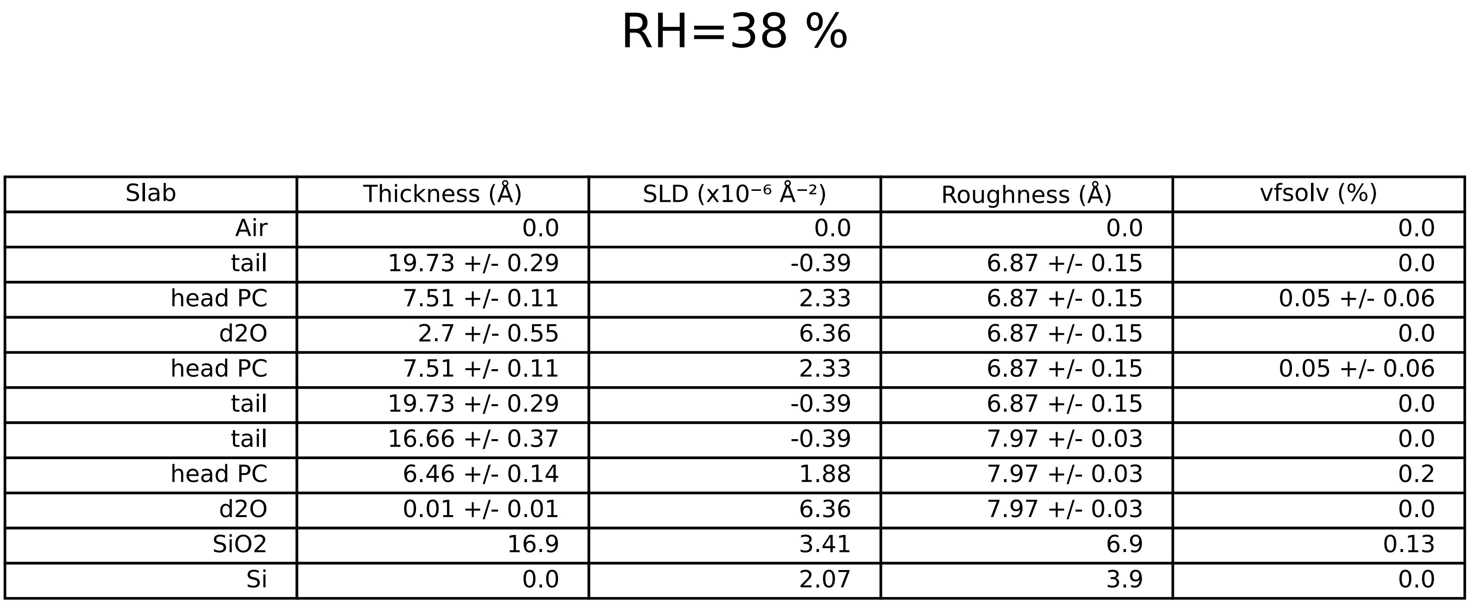

RH=38 %

Slab	Thickness (Å)	SLD (x10^{-6} Å^{-2})	Roughness (Å)	vfsolv (%)
Air	0.0	0.0	0.0	0.0
tail	19.73 +/- 0.29	-0.39	6.87 +/- 0.15	0.0
head PC	7.51 +/- 0.11	2.33	6.87 +/- 0.15	0.05 +/- 0.06
d2O	2.7 +/- 0.55	6.36	6.87 +/- 0.15	0.0
head PC	7.51 +/- 0.11	2.33	6.87 +/- 0.15	0.05 +/- 0.06
tail	19.73 +/- 0.29	-0.39	6.87 +/- 0.15	0.0
tail	16.66 +/- 0.37	-0.39	7.97 +/- 0.03	0.0
head PC	6.46 +/- 0.14	1.88	7.97 +/- 0.03	0.2
d2O	0.01 +/- 0.01	6.36	7.97 +/- 0.03	0.0
SiO2	16.9	3.41	6.9	0.13
Si	0.0	2.07	3.9	0.0

Table B.23: Best fitted parameters: Trilayer PS(60%)-PC(40%) at HR=38%

B.4.C.iii Trilayer PS(60%)-PC(40%) (HR=60%)

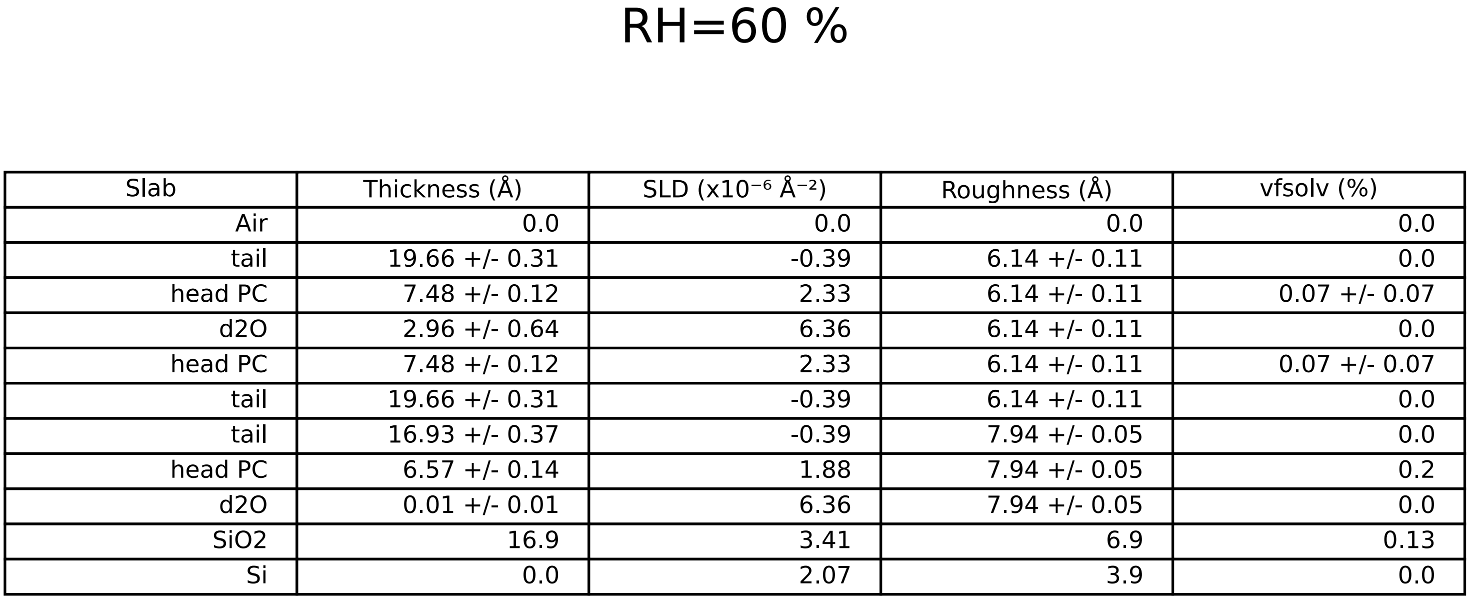

RH=60 %

Slab	Thickness (Å)	SLD (x10^{-6} Å^{-2})	Roughness (Å)	vfsolv (%)
Air	0.0	0.0	0.0	0.0
tail	19.66 +/- 0.31	-0.39	6.14 +/- 0.11	0.0
head PC	7.48 +/- 0.12	2.33	6.14 +/- 0.11	0.07 +/- 0.07
d2O	2.96 +/- 0.64	6.36	6.14 +/- 0.11	0.0
head PC	7.48 +/- 0.12	2.33	6.14 +/- 0.11	0.07 +/- 0.07
tail	19.66 +/- 0.31	-0.39	6.14 +/- 0.11	0.0
tail	16.93 +/- 0.37	-0.39	7.94 +/- 0.05	0.0
head PC	6.57 +/- 0.14	1.88	7.94 +/- 0.05	0.2
d2O	0.01 +/- 0.01	6.36	7.94 +/- 0.05	0.0
SiO2	16.9	3.41	6.9	0.13
Si	0.0	2.07	3.9	0.0

Table B.24: Best fitted parameters: Trilayer PS(60%)-PC(40%) at HR=60%

B.4.C.iv Trilayer PS(60%)-PC(40%) (HR=70%)

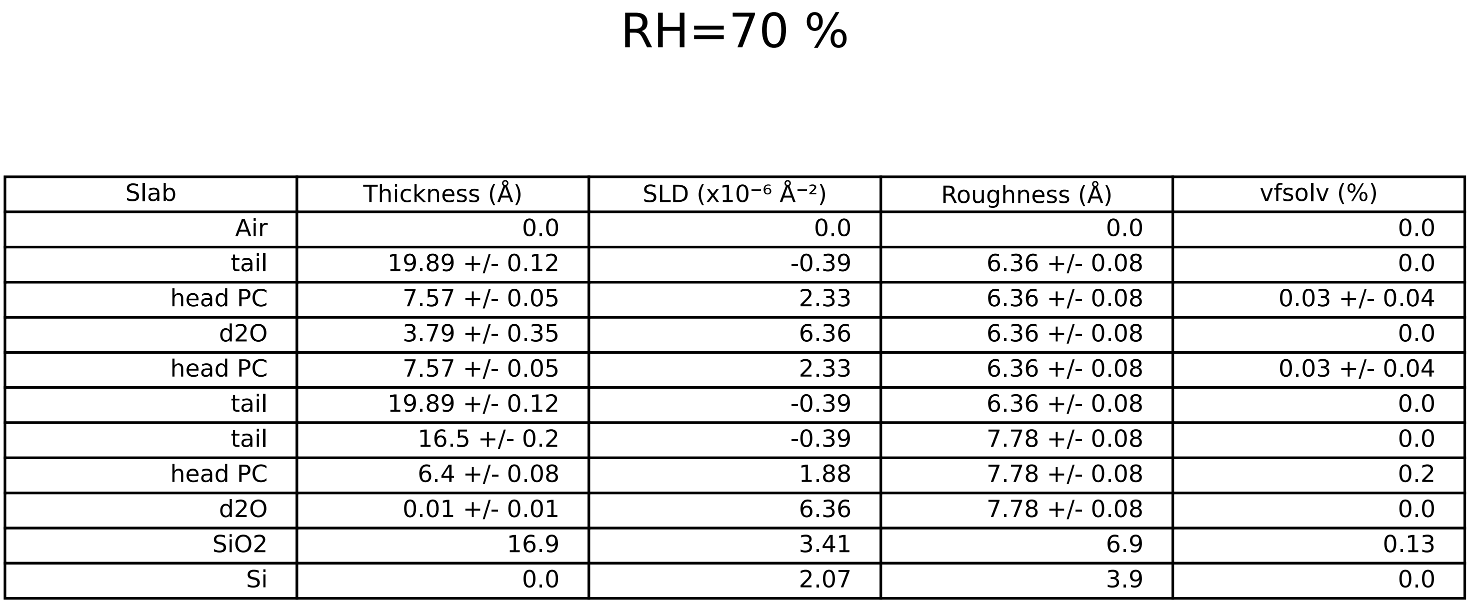

RH=70 %

Slab	Thickness (Å)	SLD (x10^{-6} Å^{-2})	Roughness (Å)	vfsolv (%)
Air	0.0	0.0	0.0	0.0
tail	19.89 +/- 0.12	-0.39	6.36 +/- 0.08	0.0
head PC	7.57 +/- 0.05	2.33	6.36 +/- 0.08	0.03 +/- 0.04
d2O	3.79 +/- 0.35	6.36	6.36 +/- 0.08	0.0
head PC	7.57 +/- 0.05	2.33	6.36 +/- 0.08	0.03 +/- 0.04
tail	19.89 +/- 0.12	-0.39	6.36 +/- 0.08	0.0
tail	16.5 +/- 0.2	-0.39	7.78 +/- 0.08	0.0
head PC	6.4 +/- 0.08	1.88	7.78 +/- 0.08	0.2
d2O	0.01 +/- 0.01	6.36	7.78 +/- 0.08	0.0
SiO2	16.9	3.41	6.9	0.13
Si	0.0	2.07	3.9	0.0

Table B.25: Best fitted parameters: Trilayer PS(60%)-PC(40%) at HR=70%

B.4.C.v Trilayer PS(60%)-PC(40%) (HR=90%)

RH=90 %

Slab	Thickness (Å)	SLD (x10⁻⁶ Å⁻²)	Roughness (Å)	vfsolv (%)
Air	0.0	0.0	0.0	0.0
tail	19.85 +/- 0.18	-0.39	6.12 +/- 0.07	0.0
head PC	7.55 +/- 0.07	2.33	6.12 +/- 0.07	0.2 +/- 0.08
d2O	4.53 +/- 0.74	6.36	6.12 +/- 0.07	0.0
head PC	7.55 +/- 0.07	2.33	6.12 +/- 0.07	0.2 +/- 0.08
tail	19.85 +/- 0.18	-0.39	6.12 +/- 0.07	0.0
tail	17.15 +/- 0.31	-0.39	6.62 +/- 0.08	0.0
head PC	6.65 +/- 0.12	1.88	6.62 +/- 0.08	0.2
d2O	0.02 +/- 0.02	6.36	6.62 +/- 0.08	0.0
SiO2	16.9	3.41	6.9	0.13
Si	0.0	2.07	3.9	0.0

Table B.26: Best fitted parameters: Trilayer PS(60%)-PC(40%) at HR=90%

B.5 Pentalayer DPPS(70%)-DPPC(30%)

B.5.A Data and best fits-Pentalayer DPPS(70%)-DPPC(30%)

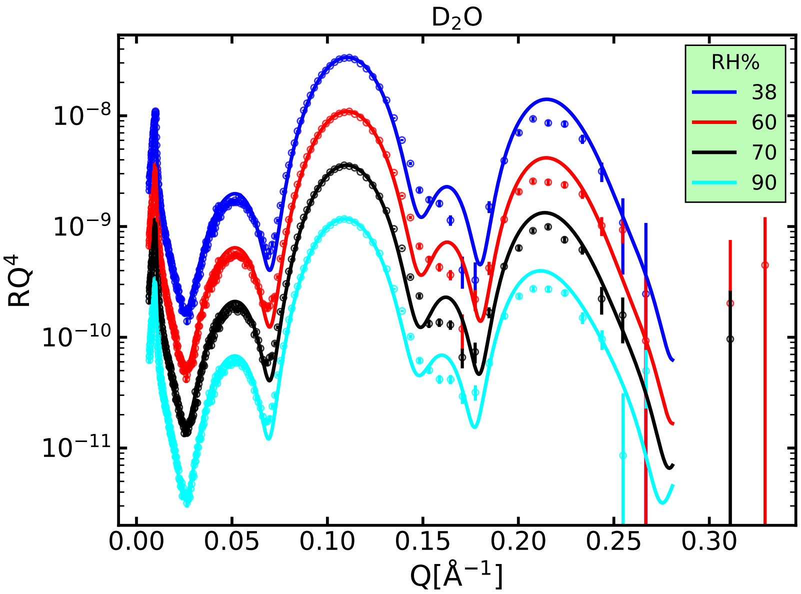

Figure B.7: NR data are presented as Rq_z^4 on a semilog scale with one contrast (D_2O). Solid lines represent the best fits corresponding to the SLD_n profiles.

B.5.B SLD profiles-Pentalayer DPPS(70%)-DPPC(30%)

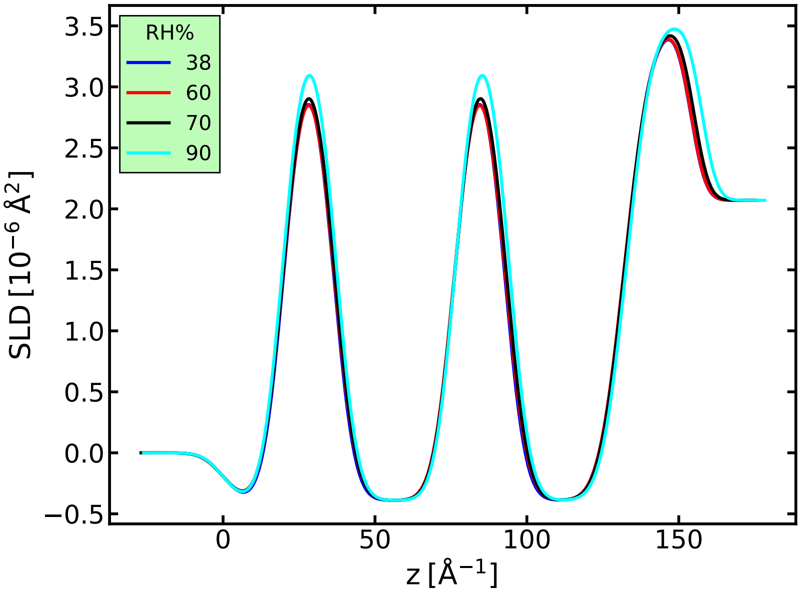

Figure B.8: SLD profiles for NR obtained by fitting of D_2O curves (see Figure B.7).

B.5.C Fitted parameters-Pentalayer DPPS(70%)-DPPC(30%)

B.5.C.i Fitted parameters (HR=38%)

RH=38 %

Slab	Thickness (Å)	SLD (x10⁻⁶ Å⁻²)	Roughness (Å)	vfsolv (%)
Air	0.0	0.0	0.0	0.0
tail	19.61 +/- 0.03	-0.39	5.32 +/- 0.04	0.0
head PS70	7.27	2.47	5.32 +/- 0.04	0.38
d2O	2.53 +/- 0.04	4.0	5.32 +/- 0.04	0.0
head PS70	7.27	2.47	5.32 +/- 0.04	0.38
tail	19.61 +/- 0.03	-0.39	5.32 +/- 0.04	0.0
tail	19.61 +/- 0.03	-0.39	5.32 +/- 0.04	0.0
head PS70	7.27	2.47	5.32 +/- 0.04	0.38
d2O	2.53 +/- 0.04	4.0	5.32 +/- 0.04	0.0
head PS70	7.27	2.47	5.32 +/- 0.04	0.38
tail	19.61 +/- 0.03	-0.39	5.32 +/- 0.04	0.0
tail	17.45 +/- 1.41	-0.39	6.0 +/- 0.13	0.0
head PC	6.77	1.88	6.0 +/- 0.13	0.15 +/- 0.49
d2O	0.21 +/- 1.88	4.0	6.0 +/- 0.13	0.0
SiO2	16.9	3.41	6.9	0.13
Si	0.0	2.07	3.9	0.0

Table B.27: Best fitted parameters Pentalayer DPPS(70%)-DPPC(30%) at HR=38%

B.5.C.ii Pentalayer DPPS(70%)-DPPC(30%) (HR=60%)

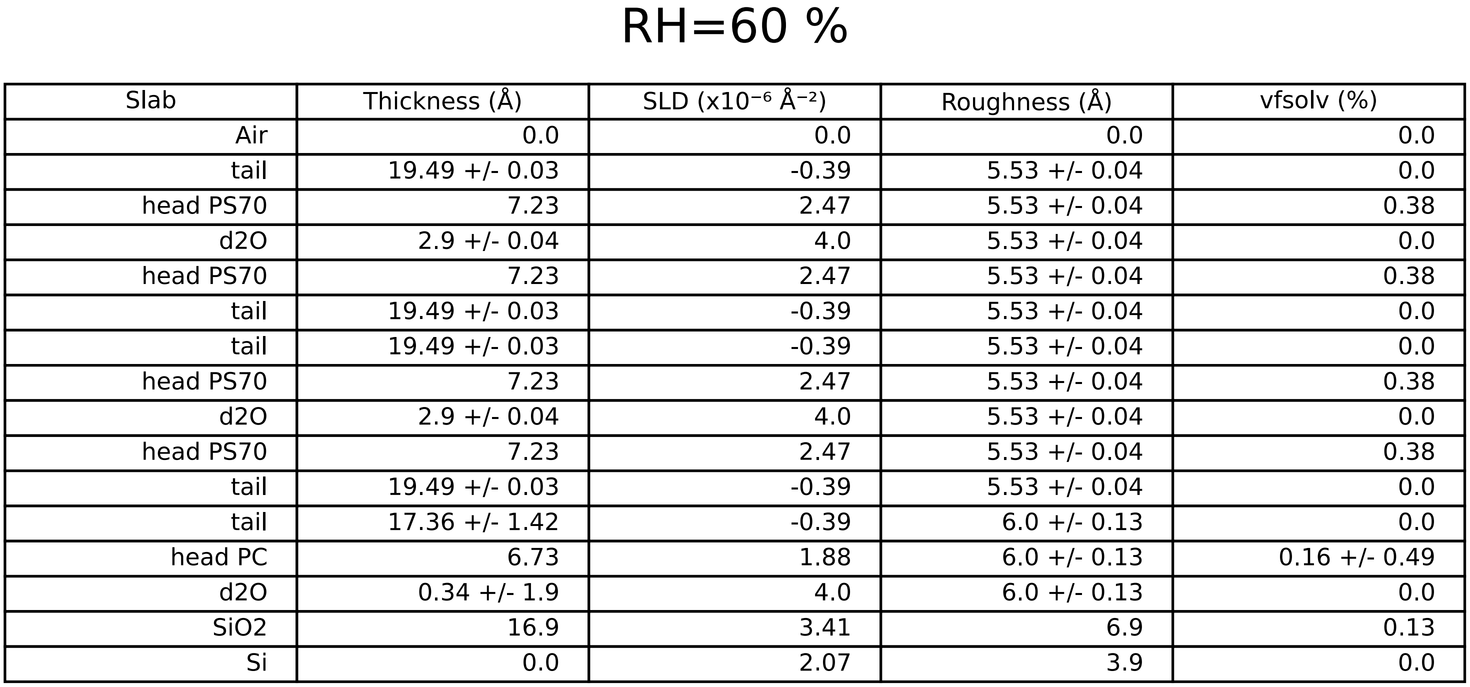

RH=60 %

Slab	Thickness (Å)	SLD (x10^{-6} Å^{-2})	Roughness (Å)	vfsolv (%)
Air	0.0	0.0	0.0	0.0
tail	19.49 +/- 0.03	-0.39	5.53 +/- 0.04	0.0
head PS70	7.23	2.47	5.53 +/- 0.04	0.38
d2O	2.9 +/- 0.04	4.0	5.53 +/- 0.04	0.0
head PS70	7.23	2.47	5.53 +/- 0.04	0.38
tail	19.49 +/- 0.03	-0.39	5.53 +/- 0.04	0.0
tail	19.49 +/- 0.03	-0.39	5.53 +/- 0.04	0.0
head PS70	7.23	2.47	5.53 +/- 0.04	0.38
d2O	2.9 +/- 0.04	4.0	5.53 +/- 0.04	0.0
head PS70	7.23	2.47	5.53 +/- 0.04	0.38
tail	19.49 +/- 0.03	-0.39	5.53 +/- 0.04	0.0
tail	17.36 +/- 1.42	-0.39	6.0 +/- 0.13	0.0
head PC	6.73	1.88	6.0 +/- 0.13	0.16 +/- 0.49
d2O	0.34 +/- 1.9	4.0	6.0 +/- 0.13	0.0
SiO2	16.9	3.41	6.9	0.13
Si	0.0	2.07	3.9	0.0

Table B.28: Best fitted parameters: Pentalayer DPPS(70%)-DPPC(30%) at HR=60%

B.5.C.iii Pentalayer DPPS(70%)-DPPC(30%) (HR=70%)

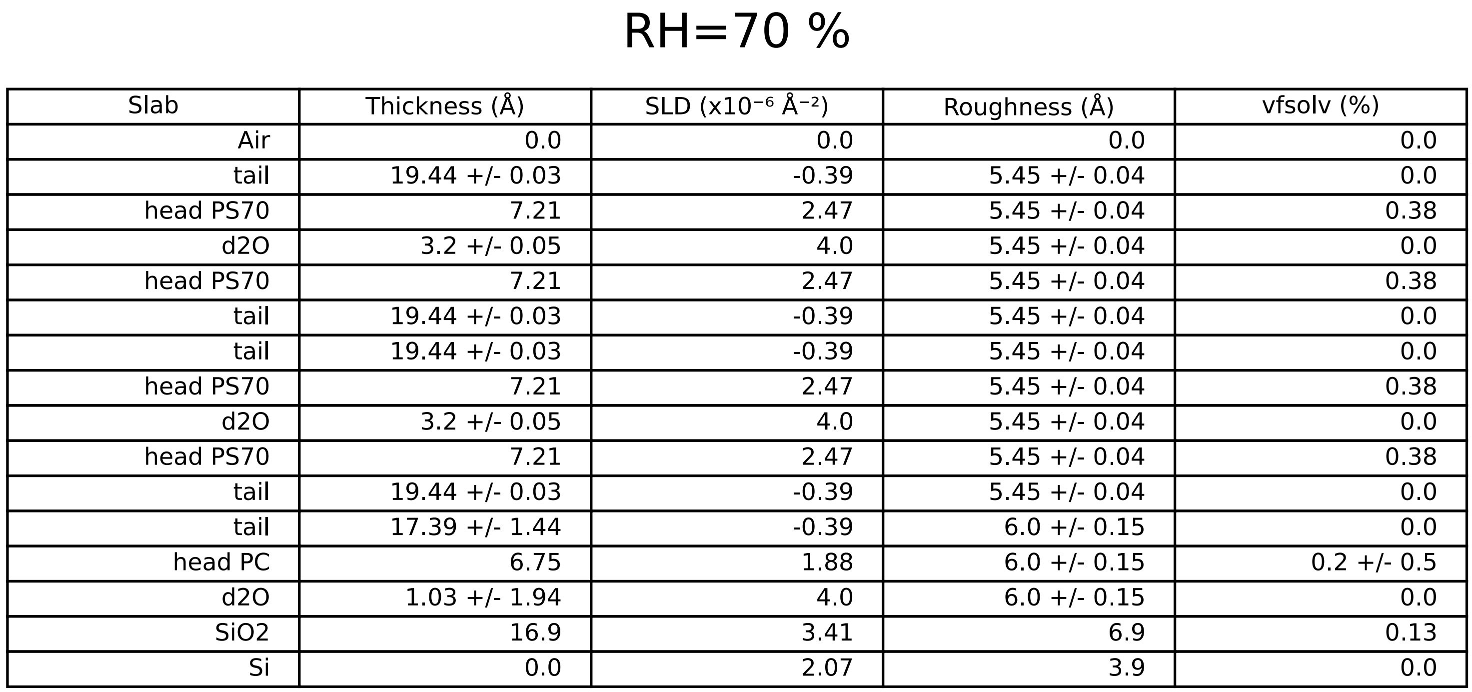

RH=70 %

Slab	Thickness (Å)	SLD (x10^{-6} Å^{-2})	Roughness (Å)	vfsolv (%)
Air	0.0	0.0	0.0	0.0
tail	19.44 +/- 0.03	-0.39	5.45 +/- 0.04	0.0
head PS70	7.21	2.47	5.45 +/- 0.04	0.38
d2O	3.2 +/- 0.05	4.0	5.45 +/- 0.04	0.0
head PS70	7.21	2.47	5.45 +/- 0.04	0.38
tail	19.44 +/- 0.03	-0.39	5.45 +/- 0.04	0.0
tail	19.44 +/- 0.03	-0.39	5.45 +/- 0.04	0.0
head PS70	7.21	2.47	5.45 +/- 0.04	0.38
d2O	3.2 +/- 0.05	4.0	5.45 +/- 0.04	0.0
head PS70	7.21	2.47	5.45 +/- 0.04	0.38
tail	19.44 +/- 0.03	-0.39	5.45 +/- 0.04	0.0
tail	17.39 +/- 1.44	-0.39	6.0 +/- 0.15	0.0
head PC	6.75	1.88	6.0 +/- 0.15	0.2 +/- 0.5
d2O	1.03 +/- 1.94	4.0	6.0 +/- 0.15	0.0
SiO2	16.9	3.41	6.9	0.13
Si	0.0	2.07	3.9	0.0

Table B.29: Best fitted parameters: Pentalayer DPPS(70%)-DPPC(30%) at HR=70%

B.5.C.iv Pentalayer DPPS(70%)-DPPC(30%) (HR=90%)

RH=90 %

Slab	Thickness (Å)	SLD (x10^{-6} Å^{-2})	Roughness (Å)	vfsolv (%)
Air	0.0	0.0	0.0	0.0
tail	19.12 +/- 0.03	-0.39	5.3 +/- 0.04	0.0
head PS70	7.09	2.47	5.3 +/- 0.04	0.38
d2O	4.49 +/- 0.05	4.0	5.3 +/- 0.04	0.0
head PS70	7.09	2.47	5.3 +/- 0.04	0.38
tail	19.12 +/- 0.03	-0.39	5.3 +/- 0.04	0.0
tail	19.12 +/- 0.03	-0.39	5.3 +/- 0.04	0.0
head PS70	7.09	2.47	5.3 +/- 0.04	0.38
d2O	4.49 +/- 0.05	4.0	5.3 +/- 0.04	0.0
head PS70	7.09	2.47	5.3 +/- 0.04	0.38
tail	19.12 +/- 0.03	-0.39	5.3 +/- 0.04	0.0
tail	17.25 +/- 1.38	-0.39	5.99 +/- 0.13	0.0
head PC	6.69	1.88	5.99 +/- 0.13	0.19 +/- 0.48
d2O	3.03 +/- 1.86	4.0	5.99 +/- 0.13	0.0
SiO2	16.9	3.41	6.9	0.13
Si	0.0	2.07	3.9	0.0

Table B.30: Best fitted parameters: Pentalayer DPPS(70%)-DPPC(30%) at HR=90%

B.6 Pentalayer DPPS(80%)-DPPC(20%)

B.6.A Data and best fits-Pentalayer PS(80%)-PC(20%)

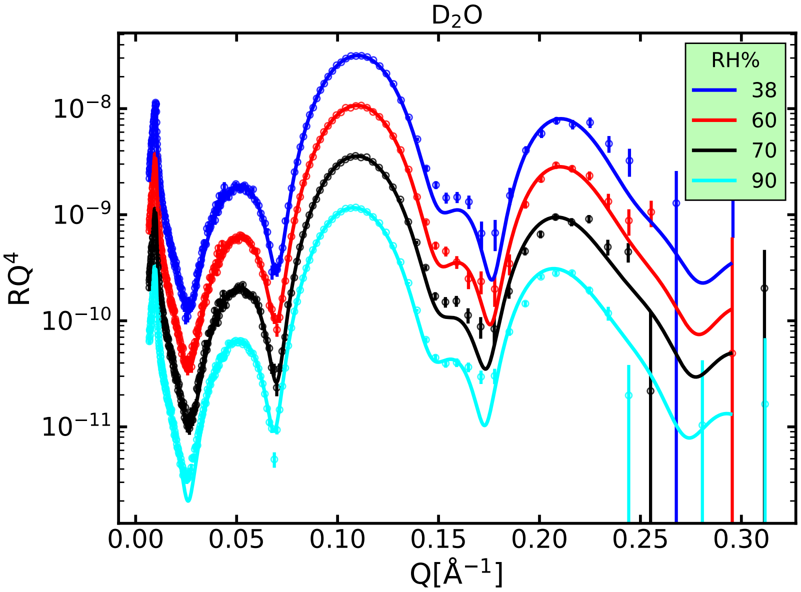

Figure B.9: NR data are presented as Rq_z^4 on a semilog scale with one contrast (D_2O). Solid lines represent the best fits corresponding to the SLD_n profiles.

B.6.B SLD profiles-Pentalayer PS(80%)-PC(20%)

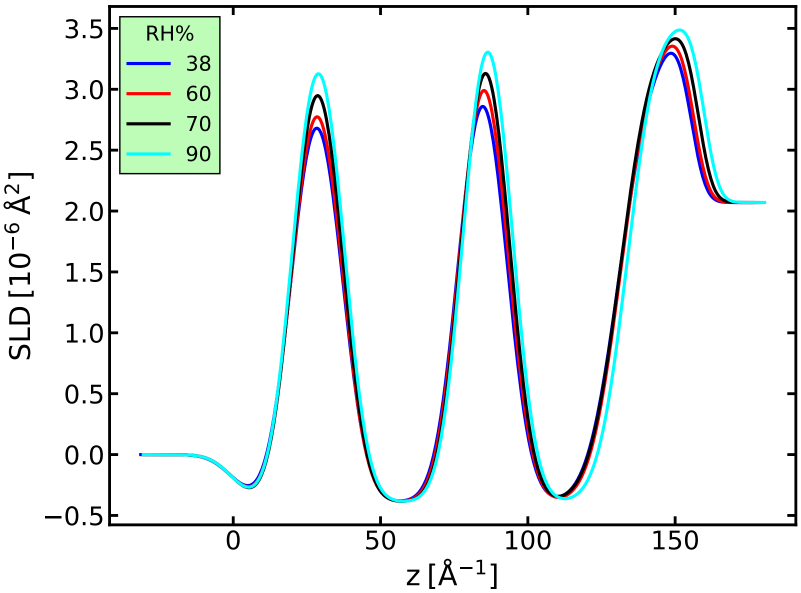

Figure B.10: SLD profiles for NR obtained by fitting D_2O curves (see Figure B.9).

B.6.C Fitted parameters-Pentalayer PS(80%)-PC(20%)

B.6.C.i Pentalayer PS(80%)-PC(30%) (HR=38%)

RH=38 %

Slab	Thickness (Å)	SLD (x10^{-6} Å^{-2})	Roughness (Å)	vfsolv (%)
Air	0.0	0.0	0.0	0.0
tail	19.61 +/- 0.08	-0.39	6.6 +/- 0.06	0.0
head PS80	7.23	2.55	6.6 +/- 0.06	0.38
d2O	3.05 +/- 0.3	4.14 +/- 0.14	6.6 +/- 0.06	0.0
head PS80	7.23	2.55	6.6 +/- 0.06	0.38
tail	19.61 +/- 0.08	-0.39	6.6 +/- 0.06	0.0
tail	19.61 +/- 0.08	-0.39	6.6 +/- 0.06	0.0
head PS80	7.23	2.55	6.6 +/- 0.06	0.38
d2O	2.25 +/- 0.14	6.36	6.6 +/- 0.06	0.0
head PS80	7.23	2.55	6.6 +/- 0.06	0.38
tail	19.61 +/- 0.08	-0.39	6.6 +/- 0.06	0.0
tail	18.25 +/- 0.25	-0.39	8.63 +/- 0.13	0.0
head PC	7.08	1.88	8.63 +/- 0.13	0.49 +/- 0.07
d2O	0.49 +/- 0.44	4.14 +/- 0.14	8.63 +/- 0.13	0.0
SiO2	16.9	3.41	6.9	0.13
Si	0.0	2.07	3.9	0.0

Table B.31: Best fitted parameters: Pentalayer PS(80%)-PC(20%) at HR=38%

B.6.C.ii Pentalayer PS(80%)-PC(20%) (HR=60%)

RH=60 %

Slab	Thickness (Å)	SLD (x10⁻⁶ Å⁻²)	Roughness (Å)	vfsolv (%)
Air	0.0	0.0	0.0	0.0
tail	19.71 +/- 0.07	-0.39	6.45 +/- 0.06	0.0
head PS80	7.26	2.55	6.45 +/- 0.06	0.38
d2O	2.99 +/- 0.26	4.27 +/- 0.12	6.45 +/- 0.06	0.0
head PS80	7.26	2.55	6.45 +/- 0.06	0.38
tail	19.71 +/- 0.07	-0.39	6.45 +/- 0.06	0.0
tail	19.71 +/- 0.07	-0.39	6.45 +/- 0.06	0.0
head PS80	7.26	2.55	6.45 +/- 0.06	0.38
d2O	2.4 +/- 0.12	6.36	6.45 +/- 0.06	0.0
head PS80	7.26	2.55	6.45 +/- 0.06	0.38
tail	19.71 +/- 0.07	-0.39	6.45 +/- 0.06	0.0
tail	18.24 +/- 0.22	-0.39	8.36 +/- 0.12	0.0
head PC	7.07	1.88	8.36 +/- 0.12	0.54 +/- 0.06
d2O	0.73 +/- 0.39	4.27 +/- 0.12	8.36 +/- 0.12	0.0
SiO2	16.9	3.41	6.9	0.13
Si	0.0	2.07	3.9	0.0

Table B.32: Best fitted parameters: Pentalayer PS(80%)-PC(20%) at HR=60%

B.6.C.iii Pentalayer PS(80%)-PC(20%) (HR=70%)

RH=70 %

Slab	Thickness (Å)	SLD (x10^{-6} Å^{-2})	Roughness (Å)	vfsolv (%)
Air	0.0	0.0	0.0	0.0
tail	19.78 +/- 0.07	-0.39	6.3 +/- 0.06	0.0
head PS80	7.29	2.55	6.3 +/- 0.06	0.38
d2O	3.17 +/- 0.26	4.5 +/- 0.13	6.3 +/- 0.06	0.0
head PS80	7.29	2.55	6.3 +/- 0.06	0.38
tail	19.78 +/- 0.07	-0.39	6.3 +/- 0.06	0.0
tail	19.78 +/- 0.07	-0.39	6.3 +/- 0.06	0.0
head PS80	7.29	2.55	6.3 +/- 0.06	0.38
d2O	2.5 +/- 0.13	6.36	6.3 +/- 0.06	0.0
head PS80	7.29	2.55	6.3 +/- 0.06	0.38
tail	19.78 +/- 0.07	-0.39	6.3 +/- 0.06	0.0
tail	17.47 +/- 0.21	-0.39	8.74 +/- 0.13	0.0
head PC	6.78	1.88	8.74 +/- 0.13	0.41 +/- 0.06
d2O	2.73 +/- 0.37	4.5 +/- 0.13	8.74 +/- 0.13	0.0
SiO2	16.9	3.41	6.9	0.13
Si	0.0	2.07	3.9	0.0

Table B.33: Best fitted parameters: Pentalayer PS(80%)-PC(20%) at HR=70%

B.6.C.iv Pentalayer PS(80%)-PC(30%) (HR=90%)

RH=90 %

Slab	Thickness (Å)	SLD (x10^{-6} Å^{-2})	Roughness (Å)	vfsolv (%)
Air	0.0	0.0	0.0	0.0
tail	19.79 +/- 0.05	-0.39	6.36 +/- 0.04	0.0
head PS80	7.29	2.55	6.36 +/- 0.04	0.38
d2O	3.66 +/- 0.18	4.76 +/- 0.09	6.36 +/- 0.04	0.0
head PS80	7.29	2.55	6.36 +/- 0.04	0.38
tail	19.79 +/- 0.05	-0.39	6.36 +/- 0.04	0.0
tail	19.79 +/- 0.05	-0.39	6.36 +/- 0.04	0.0
head PS80	7.29	2.55	6.36 +/- 0.04	0.38
d2O	2.97 +/- 0.1	6.36	6.36 +/- 0.04	0.0
head PS80	7.29	2.55	6.36 +/- 0.04	0.38
tail	19.79 +/- 0.05	-0.39	6.36 +/- 0.04	0.0
tail	19.56 +/- 0.2	-0.39	8.21 +/- 0.09	0.0
head PC	7.59	1.88	8.21 +/- 0.09	0.69 +/- 0.05
d2O	0.76 +/- 0.34	4.76 +/- 0.09	8.21 +/- 0.09	0.0
SiO2	16.9	3.41	6.9	0.13
Si	0.0	2.07	3.9	0.0

Table B.34: Best fitted parameters: Pentalayer PS(80%)-PC(20%) at HR=90%

B.7 Area per molecule and Hydration number

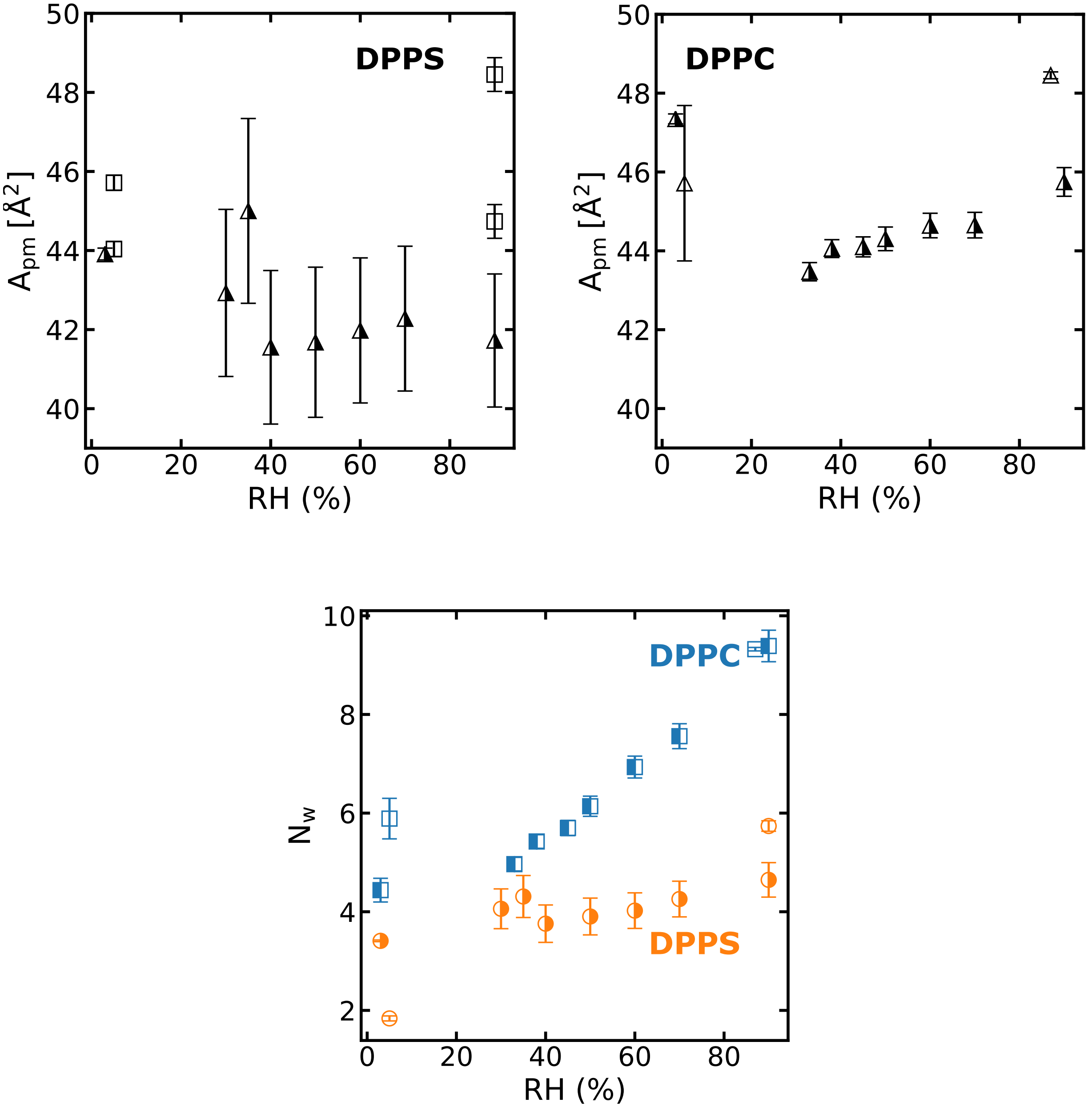

Figure B.11: (Top) Area per lipid for DPPS and DPPC, computed from tail thickness fitted by XR and NR. (Bottom) Hydration number from DPPC and DPPS trilayers: $N_w = d_{w2}A_{pm}/2V_{m,w}$ with $V_{m,w} = 30$ Å^3.

In this appendix, we present the surface area per lipid values for DPPS and DPPC, calculated from the tail thickness obtained from the XR and NR experiments (Figures B.11 top). The area per molecule remains constant within experimental uncertainties and in agreement with literature values [134, 135].

We also show the number of water per lipid molecule N_w for the DPPC and DPPS trilayers calculated as :

$$N_\mathrm{w} = \frac{d_{\mathrm{w}2} A_\mathrm{pm}}{2 V_\mathrm{m,w}}, \tag{B.1}$$

with $V_\mathrm{m,w} = 30\ \mathrm{\AA}^3$.

The number of water molecules per lipid increases with relative humidity (RH) for DPPC and remains constant within experimental uncertainties for DPPS.

Appendix C

Friction

This appendix includes supplementary work on friction experiments.

C.1 Area measurement and contact pressure

Figure C.1 plots the optically measured contact area as a function of normal force for glass-to-glass contact and in the presence of a DSPC trilayer for different relative humidities. No difference was observed between the different samples. We also show the comparison with the Hertz model:

$$\frac{4E^{\star}a^3}{3R} = F_{\mathrm{n}}, \tag{C.1}$$

and with the DMT model:

$$\frac{4E^{\star}a^3}{3R} = F_{\mathrm{n}} + 2\pi R\Delta\gamma, \tag{C.2}$$

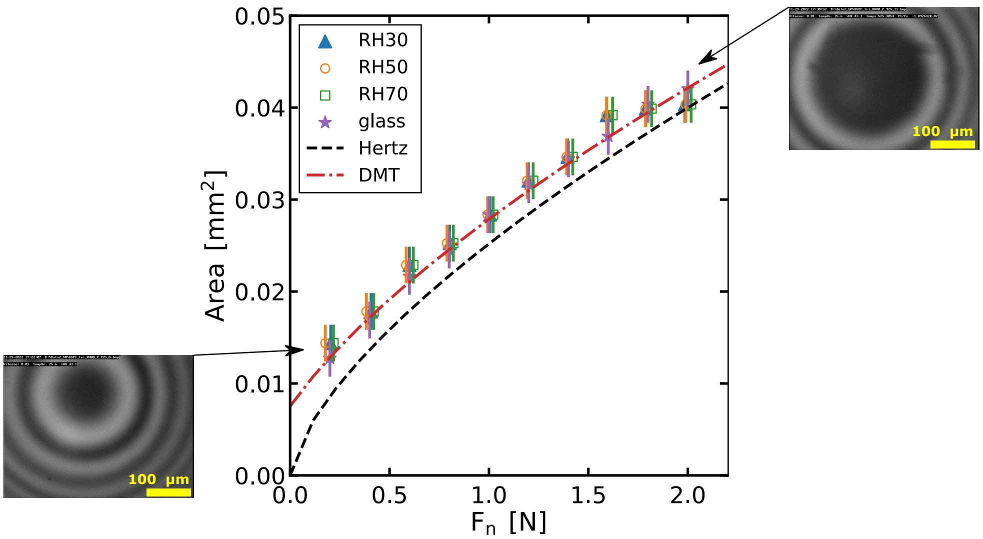

Figure C.1: Evolution of the area of contact *A* between the borosilicate glass indenter of curvature radius R=0.051 m and the soda lime substrate without monolayer (★) and with a DSPC trilayer at RH=30% (▲), RH=50% (○) and RH=70% (□). We also show the Hertz model (– – –) and the DMT model (– · –) with an adhesion energy $\Delta\gamma = 0.51$ J/m^2.

with an adhesion energy ($\Delta\gamma$). a is the contact radius, and R is the radius of curvature of the spherical cap indenter. The composite Young modulus $E^\star$ is given by

$$\frac{1}{E^\star} = \frac{1-\nu_1^2}{E_1} + \frac{1-\nu_2^2}{E_2} \tag{C.3}$$

The Hertz model is plotted with the tabulated values for $\nu_1 = 0.23, \nu_2 = 0.2, E_1 = 72.10^9$ Pa, $E_2 = 64.10^9$ Pa and $R = 0.051$ m. The DMT model fits well the data with an adhesion energy $\Delta\gamma = 0.51$ J/m^2.

Figure C.2(Top) shows the pressure distribution in the contact calculated from the Hertz and DMT models and the influence of mechanical pressure on the water thickness d_{w2} Figure C.2 (bottom). There is no significant variation, as the mechanical pressure is much lower than the osmotic pressure.

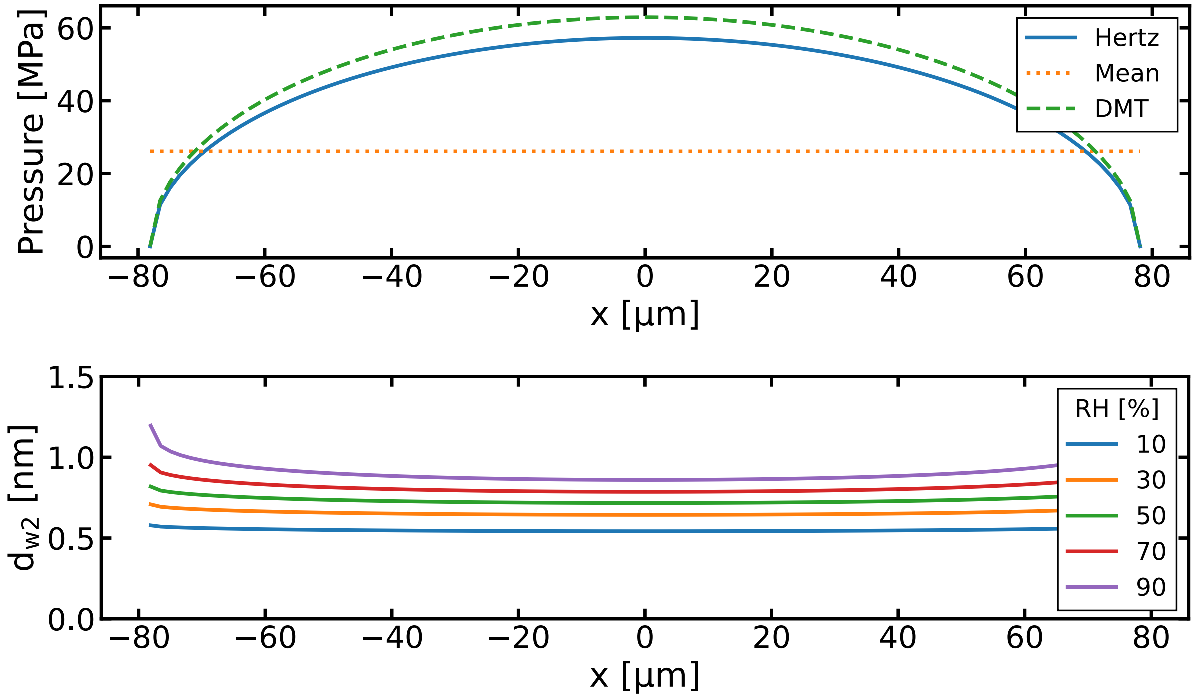

Figure C.2: (Top) Pressure distribution in the contact with the Hertz model (blue) and the DMT model (dashed green). (Bottom) Influence of the mechanical pressure $F_n/\pi a^2$ on d_{w2} for different relative humidity.

C.2 DSPC-DPPC friction comparison

In Figure C.3, we compare the shear stress τ as a function of relative humidity HR for a DPPC trilayer and a DSPC trilayer under the same normal load and velocity conditions ($F_n = 0.5$ N and $V = 10$ μm/s).

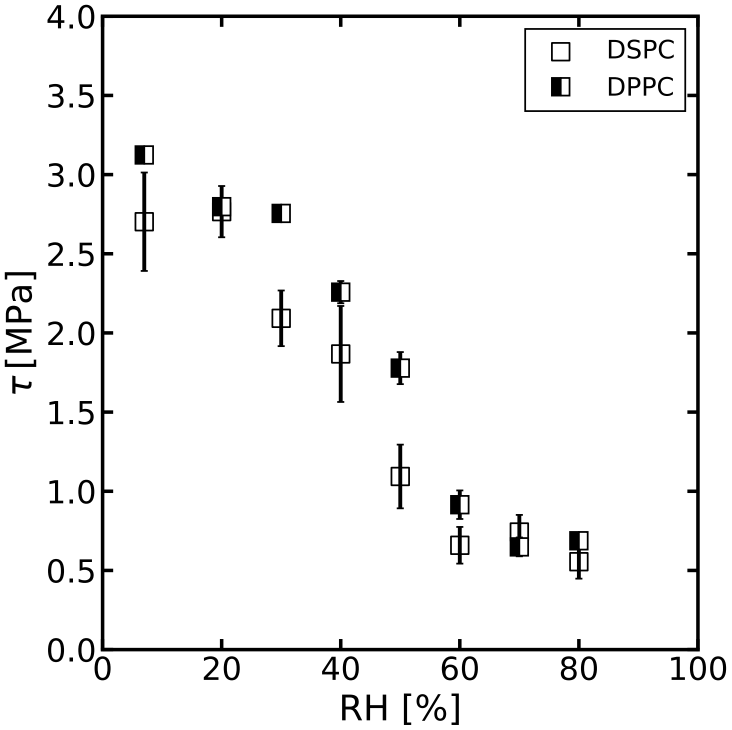

Figure C.3: Variation of shear stress $\tau = F_t/A$ which respect to relative humidity RH for a DPPC (◧) and a DSPC (□) trilayer in same conditions ($F_n = 0.5$ N and $V = 10$ μm/s).

Appendix D

TriboFRAPP

We detailed all the triboFRAPP experiments not shown in Chapter V. All figures are structured similarly: first, we display the second harmonic fluorescence signal. The signal is divided into two parts corresponding to two colors: red, associated with no velocity for the tip, and blue, associated with the sample being sheared at a constant velocity V. Experiments are performed under controlled relative humidity (RH) and at a fixed normal force $F_\mathrm{n} = 0.5\,\mathrm{N}$. Under the first figure, we show a zoom on the blue part during friction, along with the measurement of the associated friction coefficient $\mu = F_\mathrm{t}/F_\mathrm{n}$. The last figure corresponds to an FFT performed on the sliding (blue) and static (red) parts.

D.1 DSPC monolayer

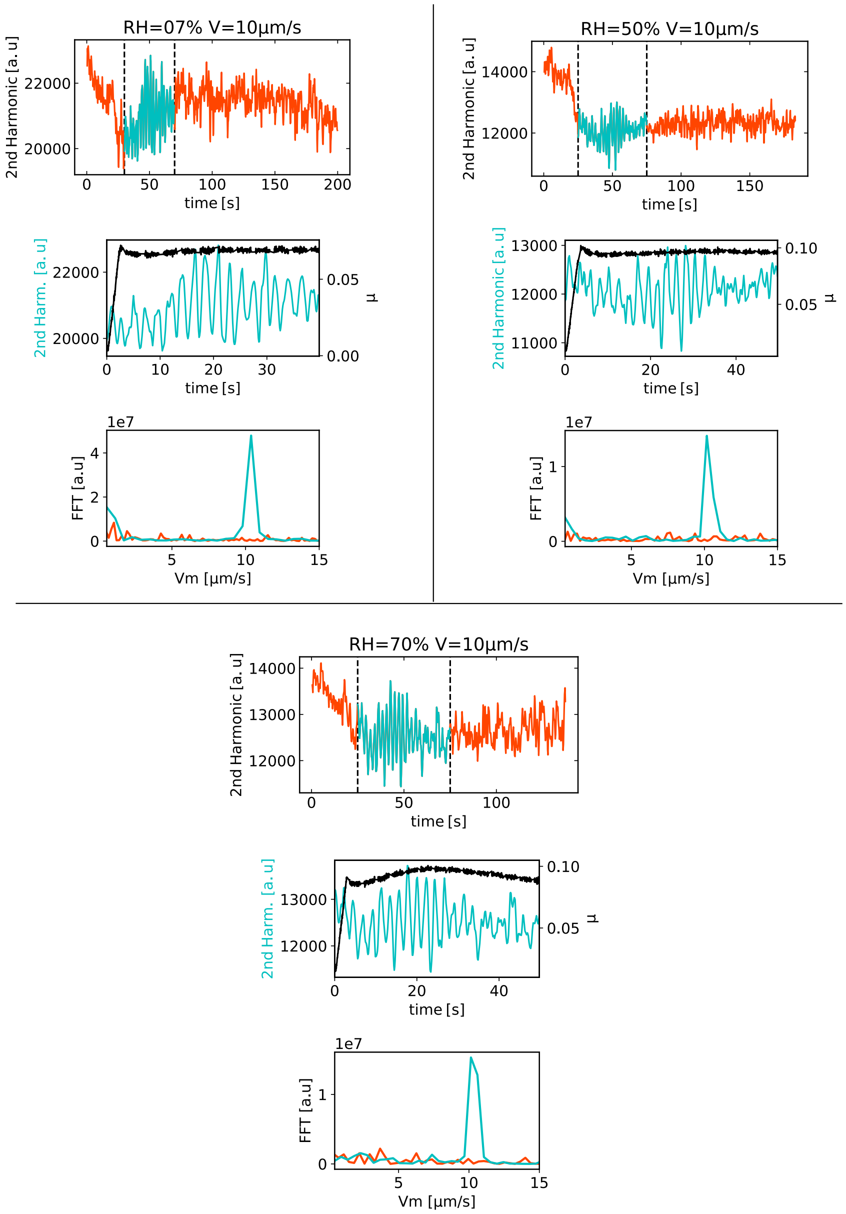

Figure D.1: Monolayer triboFRAPP experiments at constant sliding speed $V = 1\,\mu$m/s. (Top-left) RH=7%.(Top-right) RH=50%. (Bottom) RH=70%

In the case of the DSPC monolayer, our results suggest that the layer is always moving at the tip velocity V.

D.2 DSPC trilayer

D.2.A RH=30%

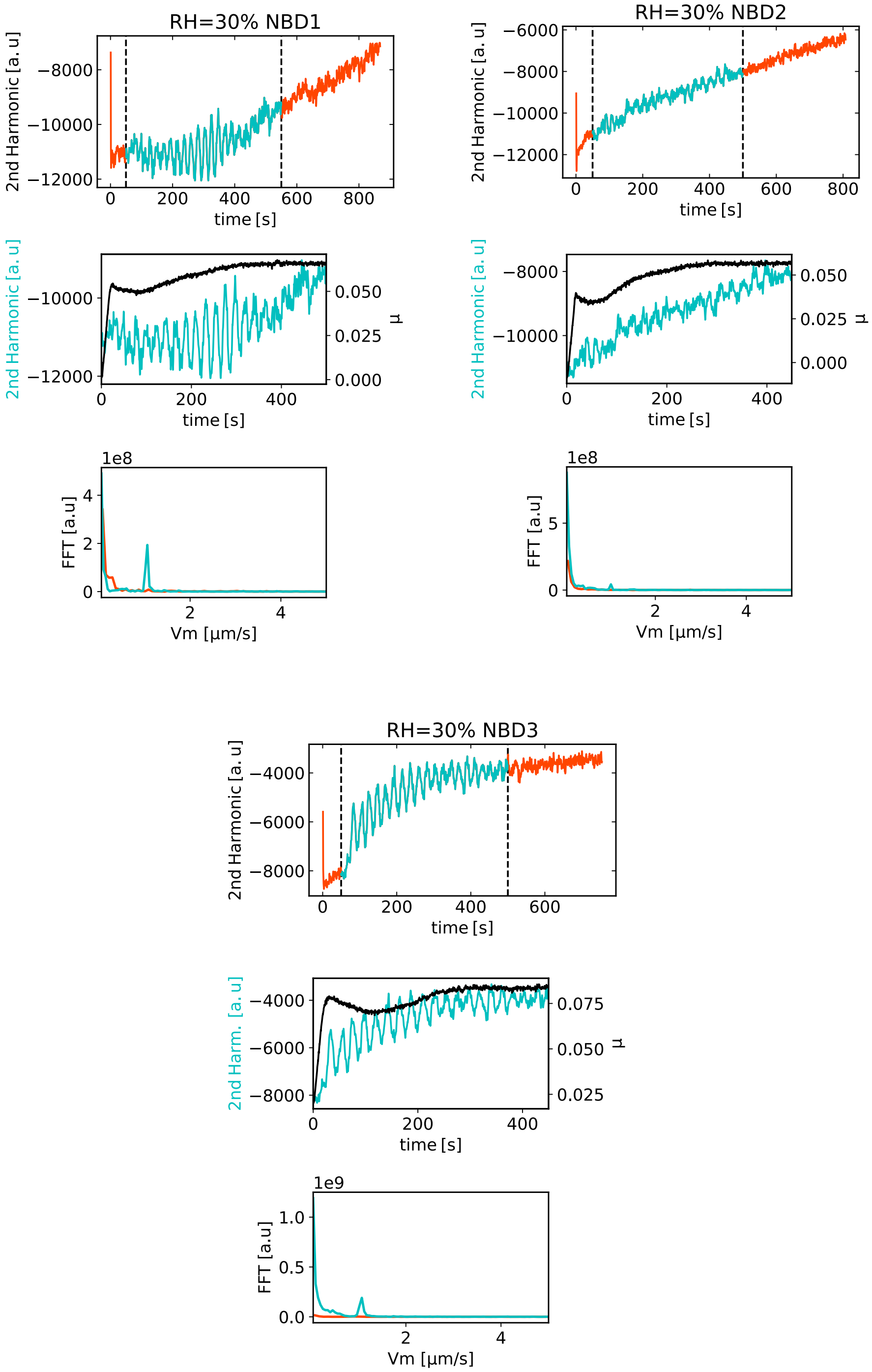

Figure D.2: Trilayer triboFRAPP experiments at constant sliding speed $V = 1\,\mu$m/s and RH=30%. (Top-left) The first layer is marked with a fluorescent label (NBD1).(Top-right) The second layer is marked with a fluorescent label (NBD2). (Bottom) The third layer is marked with a fluorescent label (NBD3).

D.2.B RH=50%

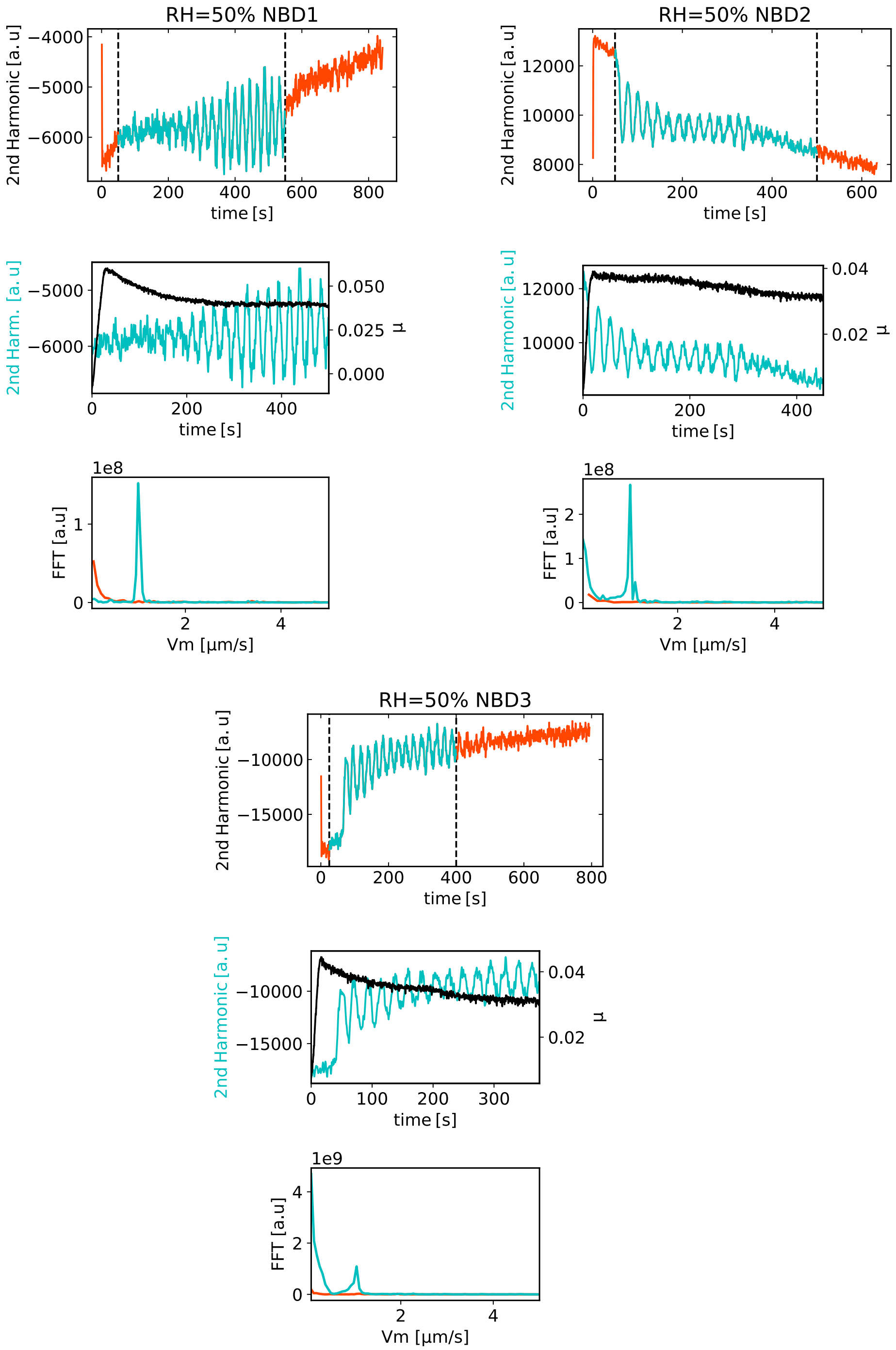

Figure D.3: Trilayer triboFRAPP experiments at constant sliding speed $V = 1\,\mu\text{m/s}$ and RH=50%. (Top-left) The first layer is marked with a fluorescent label (NBD1).(Top-right) The second layer is marked with a fluorescent label (NBD2). (Bottom) The third layer is marked with a fluorescent label (NBD3).

D.2.C RH=70%

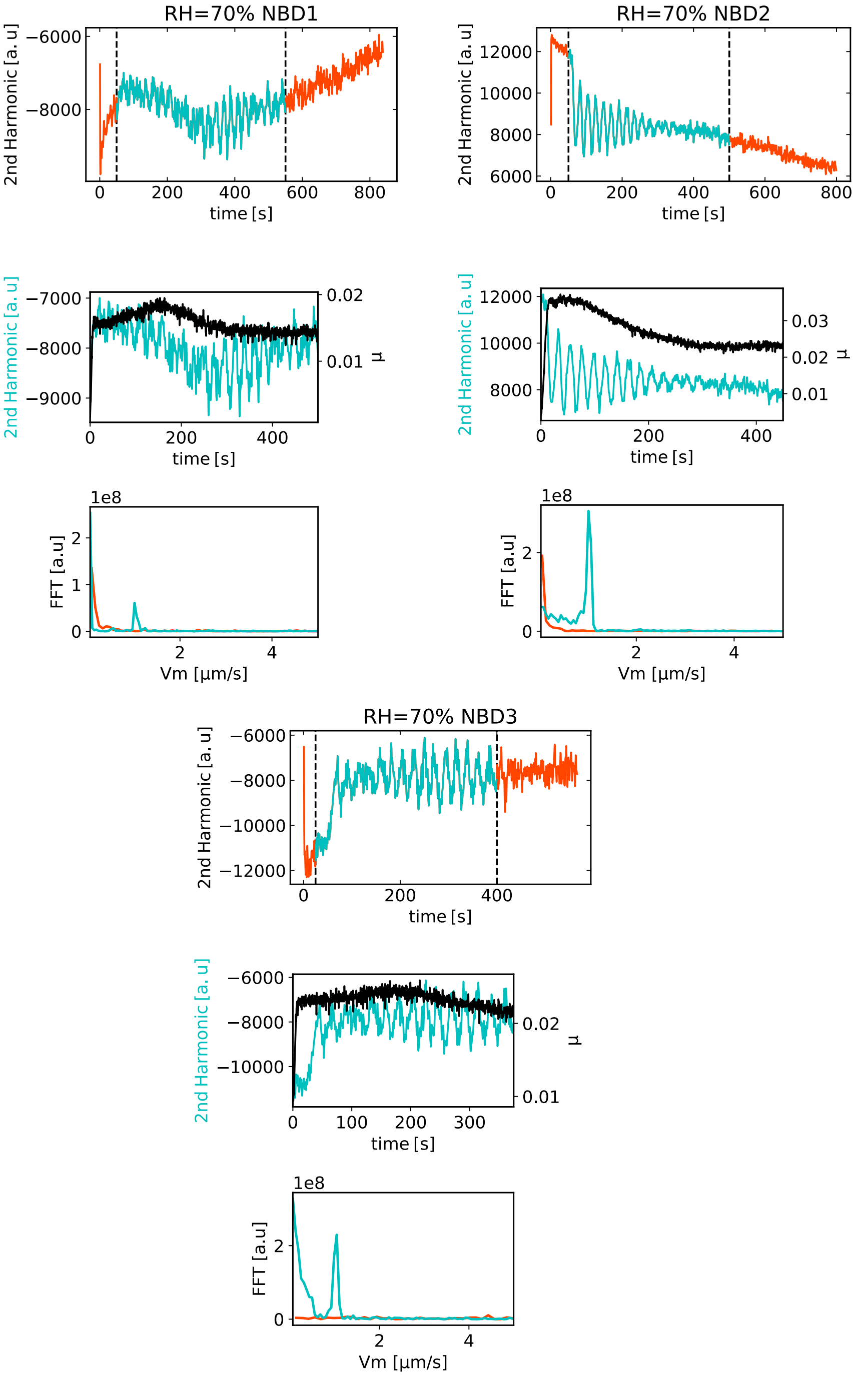

Figure D.4: Trilayer triboFRAPP experiments at constant sliding speed $V = 1\,\mu m/s$ and RH=70%. (Top-left) The first layer is marked with a fluorescent label (NBD1).(Top-right) The second layer is marked with a fluorescent label (NBD2). (Bottom) The third layer is marked with a fluorescent label (NBD3).

In the case of the DSPC trilayer with a tip velocity $V = 1\mu$m/s, our results suggest that all layers are moving for all RH studied.

Bibliography

[1] K. Holmberg and A. Erdemir. Influence of tribology on global energy consumption, costs and emissions. *Friction*, 5(3):263–284, September 2017.

[2] E. Popova and V. L. Popov. The research works of Coulomb and Amontons and generalized laws of friction. *Friction*, 3(2):183–190, May 2015.

[3] F. Blachon. *Membranes lipidiques supportées sur surfaces rugueuses : structure, dynamique et perspectives tribologiques*. PhD thesis, Université de Lyon, December 2016.

[4] J. Gao, W. D. Luedtke, D. Gourdon, M. Ruths, J. N. Israelachvili, and U. Landman. Frictional Forces and Amontons' Law: From the Molecular to the Macroscopic Scale. *J. Phys. Chem. B*, 108(11):3410–3425, March 2004.

[5] J. Williams. The Invention of Tribology: Peter Jost's Contribution. *Lubricants*, 12(3):65, February 2024.

[6] A. Dedinaite, T. Pettersson, B. Mohanty, and P. M. Claesson. Lubrication by organized soft matter. *Soft Matter*, 6(7):1520–1526, March 2010.

[7] A. Sarkar, E. Andablo-Reyes, M. Bryant, D. Dowson, and A. Neville. Lubrication of soft oral surfaces. *Curr. Opin. Colloid Interface Sci.*, 39:61–75,

February 2019.

[8] A. Z. Szeri. *Fluid Film Lubrication*. Cambridge, England, UK, December 2010.

[9] Y. Cao and J. Klein. Lipids and lipid mixtures in boundary layers: From hydration lubrication to osteoarthritis. *Curr. Opin. Colloid Interface Sci.*, 58:101559, April 2022.

[10] L. Ben-Trad, C. I. Matei, M. M. Sava, S. Filali, M. Duclos, Y. Berthier, M. Guichardant, N. Bernoud-Hubac, O. Maniti, A. Landoulsi, M. Blanchin, P. Miossec, T. Granjon, and A. Trunfio-Sfarghiu. Synovial Extracellular Vesicles: Structure and Role in Synovial Fluid Tribological Performances. *Int. J. Mol. Sci.*, 23(19):11998., October 2022.

[11] S. Jahn, J. Seror, and J. Klein. Lubrication of Articular Cartilage. *Annu. Rev. Biomed. Eng.*, (Volume 18, 2016):235–258, July 2016.

[12] H. Forster and J. Fisher. The Influence of Loading Time and Lubricant on the Friction of Articular Cartilage. *Proc. Inst. Mech. Eng. H*, 210(2):109–119, June 1996.

[13] D. J. Hunter and S. Bierma-Zeinstra. Osteoarthritis. *Lancet*, 393(10182):1745–1759, April 2019.

[14] F. Blachon. *Membranes lipidiques supportées sur surfaces rugueuses : structure, dynamique et perspectives tribologiques*. Ph.d. thesis, Université Grenoble Alpes, Feb 2017. HAL Id: tel-01466742.

[15] D. Athanasiou. *Articular Cartilage*. Andover, England, UK, December 2016.

[16] B. Abernethy. *Biophysical Foundations of Human Movement*. 2013.

[17] D. Burstein, M. Gray, T. Mosher, and B. Dardzinski. Measures of Molecu-

lar Composition and Structure in Osteoarthritis. *Radiol. Clin. North Am.*, 47(4):675–86, August 2009.

[18] H. Muir. The chondrocyte, architect of cartilage. Biomechanics, structure, function and molecular biology of cartilage matrix macromolecules. *Bioessays*, 17(12):1039–1048, December 1995.

[19] H. Muir, P. Bullough, and A. Maroudas. The distribution of collagen in human articular cartilage with some of its physiological implications. *J. Bone Joint Surg. Br.*, 52(3):554–563, August 1970.

[20] J. L. Silverberg, A. R. Barrett, M. Das, P. B. Petersen, L. J. Bonassar, and I. Cohen. Structure-Function Relations and Rigidity Percolation in the Shear Properties of Articular Cartilage. *Biophys. J.*, 107(7):1721, October 2014.

[21] R. Amad, G. Werner, and H. Neukom. Water content of human articular cartilage and its determination by gas chromatography. *Biochem. Med.*, 16(2):169–172, October 1976.

[22] J. A. Buckwalter and H. J. Mankin. Articular cartilage: tissue design and chondrocyte-matrix interactions. *Instr. Course Lect.*, 47:477-86.(;):Instr, 1998.

[23] R. Crawford. Normal and prosthetic synovial joints are lubricated by surface-active phospholipid: a hypothesis. *J. Arthroplasty*, January 2003.

[24] P. J. Basser, R. Schneiderman, R. A. Bank, E. Wachtel, and A. Maroudas. Mechanical properties of the collagen network in human articular cartilage as measured by osmotic stress technique. *Arch. Biochem. Biophys.*, 351(2):207–219, March 1998.

[25] B. A. Hills. Oligolamellar lubrication of joints by surface active phospho-

lipid. *J. Rheumatol.*, 16(1):82–91, January 1989.

[26] C. I. Matei, C. Boulocher, C. Boulé, M. Schramme, E. Viguier, T. Roger, Y. Berthier, A. M. Trunfio-Sfarghiu, and M. G. Blanchin. Ultrastructural Analysis of Healthy Synovial Fluids in Three Mammalian Species. *Microsc. Microanal.*, 20(3):903–911, June 2014.

[27] P. S. Walker, D. Dowson, M. D. Longfield, and V. Wright. "Boosted lubrication" in synovial joints by fluid entrapment and enrichment. *Ann. Rheum. Dis.*, 27(6):512, November 1968.

[28] V. Wright, D. Dowson, and M. D. Longfied. Joint stiffness–its characterisation and significance. *Biomed. Eng.*, 4(1):8–14, January 1969.

[29] J. Seror, L. Zhu, R. Goldberg, A. J. Day, and J. Klein. Supramolecular synergy in the boundary lubrication of synovial joints. *Nat. Commun.*, 6(6497):1–7, March 2015.

[30] M. C. Corneci, F. Dekkiche, A. M. Trunfio-Sfarghiu, M. Hélène Meurisse, Y. Berthier, and J.-P. Rieu. Tribological properties of fluid phase phospholipid bilayers. *Tribol. Int.*, 44(12):1959–1968, November 2011.

[31] A.-M. Trunfio-Sfarghiu, Y. Berthier, M.-H. Meurisse, and J.-P. Rieu. Role of Nanomechanical Properties in the Tribological Performance of Phospholipid Biomimetic Surfaces. *Langmuir*, 24(16):8765–8771, August 2008.

[32] G. Oncins, S. Garcia-Manyes, and F. Sanz. Study of frictional properties of a phospholipid bilayer in a liquid environment with lateral force microscopy as a function of NaCl concentration. *Langmuir*, 21(16):7373–7379, August 2005.

[33] W. H. Briscoe. Aqueous boundary lubrication: Molecular mechanisms, design strategy, and terra incognita. *Curr. Opin. Colloid Interface Sci.*,

27:1–8, February 2017.

[34] U. Raviv and J. Klein. Fluidity of bound hydration layers. *Science*, 297(5586):1540–1543, August 2002.

[35] W. H. Briscoe, S. Titmuss, F. Tiberg, R. K. Thomas, D. J. McGillivray, and J. Klein. Boundary lubrication under water. *Nature*, 444(7116):191–194, November 2006.

[36] M. Chen, W. H. Briscoe, S. P. Armes, and J. Klein. Lubrication at physiological pressures by polyzwitterionic brushes. *Science*, 323(5922):1698–1701, March 2009.

[37] R. Goldberg, A. Schroeder, Y. Barenholz, and J. Klein. Interactions between Adsorbed Hydrogenated Soy Phosphatidylcholine (HSPC) Vesicles at Physiologically High Pressures and Salt Concentrations. *Biophys. J.*, 100(10):2403, May 2011.

[38] R. Goldberg, A. Schroeder, G. Silbert, K. Turjeman, Y. Barenholz, and J. Klein. Boundary lubricants with exceptionally low friction coefficients based on 2D close-packed phosphatidylcholine liposomes. *Adv. Mater.*, 23(31):3517–3521, August 2011.

[39] R. Sorkin, Y. Dror, N. Kampf, and J. Klein. Mechanical stability and lubrication by phosphatidylcholine boundary layers in the vesicular and in the extended lamellar phases. *Langmuir*, 30(17):5005–5014, May 2014.

[40] S. Tristram-Nagle and J. F. Nagle. Lipid bilayers: thermodynamics, structure, fluctuations, and interactions. *Chem. Phys. Lipids*, 127(1):3, January 2004.

[41] L. Ma, A. Gaisinskaya-Kipnis, N. Kampf, and J. Klein. Origins of hydration lubrication. *Nat. Commun.*, 6(6060):1–6, January 2015.

[42] B. Cross, A. Steinberger, C. Cottin-Bizonne, J.-P. Rieu, and E. Charlaix. Boundary flow of water on supported phospholipid films. *Europhys. Lett.*, 73(3):390–395, February 2006.

[43] A. Boan, L. Joly, N. Fillot, and C. Loison. Mixed Mechanism of Lubrication by Lipid Bilayer Stacks. *Langmuir*, 31(44):12197–12202, November 2015.

[44] A.Allemand, M.Zhao, O.Vincent, R.Fulcrand, L.Joly, C.Ybert, and A.-L.Biance. Anomalous ionic transport in tunable angstrom-size water films on silica. *Proc. Natl. Acad. Sci. U.S.A.*, 120(25):e2221304120, June 2023.

[45] J.N.Israelachvili. *Intermolecular and Surface Forces*. 2011.

[46] L. Fu. *Rhéologie des polymères dans les contacts confinés : tribologie des interfaces étudiées par un nouveau dispositif couplant FRAPP et nanotribologie*. PhD thesis, Université de, Strasbourg, France, October 2015.

[47] Z. Pawlak and R. Pai. Friction on charged and neutral soft natural matter surfaces. *Clinical and Medical Investigations*, 4(3), January 2019.

[48] J. Li, J. Li, L. Jiang, X. Chen, and J. Luo. Cationic Surfactant Micelles Lubricate Graphitic Surface in Water. *Langmuir*, 35(34):11108–11113, August 2019.

[49] T. Han, C. Zhang, and J. Luo. Macroscale Superlubricity Enabled by Hydrated Alkali Metal Ions. *Langmuir*, 34(38):11281–11291, September 2018.

[50] T. Han, C. Zhang, J. Li, S. Yuan, X. Chen, J. Zhang, and J. Luo. Origins of Superlubricity Promoted by Hydrated Multivalent Ions. *J. Phys. Chem.*

Lett., 11(1):184–190, January 2020.

[51] H. Lodish, A. Berk, C. A. Kaiser, M. Krieger, M. P. Scott, A. Bretscher, H. Ploegh, and P. Matsudaira. *Molecular Cell Biology*. June 2007.

[52] O. G. Mouritsen and L. A. Bagatolli. *LIFE - AS A MATTER OF FAT*. Cham, Switzerland, 2016.

[53] G. van Meer. Cellular lipidomics. *EMBO J.*, September 2005.

[54] Avanti Research. Avanti Research.

[55] M. Edidin. Lipids on the frontier: a century of cell-membrane bilayers. *Nat. Rev. Mol. Cell Biol.*, 4(5):414–418, May 2003.

[56] J. Kurniawan, J. F. Ventrici de Souza, A. T. Dang, G. y. Liu, and T. L. Kuhl. Preparation and Characterization of Solid-Supported Lipid Bilayers Formed by Langmuir–Blodgett Deposition: A Tutorial. *Langmuir*, 34(51):15622–15639, December 2018.

[57] I. Langmuir. THE CONSTITUTION AND FUNDAMENTAL PROPERTIES OF SOLIDS AND LIQUIDS. PART I. SOLIDS. *J. Am. Chem. Soc.*, 38(11):2221–2295, November 1916.

[58] K. A. Davis. Katharine Blodgett and thin films. *J. Chem. Educ.*, 61(5):437, May 1984.

[59] T.Mukhina, A.Hemmerle, V.Rondelli, Y.Gerelli, G.Fragneto, J.Daillant, and T.Charitat. Attractive Interaction between Fully Charged Lipid Bilayers in a Strongly Confined Geometry. *J. Phys. Chem. Lett.*, 10(22):7195–7199, November 2019.

[60] UGAP-Dustcher. Microscope slides.

[61] A.Hemmerle, L.Malaquin, T.Charitat, S.Lecuyer, G.Fragneto, and J.Daillant. Controlling interactions in supported bilayers from weak electro-

static repulsion to high osmotic pressure. *Proc. Natl. Acad. Sci. U.S.A.*, 109(49):19938–19942, December 2012.

[62] N. Chada, K. P. Sigdel, R. R. S. Gari, T. R. Matin, L. L. Randall, and G. M. King. Glass is a Viable Substrate for Precision Force Microscopy of Membrane Proteins. *Sci. Rep.*, 5(12550):1–8, July 2015.

[63] KSV. Ksv nima lb.

[64] R. Pichot, R. L. Watson, and I. T. Norton. Phospholipids at the Interface: Current Trends and Challenges. *Int. J. Mol. Sci.*, 14(6):11767, June 2013.

[65] I. Palaia. *Charged systems in, out of, and driven to equilibrium : from nanocapacitors to cement*. PhD thesis, Université Paris-Saclay (ComUE), Paris, France, November 2019.

[66] J. Daillant and A. Gibaud. *X-Ray and Neutron Reflectivity: Principles and Applications*. Berlin, Germany, 1999.

[67] S. Combet. An introduction to neutrons for biology. *EPJ Web of Conferences*, 236:01001, January 2020.

[68] E. Schneck, F. Rehfeldt, R. G. Oliveira, C. Gege, B. Demé, and M. Tanaka. Modulation of intermembrane interaction and bending rigidity of biomembrane models via carbohydrates investigated by specular and off-specular neutron scattering. *Phys. Rev. E*, 78(6):Pt, December 2008.

[69] R. Cubitt and G. Fragneto. D17: the new reflectometer at the ILL. *Appl. Phys. A*, 74(1):s329–s331, December 2002.

[70] A. Hemmerle, N. Aubert, T. Moreno, P. Kékicheff, B. Benoît, S. Spagnoli, M. Goldmann, G. Ciatto, and P. Fontaine. Opportunities and new developments for the study of surfaces and interfaces in soft condensed matter

at the SIRIUS beamline of Synchrotron SOLEIL. *J. Synchrotron Radiat.*, 31(Pt 1):162, January 2024.

[71] C. Gauthier, S. Lafaye, and R. Schirrer. Elastic recovery of a scratch in a polymeric surface: experiments and analysis. *Tribol. Int.*, 34(7):469–479, July 2001.

[72] A. Rubin, C. Gauthier, and R. Schirrer. The friction coefficient on polycarbonate as a function of the contact pressure and nanoscale roughness. *J. Polym. Sci., Part B: Polym. Phys.*, 50(8):580–588, April 2012.

[73] É. J. Charrault. *Analyse mécanique et physico-chimique de la relation entre le frottement et l'adhésion*. PhD thesis, Université Louis Pasteur (Strasbourg) (1971-2008), Strasbourg, France, January 2007.

[74] L. Fu, D. Favier, T. Charitat, C. Gauthier, and A. Rubin. A new tribological experimental setup to study confined and sheared monolayers. *Rev. Sci. Instrum.*, 87(3):033903, March 2016.

[75] J. Davoust, P. F. Devaux, and L. Léger. Fringe pattern photobleaching, a new method for the measurement of transport coefficients of biological macromolecules. *EMBO J.*, 1(10):1233–1238, 1982.

[76] F. Pincet, V. Adrien, R. Yang, J. J. Delacotte, J. E. Rothman, W. Urbach, and D. Tareste. FRAP to Characterize Molecular Diffusion and Interaction in Various Membrane Environments. *PLoS One*, 11(7):e0158457, July 2016.

[77] E. Durliat. *Etude experimentale du glissement d'un polymere fondu sur une surface solide decoree de polymere*. PhD thesis, Paris 6, Paris, France, January 1997.

[78] H. Spikes. Stress-augmented thermal activation: Tribology feels the force. *Friction*, 6(1):1–31, March 2018.

[79] H. Eyring. Viscosity, Plasticity, and Diffusion as Examples of Absolute Reaction Rates. *J. Chem. Phys.*, 4(4):283–291, April 1936.

[80] L. Prandtl. Ein Gedankenmodell zur kinetischen Theorie der festen Körper. *Z. angew. Math. Mech.*, 8(2):85–106, January 1928.

[81] B. J. Briscoe and D. C. B. Evans. The shear properties of langmuir-blodgett layers. *Proceedings of the Royal Society of London. Series A, Mathematical and Physical Sciences*, 380(1779):389–407, 1982.

[82] Y. Fang, L. Ma, X. Wang, and J. Luo. Numerical Model for Hydration-Lubricated Contact and Its Friction Behavior at Nanoscale. *Front. Mech. Eng.*, 6:564756, September 2020.

[83] C.Herrero and L.Joly. Poisson-Boltzmann formulary: Second edition. *arXiv*, May 2021.

[84] R.R.Netz. Electrostatistics of counter-ions at and between planar charged walls: From Poisson-Boltzmann to the strong-coupling theory. *Eur. Phys. J. E*, 5(1):557–574, August 2001.

[85] A.Naji, M.Kanduč, J.Forsman, and R.Podgornik. Perspective: Coulomb fluids—Weak coupling, strong coupling, in between and beyond. *J. Chem. Phys.*, 139(15), October 2013.

[86] A.Goyal, I.Palaia, K.Ioannidou, F.-J.Ulm, H.van Damme, R.J.-M.Pellenq, E.Trizac, and E.Del Gado. The physics of cement cohesion. *Sci. Adv.*, 7(32), August 2021.

[87] V.A.Bloomfield. Condensation of DNA by multivalent cations: Considerations on mechanism. *Biopolymers*, 31(13):1471–1481, November 1991.

[88] G.C.L.Wong. Electrostatics of rigid polyelectrolytes. *Curr. Opin. Colloid Interface Sci.*, 11(6):310–315, December 2006.

[89] P.Kékicheff, S.Marcĕlja, T.J.Senden, and V.E.Shubin. Charge reversal seen in electrical double layer interaction of surfaces immersed in 2:1 calcium electrolyte. *J. Chem. Phys.*, 99(8):6098–6113, October 1993.

[90] K.Komorowski, J.Schaeper, M.Sztucki, L.Sharpnack, G.Brehm, S.Köster, and T.Salditt. Vesicle adhesion in the electrostatic strong-coupling regime studied by time-resolved small-angle X-ray scattering. *Soft Matter*, 16(17):4142–4154, May 2020.

[91] I.Palaia, A.Goyal, E.Del Gado, L.Šamaj, and E.Trizac. Like-Charge Attraction at the Nanoscale: Ground-State Correlations and Water Destructuring. *J. Phys. Chem. B*, 126(16):3143–3149, April 2022.

[92] L.Fumagalli, A.Esfandiar, R.Fabregas, S.Hu, P.Ares, A.Janardanan, Q.Yang, B.Radha, T.Taniguchi, K.Watanabe, G.Gomila, K.S.Novoselov, and A.K.Geim. Anomalously low dielectric constant of confined water. *Science*, 360(6395):1339–1342, June 2018.

[93] L. J. Lis, M. Mcalister, N. Fuller, R. P. Rand, and V. A. Parsegian. INTERACTIONS BETWEEN NEUTRAL PHOSPHOLIPID BILAYER MEMBRANES. *Biophys. J.*, 37(3):657–665, March 1982.

[94] A.Schlaich, J.O.Daldrop, B.Kowalik, M.Kanduč, E.Schneck, and R.R.Netz. Water Structuring Induces Nonuniversal Hydration Repulsion between Polar Surfaces: Quantitative Comparison between Molecular Simulations, Theory, and Experiments. *Langmuir*, 40(15):7896–7906, April 2024.

[95] A.Schlaich, A.P.dos Santos, and R.R.Netz. Simulations of Nanoseparated Charged Surfaces Reveal Charge-Induced Water Reorientation and Nonadditivity of Hydration and Mean-Field Electrostatic Repulsion. *Langmuir*, 35(2):551–560, January 2019.

[96] X.Chen, W.Hua, Z.Huang, and H.C.Allen. Interfacial Water Structure Associated with Phospholipid Membranes Studied by Phase-Sensitive Vibrational Sum Frequency Generation Spectroscopy. *J. Am. Chem. Soc.*, 132(32):11336–11342, August 2010.

[97] T. Shuichi and W. Nobuyuki. Atomic Force Microscopy Observation of the Phase Separation in Acidic Phospholipid/Neutral Phospholipid Supported Bilayers. *Jpn. J. Appl. Phys.*, 41(7S):4987, July 2002.

[98] J. Daillant and A. Gibaud. *X-Ray and Neutron Reflectivity: Principles and Applications*, volume 58. January 2008.

[99] A.R.J.Nelson and S.W.Prescott. refnx: neutron and X-ray reflectometry analysis in Python. *J. Appl. Crystallogr.*, 52(1):193–200, February 2019.

[100] A. Vishnyakov, T. Li, and A. V. Neimark. Adhesion of Phospholipid Bilayers to Hydroxylated Silica: Existence of Nanometer-Thick Water Interlayers. *Langmuir*, 33(45):13148–13156, November 2017.

[101] H. I. Petrache, N. Gouliaev, S. Tristram-Nagle, R. Zhang, R. M. Suter, and J. F. Nagle. Interbilayer interactions from high-resolution x-ray scattering. *Phys. Rev. E*, 57(6):7014–7024, June 1998.

[102] S. Tristram-Nagle, H. I. Petrache, and J. F. Nagle. Structure and interactions of fully hydrated dioleoylphosphatidylcholine bilayers. *Biophys. J.*, 75(2):917, August 1998.

[103] A.G.Moreira and R.R.Netz. Simulations of counterions at charged plates. *Eur. Phys. J. E*, 8(1):33–58, May 2002.

[104] W. Xu and F. Pincet. Quantification of phase transitions of lipid mixtures from bilayer to non-bilayer structures: Model, experimental validation and implication on membrane fusion. *Chem. Phys. Lipids*,

163(3):280–285, March 2010.

[105] H. I. Petrache, S. Tristram-Nagle, K. Gawrisch, D. Harries, V. A. Parsegian, and J. F. Nagle. Structure and Fluctuations of Charged Phosphatidylserine Bilayers in the Absence of Salt. *Biophys. J.*, 86(3):1574, March 2004.

[106] M. J. Abraham, T. Murtola, R. Schulz, S. Páll, J. C. Smith, B. Hess, and E. Lindahl. Gromacs: High performance molecular simulations through multi-level parallelism from laptops to supercomputers. *SoftwareX*, 1-2:19–25, 2015.

[107] J. B. Klauda, R. M. Venable, J. A. Freites, J. W. OConnor, D. J. Tobias, C. Mondragon-Ramirez, I. Vorobyov, A. D. MacKerell Jr., and R. W. Pastor. Update of the charmm all-atom additive force field for lipids: Validation on six lipid types. *The Journal of Physical Chemistry B*, 114(23):7830–7843, 2010.

[108] S. Izadi, R. Anandakrishnan, and A. V. Onufriev. Building water models: A different approach. *The Journal of Physical Chemistry Letters*, 5(21):3863–3871, 2014.

[109] R. W. Pastor and A. D. MacKerell Jr. Development of the charmm force field for lipids. *J. Phys. Chem. Lett.*, 2(13):1526–1532, 2011.

[110] W. Humphrey, A. Dalke, and K. Schulten. Vmd: Visual molecular dynamics. *Journal of Molecular Graphics*, 14(1):33–38, 1996.

[111] B. Maranville. Interactive, web-based calculator of neutron and x-ray reflectivity. (122), 2017-07-12 2017.

[112] N. Michaud-Agrawal, E. J. Denning, T. B. Woolf, and O. Beckstein. Mdanalysis: A toolkit for the analysis of molecular dynamics simulations. *Journal of Computational Chemistry*, 32(10):2319–2327, 2011.

[113] D. Bach and I. R. Miller. Hydration of phospholipid bilayers in the presence and absence of cholesterol. *Biochimica et Biophysica Acta (BBA) - Biomembranes*, 1368(2):216–224, 1998.

[114] M. Sturm, O. Gutowski, and G. Brezesinski. The influence of calcium traces in ultrapure water on the lateral organization in tetramyristoyl cardiolipin monolayers. *ChemPhysChem*, 20(11):1521–1526, 2019.

[115] G. Violano, G. P. Demelio, and L. Afferrante. On the DMT adhesion theory: from the first studies to the modern applications in rough contacts. *Procedia Struct. Integrity*, 12:58–70, January 2018.

[116] D. dinait, W. D. C. Florian, B. Piotr, and C. Per M. Biolubrication synergy: Hyaluronan – Phospholipid interactions at interfaces. *Adv. Colloid Interface Sci.*, 274:102050, December 2019.

[117] L. K. Li, S. Y. Shapiro, and L. J. C. M. Li. Scratch test of soda-lime glass. *Acta Mater.*, 46(15):5569–5578, September 1998.

[118] A. Schlaich, J. Kappler, and R. R. Netz. Hydration Friction in Nanoconfinement: From Bulk via Interfacial to Dry Friction. *Nano Lett.*, 17(10):5969–5976, October 2017.

[119] D. Jin and J. Klein. Tuning energy dissipation via topologically electroconvoluted lipid-membrane boundary layers. *arXiv*, March 2023.

[120] E. B. Simonsen, M. Stensvig, T. B. Andersen, and M. S. Andersen. Propulsive fractions of joint work during maximal sprint running. *Sport Sci. Health*, 20(2):455–464, June 2024.

[121] M. H. Muser. Velocity dependence of kinetic friction in the Prandtl-Tomlinson model. *Phys. Rev. B*, 84(12):125419, September 2011.

[122] T. Ree and H. Eyring. Theory of Non-Newtonian Flow. I. Solid Plastic

System. *J. Appl. Phys.*, 26(7):793–800, July 1955.

[123] T. Baumgart and A. Offenhäuser. Lateral Diffusion in Substrate-Supported Lipid Monolayers as a Function of Ambient Relative Humidity. *Biophys. J.*, 83(3):1489–1500, September 2002.

[124] X. Qin, M. Dong, and Q. Li. Insight into the hydration friction of lipid bilayers. *Nanoscale*, 16(5):2402–2408, 2024.

[125] B. N. J. Persson. *Sliding Friction*. Berlin, Germany, 2000.

[126] R. Merkel, E. Sackmann, and E. Evans. Molecular friction and epitactic coupling between monolayers in supported bilayers. *J. Phys.*, 50(12):1535–1555, June 1989.

[127] E. Evans and D. Needham. Physical properties of surfactant bilayer membranes: thermal transitions, elasticity, rigidity, cohesion and colloidal interactions. *J. Phys. Chem.*, 91(16):4219–4228, July 1987.

[128] L. Zhu, J. Seror, A. J. Day, N. Kampf, and J. Klein. Ultra-low friction between boundary layers of hyaluronan-phosphatidylcholine complexes. *Acta Biomater.*, 59:283–292, September 2017.

[129] A. Zgorski, R. W. Pastor, and E. Lyman. Surface Shear Viscosity and Interleaflet Friction from Nonequilibrium Simulations of Lipid Bilayers. *J. Chem. Theory Comput.*, 15(11):6471, September 2019.

[130] R. Pit, H. Hervet, and L. Léger. Friction and slip of a simple liquid at a solid surface. *Tribol. Lett.*, 7(2):147–152, September 1999.

[131] A. A. Anthony, O. Sahin, M. K. Yapici, D. Rogers, and A. R. Honerkamp-Smith. Systematic measurements of interleaflet friction in supported bilayers. *Biophys. J.*, 121(15):2981–2993, August 2022.

[132] L. Léger, H. Hervet, G. Massey, and E. Durliat. Wall slip in polymer melts.

J. Phys.: Condens. Matter, 9(37):7719, January 1999.

[133] L. Porcar and Y. Gerelli. On the lipid flip-flop and phase transition coupling. *Soft Matter*, 16(33):7696–7703, August 2020.

[134] J. F. Nagle, P. Cognet, F. G. Dupuy, and S. Tristram-Nagle. Structure of gel phase dppc determined by x-ray diffraction. *Chemistry and Physics of Lipids*, 218:168–177, 2019.

[135] G. Cevc, A. Watts, and D. Marsh. Titration of the phase transition of phosphatidylserine bilayer membranes. effects of ph, surface electrostatics, ion binding, and head-group hydration. *Biochemistry*, 20(17):4955–4965, 1981. PMID: 6271176.

Swen HELSTROFFER

Lubrication mechanisms of lipid layers: role of water and electrostatic interactions

Résumé

Les lipides, composants essentiels des membranes biologiques, forment des couches séparées par des films d'eau nanométriques qui assurent la lubrification de presque toutes les surfaces en contacts en biologie. Cette lubrification repose sur l'interaction complexe entre l'hydratation des têtes lipidiques et les forces électrostatiques. Cette thèse examine ces mécanismes en utilisant des techniques de réflectivité aux rayons X et aux neutrons pour analyser l'interaction entre hydratation et électrostatique en régime de couplage fort. De plus, des expériences de tribologie combinées à de la vélocimétrie permettent de lier structure et friction et de localiser les plans de glissement, offrant ainsi une meilleure compréhension des mécanismes de friction et de dissipation d'énergie dans les couches lipidiques.

Mots clés : Biolubrification, hydratation, électrostatique, réflectivité, friction.

Résumé en anglais

Lipids, essential components of biological membranes, form layers separated by nanometric water films that provide lubrication for almost all contacting surfaces in biology. This lubrication relies on the complex interaction between the hydration of lipid heads and electrostatic forces. This thesis explores these mechanisms using X-ray and neutron reflectivity techniques to analyze the interplay between hydration and electrostatics in strong coupling regimes. Additionally, tribology experiments combined with velocimetry link structure to friction and identify slip planes, offering a better understanding of friction and energy dissipation mechanisms in lipid layers.

Keywords: Biolubrication, hydration, electrostatics, reflectivity, friction